Investigation of electron acceleration and deceleration in plasmas

Shao-Wei Chou

SIGILL. UNIVERSITAT. LUDOVIC. MAXIM.

München 2016

Investigation of electron acceleration and deceleration in plasmas

Shao-Wei Chou

Dissertation
an der Fakultät für Physik
der Ludwig–Maximilians–Universität
München

vorgelegt von
Shao-Wei Chou
aus Taipei, Taiwan

München, den 16th March 2016

Erstgutachter: Prof. Dr. Ferenc Krausz
Zweitgutachter: Prof. Dr. Malte C. Kaluza
Tag der mündlichen Prüfung: 11th March 2016

Contents

List of Figures

List of Tables

Abstract

This thesis covers several aspects related to Laser WakeField Acceleration (LWFA). A strong and ultrashort laser pulse can generate plasma waves with accelerating gradients up to 100s GV/m, four orders of magnitude higher than a conventional radio frequency linear accelerator. The LWFA electrons have been characterized as an ultra-short and high brilliance source. These remarkable properties lead to a compact accelerator which is of great scientific interest for building a table-top coherent free electron laser as well as a single-shot electron diffraction device. On the other hand, a new application of LWFA is to utilize the high peak current LWFA electron bunch to drive a wakefield efficiently inside a high density underdense plasma. The resulting wakefield quickly decelerates the driver bunch or accelerates a properly designed witness bunch, and therefore the plasma is utilized as a compact beam dump or an afterburner staged after a regular LWFA.

In the first part of this work, the collective effect driven by LWFA electron bunches was demonstrated. The Ti:Sapphire based 100 TW ATLAS laser system was used to drive LWFA. The target for electron generation included a 300 μm diameter supersonic helium gas jet utilizing the so-called shock-front injection while a second 1.5 mm gas jet was used for electron deceleration. Thanks to the development of the shock-front injection, reproducible electron bunches were generated on a daily basis. The measurement has shown that the electron energy as well as the total bunch charge were dumped almost completely (>90%) after insertion of the second jet. This effect was observed even with several mm separation between the two jets. The observed peak deceleration gradient was 14 GV/m and 5.1 GV/m on average. We interpret the observation by the collective deceleration. A series of comprehensive simulations has been made to understand the physics of the process and showed a good agreement with experiment.

The second part of this work focuses on the LWFA driven by LWS-20 laser system. LWS-20 delivers laser pulses of sub-2-cycle oscillations in electric field and 70 mJ energy from which 40-50 mJ is on target. These pulses were focused within a supersonic helium jet with an exit diameter of 300 μm. Such short pulses excite wakefield in the high density plasma ($> 5 \times 10^{19}$ cm^{-3}) and are a unique tool to produce monoenergetic sub-10 MeV electrons. The corresponding high density plasma and precise control of the injection position of the shock front allowed us to retrieve the dephasing length and accelerating fields, which are two important parameters in LWFA but had never been measured precisely and directly. The experiments showed that the peak energy of the electron spectrum was tunable between 3 to 11 MeV and had an average energy spread 3.4 MeV; the total charge of the electron bunch was 1-3 pC. The density dependent dephasing length was determined to be in the 50-100 μm range with a maximum accelerating field of 100-200 GV/m. The dephasing length was in good agreement with theoretical predictions; however, the accelerating gradient deviated due to incomplete bubble structure evacuation. Our results provide a promising source for the application of single-shot electron diffraction.

Zusammenfassung

Diese Arbeit befasst sich mit verschiedenen Aspekten der Laser-Plasma-Beschleunigung von Elektronen. Hierbei erzeugt ein intensiver, ultrakurzer Laserpuls Plasmawellen mit hohen elektrischen Feldern bis zu einigen Hundert GV/m. Dies entspricht vier Größenordnungen mehr als in üblichen Linearbeschleunigern und wird daher speziell zur Erzeugung ultrakurzer Elektronenpulse mit hoher Brillanz verwendet. Aufgrund der besonderen Eigenschaften und dem kompakten Aufbau, bietet sich Laser-Plasma-Beschleunigung als interessante Quelle für freie Elektronenlaser und für Elektronenbeugung an. Zudem ergibt sich eine neue Anwendung aus dieser Arbeit. Die beschleunigten Elektronenpulse werden wieder als Erzeuger für eine Plasmawelle benutzt. Die so entstandene zweite Plasmawelle bremst die Elektronen ab oder beschleunigt sie weiter. Somit lässt sich das Plasma als kompakten Strahlblocker oder als zweiten Beschleunigungsabschnitt nutzen.

Im ersten Teil der Arbeit zeigen wir diesen kollektiven Effekt. Dafür wird das auf Titanium-Saphir basierende, hundert Terrawatt Leistung Lasersystem ATLAS benutzt. Eine supersonische Gasdüse mit 300 μm Ausgangsdurchmesser wird als Quelle für einen Heliumgasstrahl benutzt. Mithilfe der entwickelten "shock-front" Technik werden Elektronen in die Heliumplasmawelle injiziert und reproduzierbare, stabile Elektronenpulse erzeugt. Ein zweiter 1.5 mm großer Gasstrahl wird dann zur fast vollständigen (>90%) Abbremsung und Absorption - Messungen der Energie und Ladung - der Elektronen genutzt. Dieser Effekt wird auch noch mit einem Abstand von mehreren Millimetern zwischen beiden Gasstrahlen beobachtet und wird als kollektive Abbremsung der Elektronen interpretiert. Ein Mittelwert von bis zu 5.1 GV/m und 14 GV/m für das maximale abbremsende elektrische Feld wird gemessen. Um die physikalischen Prinzipien des Prozesses zu verstehen, werden mehrere nachvollziehbare Simulationen berechnet, welche eine gute Übereinstimmung mit den Messergebnissen zeigen.

Der zweite Teil der Arbeit fokussiert sich auf Laser-Plasma-Beschleunigung mit dem Lasersystem LWS-20. LWS-20 produziert ultrakurze Laserpulse mit weniger als zwei Oszillationsperioden des elektrischen Feldes und 70 mJ Energie. 40-50 mJ der Laserenergie wird in den supersonischen Heliumstrahl aus Gasdüsen mit 300 μm großen Ausgangsdurchmessern fokussiert. Der kurze Laserpuls erzeugt in den Gasstrahlen mit hoher Dichte (Elektronendichte $> 5 \times 10^{19}$ cm^{-3}) eine Plasmawelle und beschleunigt im Besonderen monoenergetische sub-10 MeV Elektronenpulse. Die präzise Kontrolle der Elektroneninjektion durch die "shock-front" Technik erlaubt uns zwei wichtige, davor noch nie genau gemessene Größen im Prozess der Laser-Plasma-Beschleunigung zu bestimmen: Die Länge der beschleunigenden Phase zwischen Plasmawelle und Elektronenpuls und die elektrischen Felder in der Plasmawelle. Im Experiment wird gezeigt, dass die maximale Elektronenenergie zwischen 3 und 11 MeV einstellbar ist, mit einer durchschnittlichen Breite des Spektrums von 3.4 MeV. Die Gesamtladung des Pulses liegt zwischen 1 und 3 pC. Die gemessene Länge der beschleunigenden Phase hängt von der Dichte ab und variiert im Bereich von 50-100 μm mit einem maximal beschleunigendem Feld von 100-200 GV/m. Mit der Theorie stimmt die gemessene Länge überein. Jedoch weicht das gemessene elektrische Feld von den theoretischen Überlegungen ab, da die Hintergrundelektronendichte in der Plasmawelle nicht Null ist. Unsere Ergebnisse liefern somit eine vielversprechende Elektronenquelle, die in Elektronenbeugungsexperimenten mit Einzelschuss Messung benutzt werden kann.

Motivation

Energetic particle beams are important tools in many applications, from basic science to healthcare. For example, one of the most important discovery in the past decade is the confirmation of the existence of the Higgs boson which was the missing building block of the standard model of elementary particles [CMS Collaboration, 2012, 2014]. Higgs bosons having a rest mass of 125 GeV were generated by colliding two proton beams at center-of-mass energy of 7 TeV. The experiment was conducted in the Large Hadron Collider (LHC) in CERN (Switzerland) which produces proton beams up to 6.5 TeV after the latest upgrade in 2015 [Evans and Bryant, 2008] and is the most powerful accelerator in the world. Beside using the high energy beams for fundamental research, ion beams of several hundred MeV per nucleon have been used in radiotherapy for tumours since decades [Amaldi and Kraft, 2005; Combs et al., 2010]. Ion therapy, compared to the traditional X-ray therapy, offers a high local dose at a certain depth inside the tissue but not before and beyond called the “Bragg peak”. The depth of the Bragg peak is adjustable by tuning the energy of ion beams. This property prevents the normal tissue along the beam path from damage during the conformal treatment [Amaldi and Kraft, 2005]. On the other hand, energetic electron beams are a crucial element to produce high quality X-ray radiation, which is generated by the light emission when the electrons are bent by the external fields. High brilliant and coherent X-ray sources are implemented in, for example, structure diagnostic, 4D molecular imagining and spectroscopy, and thus play important roles in the understanding of physics, chemistry, medicine and material science. Many methods have been used to generate high quality X-ray radiation, such as Free Electron Laser (FEL) [Deacon et al., 1977], synchrontron radiation [Elder et al., 1947] and Thomson scattering [Schoenlein et al., 1996].

These conventional accelerators are relative large due to two reasons: the first one is the limitation of the accelerating gradient, and the second one is the energy loss via synchrotron radiation. Because of the material breakdown, the acceleration gradient of radio frequency (RF) accelerators are limited to $\approx$100 MV/m and typically operated around 20 MV/m. Correspondingly, one needs almost 100 m long accelerating stage to reach 1 GeV and about one km for 10 GeV beam. One solution is to arrange the accelerator in a circular configuration and bend the tracks of particles by electromagnets. The particles keep gaining energy in each run. However, the bending magnets cause the charged particles to emit synchrotron radiation of a total power $\propto \frac{\gamma^4}{m^4 \cdot L} I_A$, where γ and m is the Lorentz factor and the mass of charged particles respectively, L is the bending radius and I_A is the current of the beam [Alexander Wu Chao and Tigner, 2013]. As a consequence, high energy circular accelerators require very large circumstances to prevent the energy loss. The cost for such huge infrastructure becomes very expansive. For example, LHC consists of accelerating sections in a 26.7 km long circular tunnel and costs ≈6 billion dollars for the construction and ≈1 billions dollars for the operational cost per year [Giudice, 2012]. Since the radiative energy loss is much more for electrons than ions due to its light weight, high energy electrons are only reachable by using linear accelerators. The upcoming International Linear Collider (ILC) is planned to get electrons up to 500 GeV in 15 km long linear accelerator. The budget of the ILC project is 25 billion dollars, and the construction takes about 10 years [Sennyu et al., 2013]. Other “smaller” facilities for the application are also significantly larger than a university scale. For example, the FEL source LCLS at SLAC (USA) is driven by 13.6 GeV electrons generated by a 1 km linear accelerator [Bharadwaj et al., 1997; Yeremian et al., 2015].

It is clear that to further scale up the achievable energies based on the current RF accelerators will go beyond the affordable cost very soon, also, even for a small machine, the price is too high to be used in university, clinic or medium-sized industry. In 1979, Tajima and Dawson proposed to accelerate electrons in the wakefield of a plasma excited by a high intensity laser pulse [Tajima and Dawson, 1979], and later in 1985, Chen et al. suggested to employ a bunched relativistic electron beam to generate the plasma wakefield for the electron acceleration [Chen et al., 1985]. These two schemes are frequently called Laser WakeField Acceleration (**LWFA**) and Plasma WakeField Acceleration (**PWFA**) respectively. Since plasma is already an ionized matter which does not suffer from the material break down, the amplitude of the electric field inside plasma can be much larger than a conventional RF accelerator. In LWFA as well as PWFA, the plasma electrons are expelled by the electromagnetic field from drivers of either laser pulses or charged particle bunches. Since the ions are much heavier than electrons, the homogeneous distribution of plasma ions is not influenced by the external field. The ion background applies a restoring force to the plasma electrons which overshoot and start harmonic or, at stronger drivers, anharmonic or even 3D oscillations and set up a plasma wave called wakefield. Because the distance of the charge separation is on the order of a plasma wavelength λ_p, the electric field within the wakefield can be as high as 100s GV/m. If some electrons are injected into the proper phase of the wakefield, they are accelerated to high energy within a distance of several order of magnitude smaller than in RF accelerators. However, neither high intensity lasers (peak power $> 10^{17}$ W/cm^2) nor suitable electron bunches (bunch duration $\leq$ few ps) were available until the late 90s. The first experimental proof of LWFA was using an external linear accelerator to inject electrons into a wakefield driven by the beat wave of a two-frequency laser beam where an energy gain of 7 MeV was observed [Clayton et al., 1993]. The first fully laser-driven wakefield experiment was demonstrated two years later [Nakajima et al., 1995]. Due to lack of powerful drivers, the early experiments are based on the linear regime, which has low efficiency of the energy transfer and delivers electrons with large divergence and thermal-like spectra [Umstadter et al., 1996; Amiranoff et al., 1998; Malka, 2002]. These low quality electrons are not usable for most of the applications. With the development of the Chirped Pulse Amplification (CPA) technology [Strickland and Mourou, 1985], laser pulses reach relativistic intensity of 10^{18} W/cm^2 with 10s of fs pulse duration.

In 2004, by using such lasers, low divergence and quasi-monoenergetic electrons of $\approx$100 MeV were generated in a highly nonlinear scheme called bubble regime [Mangles et al., 2004; Faure et al., 2004; Geddes et al., 2004]. In this regime, the electrons are accelerated in a round void following the laser pulse, which consists only ions and is surrounded by a thin layer of electrons [Pukhov and Meyer-ter Vehn, 2002; Kostyukov et al., 2004]. The next milestone in the development of LWFA was the demonstration of 1 GeV electrons from a 3 cm long capillary discharge, which corresponds to 30 GeV/m accelerating gradient [Leemans et al., 2006]. Many follow-up experiments have shown GeV-scale electrons by different approaches, e.g., [Osterhoff et al., 2008; Hafz et al., 2008; Pollock et al., 2011; Liu et al., 2011; Kim et al., 2013; Wang et al., 2013; Masson-Laborde et al., 2014]. The current record of highest electron energy from LWFA is 4.2 GeV [Leemans et al., 2014]. In the past decade, beside the race of the highest energy, the quality and the stability of LWFA electrons have been significantly improved [Osterhoff et al., 2008; Faure et al., 2010; Buck et al., 2013], and other properties have been characterized, such as ultra-low transverse emittance (normalized emittance on the order of πmm mrad), and very small source size (sub μm) [Phuoc et al., 2006; Sears et al., 2010a; Brunetti et al., 2010; Weingartner et al., 2012; Kneip et al., 2012; Plateau et al., 2013; Manahan et al., 2014] and ultra-short bunch duration ($\leq$5 fs) [Buck et al., 2011; Lundh et al., 2011; Bajlekov et al., 2013; Kotaki et al., 2015]. These unique properties make the LWFA electrons ideal drivers for compact X-ray or gamma rays sources based on, e.g., the undulator radiation [Schlenvoigt et al., 2007; Fuchs et al., 2009] and Thomson scattering [Ta Phuoc et al., 2012; Powers et al., 2013; Khrennikov et al., 2015]. Beside the generation of photons, the sub-10 MeV electron bunches from LWFA driven by sub-5 fs laser pulses are also unique for single-shot time-resolved electron diffraction experiments [Hastings et al., 2006].

On the other hand, the requirement of the electron bunches for the PWFA is even more challenging, and so far only SLAC and CERN are capable to conduct such experiments. The first demonstration of a 155 MeV energy gain in a wakefield driven by 28.5 GeV electron beam was observed in 2004 [Muggli et al., 2004]. In 2006, a landmark experiment of the PWFA operated in the bubble regime showed energy doubling of a 42 GeV electron bunch in a 1 m long lithium plasma channel [Blumenfeld et al., 2007]. In this experiment, only a very small portion of the electrons sitting in the tail of the driver bunch were accelerated, and the spectrum was very broad. This drawback was improved later by using two-bunch configuration where the first bunch drives the wakefield to accelerate a tailing bunch. By this method, 2 GeV monoenergetic energy gain of a 20 GeV electron bunch was observed [Litos et al., 2014]. One of the major challenges is the bunch length of the driver. The optimized bunch length is about $\lambda_p/2$, and the acceleration gradient of a regular PWFA is inversely proportional to the square of the bunch length [Lu et al., 2005]. Typical RF accelerators use thermal electron guns as injectors which give electron beams of ns scale pulse duration, and therefore external compression of such a bunch is necessary for PWFA. However, the electron pulse duration from the state-of-art linear accelerators are limited to an order of 100 fs [Vafaei-Najafabadi et al., 2014; Krejcik et al., 2003]. This limitation is mainly associated to the emission of synchrotron radiation from the magnetic bunch compressor [Piot, 2004]; the emission process causes the energy loss of electron bunch $\propto \gamma^4$, and the dilution of the fractional energy spread as well as the increases of the transverse emittance are $\propto \gamma^6$ and $\propto \gamma^5$ respectively [Helm et al., 1973]. These effects are pronounced not only for GeV but also for 100 MeV scale electron beams. The trade-off between the compressed pulse length and the quality of the bunch limited the achievable pulse duration. Therefore, the typical electron densities in a conventional PWFA experiment are in the range of $10^{16} - 10^{17}$ cm^{-3} which correspond to an acceleration gradient around 10s GV/m.

Heuristically, electron bunches from LWFA have intrinsically ultra-short bunch lengths, which allow the feasibility to drive PWFA in a high density plasma with the electron density up to 10^{20} cm^{-3}, and the acceleration gradient is on the order of TV/m. However, the indication of wakefield driven by the LWFA electrons have not yet been observed experimentally.

Structure of this work

Chapter one introduces physics behind the generation process of wakefield. The fundamental formulas to describe the wakefields driven by both laser pulses and charged particles are derived. The limitations as well as the nonlinear interactions between plasma and drivers which influence the performance of the wakefield accelerator are also included.

Chapter two summarizes previous results and literature as well as results from Particle-In-Cell simulations regarding the study of the propagation of LWFA electron bunches. Unlike the behavior of bunches from the linear accelerator inside plasma which have been studied for decades, similar effects for the ultra-short bunches from LWFA have not been studied comprehensively. This chapter prepares the knowledge background for the interpretation of the results of Chapter five.

Chapter three describes two laser systems, ATLAS and LWS-20, and electron diagnostics which are used in this work.

Chapter four discusses the design and the characterization of gas targets, which includes gas cells and supersonic jets. The gas cells were used in the ATLAS campaigns such as the emittance measurement and the double gas cell experiment. A significant part of this chapter devotes to determine the shock width of the shock front generated from supersonic jets. The absolute width is critical for the performance of the shock-front injection which was widely used in this work.

Chapter five mainly studies the collective effect caused by LWFA electrons, where the deceleration of an ultra-high gradient up to 14 GV/m was observed. Three different experiments are included in the discussion, which are single gas cell experiment for the emittance measurement, double gas cell and double gas jet for the observation of collective deceleration.

Chapter six discusses the generation of sub-10 MeV electrons driven by sub-2-cycle light pulses (LWS-20). Both of the self-injection and the shock-front injection are included.

Chapter seven gives summary and outlook.

Chapter 1

Concept of Wakefield Acceleration in Plasmas

When a matter is exposed to a strong enough electric field [Keldysh, 1965; Littman et al., 1978], high temperature or shock wave [Burtsev and Kalinin, 2007], it gets ionized and contains free electrons and trunks of positively charged ions. This state of matter is called plasma. Plasmas are characterized by three unique properties: the quasi-neutrality, a high conductivity and an anomalous dispersion. In plasmas, electric fields of charges are shielded. This property is quantified by the *Debye length* λ_D which specifies the minimum length scale required for the opposite-charged particles to be electrically shielded [Boyd and Sanderson, 2003]:

$$\lambda_D \equiv \sqrt{\frac{k_B T_e}{4\pi n_e e^2}} \approx 7.43 \sqrt{\frac{T_e(\mathrm{eV})}{n_e(\mathrm{cm}^{-3})}}\ \mathrm{m} \tag{1.1}$$

where k_B is the Boltzmann constant, n_e is the particle density of electrons, and T_e is specified temperature of electrons. The number of particles inside a Debye sphere is calculated by:

$$N_D = \frac{4\pi}{3}\lambda_D^3 n_e \approx 1.72 \times 10^9 \frac{T_e(\mathrm{eV})^{3/2}}{\sqrt{n_e(\mathrm{cm}^{-3})}}$$

when $N_D \gg 1$, the dynamics of plasma is dominated by the collective effects, and the contribution of collisions between particles is negligible. In the wakefield acceleration, the plasma of the wakefield experiments are usually generated by the field ionization. The T_e of such plasma has only a few eV which is negligible compared to the MeV energy from direct wiggling in the transverse electric field of laser, also typical n_e is around 10^{19} cm^{-3} which gives N_D =2830 at T_e =300 eV. As a consequence, the thermal movement of electrons is ignored, the ions acts as a static and charge-neutralizing background, and the physics behind is controlled by collective interaction. In this chapter we discuss the physics of the relevant collective phenomena, the plasma wave, under the influences of high intensity lasers or charged particle bunches. The behavior of plasma is described by the cold collision-less fluid equation.

Another important parameter to characterize plasmas is the **plasma frequency** ω_p. When a slab of plasma electrons has an infinitesimal displacement Δx in a plasma against its ion background, it experiences a restoring force $\vec{F} = m_\Delta \ddot{\Delta x} = -Q\vec{E}_{res}$ with total mass $m_\Delta = m \cdot n_e \cdot A_\Delta \cdot \Delta x$, restoring electric field $\vec{E}_{res}$ and the displaced charge $Q = -en_e A_\Delta \cdot \Delta x$ where A_Δ is the area of the cross section of the displaced slab, and m is the mass of electron. According to the Gaussian law (1.2), the electric field from an infinitesimally thin slab is $\left|\vec{E}_{res}\right| = -4\pi e n_e \cdot \Delta x$. By combing these relations, we get

$$\frac{d^2}{dt^2}\Delta x + \frac{4\pi e^2 n_e}{m}\Delta x = 0$$

The equation shows the displacement has a characteristic oscillation frequency ω_p which is called plasma frequency and is defined as:

$$\omega_p = \sqrt{\frac{4\pi e^2 n_e}{m}}$$

1.1 Wakefield Generation

A wakefield is generated by the electric field of a laser pulse or the Coulomb force of a charged particle bunch. We start from the general formula for the both cases. To derive the equations for describing a plasma wakefield, the plasma is assumed to consist of a fully ionized matter with a single component of $Z_i = 1$ and $n_i = n_0$. The electromagnetic field and the movement of electrons are calculated by the Maxwell's equations and the Lorentz equation of motion:

$$\nabla \cdot \vec{E} = 4\pi e \left(n_0 - n_e\right) \tag{1.2}$$

$$\nabla \times \vec{E} = -\frac{1}{c}\frac{\partial \vec{B}}{\partial t} \tag{1.3}$$

$$\nabla \cdot \vec{B} = 0 \tag{1.4}$$

$$\nabla \times \vec{B} = \frac{4\pi}{c}\vec{J} + \frac{1}{c}\frac{\partial \vec{E}}{\partial t} = -\frac{1}{c}\left(4\pi e n_e \vec{v} - \frac{\partial \vec{E}}{\partial t}\right) \tag{1.5}$$

$$\frac{d\vec{p}}{dt} = \frac{\partial \vec{p}}{\partial t} + (\vec{v} \cdot \nabla)\, \vec{p} = -e \left(\vec{E} + \frac{1}{c} \vec{v} \times \vec{B} \right) \tag{1.6}$$

where $\vec{v}$ is the electron velocity, $\vec{J}$ is the current density, $\vec{p} = \gamma m \vec{v}$ and $\gamma = \sqrt{1 + \frac{p^2}{m^2 c^2}}$ are the relativistic momentum and Lorentz factor respectively. Since the plasma is assumed to be fully ionized, no free electron will be created during interaction. The continuity equation must be satisfied

$$\frac{\partial n_e}{\partial t} + \nabla \cdot (\vec{v} n_e) = 0 \tag{1.7}$$

From (1.3) and (1.4) a gauge transformation is made by introducing a vector potential $\vec{A}$ and a scalar potential ϕ such that

$$\vec{E} = -\frac{1}{c} \frac{\partial \vec{A}}{\partial t} - \nabla \phi \tag{1.8}$$

and

$$\vec{B} = \nabla \times \vec{A}$$

This transformation is, however, not unique. We choose the so-called *Coulomb gauge* which satisfies $\nabla \cdot \vec{A} = 0$. By using the relation $\nabla \times (\nabla \times \vec{q}) = \nabla (\nabla \cdot \vec{q}) - \nabla^2 \vec{q}$ from the general property of vector calculus, (1.5) is rewritten as:

$$\nabla^2 \vec{A} - \frac{1}{c^2} \frac{\partial^2 \vec{A}}{\partial t^2} = -\frac{4\pi \vec{J}}{c} + \frac{1}{c} \frac{\partial \nabla \phi}{\partial t} \tag{1.9}$$

and for (1.2)

$$\nabla^2 \phi = -4\pi e \,(n_0 - n_e) \tag{1.10}$$

The equation (1.9) is interpreted as that the vector potential $\vec{A}$ is driven by external source $\vec{J}$ and ϕ which is either Coulomb force of a charged beam or electric field of a laser pulse. If the strength of driver is not too large, the equation is solved by perturbation theory. This case is called *linear regime*, and the solution is typically a sinusoidal oscillating density modulation which is the plasma wave. In the case of an electron beam driver, this regime is applicable when

$$\frac{n_b}{n_0} < 10$$

where n_b is the peak density of the electron beam [Lu et al., 2005]. When n_b is very large, the plasma electrons along the path of beam propagation will be completely blown out and generate a large longitudinal current [Rosenzweig et al., 2004; Lu et al., 2006b]. In such situation the contribution of the nonlinear terms has to be taken into account, which is called *nonlinear regime.* Similar case happens to laser-driven wakefield. The strength of laser is characterized by a_0, which is defined as the peak value of the normalized vector potential of the laser $\vec{a} = e\vec{A}/m_e c^2$. The laser-driven wakefield needs to be treated nonlinearly when ${a_0}^2 \gg 1$. In this chapter we consider four cases that are relevant to our study: 3D linear regime of electron-driven wakefield, 1D linear and 1D nonlinear regime from laser driver, and 3D highly nonlinear case called bubble regime.

1.1.1 Excitation of a Plasma Wave in Cold Plasma by a Relativistic Electron Beam in Linear Regime

The linear fluid equation for describing the dynamics of plasma response to a low-charged relativistic electron beam is derived and solved by Chen and Dawson in 1984 [Chen et al., 1985; Chen, 1987] by perturbation theory. Since the response is expected to be a quasi-static wave following the driver of $\beta_b \equiv v_b/c \simeq 1$, where v_b is the velocity of the beam, it is convenient to introduce a co-moving coordinate system (ξ,τ) which are defined as $\xi = x - ct$ and $\tau = t$. This coordinate system is interpreted as a frame following the driver with a speed c, and ξ corresponds to the distance behind the driver at a specific time τ. The fluid equation is significantly simplified by an additional assumption: the driving field ϕ and the current $\vec{J}$ evolve slowly during the transit time of the driver through the plasma [Sprangle et al., 1990]. The corresponding derivatives along the propagation axis are simplified as

$$\frac{\partial}{\partial x} = \frac{\partial}{\partial \xi} \qquad\qquad \frac{\partial}{\partial t} = \frac{\partial}{\partial \tau} - c\frac{\partial}{\partial \xi} \simeq -c\frac{\partial}{\partial \xi}, \tag{1.11}$$

and the transverse derivatives stay the same. Assuming that the perturbed plasma electron density n_1 is very small $\frac{n_1}{n_0} \ll 1$ and the unperturbed plasma velocity $v_0 \approx 0$, the perturbation form of (1.6) and (1.7) are

$$-mc\frac{\partial \vec{v_1}}{\partial \xi} = -e\vec{E}_1 \tag{1.12}$$

$$-c\frac{\partial n_1}{\partial \xi} + n_0 \nabla \cdot \vec{v_1} = 0 \tag{1.13}$$

where the subscript "1" stands for the perturbation. Because of $\frac{\partial^2}{\partial x^2} - \frac{1}{c^2}\frac{\partial^2}{\partial t^2} \approx 0$, (1.9) and (1.10) give:

$$\nabla_\perp^2 \vec{A}_1 = -\frac{4\pi}{c}\vec{J}_1 - \frac{\partial \nabla \phi_1}{\partial \xi} \tag{1.14}$$

where $\nabla_\perp^2 \equiv \frac{\partial^2}{\partial y^2} + \frac{\partial^2}{\partial z^2}$, and

$$\nabla^2 \phi_1 = -4\pi \rho_1 \tag{1.15}$$

where the source terms of the electron charge density ρ_1 and the current density $\vec{J}_1$ are established by the common contribution of the plasma perturbation and the external electron bunch with a charge density $-e\sigma\left(\vec{x}\right)$. The electron bunch is assumed to be highly relativistic with a velocity $\vec{v} \sim \vec{c}$; hence the contribution to the transverse current in the bunch is negligible, we get the source terms:

$$\begin{cases} \rho_1\left(\vec{x}\right) = -en_1\left(\vec{x}\right) - e\sigma\left(\vec{x}\right) \\ \vec{J}_1\left(\vec{x}\right) = -en_0\vec{v_1}\left(\vec{x}\right) - e\vec{c}\sigma\left(\vec{x}\right) \end{cases} \tag{1.16}$$

By substituting these terms into (1.12)-(1.15), after rearrangement, one gets

$$\left(\frac{\partial^2}{\partial\xi^2} + k_p^2\right) n_1 = -k_p^2\sigma\left(\vec{x}\right) \tag{1.17}$$

where $k_p \equiv \frac{\omega_p}{c} = \sqrt{\frac{4\pi e^2 n_0}{mc^2}}$ is the wavenumber of the plasma wave. The equation (1.17) is a standard inhomogeneous Helmholtz equation which is solved by the Green's function once the function of the source is known, and the electric and magnetic fields are calculated straightforward by using the solution of n_1 and Maxwell's equations.

The electron bunches used in the PWFA are normally assumed to have a cylindrical symmetry bi-Gaussian density distribution [Bajlekov et al., 2013; Weingartner et al., 2012].

$$\sigma\left(\vec{x}\right) = \sigma_b\left(r,\xi\right) = -en_b e^{-\xi^2/2\sigma_x^2} e^{-r^2/2\sigma_r^2} \tag{1.18}$$

In this case, the wakefield is solved analytically [Lu et al., 2005], and the maximum amplitude of the longitudinal wakefield along the symmetry axis ($r = 0$) and far behind the driver ($\xi \ll 0$) is obtained

$$\frac{E_{x-max}}{E_0} = \sqrt{2\pi}\left[\left(\frac{n_b}{n_0}\right)\left(k_p\sigma_x e^{-k_p{}^2\sigma_x{}^2/2}\right)\left(\frac{k_p{}^2\sigma_r{}^2}{2}\right) \times \left(e^{\frac{k_p{}^2\sigma_r{}^2}{2}}\right)\Gamma\left(0,\frac{k_p{}^2\sigma_r{}^2}{2}\right)\right] \tag{1.19}$$

where $\Gamma\left(\alpha,\beta\right) \equiv \int_\beta^\infty t^{\alpha-1}e^{-t}dt$ is the upper incomplete gamma function, and $E_0 \equiv m\omega_p c/e$ is the cold non-relativistic wave breaking field [Dawson, 1959] which is explained in detail in section 1.2.1.

Nowadays, electron sources from almost all of the conventional linear accelerators are based on thermionic emission of electron guns which typically deliver pulses of a duration from ps to ns [Munawar and Ul, 2013; Yang et al., 2002; Grabenhofer et al., 2014]. In order to increase n_b, all of the currently running PWFA experiments are focusing the electron beams externally, and this way reaching the condition $\sigma_r \ll \sigma_x$. We recover that, by maximizing (1.19) with respect to k_p, the largest wake amplitude occurs when $k_p\sigma_x = 1$, which is called the "matching condition". Under these two conditions and using the asymptotic form of $\Gamma\left(0, \frac{{k_p}^2{\sigma_r}^2}{2}\right)$, a useful engineering expression of the maximum amplitude E_{x-max} is written [Joshi et al., 2002]

$$E_{x-max} \approx \left(236\ \frac{MV}{m}\right)\left(\frac{N}{4\times 10^{10}}\right)\left(\frac{600\ \mu m}{\sigma_x}\right)^2 ln\left(\frac{50\ \mu m}{\sigma_r}\sqrt{\frac{10^{16}\ cm^{-3}}{n_0}}\right), \tag{1.20}$$

where N is the total number of electrons in the driver bunch. This formula is widely used in PWFA literature [Hogan et al., 2010; Caldwell et al., 2009; Joshi and Mori, 2006; Muggli and Hogan, 2009]. One of the most important conclusion is that $W_{\parallel max}$ scales as σ_x^{-2} which motivates efforts to greatly compress the electron bunch longitudinally [Grabenhofer et al., 2014]. It is possible to prove from (1.19) that $E_{x-max} \propto n_0^2$ under matching condition. For example, in the first FACET experiment [Hogan et al., 2010], the parameters were $n_0 = 10^{17}$, $\sigma_x = 100$ μm, $\sigma_r = 5$ μm and $N = 2\times 10^{10}$ which gave $W_{\parallel max}$ =5 GV/m. The acceleration gradient was increased by a factor of 16 by compressing the bunch to $\sigma_x = 25$ μm [Litos et al., 2014].

1.1.2 Laser-Driven Wakefield in Linear Regime

Similarly to charged particle beams, plasma waves can also be excited by an intense and localized electromagnetic field from a laser pulse. The dynamics of an electron within a weak laser beam is dominated by the transverse quiver movement along the direction of polarization of the electric field. However, when the laser beam is relatively strong, the velocity of the quiver motion is close to the speed of light, and therefore the contribution from the magnetic field become significant. The force from this higher order effect is called the "ponderomotive force". By using perturbation approach, the ponderomotive force $\vec{F_p}$ is written as [Esarey and Sprangle, 1996]

$$\vec{F_p} = -mc^2\nabla\frac{a^2}{2}.$$

Consequently, the laser-driven wakefield is derived in a similar way as the electron-driven wakefield. Firstly, we notice the source term on the RHS of (1.12) is added by $\vec{F_p}$. By applying the quasi-static approximation, we get the new expression of the Helmholtz equation of (1.17)

$$\left(\frac{\partial^2}{\partial\xi^2} + k_p^2\right)\frac{n_1}{n_0} = \nabla^2\frac{a^2}{2}. \tag{1.21}$$

With the help of Poisson equation (1.15), the scalar potential is solved by using the Green's function. For example, the maximum amplitude of the longitudinal wakefield of a Gaussian pulse $a^2 = a_0^2 exp\left[-\xi^2/2(\tau_L c)^2\right]$ is [Gorbunov and Kirsanov, 1987; Amiranoff et al., 1998]

$$\frac{E_{x-max}}{E_0} = \frac{\sqrt{\pi} k_p \tau_L c}{2} a_0^2 e^{-k_p^2(\tau_L c)^2/4} \tag{1.22}$$

The amplitude reaches a maximum $\mathbf{\frac{E_{x-max}}{E_0} = \sqrt{\frac{\pi}{2e}} a_0^2 \approx 0.76 a_0^2}$ when $\mathbf{k_p \tau_L c = \sqrt{2}}$ and $\mathbf{a_0 < 1}$, which is the matching condition for the laser-driven wakefield. Since the transverse quiver field in the laser is $E_q = a_0 E_0$ [Esarey et al., 2009], the ratio $E_{x-max}/E_q \approx 0.76 a_0$. For example, when $a_0 = 0.2$, $E_{x-max}/E_q = 0.15$.

Another important quantity in the linear regime is the plasma dispersion relation. We first notice that the dominant component of the current density is the quiver current:

$$\vec{J_q} = -en_0 \frac{\vec{p_q}}{m} = -\frac{e^2 n_0}{mc} \vec{A}$$

where $\vec{p_q} = \frac{e}{c}\vec{A} = mc\vec{a}$ is the quiver momentum driven by the laser [Gibbon, 2005]. Under this assumption $\nabla\phi$ is negligible, the wave equation (1.9) becomes

$$\nabla^2 \vec{A} - \frac{1}{c^2}\frac{\partial^2 \vec{A}}{\partial t^2} \approx -\frac{4\pi \vec{J_q}}{c} = \frac{4\pi e^2 n_0}{mc^2}\vec{A} = \frac{\omega_p^2}{c^2}\vec{A}$$

A more general form of linearly polarized plane wave by assuming $\vec{A} = Re\left[\vec{A_0} e^{i\left(\vec{k}\cdot\vec{r} - \omega t\right)}\right]$ is taken into account, then the above equation is reduced to

$$\omega^2 = \omega_p^2 + k^2 c^2 \tag{1.23}$$

By using the definitions [Jackson, 1999], the expressions of the phase velocity v_{ph} and the group velocity v_g of a electromagnetic wave are

$$v_{ph} = \frac{\omega}{k} = \frac{c}{\eta}, \qquad v_g = \frac{d\omega}{dk} = c\eta, \qquad \text{with} \quad \eta \equiv \sqrt{1 - \frac{\omega_p^2}{\omega^2}}. \tag{1.24}$$

The η is imaginary when $\omega_p \geq \omega$, which means the plane wave will be absorbed by the plasma. The electron density for $\omega_p = \omega$ is called the critical density n_c which is translated into practical units

$$n_c \approx 1.1 \times 10^{21} \times \lambda_L{}^{-2}\,(\mu\mathrm{m})\ \ \mathrm{cm}^{-3}$$

where λ_L is the central wavelength of the electromagnetic wave/laser. The plasma is called *underdense* when $n_0 < n_c$. In the underdense regime, the physics is dominated by the interaction between laser and plasma wave such as the wakefield acceleration and the three dimensional self-modulation of laser [Kelley, 1965; Sprangle et al., 1990; Esarey et al., 1997b; Karsch et al., 2007]. In the overdense regime, where $n_0 > n_c$, the waves are reflected as they approach $n_0 = n_c$, and the observed phenomena are mainly contributed by the electron transportation and the interaction between the reflected fields and surface electrons, e.g. the ion acceleration [Yin et al., 2007] and the surface high harmonic generation [der Linde et al., 1995]. The laser pulses used in this work have $\lambda_L \approx 800$ nm which corresponds to $n_c = 1.7 \times 10^{21}$ cm^{-3}. Since the typical $n_0 \approx 10^{18}$ cm^{-3}, the physics covered by this work is in the underdense regime.

1.1.3 Laser-Driven Wakefield in 1D Non-linear Regime

For a high intensity laser of $a_0 \geq 1$, the perturbation treatment is no longer applicable. In this section, a general analytical solution of a wakefield in the 1D case without assuming $\gamma = 1$, $n_e \approx n_0$ and $v_p \approx c$ is derived [Esarey et al., 1997b; Gibbon, 2005]. The 1D condition means the plasma properties are isotropic in the transverse dimension, i.e., $\frac{\partial}{\partial \perp} = 0$. For other more general conditions, analytical solutions are generally not available, and numerical simulations based on the particle in cell (PIC) algorithm are required, which will be discussed later.

Similar to the derivation in section 1.1.2, we start from a linear polarized plane wave with vector potential $\vec{A} = A\left(x - v_g t\right)\hat{y}$ propagates with the speed of group velocity v_g. Here we apply again a co-moving coordinate transformation, but the frame moves with a speed of the group velocity v_g instead of c such that $\xi = x - v_g t$ and $\tau = t$. The corresponding derivatives are

$$\frac{\partial}{\partial x} = \frac{\partial}{\partial \xi}, \qquad \frac{\partial}{\partial t} = \frac{\partial}{\partial \tau} - v_g \frac{\partial}{\partial \xi}.$$

Given the benefit of a hindsight, the evolution rate of a laser pulse is typically at the time scale of the Rayleigh diffraction time z_R/c, where z_R is the Rayleigh length, which is much longer than plasma period. Therefore the temporal derivative $\partial/\partial\tau$ is negligible compared to $\partial/\partial\xi$. By applying this quasi-static approximation and the transformation to (1.2)-(1.7), the following relations are derived [Gibbon, 2005]:

$$n = \frac{\beta_g}{\beta_g - \beta_x}, \tag{1.25}$$

$$\Phi - \gamma\left(1 - \beta_x \beta_g\right) + 1 = 0. \tag{1.26}$$

$$\gamma = \gamma_g^2 \left(1 + \Phi\right)\left(1 - \beta_g \varphi\right),$$

and

$$\beta_x = \frac{1}{\beta_g}\left[1-\gamma_g^{-2}(1-\beta_g\varphi)^{-1}\right] = \frac{\beta_g-\varphi}{1-\beta_g\varphi}$$

where $n = n_e/n_0$, $\beta_x = v_x/c$, $\beta_g = v_g/c$, $\Phi = \frac{e\phi}{mc^2}$, $\varphi \equiv \sqrt{1-\frac{1+a^2}{\gamma_g^2(1+\Phi)^2}}$ and $\gamma_g = \sqrt{1-\beta_g^2}^{-1}$. Here the boundary condition $\{\Phi, \beta_x\} = 0$ and $\{n, \gamma\} = 1$ at $\xi \to +\infty$ are used implicitly because of the absence of plasma wave at $\xi \to +\infty$.

By providing the representation of β_x to the conservation equation of density (1.25), we get

$$n = \gamma_g^2\beta_g\left(\varphi^{-1}-\beta_g\right), \tag{1.27}$$

and finally the Poisson equation (1.10) is rewritten in the new coordinate system of the 1D case with only the dependence on the external parameters:

$$\frac{\partial^2\Phi}{\partial\xi^2} = k_p^2\,(n-1) = k_p^2\gamma_g^2\left[\frac{(1+\Phi)\,\beta_g}{\sqrt{(1+\Phi)^2-\gamma_g^{-2}\,(1+a^2)}}-1\right]. \tag{1.28}$$

This nonlinear differential equation is solved numerically for most of cases. One exception is that when the pump pulse is square-like and in the limit $\beta_g \approx 1$, an exact analytical solution is derived [Berezhiani and Murusidze, 1990], and

$$E_{x-max} \propto \frac{{a_0}^2}{\sqrt{1+{a_0}^2}}.$$

One example of a wakefield driven by a Gaussian laser pulse of $a_0 = 2$ is shown in Fig. 1.1, where several features of a nonlinear wakefield is noticed: the density distribution as well as the normalized potential are no longer sinusoidal. The phase of the largest acceleration gradient shifts to the end of a plasma period. The oscillation period is also significantly larger than the λ_p. These features becomes more significant with the increase of a_0.

1.1.4 Bubble Regime

Our discussion so far is limited to either the perturbation of plasma or the simplified 1D regime. In another extreme of a strong driver in a 3D plasma, the theoretical work has shown a robust and promising acceleration process which is called bubble or blow-out regime [Pukhov and Meyer-ter Vehn, 2002; Rosenzweig et al., 1991]. This regime requires either high-charged and energetic particle bunches or high intensity laser pulses of lengths much smaller than λ_p. The resulting strong transverse electric field as well as the ponderomotive force of the laser expel all plasma electrons radially and leave an ion channel behind the driver. The channel

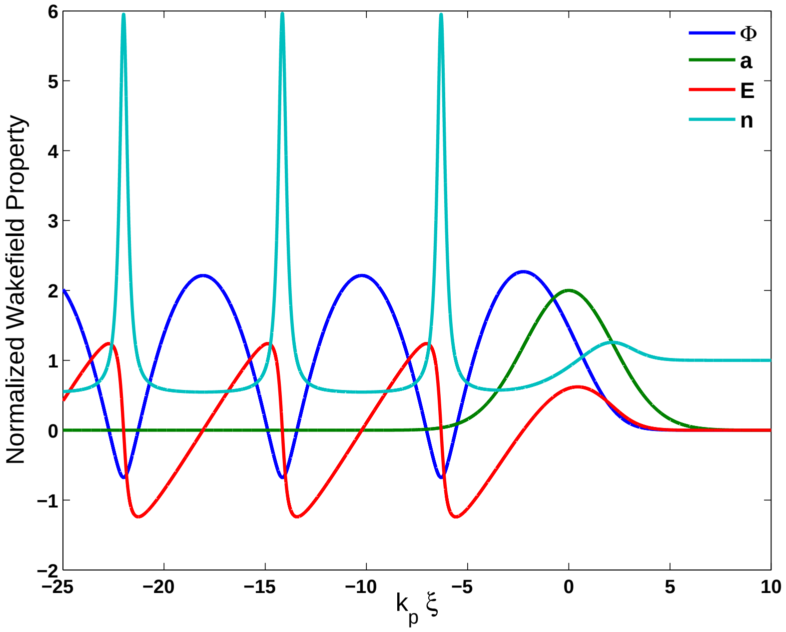

Figure 1.1: A nonlinear 1D wakefield driven by laser with $a_0 = 2$.

is formed by a thin and dense layer of expelled electrons of a thickness δ_s, and a slightly perturbed plasma surrounds the outside of the layer. The strong static field of the ion channel pulls back the expelled electrons after a distance about λ_p. The trajectories of the electrons overshoot and oscillate around the propagation axis, which forms a wakefield. The process creates a cavity of pure ions behind the driver. The geometry of the bubble is illustrated in Fig. 1.2. The geometry of the bubble is calculated by assuming a homogeneous distribution of electron density within the thin layer and ignored the perturbation of plasma outside of bubble [Lu et al., 2006a]. We start by considering a wakefield driven by a bi-Gaussian electron bunch as defined by (1.18) with $k_p\sigma_x \ll 1$ and $k_p\sigma_r \ll 1$. The transverse

Figure 1.2: Density distribution of plasma electrons in the bubble regime. The driver is a electron bunch as shown in blue, and a cavity free of electrons follows behind the bunch.

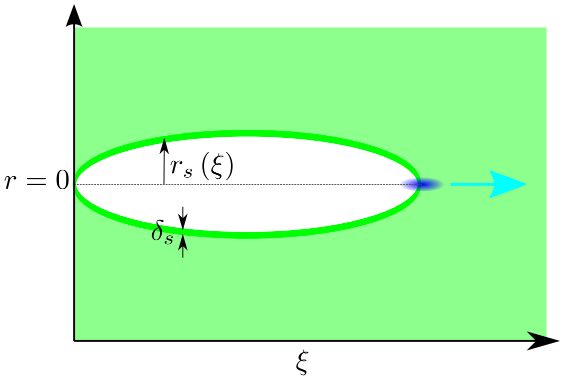

density profile of the plasma electrons is assumed to be cylindrically symmetric and consists a cavity ($n_e = 0$ when $r < r_s$) and a homogeneous plasma ($n_e = n_0$) separated by a thin layer electrons of thickness δ_s. Under these boundary conditions, we get the equation of motion of electrons sitting in the layer [Mora and Antonsen, 1997; Lu et al., 2006b]

$$r_s \frac{d^2 r_s}{d\xi^2} + 2\left(\frac{dr_s}{d\xi}\right)^2 + 1 = \frac{4\vartheta}{{r_s}^2} \tag{1.29}$$

where $\vartheta(\xi) = \int_0^{r \gg \sigma_r} \sigma_b(r,\xi)\, r dr$ and σ_b as defined in (1.18). Since $\sigma_x \ll r_s$, the source term on the RHS is ignored for most of the trajectories of the layer electrons. As (1.29) describes, the shape of the bubble is almost a perfect circle [1].

In the case of the laser-driven wakfield, the ponderomotive force only influences the region of a laser pulse while the space-charge force of an electron bunch extend much beyond the location of the bunch. In addition, an over focused laser pulse cannot be guided inside a fully evacuated ion channel because there is not enough refraction index gradient to introduce self-focusing (see section 1.3.1). Therefore, the compromised situation is that the spot size of the laser (σ_L) needs to match the maximum radius of the bubble. Based on 3D PIC simulations, the optimized condition for the laser-driven bubble is [Lu et al., 2007]

$$k_p (r_s)_{max} \simeq k_p \sigma_L = 2\sqrt{a_0}, \qquad \text{and} \qquad a_0 \geq 4. \tag{1.30}$$

It is important to notice that the cavitation still happens when $4 > a_0 \geq 2$ except that the shape of the bubble is detuned from a sphere.

The bubble regime has several unique properties. Firstly, the acceleration gradient is constant, and the transverse focusing force is linear as long as the strength of the driver is strong enough to maintain a stable structure of a bubble during the propagation. Secondly, the injection happens when some of the expelled electron trajectories cross the shell of the bubble, which causes the injection only starting from the end of bubble, which, in the case of laser driver, prevents the electrons to interact with the laser pulse [Pukhov and Meyer-ter Vehn, 2002]. Moreover, the trapped electrons partially neutralize the ionic charge and suppress further injection. During the acceleration, the rotation of the phase space improves the quality of the spectrum. All these facts together generate electron bunches of quasi-monoenergetic spectra and low emittance, which have been observed experimentally in the laser-driven case [Faure et al., 2004; Geddes et al., 2004; Mangles et al., 2004] as well as electron-driven case [Hogan et al., 2005; Blumenfeld et al., 2007; Litos et al., 2014]. The bubble regime in this work are discussed in section 5.1 and chapter 6.

---

[1] For a perfect circle, $r_s \frac{d^2 r_s}{d\xi^2} + \left(\frac{dr_s}{d\xi}\right)^2 + 1 = 0$. Additional contribution of $\left(\frac{dr_s}{d\xi}\right)^2$ causes the circle to be distorted in the very beginning and the very end of the bubble.

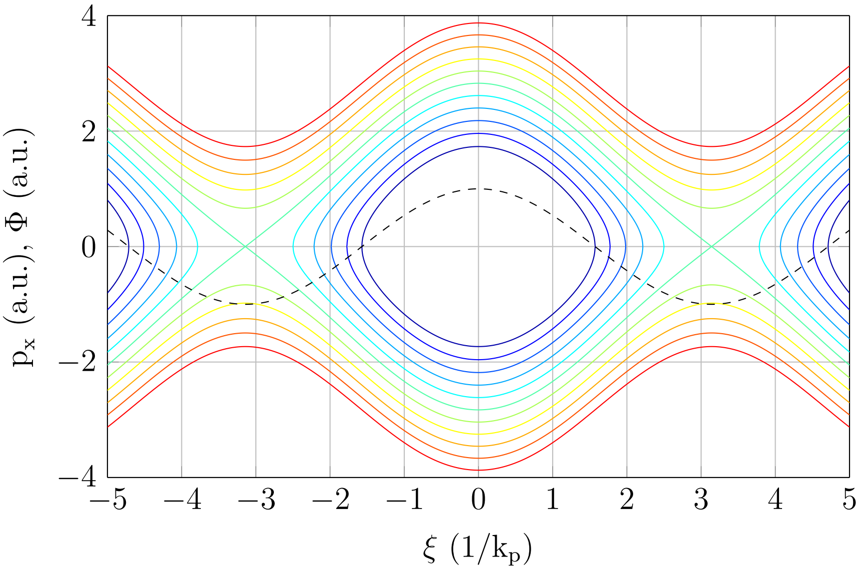

Figure 1.3: Phase space of the electrons in a plasma wave. Each color of solid lines corresponds to trajectory of different values of the Hamiltonian. The dashed line shows the magnitude of the assumed scalar potential.

1.2 Electron Injection

Till now we have discussed only the generation mechanism of the wakefield. In order to use the wakefield as an accelerator, some electrons must be injected into the acceleration phase. The classical description of the injection process is based on the analysis of the single electrons motion in a Hamiltonian system which is described as [Brantov et al., 2008; Esirkepov et al., 2006; Esarey and Sprangle, 1996]:

$$H = m_e c^2 \left[\sqrt{1 + \left(\frac{p}{m_e c} \right)^2} - \Phi \left(x - c\beta_{ph} t \right) \right] \tag{1.31}$$

where $\beta_{ph} \equiv v_{ph}/c$ is the dimensionless phase velocity of the wake wave. The paths of electrons in phase space which corresponds to different total energies of the integral of motion of (1.31) are called trajectories. One example of the trajectories of the plasma wave driven by a sinusoidal potential are shown in Fig. 1.3. There are two types of trajectories: the trajectories of trapped electrons by the wake wave are closed trajectories, and the electrons of too high or too low initial energies which escape from one plasma period are indicated by opened trajectories. The trajectory which separates these two types of trajectories is called separatrix To inject an electron into a closed trajectory of a specific total energy, the electron must have an energy which is larger than the minimum energy of an electron on the separatrix with momentum p_{min} which is

$$\frac{p_{min}}{m_e c} = \gamma_{ph}^2 \left(\frac{\beta_{ph}}{\gamma_{ph}} + \beta_{ph}\Delta\Phi - \sqrt{\Delta\Phi^2 + 2\frac{\Delta\Phi}{\gamma_{ph}}} \right) \tag{1.32}$$

where $\Delta\Phi$ is the amplitude of the normalized electrostatic potential.

If the plasma wave is in a steady state, and the properties of the driver do not evolve during propagation, the equation of motion based on (1.31) can be solved analytically. Since the phase velocity of the wake wave should be of the same order of magnitude as the group velocity of the driver bunch, we have $\beta_{ph} \sim 1$ and $\gamma_{ph} \gg 1$, the p_{min} is approximated by

$$\frac{p_{min}}{m_e c} \approx \gamma_{ph}^2 \left(\frac{\beta_{ph}}{\gamma_{ph}} + \Delta\Phi - \sqrt{\Delta\Phi^2} \right) = \gamma_{ph}\beta_{ph} \approx \gamma_{ph}. \tag{1.33}$$

In a classical wakefield theory, only the electrons which move faster than the phase velocity of the wakefield catch up to the wave and are accelerated. As a consequence, the probability of the injection is strongly dependent on γ_{ph}/β_{ph}.

The injection condition is fulfilled by many ways depending on the experimental conditions. These methods are catalogued into two groups. The first one is to modify the evolution of the wakefield such that some plasma electrons which form the wake are injected into the acceleration structure. For example, the self-injection, density transition and shock-front injection belong to this group, which are used in this work will be discussed in details in the next section. The other group is to inject the background electrons into stable wakes such as the ionization injection and the colliding pulse injection [Esarey et al., 1997a; Schroeder et al., 1999; Fubiani et al., 2004; Faure et al., 2006]. In the case of the ionization injection, the gas medium is a mixture of low-Z and high-Z elements where the low-Z element is fully ionized, and the high-Z is partially ionized. The injected electrons are released into the proper phase of the wake from the higher ionization states of the high-Z element by either the highest intensity part of the driver [Clayton et al., 2010; Pak et al., 2010; McGuffey et al., 2010; Pollock et al., 2011; Liu et al., 2011; Martinez de la Ossa et al., 2013] or an additional co-propagating laser pulse behind the charged bunch in the PWFA [Hidding et al., 2012]. The colliding pulse injection uses two counter-propagating pulses of the same wavelength to generate a beatwave of a zero phase velocity inside the wake. The ponderomotive force of the beatwave is very large $\propto 2(a_0)_{1st-pulse} \cdot (a_0)_{2nd-pulse}/\lambda_L$ [Faure et al., 2006]. Due to this large ponderomotive force and the zero phase velocity, the beatwave accelerates the background electrons to β_{ph} for the injection.

1.2.1 Wave breaking and Self-injection

An important question accompanying injection is that what is the maximum of the amplitude of the wakefield. As visible in (1.25) and (1.26), when $\beta_x \to \beta_g$, n is diverged, but Φ is finite, which implies the amplitude cannot increase indefinitely. To find the maximum amplitude of the wakefield independently from drivers, we focus on a 1D wave solution of the form $f\left(x - v_{ph}t\right)$ and assume $v_{ph} \approx v_p = \frac{\omega_p}{k_p}$ [Dawson and Oberman, 1962; Gibbon, 2005]. By introducing a co-moving parameter $s = x - v_p t$ and using the properties

$$\frac{\partial}{\partial x} = \frac{\partial}{\partial s}, \qquad \frac{\partial}{\partial t} = -v_p \frac{\partial}{\partial s},$$

(1.2), (1.6) and (1.7) are written as

$$\frac{\partial E_x}{\partial s} = 4\pi e \left(n_0 - n_e\right), \tag{1.34}$$

$$\left(\beta_x - \beta_p\right) \frac{\partial}{\partial s} \left(\gamma \beta_x\right) = -\frac{e E_x}{mc^2}, \tag{1.35}$$

$$\frac{\partial}{\partial s} \left[\left(\beta_x - \beta_p\right) n_e\right] = 0. \tag{1.36}$$

(1.36) can be integrated by assuming that there is no perturbation of the electron density when $s \to \infty$, and then the solution is revisited in the same form as (1.25). The only difference is that now $n = n\left(s\right)$ instead of $n = n\left(\xi, \tau\right)$. By substituting (1.25) into (1.34) and combining the result with (1.35), we get

$$\beta_x \frac{\partial}{\partial s} \gamma \beta_x = -\frac{E_x}{E_0} \frac{\partial}{\partial s} \frac{E_x}{E_0}.$$

This equation can be integrated by noticing the identity $\frac{\partial \gamma}{\partial s} = \beta_x \frac{\partial}{\partial s} \gamma \beta_x$, and then the electric field is solved, which is

$$\frac{E_x}{E_0} = \sqrt{2\left(\gamma_{max} - \gamma\right)}$$

where γ_{max} is the constant of integration corresponding to the maximum fluid velocity of the plasma. The maximum of the field occurs when $\gamma \to 1$. Since the maximum fluid velocity cannot go beyond the phase velocity of the wave, one sets $\gamma_{max} = \gamma_p$, and therefore

$$\left(\frac{E_x}{E_0}\right)_{max} = \sqrt{2\left(\gamma_p - 1\right)} \tag{1.37}$$

This maximum is called the *cold non-relativistic wave-breaking limit* [Dawson and Oberman, 1962]. When the amplitude of the driven field goes above this limit, some of the electrons overrun the plasma wave and being injected into the wakefield. If the initial energy of the electrons is larger than the minimum energy, as shown in (1.32), required for closed trajectories, these electrons will be trapped and accelerated. This process is called the *self-injection.*

The derivation is based on the 1D fluid equation. It has been shown from simulations that the achievable amplitude of the wakefield in the 3D nonlinear regime can be much higher than (1.37) [Pukhov, 2003; Pukhov and Meyer-ter Vehn, 2002; Lu et al., 2006b]. From the experimental point of view, the self-injection is easy to implement, but the stability is usually poor, and the electron spectra have a large thermal background. The self-injection happens by both transverse and longitudinal wake braking. The transverse wave breaking gives low stability and poor quality electron beams because the process is sensitive to the initial transverse momentum of the electrons while the longitudinal wave breaking gives more reproducible spectrum and a better pointing stability and low charge [Bulanov et al., 1997; Malka et al., 2002]. The longitudinal wave breaking takes place in the beginning of the acceleration, and the following transverse wave breaking is due to the too long and strong self-focusing and too long [Zhidkov et al., 2004; Corde et al., 2013]. A proper control of the beam loading and the self-modulation of the laser is required to produce quasi-monoenergetic electron beams [Geddes et al., 2004; Mangles et al., 2004; Faure et al., 2004; Osterhoff et al., 2008; Leemans et al., 2014].

1.2.2 Density Transition and Shock-front Injection

As discussed in (1.33), the electron starts to inject into the wakefield when the fluid velocity of the electron reaches the phase velocity of the wakefield. One way to achieve this condition is to reduce the β_{ph} by using a density transition [Bulanov et al., 1998; Brantov et al., 2008]. In the 1D case, the local phase of the wakefield during the density transition is approximated by

$$\phi\left(x\right) = \xi \cdot k_p\left(x\right)$$

where we assume that β_g is slowly varing and $\beta_g \simeq 1$. By the definition, the effective frequency $\omega_{p,eff} = -\frac{\partial\phi}{\partial t}$ and the effective wavenumber $k_{p,eff} = \frac{\partial\phi}{\partial x}$. The local phase velocity of the wakefield is expressed as

$$\beta_{ph} = \frac{\omega_{p,eff}}{ck_{p,eff}} = \left[1 + \frac{\xi}{k_p}\frac{\partial k_p}{\partial x}\right]^{-1} = \left[1 + \frac{\xi}{2n_0}\frac{\partial n_0}{\partial x}\right]^{-1} \approx 1 - \frac{\xi}{2n_0}\frac{\partial n_0}{\partial x}. \tag{1.38}$$

Since ξ is negative behind the driver according to the definition, (1.38) shows that a phase velocity decreases during a density down ramp. The formula also shows that the phase velocity keeps slowing down with respect to ξ, which indicates that the the injection happens at a sufficient large distance behind the driver if the wakefield is not damped yet. For example, if the electron has a initial velocity $\beta = 0.5$ and $\frac{\partial n_0}{n_0 \partial x} = \frac{1}{4\lambda_p}$, the injection happens at $\xi = 4\lambda_p$. On the other hand, the evolution of the laser intensity due to the self-modulation can cause a similar effect. Since λ_p increases with a_0 in the nonlinear regime, as shown in table 1.1, the injection happens during the self-focusing where the local phase velocity in the end of the first plasma period is reduced due to the the increase of the nonlinear plasma wavelength.

Nevertheless, a long range density down ramp will inevitably causes a continuous injection and leads to a large energy spread [Geddes et al., 2008; Hansson et al., 2015], which is not preferable for the further application. This issue is prevented by using the shock-front injection where the density jump occurs in a very short transition length $\ll \lambda_p$, as depicted in Fig. 1.4. In this case, the adaption of the plasma wavelength is not fast enough, and therefore the density peak of the first plasma period (orange area in Fig. 1.4) enters the acceleration phase of longer plasma wavelength in the lower density regime. Unlike the case of a slow transition, the shock-front injection is due to the sudden jump of the local phase instead of the slowdown of the plasma wave. Moreover, only the electrons injected in the first plasma period survive during acceleration, and the plasma electrons behind the second period will be injected into a wrong phase of the wakefield and eventually drop out. As a consequence, the shock-front injection generates monoenergetic electron beams of very low energy spread [Buck et al., 2013].

1.3 Laser Dynamics in Plasma

1.3.1 Self-focusing of Laser Pulse in Plasma

On of the major challenge of an efficient LWFA is to overcome the diffraction limit by guiding the laser pulse through a distance much beyond the Rayleigh length Z_R. To achieve this, the transverse refraction index must be shaped. The three typical options are: relativistic effect which increases the mass of electron, plasma channeling caused by the transverse ponderomotive force and the external guiding channel. These effects are summarized by including the mass correction of ω_p in (1.23)

$$\omega^2 = \omega_p^2/\gamma'(r) + k^2c^2$$

For example, if the correction only comes from the relativistic quiver motion of the electrons in a linearly polarized laser field, the time average of the total momentum gives $\gamma'(r) = \sqrt{1 + a(r)^2/2}$ [Gibbon, 2005]. If the modulation of the density is small, the index of refraction (1.24) will be approximated by [Esarey and Sprangle,

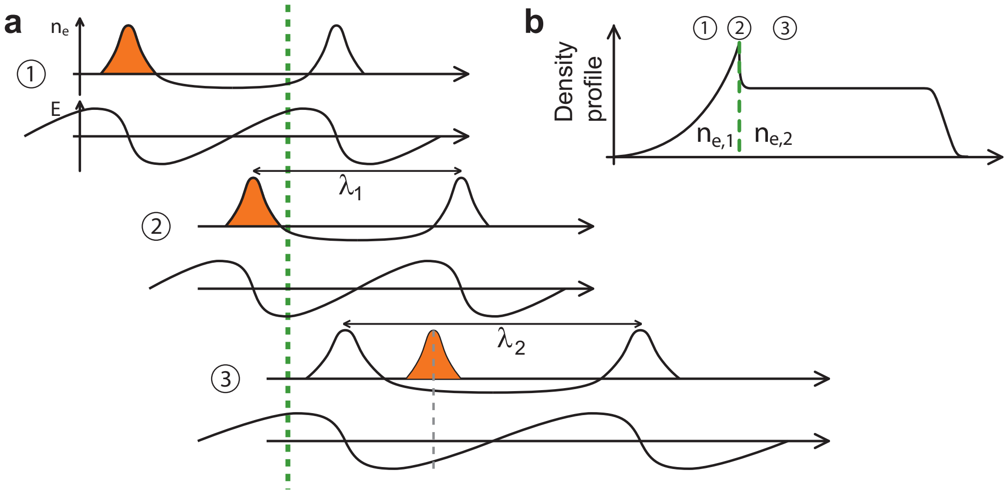

Figure 1.4: Mechanism of the shock-font injection [Buck, 2011]. The plots in the LHS show the longitudinal density oscillation of the plasma density and the longitudinal electric field, and the density profile is shown in RHS. In the first step, the laser crosses the sharp density jump from $n_{e,1}$ of the target and drives a non-linear plasma wave with $\lambda_p = \lambda_1$. In the second step, the density peak in the end of the first plasma period crosses the sharp density jump, the oscillation of plasma electrons after the jump starts to adapt to $\lambda_p = \lambda_2$. In the last step, the density peak from the high density regime enters the acceleration phase of the plasma wave in the low density regime.

1996]

$$\eta \simeq 1 - \frac{{\omega_p}^2}{2\omega^2}\left(1 - \frac{a\left(r\right)^2}{4} + \frac{\delta n_{ext}}{n_0}\frac{r^2}{{r_c}^2} + \frac{\delta n_c}{n_0}\right) \tag{1.39}$$

where the first term is again the contribution of the relativistic quiver motion, the second term states for an externally preformed plasma channel of a density profile described by $n = n_0 + \delta n_{ext}\frac{r^2}{{r_c}^2}$, and the last term is the plasma channeling by the ponderomotive force where δn_c is the density depth of the ponderomotive channel. In the laser-plasma interaction, the evolution of the laser pulse is much slower than the oscillation period of the light field. Consequently, the evolution of the laser field is approximated by using the paraxial wave equation [Esarey et al., 1997b]

$$\left(\nabla_\perp^2 + 2ik\frac{\partial}{\partial x}\right)\vec{E} = k^2\left(1 - \eta^2\right)\vec{E}.$$

If the external guiding channel is absent, and the relativistic effect dominates the process, the evolution of the spot envelope of the a Gaussian beam of the form $a^2 = {a_0}^2 e^{-r^2/2{\sigma_L}^2}$ will be described by

$$\frac{d^2}{dx^2}\Omega = \frac{1}{{Z_R}^2\Omega^3}\left(1 - \frac{P}{P_c}\right) \tag{1.40}$$

where $\Omega = \sigma_L/r_0$, r_0 and Z_R are the spot size and the Rayleigh range in vacuum respectively, P is the total beam power, and

$$P_c = 2c\left(\frac{e}{r_e}\frac{\omega}{\omega_p}\right)^2 \simeq 17.4\left(\frac{\lambda_p}{\lambda_L}\right)^2 \text{ GW} \tag{1.41}$$

is the *critical power*, where $r_e = e^2/m_e c^2$ is the classical electron radius. Equation (1.40) shows that the laser will be self-focused when $P > P_c$ because of the negative gradient in the RHS. For example, in the ATLAS experiment, the total power is ≈40 TW which is significantly larger than P_c =11 TW for $n_0 = 3 \times 10^{18}$ cm^{s}. Similarly, in the case LWS-20, P ≈9 TW and $P_c = 0.8$ TW for $n_0 = 4 \times 10^{19}$ cm^{s}. The self-focusing is expected to happen in LWFA experiment discussed in this work. However, this process will not cause an infinitely small focused beam. In reality, plasma dynamics happens in the scale of λ_p which limits the self-focusing spot size.

This analysis so far does not consider the factor of laser pulse length. The perturbation of refraction index needs a time of $\sim {\omega_p}^{-1}$ to be set up, which means the front of the pulse cannot be guided even when $P/P_c \gg 1$. This indicates an ultra-short laser pulse of a temporal duration $\tau_L \leq \lambda_p$ can only be guided by using external channel. However, new studies have shown that it is possible to guide a short pulse because the erosion of the leading edge of the pulse happens before the diffraction, and the back side of the pulse is still guided in the ion channel [Gorbunov et al., 2005]. The self-guiding of an ultra-short pulse has been observed in many experiments [Gahn et al., 1999; Faure et al., 2002; Chen et al., 2007; Ralph et al., 2009] and also in our case of sub-5 fs laser pulse which is discussed in chapter 6.

1.3.2 Self-modulation and Pulse Shortening

Similar to the self-focusing which is due to the transverse modulation of refraction index, the longitudinal modulation of the refraction index also shapes the temporal profile of a laser pulse. The longitudinal refraction index is written in a form similar to (1.39) [Mori, 1997; Beaurepaire et al., 2014]

$$\eta \simeq 1 - \frac{{\omega_p}^2}{2\omega^2}\left(1 - \frac{a\left(\xi\right)^2}{4} + \frac{\delta n\left(\xi\right)}{n_0} - 2\frac{\delta\omega\left(\xi\right)}{\omega}\right) \tag{1.42}$$

where the first term is again the perturbation due to the laser-induced nonlinearity but in the longitudinal direction, the second term accounts for the density perturbation due to the plasma wave, and the last term originates from pre-chirped incoming laser. The optical frequency variation due to the local modulation of the refraction index is easily derived from the first principle [Mori, 1997]:

$$\frac{1}{\omega}\frac{\partial\omega}{\partial\tau} = \frac{-1}{\eta^2}\frac{\partial\eta}{\partial\xi}.$$

For a laser pulse of a Gaussian-like temporal profile, the negative gradient of the front side of the pulse is red-shifted and the back side of the pulse blue-shifted, which causes a symmetric broadening of the spectrum. This effect is called relativistic Self-Phase Modulation (SPM). If the density gradient of the plasma wave, i.e., δn, is significant, the local frequency of the laser pulse increases when the resulted density gradient is positive and vice versa. This phenomenon is literally called photon acceleration (or deceleration for a negative gradient) [Murphy et al., 2006]. In the typical laser wakefield situation, the density only decreases, and therefore the spectrum is only red-shifted. Due to the negative Group Velocity Dispersion (GVD) of plasma and decreasing density, these effects is accompanied by compression of the laser pulse which significantly increases the ponderomotive potential in LWFA [Ren et al., 2001; Gordon et al., 2003; Wang et al., 2011; He et al., 2014; Vieira et al., 2010]. The self-compression has been observed in many studies where the laser pulse was compressed >3 times shorter than the original Fourier-limited pulse length [Faure et al., 2005; Schreiber et al., 2010], and a scheme to generate single-cycle pulse by photon deceleration of a high intensity laser pulse ($> 10^{20}$ W/cm^2) has been proposed [Tsung et al., 2002].

1.4 Limitation of Wakefield Acceleration

1.4.1 Hosing Instability

In a wakefield experiment, the driver does not always propagate along the middle of a cylindrically symmetric ion channel. This happens when, for example, the longitudinal axis of a driver is not the same as the propagation axis, or the transverse field of the driver is not radially symmetric. If there is an offset between the centroid of a witness bunch, or a trapped bunch, and the centroid of the channel, the focusing force from the ion channel will cause the witness bunch to realign to the channel, thus oscillating transversely around the propagation axis. This is called the *hosing instability* [Lampe et al., 1993; Whittum et al., 1991; Krall and Joyce, 1995; Whittum, 1997; Huang et al., 2007]. The structure of the generated wakefield is significantly modified due to the presence of these instabilities, which reduces the efficiency of the energy transfer and leads to bunch breakup [Vieira et al., 2014].

In the case of a PWFA experiment, the hosing instability can be caused by the misalignment between the ionization laser beam and the electron driver [Muggli et al., 2004]. If the experiment is operated in the self-ionization regime, the tilt between the longitudinal axis of the driver and the propagation axis causes an asymmetric ionization channel which will also trigger the hosing instability [Deng et al., 2006; Adli et al., 2012].

In the case of LWFA, the transverse hosing is usually accompanied by the self-modulation of the laser pulses. There are two types of hosing: the fast one has the hosing period of around λ_p which exists in both a uniform plasma or an ion channel, and the slow one happens after several Rayleigh lengths. The mechanism of the fast hosing is similar to the discussion above, which is modelled by a nonuniform head-to-tail centroid displacement of a tilted laser pulse, i.e., angular chirp [Sprangle et al., 1994; Ren and Mori, 2001]. On the other hand, the slow hosing is caused by contributions of the transverse self-modulation and a spatiotemporal asymmetry of the intensity distribution which happens when the parabolic focusing mirror or the laser system is misaligned [Duda et al., 1999; Kaluza et al., 2010].

From the experimental point of view, the major consequence of a strong hosing instability of laser is the current filamentation of accelerated electrons which causes the pointing instability and the splitting of the generated bunches. These effects appear as dispersed “halos” of the beam profiles as well as multiple-line images on the electron spectrometer [Mangles et al., 2005; Huntington et al., 2011].

1.4.2 Beam Loading

Regardless the mechanisms and drivers of the wakefield, the acceleration structure is built up by the combination of the electric field of the plasma electrons and the ion channel. If too much number of electrons are injected, the electrons inevitably partially neutralize the ion channel and significantly modify the acceleration field. This effect is called the *beam loading*. In the case of PWFA, a properly shaped witness bunch flattens the acceleration field across the the bunch. Since the driver and the witness bunch are usually highly relativistic, the effect of the beam loading suppresses the energy spread due to the gradient of the wakefield and accelerate the bunch monoenergetically. This is the opposite for the LWFA, the structure of the injected bunch is not yet controllable, and the phase velocity of the plasma wave is slower than the accelerated bunch due to the momentum requirement for the injection. The beam loading leads to a higher energy spread, which is usually unprofitable and should be avoided. This effect has been observed during experiments, as discussed in section 5.1.

1.4.3 Limitation of LWFA and the Scaling Rules

In an ideal design of LWFA the highest efficiency of energy transfer between the laser pulse and the trapped electrons is reached. Beside the instability and the modulation process what have been discussed, three of the most important mechanisms which limit the performance in the LWFA experiment are: laser diffraction, pump depletion and electron dephasing.

The first limitation of the acceleration length is the natural **diffraction of a laser beam**. When the laser beam propagates in vacuum, the evolution of the spot size is described by the Gaussian solution

$$\sigma_L\left(x\right) = \sigma_L\left(x=0\right)\sqrt{1+\frac{x^2}{{Z_R}^2}}$$

where $Z_R = \frac{\pi{\sigma_L}^2(0)}{\lambda_L}$ is called the *Rayleigh range*, and $2Z_R$ is called the confocal length which is often used as a zeroth order approximation to estimate the accuracy of target position in the experiment. This natural limit is overcome by the self-guiding or the external guiding in a preformed plasma channel as discussed in section 1.3.1.

As discussed in section 1.2, the injected electrons undergo first a cycle of acceleration and after that deceleration in the momentum phase space. The second limitation factor is the maximum length in the laboratory frame that the electrons are accelerated, which is called the **dephasing length** L_d. By assuming a non-linear and stable wakefield driven by a laser pulse moving at v_g, and electrons of speed β are accelerated from the end of a plasma period, the maximum acceleration length in the co-moving frame is $\lambda_p/2$. This is formulated in the laboratory frame as

$$(c\beta - v_g)\,\frac{L_d}{c\beta} = \frac{\lambda_p}{2}.$$

With the assumption $\beta \sim 1$ and the approximation of (1.24), the dephasing length is expressed by

$$L_d \approx \frac{\lambda_p}{2} / \left(1 - \frac{v_g}{c}\right) \approx \frac{{\lambda_p}^3}{{\lambda_L}^2} \propto {n_0}^{-\frac{3}{2}}$$

In the case $a_0 > 1$, the plasma wavelength of the wakefield elongates [Ting et al., 1990].

The third limitation is the pump depletion which is due to the energy loss of the laser by driving the plasma wave. The **depletion length** L_{pd} is estimated by equating the total energy of the driving pulse and the energy stored in the wakefield, which is written as [Shadwick et al., 2009]

$$L_{pd} \approx 8.68 \frac{{k_L}^2}{{k_p}^3} \frac{2 + {a_0}^2}{{a_0}^2}.$$

So far we consider only a linear or a 1D non-linear wakefield. If the laser intensity is substantially higher, i.e., $a_0 \gg 1$, the wakefield becomes highly nonlinear, and the evolution of the laser pulse must be considered [Lu et al., 2007; Shadwick et al., 2009]. For example, the laser etching happens when the leading part of the laser pulse losses a significant amount of energy by driving the plasma electrons. The etching rate of the laser pulse dominates the depletion length, and the v_g decreases due to the shift of the energy front of the laser pulse [Decker and Mori, 1994], which decreases L_d. Other effects, such as the pulse-steepening, the pulse-lengthening and the spectrum redshifting influence the scale lengths as well [Shadwick et al., 2009]. In the 3D nonlinear region, the analytical approach alone is not sufficient. The scaling rules based on the phenomenological description [Lu et al., 2007] and the similarity analysis [Gordienko and Pukhov, 2005] have been derived. In these approaches, the pre-factors of the model are retrieved either by simulations or experiments. The results of different theories as well as the optimized conditions are summarized in table 1.1. The examples of the scaling lengths of LWFA driven by LWS-20 and ATLAS are compared in table 1.2.

In the bubble regime driven by the laser pulse, the maximum number of the electrons N_{max} which is possible to injected into a plasma wave is estimated from the energy balance [Lu et al., 2007]. The total energy of the field energy within the first bucket of the bubble and the kinetic energy of plasma should equal to the energy absorbed by the trapped electron, under the matching condition (1.30), which gives

$$N_{max} \simeq \frac{8/15}{k_0 r_e}\sqrt{\frac{Pe^2}{{m_e}^2 c^5}} \simeq 3.1\times 10^7 \lambda_L(\mu\mathrm{m})\sqrt{P\,(\mathrm{TW})}. \tag{1.43}$$

The formula shows the maximum charge from a typical 100 TW Ti:Sapphire laser system like ATLAS is ≈1 nC, and ≈60 pC for a sub-2 cycle laser pulse like LWS-20.

Table 1.1: Scaling rules of LWFA from different theories. σ_{LO} is the optimized spot size of the laser pulse with the wavenumber k_L, $c\tau_{LO}$ is the optimized pulse length, λ_w is the nonlinear relativistic plasma wavelength, and $\gamma_{max} m_e c^2$ is the maximum peak energy of the trapped electrons. In this table, only the last regime is based on the circularly polarized laser and all the rest use linearly polarized laser.

Regime	a_0	σ_{LO}	$c\tau_{LO}$	L_d	L_{pd}	λ_w	γ_{max}
Linear$^+$	$\ll 1$	$\frac{2\pi}{k_p}$	$\frac{\sqrt{2}}{k_p}$	$2\pi\frac{{k_L}^2}{{k_p}^3}$	$12.3\frac{c\tau_L {k_L}^2}{{k_p}^2{a_0}^2}$	$\frac{2\pi}{k_p}$	$2\pi a_0^2\frac{{k_L}^2}{{k_p}^2}$
1D Nonlinear$^\sharp$	$\gg 1$	$\frac{2\pi}{k_p}$	$\frac{\sqrt{2}}{k_p}$	$2\sqrt{2}a_0\frac{{k_L}^2}{{k_p}^3}$	$6.15\frac{c\tau_L {k_L}^2}{{k_p}^2}$	$2\sqrt{2}\frac{a_0}{k_p}$	$2\sqrt{2}a_0^2\frac{{k_L}^2}{{k_p}^2}$
3D Nonlinear$^\natural$	> 2	$\frac{2\sqrt{a_0}}{k_p}$	$\leq \frac{\sqrt{a_0}}{k_p}$	$\sqrt{a_0}\frac{2}{3}\frac{{k_L}^2}{{k_p}^3}$	$\frac{c\tau_L {k_L}^2}{{k_p}^2}$	$\frac{2\pi\sqrt{a_0}}{k_p}$	$\frac{2}{3}a_0\frac{{k_L}^2}{{k_P}^2}$
3D Nonlinear$^\flat$	> 4	$\frac{1.19\sqrt{a_0}}{k_p}$	$\leq \frac{\sqrt{a_0}}{k_p}$		$a_0\frac{c\tau_L {k_L}^2}{{k_p}^2}$		$a_0^{\frac{3}{2}} c\tau_L\frac{{k_L}^2}{k_p}$

$^+$ [Shadwick et al., 2009] $^\sharp$ [Esarey and Shadwick, 2004; Shadwick et al., 2009] $^\natural$ [Lu et al., 2007] $^\flat$ [Gordienko and Pukhov, 2005; Jansen et al., 2014]

Table 1.2: Example of the scaling lengths of LWFA driven by LWS-20 and ATLAS based on the 3D Nonlinear theory [Lu et al., 2007]. In the case of LWS-20, $n_0 = 4\times 10^{19}$ cm^{-3}, τ_L =2 fs (4.7 fs in FWHM) and λ_L =740 nm; the parameters for the example of ATLAS driving LWFA are $n_0 = 3\times 10^{18}$ cm^{-3}, τ_L =11 fs (25.9 fs in FWHM) and λ_L =800 nm. The numbers inside the parentheses are the expected energy predicted by the similarity scaling law [Gordienko and Pukhov, 2005].

Case	a_0	σ_{LO}	τ_{LO}	L_d	L_{pd}	λ_w	γ_{max}
LWS-20	2.2	2.49 μm	≤4.2 fs	42.2 μm	29 μm	7.83 μm	74.6 (112.7)
ATLAS	1.7	8 μm	≤13.3 fs	1.55 mm	2 mm	25.1 μm	657 (1495)

1.4.4 Limitation of PWFA

Transformer Ratio

In the conventional PWFA, both the driver bunch and the trapped bunch are highly relativistic. The trapped bunch will not outrun the wakefield, and therefore the dephasing effect is negligible. The major limitations of the achievable energy are the efficiency of the energy transfer and the erosion of the driver. The efficiency of the PWFA is quantified by the *transformer ratio* R which is defined as [Ruth et al., 1985; Katsouleas, 1986; Keinigs and Jones, 1987; Krall and Joyce, 1995]

$$R_T \equiv \frac{|\langle E_{max-a}\rangle|}{|\langle E_{max-d}\rangle|}$$

where $\langle E_{max-a}\rangle$ is the average maximum acceleration field experienced by the witness bunch, and $\langle E_{max-d}\rangle$ is the average maximum deceleration field experienced by the driver bunch. The meaning of the transformer ratio is the following: if the acceleration length is L', and the structure of the wakefield is in steady state, the ratio of the energy transfer from the driver to the witness through the plasma is $\frac{|E_{max-a}|\cdot L'}{|E_{max-d}|\cdot L'} = R_T$.

In the case of the linear wakefield by a longitudinally symmetric driver, it is shown that

$$|E_{max-d}| = |E_x\left(r=0,\xi=0\right)| = \frac{1}{2}\left|E_{x-max}\right|.$$

which is because only the first half of the bunch contributes to the field in the middle of the bunch. The maximum of R_T occurs when the witness bunch is injected at the phase of E_{x-max}, and we get

$$R_T \leq 2.$$

This limit has been studied experimentally [Blumenfeld et al., 2010].

The upper limit of R_T can be overcome by using an asymmetric charge distribution or multiple bunches [Su et al., 1987; Hidding et al., 2010; Massimo et al., 2014]. It has been shown that $R_T \simeq 6$ is possible by using linearly ramped electron drivers [Katsouleas, 1986; England and Ng, 2012], and $R_T \simeq 7$ by using high-charged bunches to drive the wakefield in the nonlinear regime [Rosenzweig, 1987; Joshi et al., 2002].

1.5 Particle-in-cell (PIC) simulation

The general behaviour of the plasma includes abundant physics and is highly complicated to be solved analytically. In order to understand the experimental results, numerical approaches are necessary. However, typical plasma systems of the LWFA or the PWFA contain $\approx 10^{10}$ particles, solving the complete phase space of each particles needs to calculate 10^{20} interactions in $\approx 10^{5}$ time steps, which is beyond the computing power of any available clusters.

To solve this issue, the concept of the Particle-In-Cell (PIC) simulation was firstly introduced by Tajima and Dawson [Tajima and Dawson, 1979]. In the PIC simulations, the number of particles is greatly reduced by using macro-particles. Each macro-particle represent a large amount of real plasma particles and moves in a continuous phase space. By contrast, the magnetic and electric fields are only solved on discrete spatial grids, and the fields applied to the macro-particles are calculated by interpolating the values of the nearest grids. The number of operations per time steps is reduced to $\approx N \log N$ where N is the number of the macro-particles [Büchner et al., 2003]. Although some PIC codes have the module to calculate n_0 based on the ionization probability [Martins et al., 2004; Chen et al., 2013], regular simulations assume a fully ionized plasma and ignore the electron-ion collisions because a high temperature plasma is generated much before the driver in experiments.

The algorithm conducts four steps in a loop which is depicted in Fig. 1.5 [Mehrling, 2011]:

Source Scatter The currents deposited on the individual grid points are calculated from the charge and the momentum distribution of the nearest macro-particles, which means one macro-particle deposits its charge and current to the 4 closest grids in 2D or 8 grids in 3D.

Maxwell Solver The self-consistent fields on the grid points are solved by using the complete set of the Maxwell's equation (1.2)-(1.5) with the source terms deposited by the source scatter taking into account retardation effects.

Field Solver The fields are interpolated from the grids to the positions of the particles. The interpolation scheme must be consistent with the scheme used by the source scatter to prevent a self-interaction of a particle.

Particle Pusher The new position and the momentum of the particles after a specific time step are calculated by solving the Lorenz equation (1.6).

The PIC code *OSIRIS* is used in this work, which is a 3D, relativistic, object oriented and massively parallel code [Fonseca et al., 2002]. Since both the LWFA and PWFA require long plasmas, OSIRIS provides capability of using the co-moving frame of the speed of light which moves in the propagation axis of the driver and significantly reduces the simulation volume. In the LWFA simulations, since the evolution of the laser pulse plays a substantial rule, the resolution of

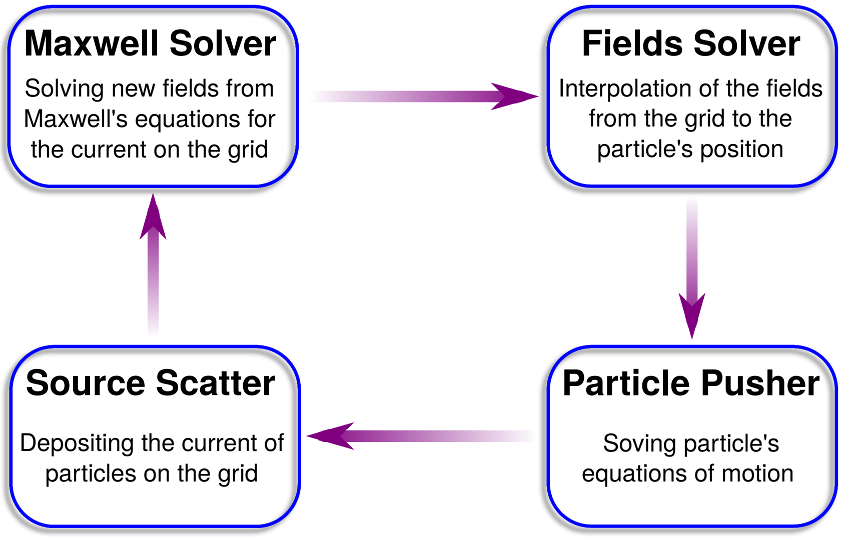

Figure 1.5: The flowchart of the PIC simulation.

grids in the propagation direction must be able to solve the λ_L. As a rule of thumb, the size of the grids in the longitudinal direction should be set $< \frac{\lambda_L}{40}$. The physics in the transverse dimension is dominated by plasma oscillation, hence the transverse grid size should be $< \frac{\lambda_p}{40}$. In the PWFA simulations, however, the transverse self-focusing can be very strong, and the charge density will be significantly underestimated if the resolution is too low. An empirical option is to make the grid size $< \frac{\lambda_p}{100}$. The simulation time step should be as close to the Courant-Friedrichs-Lewy (CFL) condition as possible to minimize the numerical errors. The CFL conditions guarantee the stable solution of partial differential equations by the Finite Difference Time Domain (FDTD) method [Courant et al., 1928], and is defined as

$$\Delta t_{CFL} \geq \frac{\sqrt{\Delta x^2 + \Delta y^2 + \Delta z^2}}{c}$$

where Δx,Δy,Δz are the grid sizes of each axis.

In this work, we conducted the simulations on the supercomputer Hydra from the Max Planck Computing and Data Facility in Garching. Complete 3D simulations took 24h to 72h on 1024 to 4096 processors.

Chapter 2

The Physics of Propagation of Ultrashort Electron Bunches in Underdense Plasma

The study of transportation of energetic charged particles in plasma has been a key issue in a number of disciplines ranging from linear accelerator research to astrophysics. In astrophysics and magnetic confinement fusion, one major interest is to understand the interaction between charged particles, for example, alpha particles and accelerated ion beams, or magnetic turbulence etc. In space physics, similarly, one major concern is the propagation of cosmic rays and solar energetic particles through the interstellar plasma and the solar system with large scale turbulence [Shalchi, 2011; Hauff et al., 2010]. In linear accelerators, the lensing effect of charged particles inside the plasma, the so-called plasma lensing, has been suggested to enhance the luminosity for high energy experiments [Bennett, 1934; Roberts and Bennett, 1968; Chen, 1987; Su et al., 1990; Ng et al., 2001; Goncharov et al., 2014; Goncharov, 2013]. The plasma lensing is caused by the focusing of a self-generated magnetic field when electric expelling force is reduced due to partial neutralization by the plasma. Recently, thanks to the development of advanced post-compression schemes for linear accelerators, it is possible to generate electron bunches with temporal duration in the sub-ps range [Kung et al., 1994; Grabenhofer et al., 2014; Nozawa et al., 2014] with high charges, on the order of nC [Emma and Iverson, 2001; Krejcik et al., 2003; Yang et al., 2006]. On the other hand, an electron bunch from LWFA has an ultrashort bunch duration on the order of a few fs by its nature. Both of these high current beams, or bunches, exhibit significant magnetic and electrostatic forces which expel free electrons of the plasma. The resulting space charge configuration will interact with the beams collectively. This process causes energy transfer between charged particle bunches and plasma. Therefore, the early studies have been motivated by exploiting such collective movement for fast ignition of inertial confinement target [Key, 2007; Kodama, 2002; Kodama et al., 2001]. In one case, electrons on the order of several MeV and amount to a current of 10^8 A are generated by hole boring of high intensity laser pulses of 100s kJ and 20 ps pulse duration [Tabak et al., 1994; Pukhov and Meyer-ter Vehn, 1997]. The electrons dissipate a significant fraction of the energy into transverse electron heating via a collective coalescence of coaxial filamentary structures [Honda et al., 2000]. This approach greatly reduces the laser energy requirement of density compression to one tenth of what required for central hot spot ignition [Hurricane et al., 2014; Azechi and Project, 2008]. Other similar ideas based on laser-driven proton sources are also proposed [Roth et al., 2001; Honrubia and Murakami, 2015]. However, these concepts have not been implemented so far due to experimental challenges. On the contrary, recent technology developments have enabled the generation of ultrashort electron bunches by externally compressing the electron beams of conventional linear accelerators to drive plasma wakefields and accelerate electrons from 42 GeV to 84 GeV within 1 m of plasma [Blumenfeld et al., 2007; Hogan et al., 2010]. It is necessary to use an ultrashort driver bunch because, as discussed in Chapter 1, a shorter bunch matches higher plasma density to drive a plasma wakefield with larger amplitude. Therefore, a few proposals notice the potential of LWFA electron bunches in driving accelerating wakefield, which are similar to those driven by the electron beams of conventional linear accelerator but with much higher accelerating gradients and shorter duration [Hidding et al., 2010; Masson-Laborde et al., 2014]. In this chapter, we first review a previous study of the propagation of ‘long’ electron bunches inside plasma. Next we focus on the plasma wakefield driven by electron bunches from LWFA. Most previous studies are based on the properties of linear accelerators, with electron sources offering bunch charge on the order of nC and ps to 10 fs duration. The process is approximated by using fluid equations and quasi-static propagation [Lawson, 1958; O’Neil, 1971; Buchanan, 1987; Swanekamp et al., 1992; Miller et al., 1992]. In the case of LWFA bunches, because of considerable self-modulation of the electron driver by the feedback from the wakefield, the process is rather complicated and cannot be simplified by the approximation of quasi-static propagation. Consequently, in the majority of this chapter, series of PIC simulations instead of analytical models are utilized to understand the fundamental phenomena.

2.1 Classical Description of Propagation of Electron Bunches in Underdense Plasma

The interaction of the electrons beam and plasma is described by the total contribution of collisional and collective forces. The collisional force is the direct interaction between the electrons of the beam and its immediate neighbors in the beam as well as background plasma while the collective force is a space charge effect which is contributed by the global distribution of particles. The collisional force causes a small random movement of the trajectory and a statistical fluctuation of density distribution whiles the general trajectory and the density distribution is determined by the collective force. The comparison of the relative importance of these two forces is measured by the number of particles inside the Debye length λ_D which is defined in (1.1). The single-particle interaction is important when the beam size is smaller than λ_D. This effect is, however, relatively small, and the mutual interaction is dominated by the collective force in most practical beams. Therefore the contribution of the collisional force is ignored in the following discussion. If an electron beam without any energy distribution moves laminarly in one direction, the radial electric field E_r and azimuthal magnetic field B_ϕ which are experienced by electrons inside the beam are calculated by Gauss's law and Ampère's law, and one obtains

$$E_r(r) = \frac{2I_t(r)}{v \cdot r} \qquad\qquad B_\phi(r) = \frac{2I_t(r)}{c \cdot r} \tag{2.1}$$

where r is the distance to the central axis of the beam, and $I_t(r)$ is the total current within radius r. The equations show that the electric expelling force is balanced by the magnetic restoring force for a highly relativistic beam in which $v \approx c$. When injecting a high brightness[1] electron beam into an underdense neutral plasma, the plasma electrons are expelled from the path of the beam to build up an ion channel [Takayama and Hiramatsu, 1988]. The channel applies a restoring focusing force to the beam and compensates the self-field from the space charge of the beam. The strength of the ion focusing is given for a cylindrically symmetric beam by

$$K \equiv -\frac{F_r}{r\gamma mc^2\beta^2} \simeq \frac{2\pi r_e n_0}{\gamma} = \frac{k_p^2}{2\gamma} \equiv k_\beta^2 \tag{2.2}$$

---

[1] The The brightness of a beam at a given point in a given direction is defined as the current per unit area normal to the given direction, per unit solid angle, or is mathematically defined as

$$Brightness \equiv \lim_{\Delta A \to 0} \lim_{\Delta\Omega \to 0} \frac{\Delta I}{\Delta A \Delta\Omega}$$

, where A is the area of the cross section and Ω is the solid angle.

where F_r is the radial force, r_e is the classical radius of an electron, n_0 is the plasma density, and k_β is called the betatron wavenumber. For the sake of simplicity, before considering the specific case of LWFA driven bunch, we first revise classical models of high current (> 1 kA) and long pulse (> 1 ns) relativistic electron beams [Krall et al., 1989; Su et al., 1990]. The current density as well as charge density is treated as steady state, and the distribution within the beam is determined. We also ignore the energy gain and loss due to electric force $-eE_\parallel$ of longitudinal wakefield, i.e., assume that the transverse dynamic characteristic length of beams, which include the electron-hose instability growth length [Lampe et al., 1993] and the wavelength of betatron oscillation λ_{beta} [Dawson, 1959], is much smaller than the length,

$$L_E \simeq \frac{\gamma m_e c^2}{\left|-eE_\parallel\right|_{max}}$$

which causes significant energy loss [Barov and Rosenzweig, 1994; Uhm and Joyce, 1991]. For such a long and non-dissipated bunch, the transverse profile evolution within the beam is described by three distinct regions (Fig. 2.1):

1. The leading edge of the bunch which does not experience the full effects of the ion focusing. This is because of the finite time that plasma electrons require to move, which turns out to be a freely expanding beam head

2. After the plasma electrons are rarefied from the beam path, a pinch region where the ion channel applies a restoring force and reduces the beam radius.

3. The main body of the beam expands to a constant radius r_m which is matched to the ion focusing strength.

To estimate the time scale which is required for plasma electrons to be rarefied, we first assume the force on the plasma electrons is dominated by radial electric field from a highly relativistic electron beam which has a uniform density n_b and hence the electric field is simply calculated by Gauss's law. By defining the distance from the beam head as a independent variable $\xi = ct - z$, we get the equation to describe the radial motion of plasma electrons,

$$\frac{\partial^2 r}{\partial \xi^2} - k_{bp}^2 r = 0 \tag{2.3}$$

with $k_{bp}^2 = 2\pi n_b r_e = (n_b/n_0)\left(k_p^2/2\right)$ from Gauss's law. The solution for eq. (2.3) is straightforward. By assuming the plasma electrons has an initial stationary radius r_0, we have

$$r = r_0 cosh\left(k_{bp}\xi\right) \tag{2.4}$$

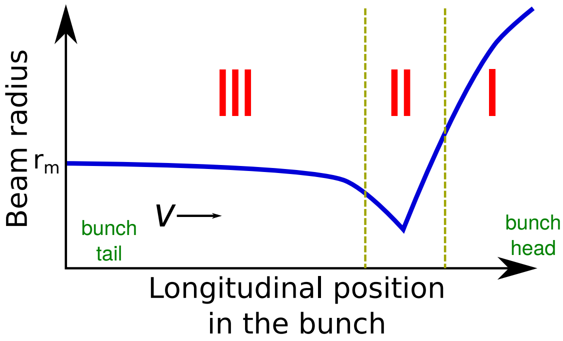

Figure 2.1: Typical scenario of the evolution of a long electron bunch propagates in the plasma. Three distinct regions: I: free expanding beam head, II: a pinch region, and III: main body of beam with matching radius r_m.

. Consequently, the diluted density of plasma electrons is

$$n\left(k_{bp}\xi\right) = n_0/\cosh^2 k_{bp}\xi$$

which is used to estimate how fast the plasma electrons will be rarefied. For example, if the rarefied condition is defined as $n\left(k_{bp}\xi\right)/n_0 \leq 10^{-3}$, this implies that the bunch length has to be larger than $4.15/k_{bp}$. Since this analysis completely ignores the longitudinal dynamics and transients of plasma gradient, it is only used for the core regime of a bunch with inhomogeneous density distribution. A complete description of the details of the interaction between the bunch head and plasma electrons have to been analyzed by numerical simulation. However, by assuming a preformed homogeneous ion channel and cylindrically symmetric beam, it's possible to use an envelope equation to describe beam size evolution [Reiser, 1994]. This approach is equivalent to the analysis based on Twiss or Courant-Snyder parameters [Weingartner et al., 2012]. The envelope equation of an electron bunch with a rms radius R for this uniform linear focusing system is written as

$$\frac{d^2R}{dz^2} + \left(K + K_g/R_0^2\right) \cdot R - \frac{\epsilon^2}{R^3} = 0 \tag{2.5}$$

where R_0 is the initial radius of the bunch, K_g is the generalized perveance [Lawson, 1958], and ϵ is the rms natural emittance of the bunch (see Fig. 2.2). The value of K_g is proportional to $I/(\gamma^2-1)^{3/2}$ and is usually much smaller than the contributions from emittance and ion focusing (K) for a relativistic electron bunch, and it is neglected in the following discussion [2]. First considering the case of $K=0$ and ignoring K_g which corresponds to the free propagation in vacuum, the equation (2.5) is integrated twice yielding the hyperbolic solution:

$$R\left(z\right) = \sqrt{\left(\frac{\epsilon}{R_0}^2 + R'^2_0\right) z^2 + R_0^2 + 2R_0R'_0 z} \tag{2.6}$$

---

[2] In the case of an LWFA electron bunch decelerated in an underdense plasma, this magnetic field and the space charge are, however, significant of the self-focusing of low energy bunches during propagation.

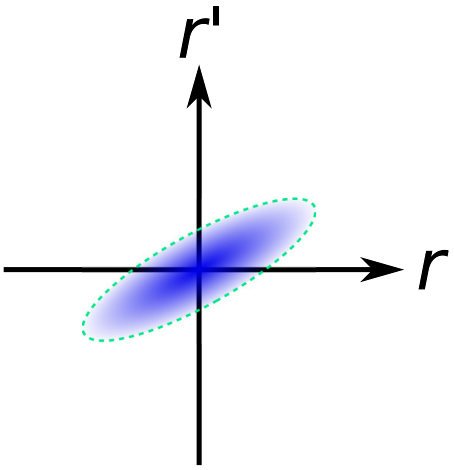

Figure 2.2: Example of the distribution function of electron bunches in the phase space. In this case, $\epsilon = \left(\overline{r^2}\,\overline{r'^2} - \overline{rr'}^2\right)^{1/2}$. If the hyperellipsoidal volume inside the dashed line is populated with uniform density, which is called waterbag distribution, $\epsilon\pi$ is equal to the area of the ellipse.

where R'_0 is the initial slope of the envelope. The solution shows that the bunch expands exactly like a Gaussian laser beam propagating in vacuum with beam waist R_0 when $R'{}_0 = 0$. In the case of the present of ion channel, the radius of the bunch envelope will stay constant if the focusing force balances with the emittance. This radius is called matched size r_m which is obtained by balancing the second and third terms in the LHS of Eq. (2.5):

$$r_m = \sqrt{\frac{\epsilon}{k_\beta}} = \sqrt{\frac{\epsilon_N}{k_p}\sqrt{\frac{2}{\gamma}}} = \left(\frac{\epsilon_N}{\sqrt{2\pi r_e n_0 \gamma}}\right)^{1/2} \tag{2.7}$$

where $\epsilon_N = \gamma\epsilon$ is the normalized emittance. For the case that the initial radius of the envelope is not matched to the focusing strength, the envelope will oscillate anharmonically around the propagation axis in the absence of additional energy dissipation and constant n_0 as shown in Fig. 2.3(a). The period of oscillation is shorter with higher density. This dependence is exploited to adjust the divergence of the electron bunch by density gradient. For example, the electron bunch from the LWFA typically has a small beam diameter but large divergence which is unfavorable for applications. In this situation, a density down ramp will help to collimate or focus the electron beam, see Fig. 2.3 for example. Conversely, the electron sources from the conventional linear accelerator provide collimated beams but with large size. It has been proposed to use plasma with density upramp to adiabatically focus a beam into a guiding channel [Martin et al., 1985; Takayama and Hiramatsu, 1988]. It needs to be emphasized that the analysis here is based on an ideal focusing channel and homogeneous radial expansion (contraction). In reality, even for a uniform neutral density background, there usually exists a transverse density gradient of plasma which is likely caused by inhomogeneous ionization or the radial gradient of the electric field from any finite size electron bunch. In this case, electrons from different parts of the bunch will oscillate with

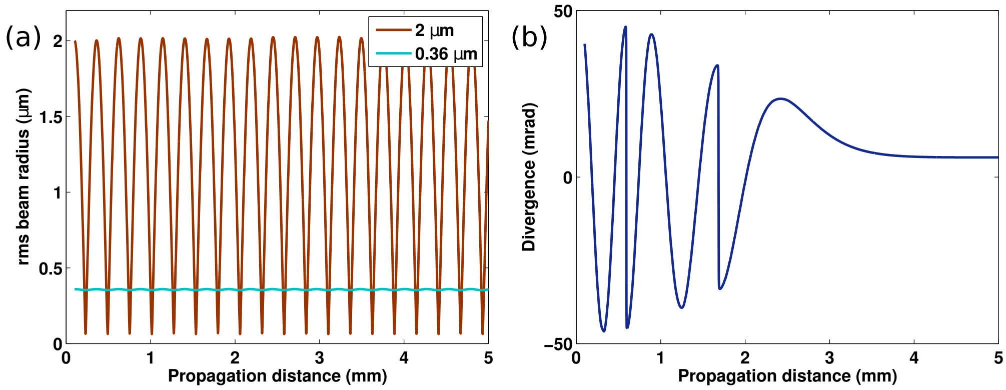

Figure 2.3: Evolution of the radius and divergence of the envelope of the electron bunch. (a) Example of the anharmonic oscillation of an electron bunch with different initial beam size as shown in the legend. The initial divergence is 0, $\lambda_p = 26.4\ \mu$m, electron energy is 100 MeV and $\epsilon_N = 0.3$ mm mrad which corresponds to a matched radius $r_m = 0.357\ \mu$m. It is seen that the oscillation amplitude is small when the radius is closed to a matched one. (b) Adiabatic damping of the divergence of the envelope in a plasma down ramp which is assumed to be a Gaussian decay with rms width 1 mm. The initial beam radius and divergence are 2 μm and 40 mrad respectively, and the values of the rest of the parameters are same as in (a). The divergence is reduced to 5.7 mrad in the end of the density down ramp.

different periods and pinch into separated longitudinal positions. A representative demonstration of this effect is the scalloping of the beam head which has been studied numerically and observed experimentally [Blumenfeld et al., 2007; Wu et al., 2010].

2.2 Propagation of Electron Bunches Driven by LWFA

The conventional radio frequency linear acceleration electron sources deliver up to 100s GeV and several nC beams. Since these kind of source are based on thermal electron gun, the pulse duration is limited by the thermal fluctuation and is usually limited to ≥ps. On the other hand, the electron bunch from a typical LWFA has much lower charge, between 0.1 pC and 1 nC with energy from several MeV to several GeV [Walker et al., 2012; Leemans et al., 2006; McGuffey et al., 2010; Buck et al., 2013; Geddes et al., 2008; Faure et al., 2006] but much smaller source size with comparable $epsilon_N$ and much shorter bunch duration. Since the typical plasma density which matched to the regular Ti:sapphire based TW laser system is around 10^{18} to 10^{19} cm^{-3}, the source size of the LWFA electron bunch in the bubble is considered to be on the scale of r_m and in the range of sub-μm to few μm. The source size has been determined experimentally by using the angular resolved spectra of betatron radiation [Phuoc et al., 2006; Schlenvoigt et al., 2007; Fuchs et al., 2009; Rousse et al., 2004; Malka et al., 2008] . Additionally, by measuring the transition radiation, which is generated when relativistic charged particles penetrated through a boundary of different materials, [Bajlekov et al., 2013; Debus et al., 2010; Glinec et al., 2007] or by the direct imaging of plasma wave [Buck et al., 2011], it has been shown that the bunch duration from control injection is on the order of a few fs [Leemans et al., 2003; Lundh et al., 2011, 2013; Ohkubo et al., 2007; van Tilborg et al., 2006]. Such unique properties are very distinct from regular electron sources, the behavior of the bunch during transportation inside a plasma has not yet been studied comprehensively.

As mentioned in the last section, the analytical model is only applied for a slowly varying system with $\geq L_E \gg \lambda_\beta$. In the case of LWFA driven electron bunches, due to relatively low energy and the interaction with a strong self-generated wakefield, the bunch starts to self-modulate as soon as it propagates into the plasma. This will quickly distort the distribution of the bunch in phase space. Accordingly we use computer simulations in this section to understand the complex physics behind it. First of all, in order to prevent modeling error and seek a compromise between correct physics and computational efficiency, it's necessary to choose proper input parameters for the simulations. For example, to resolve the density modulation of the self-pinch properly, the grid size has to be smaller than r_m, and the transverse dimension of simulation window needs to be large enough to cover the whole bunch after several mm of propagation. When the grid resolution is too high, a large amount of data is generated and substantial computational resources are required. As a compromise, the grid size is chosen to be slightly smaller than r_m which is around 300 nm in these conditions.

A typical evolution of the charge distribution and longitudinal electric field during propagation is shown in Fig. 2.4. In this 3D simulation, the initial condition for the electron bunch is $\sigma_r = 2.1{k_p}^{-1} = 5.86$ μm , $\sigma_z = 0.14{k_p}^{-1} = 0.39$ μm, $\gamma = 71$, and total charge of 40 pC. The density profile of the plasma is a step function beginning from $x = 46$ with a constant density $n_e = 3.6 \times 10^{18}$ cm^{-3} and the same density for ion background. Similar to the case of a long electron bunch, the propagation evolution of LWFA bunches is divided into 4 steps:

1. The electron bunch propagates in vacuum with a quasi-self-consistent elec-

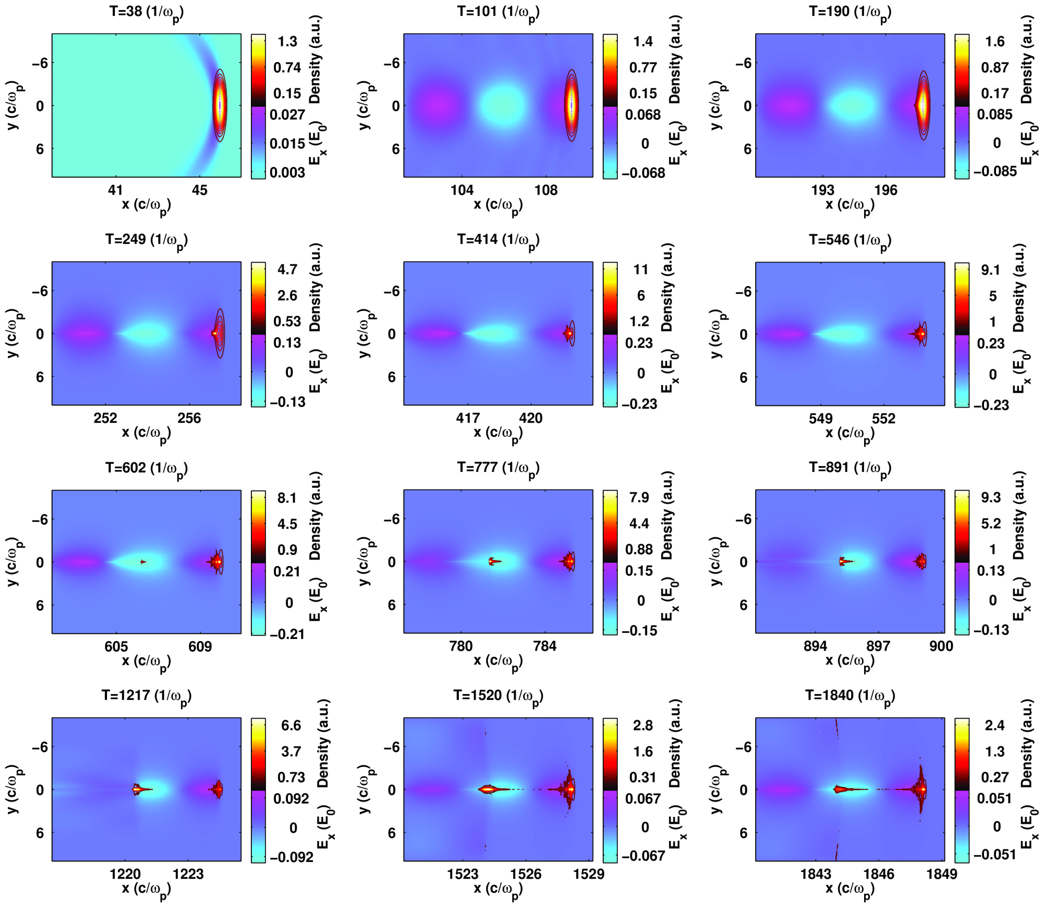

Figure 2.4: Electron bunch evolution inside plasma. The contour lines show the distribution of the relative density of the electron bunches which is normalized to $n_e = 3.6 \times 10^{18}$ cm^{-3}, and the color gradients in the background indicates the strength of the longitudinal electric field which is normalized to the cold non-relativistic wave breaking field $E_0 = 182.6$ GV/m. The initial condition for the electron bunch is $\sigma_r = 2.1{k_p}^{-1} = 5.86$ μm, $\sigma_z = 0.14{k_p}^{-1} = 0.39$ μm and initial energy of 35 MeV. The density profile of the plasma is a step function beginning from $x = 46$ with a constant density $n_e = 3.6 \times 10^{18}$ cm^{-3} and the same density for ion background.

tromagnetic field[3] , as shown in Fig. 2.4 at T=38. Its field is very similar to what is calculated from Liénard-Wiechert potential [Jackson, 1999]. A small discrepancy originates from the fact that the exact self-consistent field will require an infinite amount of acceleration steps.

2. The electron bunch drives a linear wakefield right after propagating into plasma at T=101. The strength of the electric field matches the theoretical formula (1.19).
3. From T=190, the rear side of the bunch is decelerated by a self-driven wakefield and starts to self-focus. This process is called **collective deceleration**. The wakefield is enhanced significantly and correspondingly, the local electron density increases. The self-focusing generates a series of fine structures at T=546, which is the so-called scalloping, as was mentioned before.
4. As the deceleration continues, more and more electrons lose their energy. If the plasma is long enough, some electrons will be trapped in the acceleration phase of the wakefield and re-accelerated during propagation, as is shown at T=602. At the end of the process, the decelerated electrons are scattered out of the simulation window (T=1840).

The physics of the last two steps as well as collective deceleration will be discussed in next sections separately.

2.2.1 Collective Deceleration of Electron Bunch

The collective deceleration of the electron bunches in the self-driven wakefield plays an important role in the evolution of the bunch in plasma, and it will be studied experimentally in chapter 5. During the deceleration, the total energy of the electron bunch is decreased, and its spectrum gets broader, as shown in Fig. 2.5, because the rear side of electron bunch sits in the non-uniform decelerating electric field. We define a global parameter called the Remaining Energy Fraction (REF) to quantify the energy loss, where the REF is defined as the ratio of the total energy of the bunch after propagation to the total initial energy. The REF evolution of Fig. 2.4 is shown in Fig. 2.6[4] , which shows two distinguishable phases with a transition at T$\approx$ 750. In the first phase (T$\leq$750), the front side of the bunch

---

[3] Since the simulation is initialized with zero field, the electron bunch is forced to propagate in free space without any evolution to build up a self-consistent field. This process is called numerical acceleration.

[4] It has to be noticed that the temporal scale in Fig. 2.4 mainly depends on the initial bunch diameter and spectrum. What is observed experimentally depends on to which phase the bunch is evolved when the plasma is terminated.

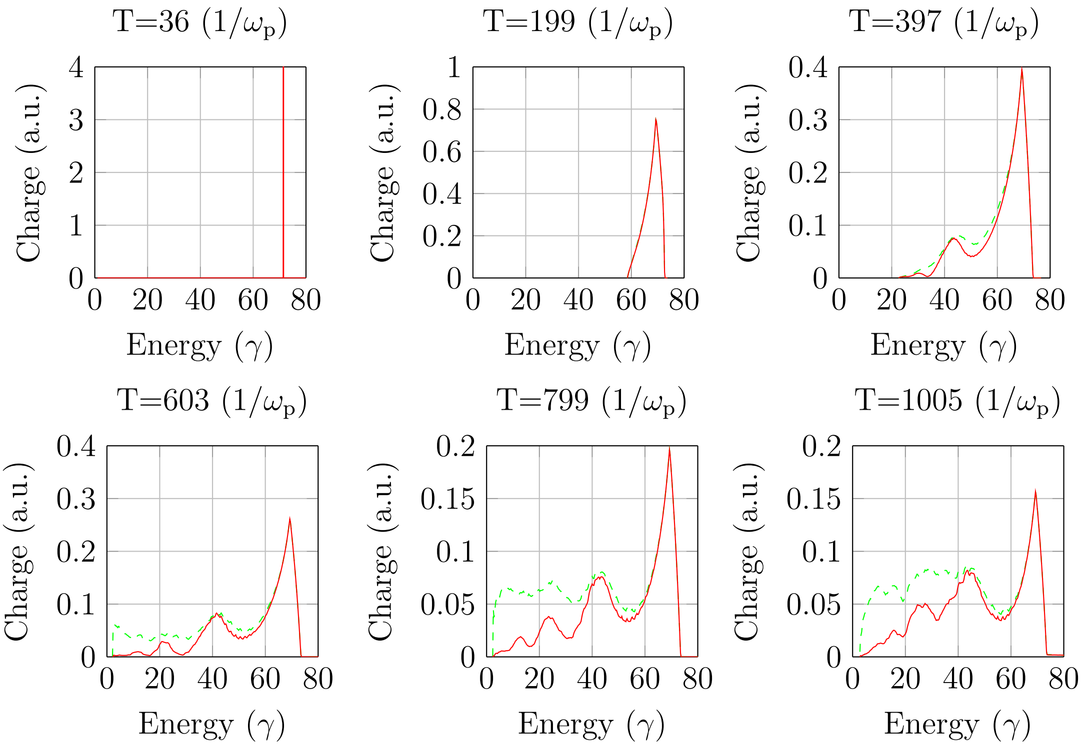

Figure 2.5: Evolution of electron spectra at different time steps. The parameters of the simulation are the same as in Fig. 2.4. The spectra of particles which have divergence below 30 mrad are shown in red solid lines, and the spectra of all particles are shown in green dashed lines.

expels the plasma electrons and drives a weak wakefield, then the back side of the bunch experiences a strong focusing due to the static electric field of ions and self-driven magnetic field [Barov and Rosenzweig, 1994]. The details of self-focusing will be discussed in the next section. The strong focusing enhances the wakefield significantly which quickly decelerates the electrons in the backside of the bunch and causes a fast drop in REF curve.

The process continues until the second phase (T> 750) where a significant amount of electrons are trapped in the acceleration phase of the wave. The bunch is split into two parts where the first part drives the plasma wave while the second part of the bunch gains energy (Fig. 2.13). When the rate of energy loss from the driving part is comparable to the rate of energy gain of the trapped part, the decrease in REF reaches saturation and forms a shoulder. The spectra (see green dashed line in Fig. 2.5 at T=799 and T=1005) show a plateau which contains most of the charge and is separated from the original energy peak. In this specific case, the REF at saturation amounts to ≈ 0.5, and the REF is reduced to ≈ 0 for higher

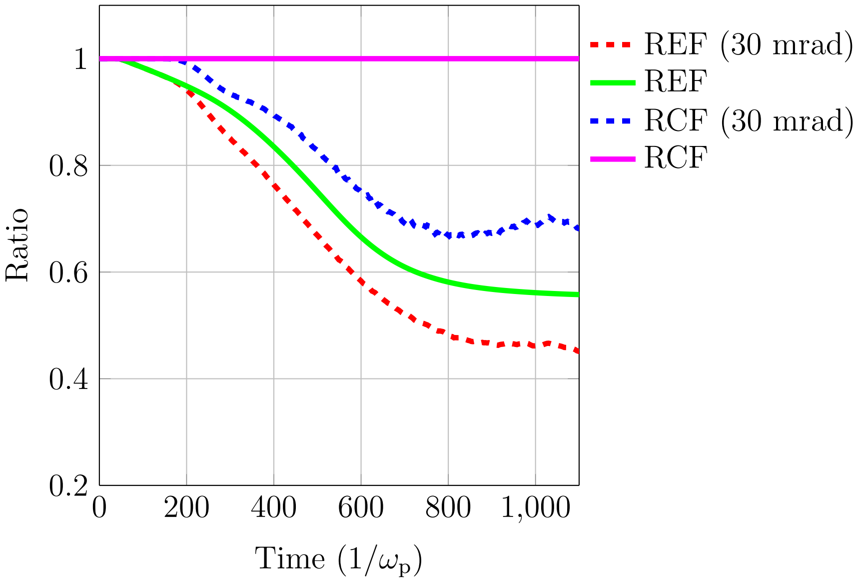

Figure 2.6: Remaining energy fraction (REF) and remaining charge fraction (RCF) evolution from the case of Fig. 2.4. The solid lines show the results of all particles, and the dashed lines show the results of particles with the divergence below 30 mrad.

density bunches.

Note that since only electrons within the spectrometer's acceptance angle during experiment are observed, an accompanying charge loss of highly divergent electrons is expectable. Similar to REF, we define Remaining Charge Fraction (RCF) to quantify this charge loss, which is defined as the ratio of the total charge of the bunch after propagation to the initial charge. To understand the relation between charge loss and energy loss, we compare the results from Fig. 2.6 and Fig. 2.5; in the case of including all particles, the RCF remains constant, which is a direct proof that there is no energy loss due to charge loss beside the collective deceleration in the simulation. On the other hand, in the case of the particles with the divergence below 30 mrad, a positive correlation between RCF and REF and a suppression of the low energy part of the electron spectrum shows that only the decelerated low-energy electrons get lost by scattering. The simulations with different initial beam sizes show that the energy loss due to the fraction of electrons outside the acceptance angle of the spectrometer contributes to less than 20% of the final beam energy (in this specific case the contribution is 14% at T=700 which is approximate 2 mm of plasma).

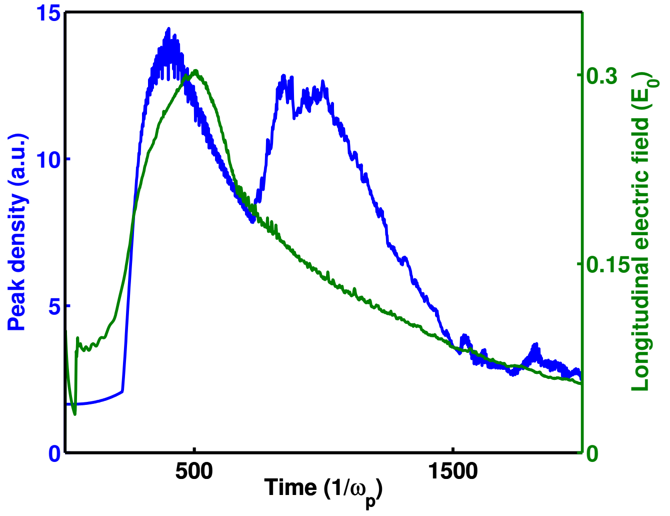

Figure 2.7: Evolution of the peak density of the bunch and the peak value of the longitudinal electric field of the wakefield shown in Fig. 2.4. In this specific case, the second peak of the density curve results from migration of lots of electrons to the secondary bunch in the rear side of the first wakefield period and causes a higher density than the primary bunch.

2.2.2 Self-focusing of Electron Bunch

The self-focusing of the bunch increases the peak density and shrinks the radius dramatically, which boosts the strength of wakefield as shown in Fig. 2.7. In PIC simulations, the electrons are represented by macroparticles. In order to understand the self-focusing mechanism, we use a particle tracking algorithm to monitor the moving path as well as the changing of energy and the experienced fields of selected particles. Since the density profile of the electron bunch is assumed to fit a bi-Gaussian distribution, the bunch temporal evolution is assumed to be cylindrically symmetric, and the macroparticles which are located within the slice nearest to the center of axis are chosen to be analyzed as shown in Fig. 2.8(a). We first take an overview of the global behavior of the selected macroparticles. Fig. 2.8(b) and (c) show the transverse movement of particles in relative spatial coordinates in a comoving frame and temporal domain respectively. The paths and energy evolutions of the particles are almost perfectly mirror symmetric to the central axis. A minor asymmetric behavior is caused by the small discrepancies between the perfectly symmetric positions (the central position of solid circles in Fig. 2.8(a)) and chosen ones (the crosses). The tracking results show that at the initial stage of propagation, the particles are decelerated and migrate to the backside of the first period of the wakefield (as indicated in Fig. 2.4). The results also show the particles which are closer to axis are decelerated and self-focused faster than the particles outside. This is explained by stronger wakefield near axis.

The self-focusing of the bunch is caused by the self-generated field and ion-focusing channel, as is described by K_g and K in eq. (2.5). To clarify this issue, we focus on the field progression of the particles in the middle of the bunch (Fig. 2.9).

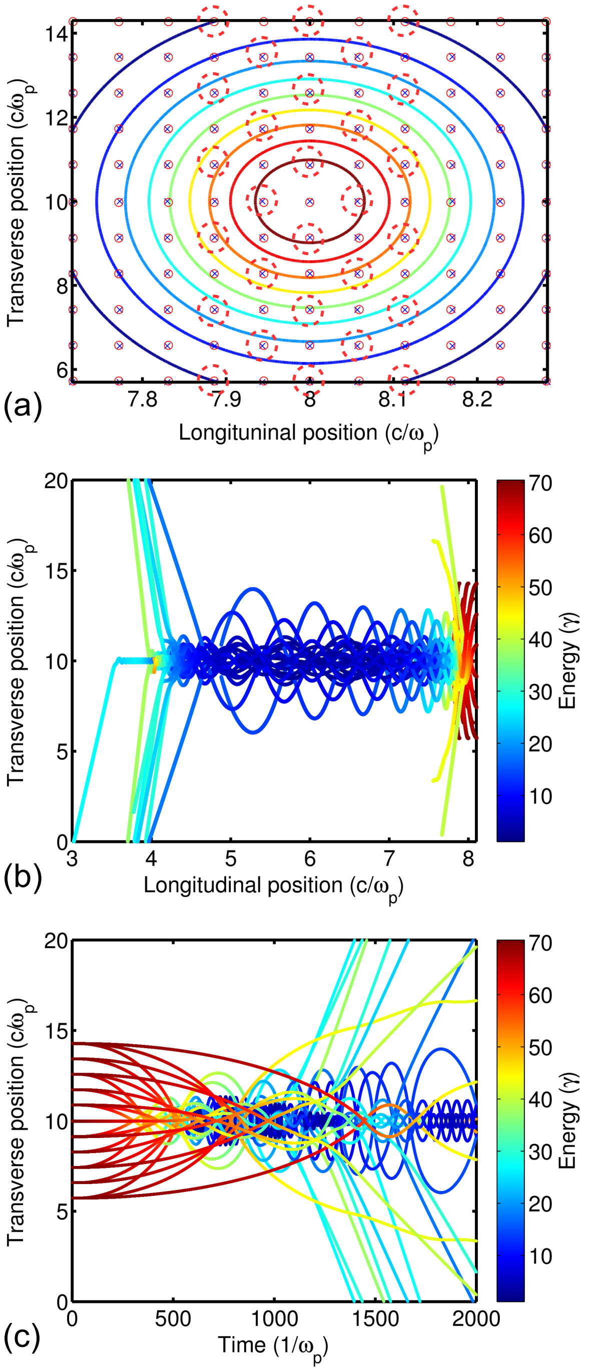

Figure 2.8: Paths of selected macroparticles during interaction. The input parameters are the same as what is used in Fig. 2.4. (a) shows the cross section of the middle of the electron bunch at T=0, where the points enclosed by dashed circle define the positions of selected macro particles. The color contour lines indicate the density distribution of the electron bunch. The paths of the particles in the co-moving frame are shown in (b) where the tracks are color coded by energy which is represented by the Lorentz factor, and the longitudinal positions of the x-axis is defined as x(t)-ct where x(t) is the longitudinal position at t. (c) shows temporal evolutions of transverse position and energy of the particles.

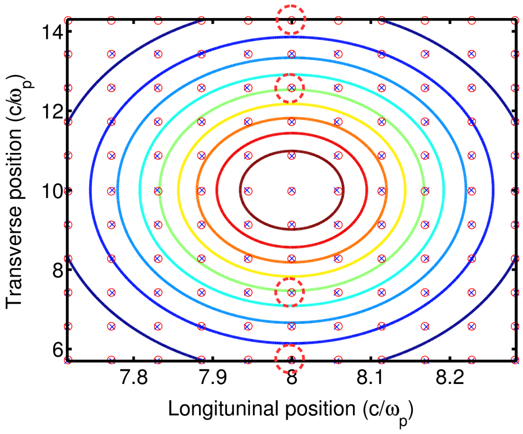

Figure 2.9: Position of macroparticles for self-focusing analysis at T=0. The particles inside the red dashed line are investigated in Fig. 2.10. The input parameters are the same as what is used in Fig. 2.4.

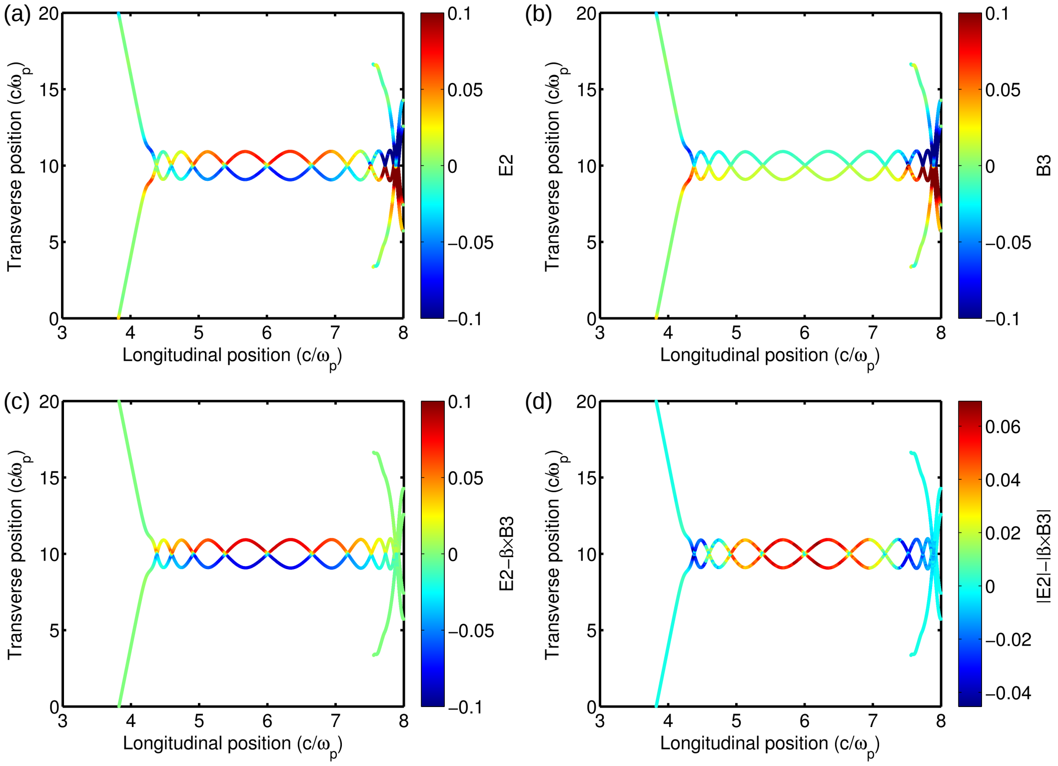

Figure 2.10: Evolution of focusing fields along particle's trajectories in a co-moving frame. The color scale E2 in (a) is the strength of the transverse electric field in units of E_0, and B3 in (b) is the strength of the magnetic field in the direction perpendicular to the paper in the unit of E_0/c. The color scales are adjusted to show the minor variation during propagation. The total effective transverse field is shown in (c), and (d) compares the contribution from E2 and B3.

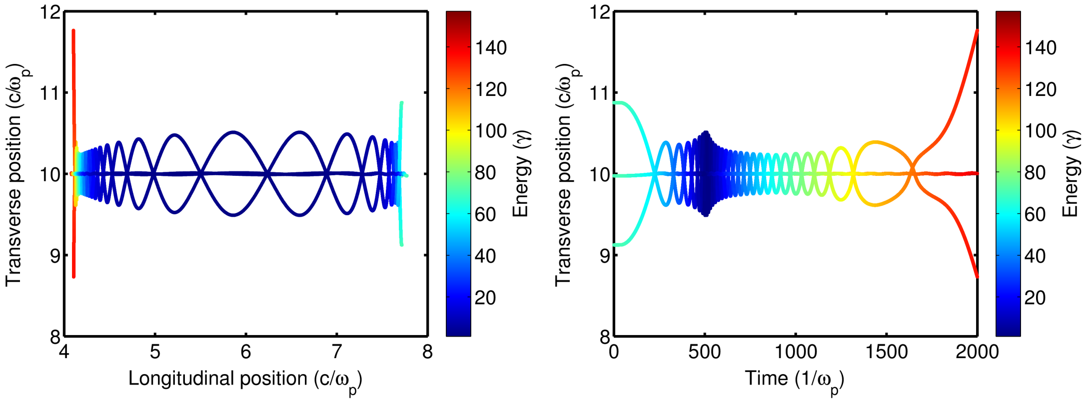

Figure 2.11: Demonstration of re-acceleration and temporal evolution of trapped particles in a co-moving frame. The input parameters are the same as Fig. 2.4.

The comparison of electric and magnetic fields are shown in Fig. 2.10. Interestingly, the electric field defocusses the particles in the beginning as well as in the end of the process while the magnetic field is always focusing, as shown in Fig. 2.10(a) and (b), and the total contribution of both fields is always focusing within the wake as shown in (c).

2.2.3 Electron Trapping

As observed in simulations, a considerable amount of electrons from the driving bunch are trapped in the backside of the wakefield and form a secondary bunch. All of the trapped electrons will be scattered sooner or later, if the plasma is long enough, because of the abatement of the self-focusing force as mentioned in last section. A few of electrons, however, stay in the acceleration phase for long time and experience significant re-acceleration; one of the most extreme cases is shown in Fig. 2.11, where the trapped electrons are accelerated to more than double the energy of the driver bunch. This process is similar to the wave breaking of the laser-driven wakefield [Bulanov et al., 1997]. In our case, since the driving strength of electron bunch is highly dependent on time, the temporal derivation of the scalar potential of the resulting wakefield is not negligible, i.e. $\Phi = \Phi\left(t, x - c\beta_{ph}t\right)$, and therefore the integral of motion which corresponds to (1.31) with the extra Φ term cannot be solved analytically. Nevertheless, (1.33) is still able to be used to estimate the injection condition as a first order approximation. Since only the electrons which move faster than the phase velocity of the wakefield are trapped, the probability of injection is studied by monitoring the variation of β_{ph}. In an attempt to signify related phenomena that influence the trapping process, we simulate a smaller electron driver of $\gamma = 71.4 \equiv \gamma_i$, $\sigma_r = 0.54k_p^{-1} = 1.51\ \mu\text{m}$,

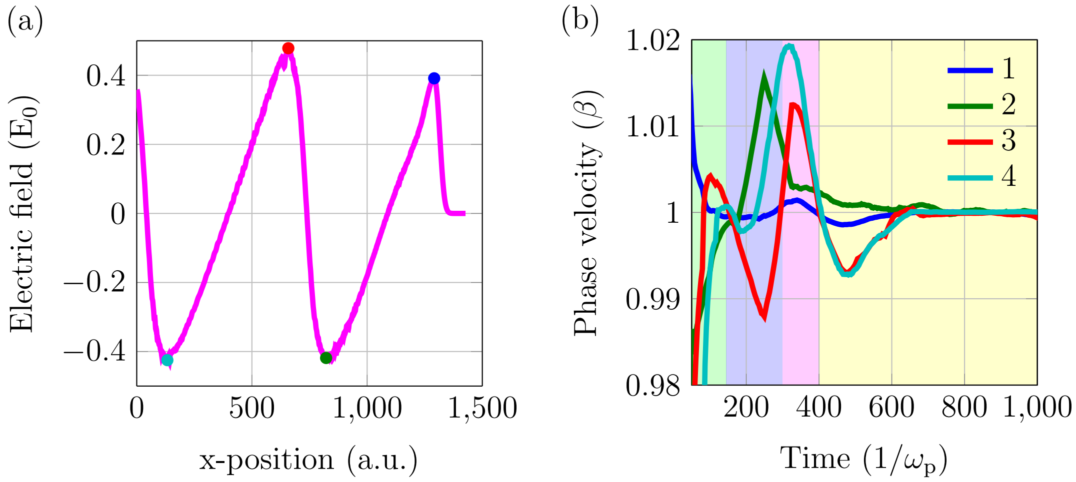

Figure 2.12: Monitoring of local phase velocity evolution of the wakefield driven by an electron bunch with parameters of $\gamma = 71.4 \equiv \gamma_i$, $\sigma_r = 1.51$ μm, $\sigma_x = 0.39$ μm, total charge of 40 pC. (a) illustrates the color-coded denotation of the selected peaks/troughs on a longitudinal electric field of the wakefield at an arbitrary time. The longitudinal position of the electron driver is located around x=1300. The corresponding phase velocity as a function of time of the selected phases with the same color-coding is plotted in (b), and the four areas with different colors correspond to four steps of evolution described in section 2.2.3.

$\sigma_x = 0.14k_p^{-1} = 0.39$ μm, total charge of 40 pC and a constant plasma density $n_e = 3.6 \times 10^{18}$ cm^{-3}. From now on, the results of this section are based on these parameters implicitly if not otherwise stated. To look for injection conditions, we focus on the local phase velocity of specific phases of the wakefield as indicated in Fig. 2.12. The local phase velocity β is defined as $\Delta x_t / c\Delta t$, where Δx_t is the difference of the position of a specific phase of the plasma wave between time step t and $t + \Delta t$, and Δt is the size of one time step in the simulation. As seen in Fig. 2.12(b), the phase velocity is not uniformly distributed across the wake and goes higher or lower than c. The mechanism behind this effect is explained by the progression of the longitudinal electric field and density distribution of the electron bunch as what are shown in Fig. 2.13. The phase velocity evolves in following steps:

1. From T=34 to T≈140: Initially, the bunch has medium strength to drive a slightly nonlinear plasma wave. This is accompanied by an increase in the driving strength due to bunch self-focusing, and the wakefield becomes more and more nonlinear. Similar to LWFA, this effect is attributed to the relativistic mass increase of plasma electrons and causes a downshift in the

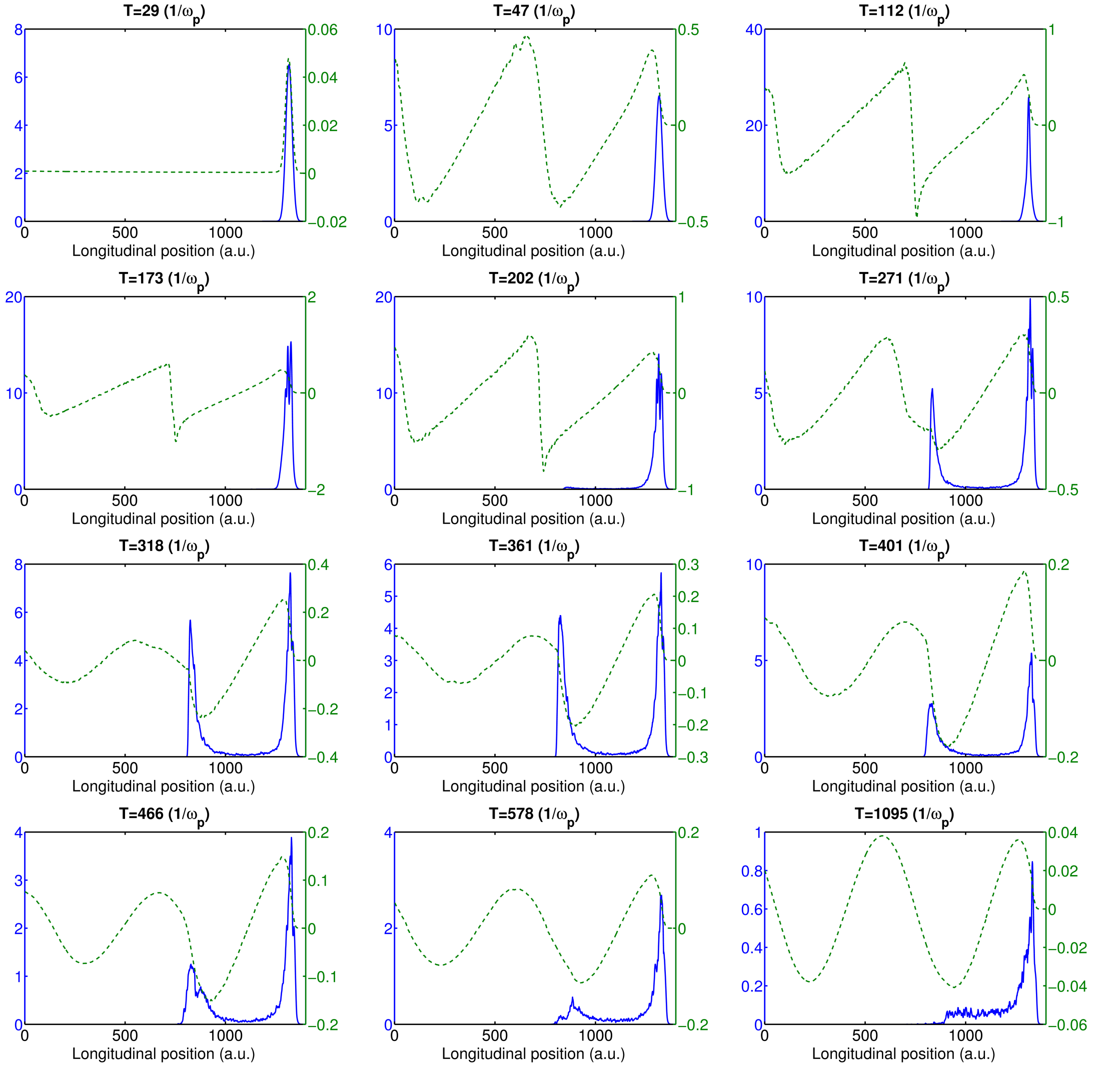

Figure 2.13: Lineouts of the longitudinal electric field (dashed green line, in units of E_0) and the density profile of the electron bunch (solid blue line, a.u.) from the middle of simulation box. The plasma background is stepwise distributed, and the bunch encounters plasma at $T \approx 34$.

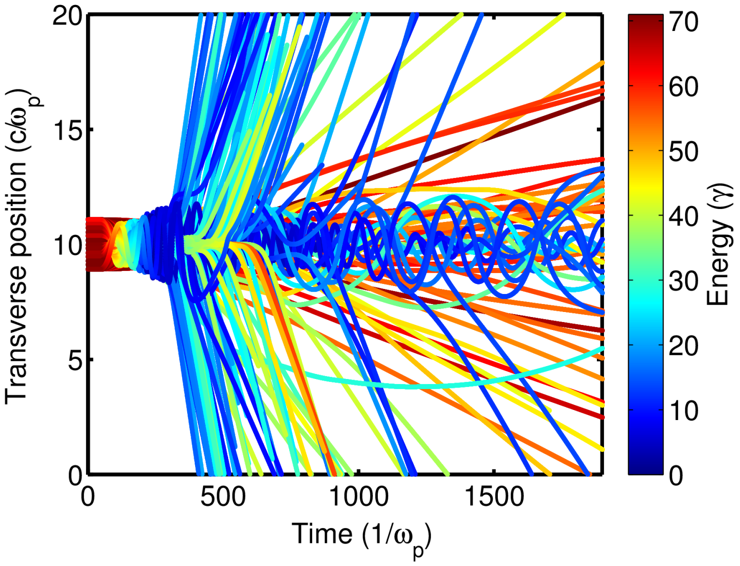

Figure 2.14: Tracks of selected particles which are color coded by energy. The particles are homogeneously distributed within the middle of the cross section of the bunch which are the same as what is indicated as crosses in Fig. 2.9. It is well visible that dominantly low energy electrons are scattered out.

oscillation frequency and increase in the corresponding plasma wavelength [Rosenzweig, 1987]. The phase velocity of the first trough (color coded with green in Fig. 2.12) is much slower than β_i, which is the corresponding normalized velocity of γ_i which is the initial energy of the driver. However, since no significant amount of particles experience strong deceleration, there are few particles trapped at this stage. On other hand, the increase in expelling force pushes the first peak forward, i.e. the lead of wakefield (blue in Fig. 2.12), and results in a phase velocity greater than c. The process approaches a quasi-steady wakefield at T≈120, where the magnitude of the longitudinal electric field also reaches its maximum.

2. From T≈150 to T≈300: The bunch starts to collapse due the low energy electrons moving backwards relative to the average position of the driving bunch, hence the whole wake is slowed down, as seen from T=145 to 177 in Fig. 2.12(b). Shortly after this intermediate step, the significant flux of electrons are decelerated to reach the backside of the first plasma period and built up the second bunch, which further pushes the second period of wakefield moving backward. This effect causes a feedback to additionally reduce the velocity and trap more and more electrons.

3. From T≈300 to T≈400: The increasing amount of charge in the second bunch neutralizes the original electric field driven by the first bunch and starts to drive its own wakefield. Because of the relatively low charge inside second bunch and the interference with the field driven by first bunch, the wakefield becomes more linear. Together with the fact that the distance between first peak and the center of mass of the second bunch is shorter than the first period of the wake, the second period moves forward. This is noticed in Fig. 2.12(b) where the velocity of the last three denoted positions are all increased until T≈350. The movement of the second period, however, shifts the second bunch into the defocusing and deceleration field, and the composite are scattered away, as observed in Fig. 2.14.

4. From T≈400 to T=∞: The charge loss reduces the driving power of the second bunch, and the dominant contribution of the driving force is gradually shifted to the first bunch again, also the electron scattering rate decreases because of weakening of the defocusing field. Therefore, the second period of plasma wave experiences a reduction of the phase velocity until T≈650. From this point, however, the wakefield becomes even weaker due to bunch elongation. Because of the resulting decrease in the electron flux from the first bunch to the second bunch, the charge in the acceleration phase is not enough to load the wakefield. The phase velocity is then determined by the remaining high energy electrons, no significant trapping happens again and considerable amount of the low energy electrons fall behind the deceleration phase which are scattered by the defocusing field and get lost eventually (see Fig. 2.14).

2.3 Conclusion

We have studied the propagation of ultrashort electron bunches driven by LWFA in plasma. Unlike classical long electron beams, the propagation of the ultrashort electron bunch is highly nonlinear and cannot be treated as quasi-static evolution. The ultrashort bunches drive a wakefield with considerable strength. The resulting significant self-modulation due to strong self-focusing and collective deceleration change the driving wakefield, which may trap and finally scatter most electrons away at much lower energy than original energy. The ultrashort bunches from LWFA show the potential to make a tabletop driver for PWFA experiment. Also, the property of strong collective deceleration inside plasma can also be applied as a compact and economic electron beam dump, which will be discussed in Chapter 5.

Chapter 3

Experimental Facilities

3.1 High Power Laser Facilities

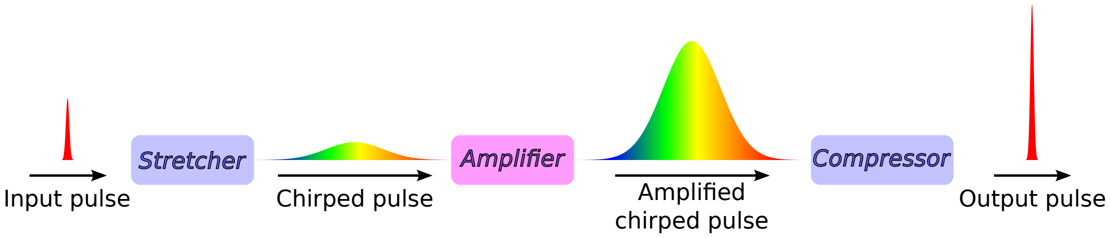

Figure 3.1: Concept of the chirped pulse amplification (CPA) scheme.

Currently, the most well-developed high power laser systems for the electron acceleration are based on the Chirped Pulse Amplification (CPA) [Strickland and Mourou, 1985; Mourou et al., 2006], as shown in Fig. 3.1. Two major issues are overcome with the invention of CPA during amplification of ultrashort pulses which are generated from, for example, a passive mode-locking Titanium:sapphire oscillator [Asaki et al., 1993; Apolonski et al., 2000; Ell et al., 2001]. Firstly, the intensity of direct amplification is limited to the damage threshold of the gain medium and all of the reflective and transmissive optics in the beam path. Secondly, the propagation of high intensity beam in a medium will cause a series of nonlinear effects which include the spatial and temporal phase distortions by self-phase modulation, self-focusing or filamentation [Perry et al., 1994; Couairon and Mysyrowicz, 2007]. Therefore, the reachable maximum intensity of the laser from the direct amplification is limited to GW/cm^2. These issues are not solved by simply enlarging the beam size because of the dramatical increase of the cost for large aperture optics, also the reduction of the input-energy fluence of the seed laser decreases the energy extraction efficiency of amplification.

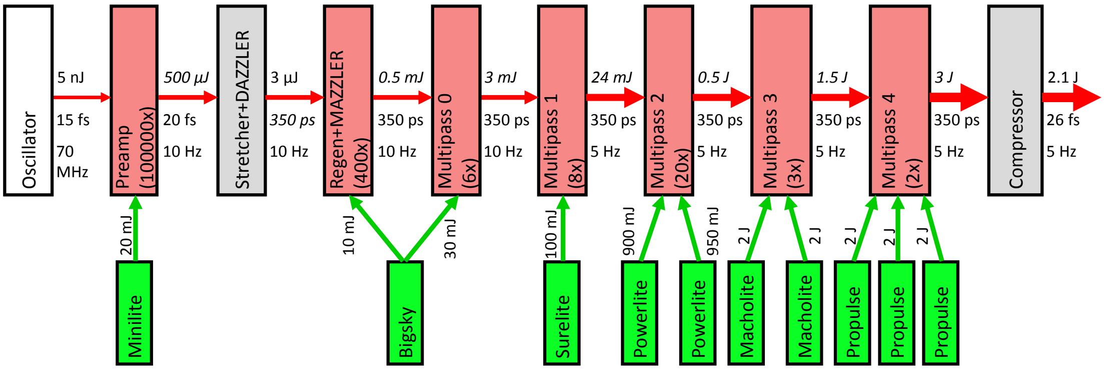

Figure 3.2: Layout of the ATLAS laser system. The number in parentheses shows the energy gain in each amplifier (Courtesy of K. Khrennikov).

In the CPA scheme, before the main amplifier, the seed laser is chirped by a device introducing Group-Delay Dispersion (GDD) called *stretcher* which is usually composed by a pair of diffraction gratings, prisms or the combination of both. Inside the stretcher, the spectral components are separated in time and therefore it elongates the pulse duration. The stretching factor is typically around 10^5 for the most of the Ti:Sapphire based systems. This way, the seed preserves high fluence but is amplified with much lower peak intensity as well as smaller optics. In the end, the amplified chirped pulse is compressed by using another GVD device (*compressor*) to compensate the GVD introduced in the stretcher and the material dispersion in the beam path. The CPA boosts the peak power to PW scale compared to GW by the direct amplification.

3.1.1 ATLAS Laser System

In this study, the ATLAS (Advanced Titanium:Sapphire LASer) laser system was used to drive the primary electron bunches in the collective deceleration experiment and the emittance measurement, see chapter 5. ATLAS utilizes Ti-Sapphire crystals as gain media and is based on the CPA technology, which provided compressed pulses during experiment of 1.8 J, 26 fs at a central wavelength of 800 nm with a repetition rate of 5 Hz. The gain media are pumped by the frequency-doubled pulses at 532 nm from flash-lamp pumped Nd:YAG lasers. The layout of amplifiers is shown in Fig. 3.2, which includes one regenerative amplifier (regen) and several multi-pass amplifiers [Norris, 1992; Osterhoff, 2009]. The laser is seeded by a commercial passive Kerr-lens mode-locked Titanium:Sapphire oscillator (Rainbow, Femtolasers GmbH) which delivers pulses with 5 nJ at 15 fs pulse duration [Brabec et al., 1992]. The pulses are stretched to 350 ps in a grating-based stretcher after a multi-pass pre-amplifier. Additionally, an acousto-optic programmable dispersive filter (AOPDF) or DAZZLER[1] (Fastlite, Ltd.) is introduced after the stretcher to pre-compensate the residual spectral phase distortion after the compressor to achieve a better compression, which is also used to modify the pulse shape for the optimization of electron quality during experiment [Pathak et al., 2012]. The stretched pulses are then sent into a regenerative amplifier. Inside the regenerative amplifier, there is another key component called MAZZLER (Fastlite, Ltd.), which is a similar device like DAZZLER except the ordinary beam is used. The MAZZLER suppresses the spectral components which have highest energy gain in order to compensate the gain narrowing during amplification [Trisorio et al., 2011]. Consequently, the spectrum of the pulses after the regen has a FWHM bandwidth >80 nm, and the final amplified pulses preserve a bandwidth of 60 nm which gives sub-20 fs pulse duration in the Fourier limit. The pulses are further amplified in four multi-pass amplifiers to 3 J and sent into a grating compressor in a vacuum chamber. The design of stretcher and compressor has a Martínez-Treacy configuration[2] [Martinez, 1987; Ohmae et al., 2000; Treacy, 1969], in which the stretcher is introducing a positive chirp and correspondingly a negative chirp compressor is used. The alignment of gratings has to minimize the higher order dispersion and angular chirp, where higher order dispersion increases the pulse duration while angular chirp causes a tiled pulse front [Pretzler et al., 2000]. In order to achieve better focusing quality in the experiment, ATLAS is equipped with a deformable mirror which receives the feedback signal from a wavefront sensor, which takes the leakage from the mirror before the compressor chamber, and is operated in a closed-loop configuration to correct wave-front distortion during amplification.

---

[1] DAZZLER includes an acoustic wave generator and a birefringent uniaxial crystal. The laser beam propagates along the ordinary axes of the crystal. The anharmonic acoustic wave modulates the refractive index of the crystal which forms a variable grating and diffracts the individual frequency components of the incoming pulse from ordinary to extraordinary axes at different positions. This way, the desired higher order chirp is superimposed on the laser pulse through controlling the chirp of the acoustic wave.

[2] The ATLAS actually uses a modified version of Martínez stretcher to save space, which is called *Öffner's design* [Bromage et al., 2012].

3.1.2 LWS-20 Light Source

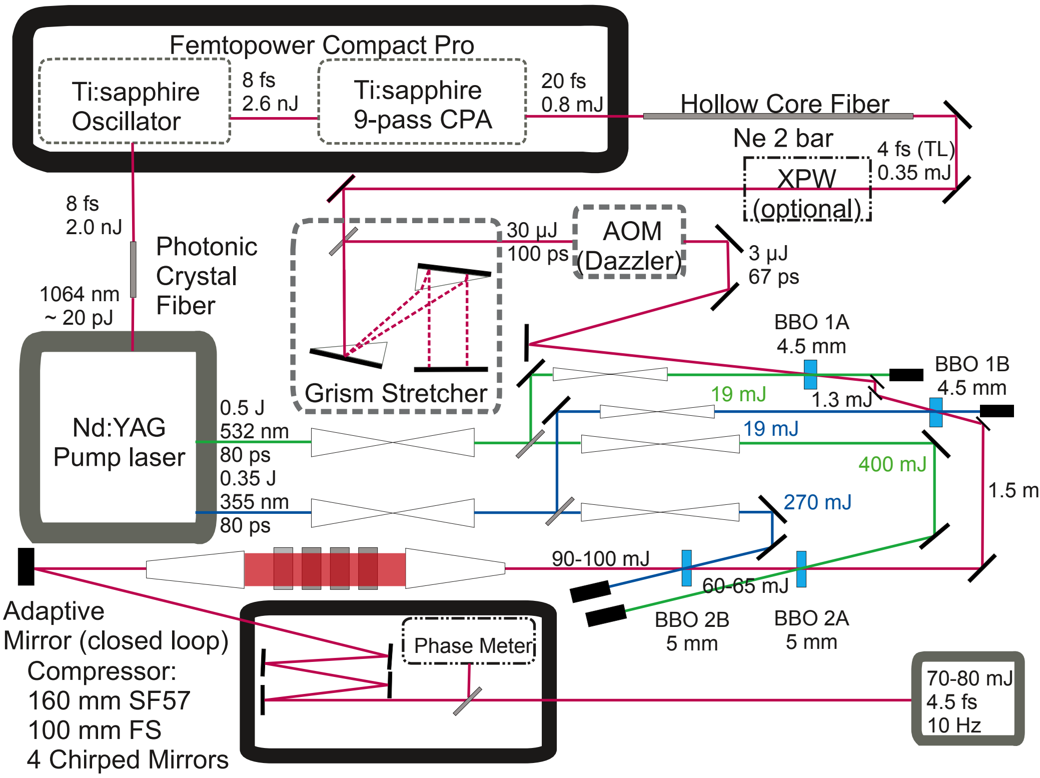

Figure 3.3: Layout of LWS-20 light source.

In the second part of this work, we used the Light Wave Synthesizer 20 (LWS-20) to generate sub-10 MeV electrons. The layout of LWS-20 is shown in Fig. 3.3. The system is based on the optical parametric synthesizer principle, i.e., two-colour pumped Noncollinear Optical Parametric Chirped Pulse Amplification (NOPCPA) [Herrmann et al., 2010] to cover a super broadband spectrum which spans from 580 to 1020 nm with a central wavelength at 740 nm as shown in Fig. 3.4. The Fourier limit of this broad spectrum offers sub-5 fs pulse duration which corresponds to sub-2-cycle optical oscillation. The pulse duration is confirmed by second order autocorrelation measurement (Fig. 3.5) and many other techniques. The energy of the compressed pulse reaches 80 mJ at 10 Hz which gives a peak power of almost 20 TW. So far, LWS-20 is the most intense few-cycle laser system in the world.

The front end of the system starts from a Ti:sapphire based oscillator which gives 8 fs pulses of a few nJ scale at a repetition rate of 80 MHz. About 2/3 of the pulse energy is sent to a stretcher and a 1 kHz multi-pass amplifier. The amplified pulses are compressed by a prism compressor to provide 800 μJ and 20 fs pulse duration. The oscillator together with the kHz amplifier and the prism

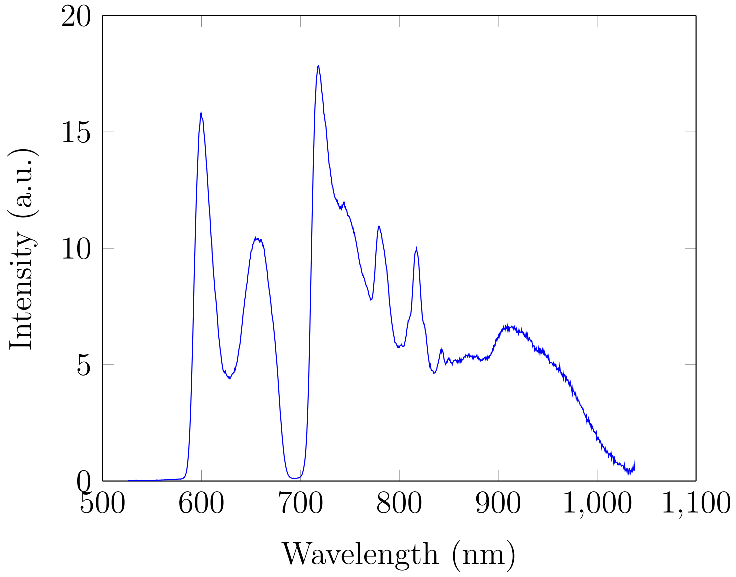

Figure 3.4: Laser spectrum of LWS-20.

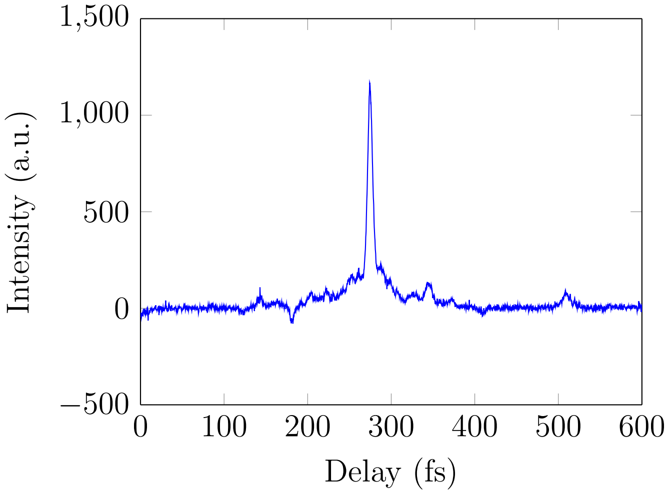

Figure 3.5: Single-shot second order autocorrelation measurement of LWS-20. The retrieved pulse duration is 4.7 fs in FWHM.

compressor belongs to a commercial system (Femtopower Compact Pro, Femtolasers GmbH). The spectrum of the compressed pulses are broadened by self-phase modulation inside a Ne-filled hollow-core fiber. These pulses are sent through a GRISM stretcher [Dou et al., 2010] which adds negative dispersion and stretches the pulses to 100 ps pulse duration. Similar to ATLAS, a DAZZLER is implemented after the stretcher and before the OPCPA stages to remove the residual phase at the end of the system.

The pump beam is optically synchronized to the seed beam by using the rest 1/3 of the pulse energy from the oscillator. The pulses from the oscillator are focused by a lens to a photonic crystal fiber which shifts the central wavelength to 1064 nm. These pulses are pre-amplified by a fiber amplifier before seeding a commercially customized flash-lamp pumped Nd:YAG laser system (EKSPLA) which delivers two arms of amplified pulses of 1 J with 80 ps pulse duration at 10 Hz. One arm of the amplified pulses are frequency-doubled in a LBO (Lithium triborate) crystal and generate pulses of 500 mJ at 532 nm. The other arm is frequency-tripled in two LBO crystals to deliver pulses of 350 mJ at 355 nm.

The seed pulses after the DAZZLER are overlapped with the pump pulse spatially and temporally at four sequential NOPCPA stages by using four BBO (Beta Barium borate) crystals which are cut for type I phase matching condition. The green pumps of 532 nm amplify the seed pulses in two stages to 65 mJ with the spectral range from 700 nm to 1020 nm, and the blue pumps of 355 nm amplify the pulses in the other two stages to 25 mJ from 580 nm to 700 nm. The alignment between the pump and the seed needs to be accurate within 200 μrad precision, which is automatized by using separate position and pointing imaging system behind each NOPCPA stage. The final amplified beam is expanded to a diameter of 100 mm and then compressed to 200 fs by using bulk glasses which include 160 mm SF57 and 100 mm fused silica. The partially compressed beam is then telescoped to a diameter of 50 mm and compressed by four chirped mirrors in vacuum. This arrangement is to prevent nonlinear effects in the glasses. A deformable mirror and a wavefront sensor in a closed loop configuration is installed before the compressor chamber to shape the wavefront. Additionally, one part of the beam which is picked up by a 5 mm diameter silver mirror coated on a 2 μm thick pellicle (National Photocolor) is sent to a single-shot phasemeter to measure the carrier-envelope phase (CEP) of the pulses [Wittmann et al., 2009].

3.2 Electron Detection

The major part of this work requires the study of the electron properties which include the spatial profile, charge and the energy distribution. In order to acquire the data on the single-shot mode with a high repetition rate, the electrons are

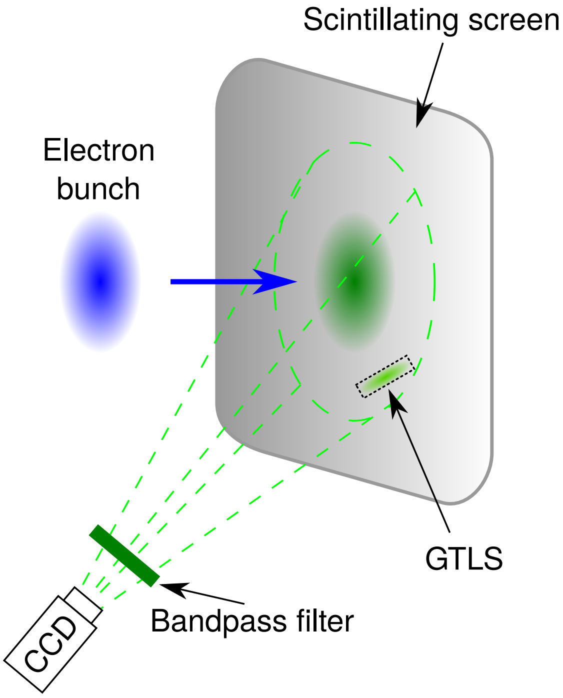

Figure 3.6: Electron beam profile detector. The imaging system between the scintillating screen and the camera is not shown.

detected by absolute charge-calibrated scintillating screens (Biomax MS, Kodak) imaged onto CCDs, and the sensitivity is about 0.35 fC/pixel [Buck et al., 2010]. The scintillating screen has a layer of rare earth doped powdered phosphor which emits light at 546 nm, and the amount of light from a certain area is proportional to the total charge of electrons and is independent of the electron energies in the range of interest in this work. Comparing to image plates (IPs), which are also common for the charged particle detection [Nakanii et al., 2008], the data from the scintillating screen is read out in situ during experiments while the IPs have to be removed from the vacuum chamber to retrieve the data. A typical setup of the electron beam profile measurement is shown in Fig. 3.6. The light from the scintillating screen is collected by an imagining system and detected by a 12bit CCD camera (Grasshopper, PointGrey Ltd). A bandpass filter (FB550-40, Thorlabs GmbH) is installed in front of the camera to minimize the influence of the scattered light from the the laser-plasma interaction. The signal transmission is calibrated through a gaseous tritium light source (GTLS, trigalight®) beside the screen. The GTLS is a laser-sealed cylindrical capsule which is coated with zinc sulfide based phosphor and filled with tritium gas. The radiation from the tritium causes the phosphor to emit photons at 535 nm with an almost-constant fluence. The absolute charge is calculated according to the ratio between the detected photon counts from scintillating screen and the GTLS. Due to 12 years half-life time of tritium and the ageing phosphor, the GTLS needs to be recalibrated with other calibrated light sources, for example, a stable laser diode around once per year.

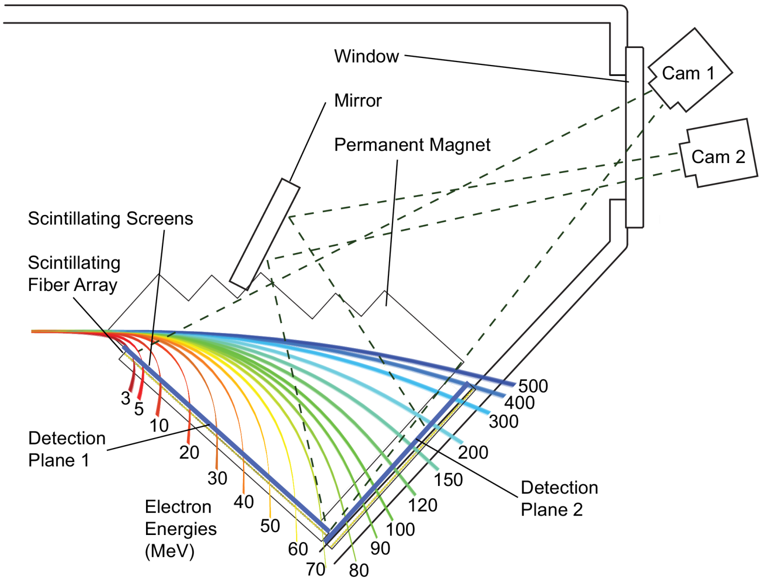

Figure 3.7: Electron spectrometer used in the collective deceleration measurement. The electron trajectories of different energies inside the dipole magnet are depicted with coloured line. The electrons are detected by two scintillating screens which are imaged to two CCD cameras outside of the vacuum chamber. In this experiment, since the maximum of electron energy is less than 40 MeV, only the first detection plane was used [Buck, 2011].

Figure 3.8: Dispersion curve of the low energy detection plane (detection plane 1 in Fig. 3.7).The intersection of the low energy and the high energy detection plane is at 400 mm. The distance is measured from the top of the scintillating screen.

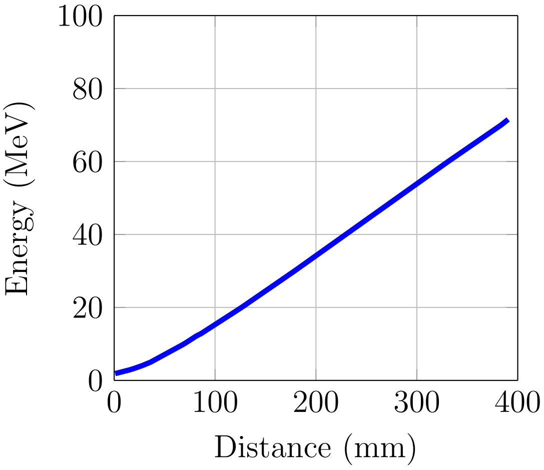

The energy spectrum of the electrons is measured by using permanent magnet dipoles which deflect the electrons a different amount according to their energies. The electron spectrometer used in the collective deceleration measurement is shown in Fig. 3.7. The magnet dipoles with a magnetic field of 0.91 T have a gap of 5 cm which allows the acceptance angle of detecting electron divergence up to 35.7 mrad (full opening angle) in the experiment. The energy calibration was done by general particle tracer (GPT) simulation of electron trajectories based on the experimentally measured magnetic field map by a Hall probe. The electrons with energies below 70 MeV are bent to the first detection plane which is at an angle of $\pi/4$ with respect to the propagation axis of the beam before the dipole, and the electrons with energies between 70 MeV and 400 MeV are measured in the second detection plane. The spectrometer has a resolution around 2% for the electron energies of 10-400 MeV. In this work, we used only the low energy detecting plane. The dispersion curve of the low energy detection plane (detection plane 1 in Fig. 3.7) is shown in Fig. 3.8. The intersection of the low energy and the high energy detection plane is at 400 mm. The distance is measured from entrance plane of the spectrometer. Additionally, an array of 256 bundles of 3 scintillating fibers directly attached to the backside of the scintillation screen was used, which was connected to a 16bit camera. Although the energy resolution of the fiber detector is not as good as the scintillation screen, the sensitivity of the detector is much higher and is useful to crosscheck the signal from the direct imagining of the screens during the measurement. The design is detailed in [Cuevas, 2007; Sears et al., 2010b].

In the measurement of the LWFA driven by LWS-20, sub-10 MeV electrons were generated, and a smaller electron spectrometer was used to measure the low energy electrons. The design of the spectrometer is shown in Fig. 3.9. The gap between the dipoles is 1.5 cm, and the entrance has an aperture of 1 cm diameter which all together corresponds to $\approx$20 mrad divergence of the incoming electron beams in the experiment. The maximum strength of the magnetic field is 150 mT, and the calculated dispersion curve is shown in Fig. 3.10. The theoretical calculation shows that energy resolution is about 10%. The detail of the dipole can be found in [Gahn et al., 2000].

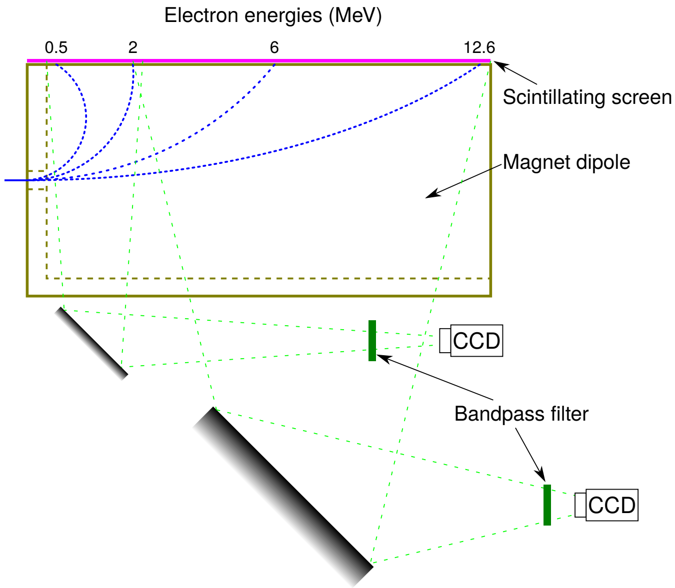

Figure 3.9: Setup of the electron spectrometer used in the LWS-20 experiment. Due to the limitation of the size of the experimental chamber, the electron energies from 0.5 to 2 MeV and from 2 to 12 MeV are detected by two CCD cameras located in the vacuum chamber. A GTLS (not shown) attached to the scintillation screen inside the overlapping region of both cameras is used to connect the signal detected by different cameras.

Figure 3.10: Dispersion curve of the low energy electron spectrometer shown in Fig. 3.9.

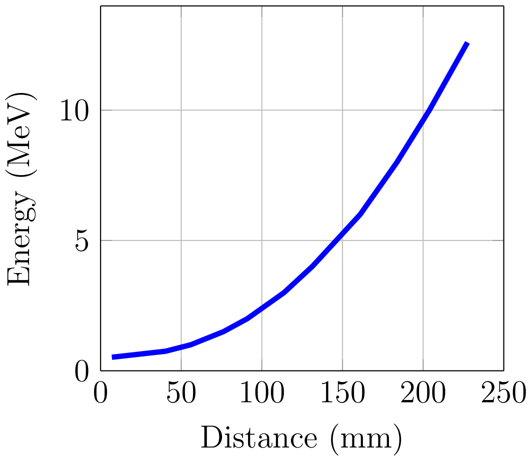

Chapter 4

Design and Characterization of Gas Targets

The electron density plays an essential role in the study of plasma physics; it significantly influences the growth rate of the plasma instabilities and properties of the plasma wave. In the field of the LWFA, the interaction of plasma with an intense laser pulse is dominated by the relation between the plasma wavelength and the wavelength of the laser. The injection process is also greatly influenced by the change of the electron density. Similarly, the ratio between the electron density of plasma and the density of charged particles as well as the ratio of the temporal bunch duration to the plasma wavelength determines the coupling efficiency of the Coulomb force from charged particles to the plasma in the field of PWFA. Therefore, stable and well-characterized gas targets are crucial for all experiments. In this chapter, we discuss the design and the performance of our targets which include gas cells and supersonic jets.

4.1 Design of Gas Cell

In a low density LWFA experiment, the dephasing length as well as the depletion length is relatively long; hence mm scale gas targets are required. In our case, we used length tunable gas cells to generate up to 600 MeV electrons for the emittance measurements [Weingartner et al., 2011, 2012] and in the experiment of the collective deceleration, which is described in section 5.1. The design of the gas cell is shown in Fig. 4.1. The gas cell was composed of the entrance part and the exit part which were made of stainless steel and brass respectively. The length of the gas cell was tunable between 2 to 14 mm by micrometers adjusters. The gas was filled into the gas cell from a pulsed solenoid valve to limit the amount of gas into vacuum, and the pressure inside the cell was measured through a

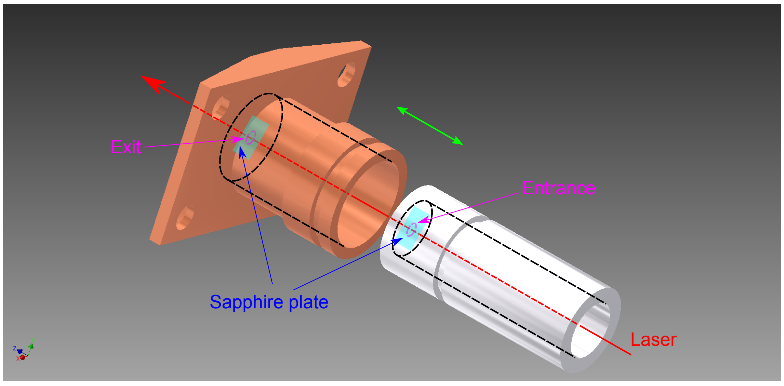

Figure 4.1: Geometry of the gas cell. The right compartment is the entrance part of the cell, and the left one is the exit part. The laser pulse propagates along the symmetric axis of the gas cell. The eight symmetrically distributed gas inlets which are not shown here located in the end of the exit part, and each gas inlet has 1 mm diameter.

fast piezoelectric sensor which had a μs response time. The minimum opening time was 30 ms to achieve a quasi-steady flow and typically operated at 50 ms before the arrival of laser pulses. The holes for the laser to pass through were located in the middle of the cell and had 0.3 mm diameter, which, however, were gradually damaged by laser pulses during experiments, and the diameter increased up to 2 mm. The enlarged holes caused a different quasi-steady flow and changed the density distribution significantly. This issue was solved by adhering sapphire plates to these holes and replaced it regularly. Since direct measurements inside the cell were not possible, the density distribution was interpreted through 3D fluid dynamics simulations. An open source code called OpenFOAM was used to do the calculation [Jasak, 2009]. The turbulence model was shear-stress transport (SST) K-ω [Menter, 1993]. The result is shown in Fig. 4.2. Two important features of the density distribution were noticed from simulations (Fig. 4.2a)

1. The density inside the cell was inhomogeneous. The density is higher in the direction of the gas flow.
2. The gas formed a *plume* around the gas exit, i.e. the path of the laser pulse.

The density drop and the inhomogeneity was caused by the acceleration of the gas particles during the expansion from gas inlets and the reflection from the corner of the gas cell, which is seen from the streamlines illustrated in Fig. 4.2b. This issue has been solved by a significant increase of the size of the inlets to two 3 mm long and 1 mm wide slits. However, to simulate the performance of the new design, a complete geometry including the gas pipes and the performance of the gas

(a) Density distribution of the gas cell. Inset: 1D on-axis density distribution.

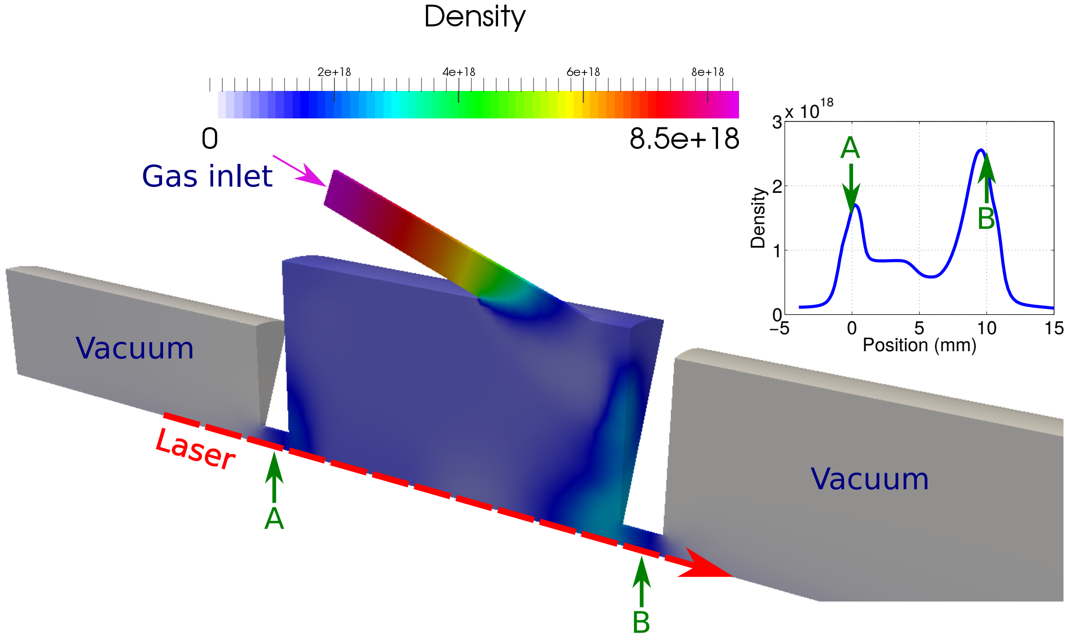

(b) The streamlines of the gas flow inside the gas cell.

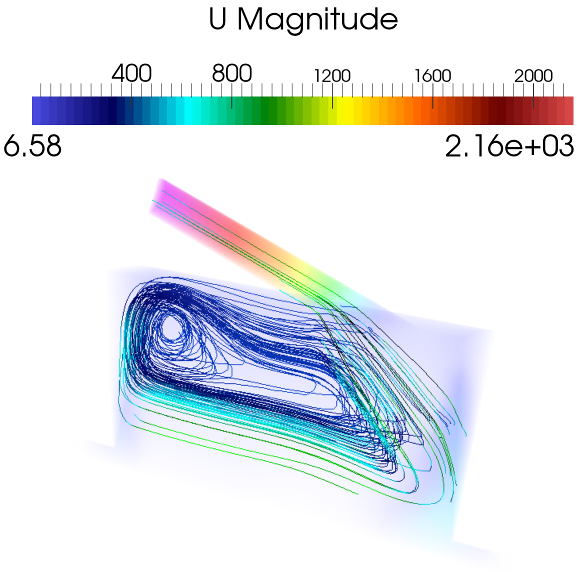

Figure 4.2: Results of the fluid dynamics simulation of the gas cell after 5.6 ms opening time of the valve. The laser propagates along the symmetric axis. The density in the unit of electrons/cm^3. **U** is the magnitude of the velocity of the particles in the unit of m/s. The gas medium was hydrogen, and the initial condition at the gas inlet was 180 mbar and **U**= 0. Since the inner geometry of the gas cell was cylindrically symmetric, the 3D simulation was accelerated by calculating 1/16 of the cell and applied symmetric boundary condition to the walls of the cell.

valve must be taken into account which is beyond the capability of our computer clusters. Nevertheless, the experimental results from both designs show a good agreement between the interpreted density and the applied pressure [Popp, 2011], which indicates the density drop between the backing pressure and the density inside the gas cell is much less critical, and the distribution is expected to be more homogeneous. We also noticed in the both cases that the length of the plume extended to several mm away from the surface of the gas exit, and it increased further when the diameter of the gas exit became larger. The plume prolonged the acceleration length of LWFA which is also expected to affect the divergence of the generated electron beams due to the adiabatic damping which is discussed in section 2.1.

4.2 Supersonic Flow and Shock Wave

4.2.1 Generation of Supersonic Flow

In this section we focus on the dynamics of high-speed flow, or usually called gas dynamics. The goal of this section is to introduce the basic equations to describe the supersonic flow and the properties of the shock in a gas medium. In fluid dynamics, the subject is a fluid which is composed of a large number of molecules whose microscopic properties are neglected, and it is treated as a continuous medium. Consequently, the macroscopic phenomena is formulated by infinitely small elements of volume which are small compared to the whole system but still contains a great number of molecules. In thermodynamics, the state of a time-invariant and homogeneous system is fully characterized by any two of the three state variables: *pressure* (p), *temperature* (T) and *density* (ρ) or *volume* (V). Therefore, the equation of state to describe such equilibrium system is expressed as:

$$f\left(p, T, \rho\right) = 0$$

For example, in the case of an ideal gas, the equation of state is $f\left(p, T, \rho\right) = p - \frac{R}{M_0}\rho T$, where R is the ideal gas constant, and M_0 is the molecular weight of the medium. On the other hand, the description of the state of a moving fluid requires an additional knowledge of the distribution of the velocity field $\vec{v}\left(x, y, z, t\right)$ together with the distribution function of two of the state variables, for example $T\left(x, y, z, t\right)$ and $\rho\left(x, y, z, t\right)$. The fundamental equations of fluid dynamics are derived from the conservation laws [Landau and Lifshits, 1959; Batchelor, 2000; Liepmann, 1957; Pirumov, 1986]. Firstly, an increase of mass within a unit volume in a unit time equals to the amount of a fluid flowing across the surface bounding this volume. This gives the equation of continuity:

$$\frac{\partial \rho}{\partial t} + \nabla \cdot (\vec{v}\rho) = 0 \tag{4.1}$$

Similarly, by considering the total force acting on the surface, the equation of motion of a volume element is written in the form:

$$\frac{\partial \vec{v}}{\partial t} + (\vec{v} \cdot \nabla)\,\vec{v} = -\frac{\nabla p}{\rho} + \vec{f} \tag{4.2}$$

where ρf is the contribution of an additional force. This so called Euler's equation is one of the most important equations of fluid dynamics. So far, the derivation has assumed an *ideal* fluid, which takes no account of the mechanism of the internal heat exchange and the energy dissipation due to the viscosity between different parts of the fluid. The dissipation processes will be revisited later when we discuss the thickness of the shock front. Similar to (4.1), if the external force is absent, the Euler's equation will be expressed in a form equivalent to the law of conservation of momentum:

$$\frac{\partial}{\partial t}\rho v_i + \sum_{j=1}^{3} \frac{\partial}{\partial x_j}\left(\rho v_i v_j + p\delta_{ij}\right) = 0 \tag{4.3}$$

where v_i is the ith component of the velocity at the point where the unit volume locates in the space; $\delta_{ij} = 1$ for $i = j$ and $\delta_{ij} = 0$ for $i \neq j$. The last equation is the law of conservation of energy which is the first law of thermodynamics. It is formulated as follows: the difference of a specific internal energy (ϵ_{in}) of the unit volume is contributed by the work done by the surrounding, and a specific energy (ϵ_{ex}) generated by external sources. The energy of the unit volume consists of the internal energy and the kinetic energy and is written as:

$$\rho\epsilon_{in} + \frac{\rho v^2}{2}.$$

By using (4.1) and (4.3), the equation of conservation of energy is deduced

$$\frac{\partial}{\partial t}\left(\rho\epsilon_{in} + \frac{\rho v^2}{2}\right) + \nabla \cdot \left[\rho\vec{v}\left(\epsilon_{in} + \frac{v^2}{2}\right) + p\vec{v}\right] = \rho\epsilon_{ex} \tag{4.4}$$

In gas dynamics, a special case called *adiabatic* process is frequently used, which occurs when the process is very fast and so the heat exchange between different parts of the medium is absent. According to the second law of thermodynamics, the entropy S of any part of the fluid remains constant. Such process is also said to be *isentropic*. If a gas flow of a density distribution ρ is adiabatic, we will have

$$\frac{d\rho}{dt} = \left(\frac{\partial \rho}{\partial p}\right)_S \frac{dp}{dt} = \frac{1}{{v_c}^2}\left(\frac{\partial p}{\partial t} + \vec{v} \cdot \nabla p\right) \tag{4.5}$$

where v_c is the speed of sound, and the suffix S indicates the process is isentropic. If the gas medium is an ideal gas, the speed of sound will be given by:

$$v_c = \sqrt{\left(\frac{\partial p}{\partial \rho}\right)_S} = \sqrt{\kappa \frac{p}{\rho}} = \sqrt{\frac{\kappa R}{M_0} T} \tag{4.6}$$

where $\kappa = c_p/c_V$ [1] . To get an intuitive insight of these equations, we assume a acoustic wave without any external sources, which means the gas flow is only in one dimension with velocity v, and all state variables are constants in transverse dimension. We simplify (4.1)-(4.5) to

$$\frac{\partial \rho}{\partial t} + \frac{\partial \rho v}{\partial x} = 0 \tag{4.7}$$

$$\frac{\partial v}{\partial t} + v \frac{\partial v}{\partial x} = -\frac{1}{\rho} \frac{\partial p}{\partial x} \tag{4.8}$$

$$\frac{\partial \rho v}{\partial t} + \frac{\partial}{\partial x}\left(p + \rho v^2\right) = 0 \tag{4.9}$$

$$\frac{\partial}{\partial t}\left(\rho \epsilon_{in} + \frac{\rho v^2}{2}\right) + \frac{\partial}{\partial x}\left[\rho v \left(\epsilon_{in} + \frac{v^2}{2} + \frac{p}{\rho}\right)\right] = 0 \tag{4.10}$$

$$\frac{\partial \rho}{\partial t} + v \frac{\partial \rho}{\partial x} = \frac{1}{{v_c}^2}\left(\frac{\partial p}{\partial t} + v \frac{\partial p}{\partial x}\right) \tag{4.11}$$

where the identity $\frac{d}{dt} = \frac{\partial}{\partial t} + \vec{v} \cdot \nabla$ is used implicitly. The next step is to solve equations of the gas flow in a nozzle, which consists a convergent inlet, a bottleneck throat and a divergent exit, as shown in Fig. 4.3. The nozzle is assumed to have a slow varying cross section $\sigma_n(x)$ along its length [Whitham, 1958], and the boundary effect of surfaces of the nozzle is negligible. The flow inside the nozzle is approximated by the one dimensional adiabatic flow. Under this assumption, a difference of the mass flow $\sigma_n \rho v$ from each side of a cross section must be due to the change of density and velocity of the fluid. We obtain an additional continuity equation for the nozzle

$$\sigma_n \frac{\partial \rho}{\partial t} = -\frac{\partial}{\partial x}\left(\sigma_n \rho v\right) \tag{4.12}$$

---

[1] c_p and c_V are specific heat capacities, which state the temperature change of a system after receiving a certain amount of the heat Q under constant pressure and constant volume condition respectively, and they are defined as

$$c_V = \left(\frac{\partial Q}{\partial T}\right)_V = \left(\frac{\partial \epsilon_{in}}{\partial T}\right)_V \qquad c_p = \left(\frac{\partial Q}{\partial T}\right)_p = \left(\frac{\partial H}{\partial T}\right)_p$$

where $H \equiv \epsilon_{in} + \frac{p}{\rho}$ is the *enthalpy* of the system.

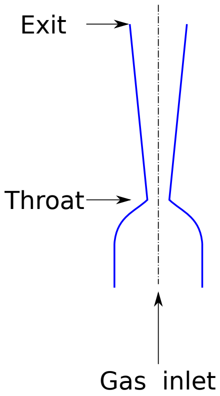

Figure 4.3: Configuration of the cross section of a de Laval nozzle. In our experiment, the nozzle has a fixed 1:3 expansion ratio between the throat and the exit diameter, and the total divergence angle of exit is 14.3°.

Since we are interested in a steady flow condition, all the temporal dependence of state variables are vanished. From (4.8) and (4.11), we get $-\frac{v}{{v_c}^2}\frac{\partial v}{\partial x} = \frac{1}{\rho}\frac{\partial \rho}{\partial x}$ and then after substituting it into (4.12)

$$\left(M - \frac{1}{M}\right)\frac{\partial M}{\partial x} = \frac{1}{\sigma_n}\frac{\partial \sigma_n}{\partial x} \tag{4.13}$$

where $M = v/v_c$ is the Mach number which is the ratio of the fluid velocity to the local speed of sound. A flow will be called supersonic if M >1 and subsonic for M <1. Assuming the initial gas velocity of the gas inlet is subsonic, (4.13) shows the gas flow accelerates with the decrease of the cross section. When the gas flow approaches the throat where $\frac{\partial \sigma_n}{\partial x} = 0$, the LHS of (4.13) gives that a possible solution at this location is $M = 1$. The gas flow becomes supersonic after the throat, from where the velocity of gas flow increases with the growing cross section. The gas jet of such converging and diverging configuration of cross section is called the de Laval nozzle, which we used broadly in our experiments to generate the supersonic flow.

4.2.2 Discontinuities of the Shock Adiabatic

The natural of a gas flow is entirely different according to whether the flow is supersonic or subsonic. One of the most distinctive features of a supersonic flow is the capability to generate *shock waves* and *shock fronts.* In a co-moving coordinate system of a gas in a steady motion, when a perturbation occurs, the influence of the perturbation travels through the gas medium with the speed of sound. In other words, the perturbation is carried along by the gas flow with the flow velocity

v and propagates in $v \pm v_s$ in the laboratory frame. In a subsonic regime, the presence of any obstacle influences the flow in all directions, which causes a smooth adaptation of state variables upstream to downstream. A supersonic flow, however, is 'blind' on the obstacle in the part of the space upstream the gas flow; the resulted perturbation only extends downstream. As a result, a shock wave is generated from the location of the obstacle. A shock wave is characterized by nearly discontinuous transitions of state variables and velocities in gas flow, and the surface where the abrupt transition happens is called **shock front**. In our experiment, we exploit this sharp density jump to trigger the electron injection by the shock front, and therefore in the second part of this section will focus on the properties of the shock front. We begin by considering the discontinuity as mathematically infinitesimally thin, and the state variables must satisfy certain boundary conditions. Since the accumulation of mass, momentum or energy cannot take place within this layer, these quantities must be equal on the both sides of shock front. Consequently, from (4.7), (4.9) and (4.10), the relation of the values on the two side of the shock front is written down

$$\rho_1 v_1 = \rho_2 v_2 \tag{4.14}$$

$$p_1 + \rho_1 {v_1}^2 = p_2 + \rho_2 {v_2}^2 \tag{4.15}$$

$$H_1 + \frac{{v_1}^2}{2} = H_2 + \frac{{v_2}^2}{2} \tag{4.16}$$

where the subscripts denote the flow going from the side 1 to the side 2. We first use (4.14) and (4.15) to solve v_1 and v_2 as a function of p and ρ. After substituting the result into (4.16), we obtain a relationship between the pressure and the density on each side of the shock front

$$H_2 - H_1 = \frac{1}{2}(p_2 - p_1)(\frac{1}{\rho_2} + \frac{1}{\rho_1}) \tag{4.17}$$

This relation is called the Rankine-Hugoniot or the shock adiabatic condition [Zeldovich, 2002]. The Hugoniot curve is defined by $p_2 = h\left(\rho_2, p_1, \rho_1\right)$, which is significantly different from the isentropic adiabatic. We assume the gas is perfect and polytropic which means the specific heat capacity is a constant and independent of the temperature. In this special case, we have

$$H = c_p T = \frac{\kappa}{\kappa - 1}\frac{p}{\rho} \qquad\qquad \epsilon_{in} = c_V T = \frac{1}{\kappa - 1}\frac{p}{\rho}$$

By implementing these relationships, (4.17) is represented in an explicit form, and we get the following equations:

$$\frac{p_2}{p_1} = \frac{(\kappa + 1)\,\rho_2 - (\kappa - 1)\,\rho_1}{(\kappa + 1)\,\rho_1 - (\kappa - 1)\,\rho_2} \tag{4.18}$$

or equivalently

$$\frac{\rho_2}{\rho_1} = \frac{(\kappa+1)\,p_2 + (\kappa-1)\,p_1}{(\kappa-1)\,p_2 + (\kappa+1)\,p_1} \tag{4.19}$$

$$\frac{T_2}{T_1} = \frac{p_2}{p_1}\frac{\rho_1}{\rho_2} = \frac{(\kappa-1)\,(p_2/p_1)^2 + (\kappa+1)\,(p_2/p_1)}{(\kappa+1)\,(p_2/p_1) + (\kappa-1)} \tag{4.20}$$

The entropy is given by $S = c_V \cdot ln\,(p/\rho^\kappa)$ for a polytropic and perfect gas [Huang, 1987], and the difference of the entropy between two sides of the shock front is derived from (4.19)

$$S_2 - S_1 = c_v \cdot ln\left(\frac{{\rho_1}^\kappa}{{\rho_2}^\kappa}\frac{p_2}{p_1}\right) = c_v \cdot ln\left\{\frac{p_2}{p_1}\left[\frac{(\kappa-1)\,(p_2/p_1) + (\kappa+1)}{(\kappa+1)\,(p_2/p_1) + (\kappa-1)}\right]^\kappa\right\} \tag{4.21}$$

Let us take the ratio p_2/p_1 as a measure of the strength of a shock wave. In a case of a very strong shock $\frac{p_2}{p_1} \to \infty$, it is evident from (4.20) that the temperature and the entropy after the shock front increase infinitely. The density, however, approaches a finite limit which depends only on the ratio of the specific heat capacity and is written as

$$\frac{\rho_2}{\rho_1} \to \frac{\kappa+1}{\kappa-1}$$

The equation shows that the maximum density jump of one shock is equal to 4 for a monoatomic gas of $\kappa = 5/3$ and is 6 for a diatomic gas of $\kappa = 7/5$ [2]. To overcome this natural limit, a possible solution is to apply multiple shocks to a system consecutively to achieve higher compression ratio. One of the most important application by exploiting this principle is the shock ignition of a conventional inertially confined fusion, where the driving laser is shaped as a four-steps pulse and each step give one shock to the hohlraum and achieved more than 30 times enhancement of the radiation temperature [Hurricane et al., 2014].

4.2.3 Thickness of Shock Front

Another important parameter is the the thickness of the shock front which directly influences the electron beam quality from the shock-front injection. So far, we only discuss the relation between the initial and the final state. In such a theory, a shock discontinuity is represented as a mathematical boundary of zero thickness, and the derivation does not include any characteristic length that determines the thickness of a shock front [Becker, 1922]. As observable from (4.21) the entropy jump increases with the magnitude of the shock wave during the compression process. The

---

[2] In reality, the pressure and the temperature cannot increase infinitely across the shock discontinuity. The reason is that a gas will be excited to a high order degree of freedom, dissociated or even ionized. Under these circumstances, κ becomes a function of the pressure and the density, and the gas is no longer polytropic [Biberman et al., 1971].

increase of entropy implies that in a irreversible energy dissipation happens in the shock wave. Therefore, to measure the thickness of shock front, we must consider the dissipative mechanism, which is included by taking into account the thermal conductivity and viscosity. It is important to notice that the change of state variables across a shock boundary is independent of the dissipative mechanism and is only determined by the conservation laws [3]. Let us again consider a 1D system of a coordinate co-moving with the shock front, we include the heat conduction and the viscous terms into (4.7), (4.9) and (4.10). The change of state variables across and inside the shock front is described by

$$\frac{d}{dx}\rho v = 0 \tag{4.22}$$

$$\frac{d}{dx}\left(p + \rho v^2 - \mu\frac{dv}{dx}\right) = 0 \tag{4.23}$$

$$\frac{d}{dx}\left[\rho v\left(H + \frac{v^2}{2}\right) - \mu v\frac{dv}{dx} - \Theta\frac{dT}{dx}\right] = 0 \tag{4.24}$$

where μ is the sum of the coefficients of kinematic and bulk viscosity, and Θ is the thermal conductivity. If we assume the system is in equilibrium when it is far before or far behind the shock front, these equations must satisfy boundary conditions such that

$$\left(\frac{d}{dx}\left\{p, v, \rho, T\right\}\right)_{x\to\pm\infty} = 0,$$

and

$$\{p, v, \rho, T\}_{x\to-\infty} = \{p_1, v_1, \rho_1, T_1\} \qquad \{p, v, \rho, T\}_{x\to+\infty} = \{p_2, v_2, \rho_2, T_2\}$$

If the values of state variables at $x \to -\infty$ are chosen as the reference, the modified version of (4.14)-(4.16) will be obtained

$$\rho v = \rho_1 v_1 \tag{4.25}$$

$$p + \rho v^2 - \mu\frac{dv}{dx} = p_1 + \rho_1 {v_1}^2 \tag{4.26}$$

$$\rho v\left(H + \frac{v^2}{2}\right) - \mu v\frac{dv}{dx} - \Theta\frac{dT}{dx} = \rho_1 v_1\left(H_1 + \frac{{v_1}^2}{2}\right) \tag{4.27}$$

---

[3] Analogously, a cup of hot tea will eventually cool to ambient room temperature independent of the mechanism of heat dissipation, while the mechanism only determines how fast the process takes.

It is important that if the flow variables in the shock front had a jump, the gradient terms which contain d/dx in (4.26) and (4.27) would be infinite; therefore, the existence of these terms indicate a continuous change of the flow variables. By using the definition of the entropy $TdS = dH - dp/\rho$ together with (4.22) and (4.23), the equation of energy (4.24) is rewritten in the form of the entropy equation

$$\rho v T \frac{dS}{dx} - \mu \left(\frac{dv}{dx} \right)^2 - \frac{d}{dx} \left(\Theta \frac{dT}{dx} \right) = 0. \tag{4.28}$$

This equation is no analytically solvable. To get an intuitive impression of the dependence of thickness of a shock front, we consider a special situation of a weak shock front, and assume there exists no viscosity but only the heat conduction, then from (4.28) [4]

$$\rho v T \frac{dS}{dx} = \frac{d}{dx} \left(\Theta \frac{dT}{dx} \right) \approx \Theta \frac{d^2 T}{dx^2} \tag{4.29}$$

After dividing both side of (4.29) by T and integrating with respect to x from $x \to -\infty$ to $x \to -\infty$, we obtain

$$\rho_1 v_1 (S_2 - S_1) = \Theta \int_{T_1}^{T_2} \frac{1}{T^2} \frac{dT}{dx} dT \tag{4.30}$$

Here the mass conservation (4.25) is implemented. It is proved that T changes continuously and monotonically [Landau and Lifshits, 1959], so there exists a maximum temperature gradient in the middle of the shock front. We define the effective thickness δx by

$$\frac{T_2 - T_1}{\delta x} = \left| \frac{dT}{dx} \right|_{max},$$

and δx is also called the Prandtl front thickness. In order to find the lower limit of the thickness, the maximum value of the RHS of (4.30) is estimated by setting

$$T \approx T_1 \qquad \text{and} \qquad \frac{dT}{dx} \approx \left| \frac{dT}{dx} \right|_{max}$$

Since we have assumed a weak shock wave, we make Taylor expansion of (4.20) and (4.21) with respect to $\frac{p_2}{p_1} - 1$ [5] together with the properties that

$$\Theta \approx \rho c_p \bar{v} l$$

---

[4] Typically, the heat conductivity Θ is a function of the temperature. Since we consider a weak shock front, the temperature varies only slightly and continuously across the shock front. As a result, Θ is assumed to be a constant at all positions of the flow.

[5] A more general but also complicated approach without assuming the ideal gas condition is to expand the Hugoniot curve (4.17) directly with respect to S, ρ and p. Similarly, the ρ_2/ρ_1 is expanded with respect to $\frac{p_2}{p_1} - 1$. The final result of the estimated thickness is the same as by assuming an ideal gas [Zeldovich, 2002].

where l is the mean free path, and $\bar{v} \approx v_1$ is the mean particle velocity. Finally, we substitute all these approximation into (4.30) and obtain the estimate of the thickness of shock front

$$\delta x \approx l_1 \frac{1}{p_2/p_1 - 1} \approx l_1 \frac{M}{M^2 - 1} \tag{4.31}$$

Interestingly, in another extreme case $\Theta = 0$ but $\mu \neq 0$, exactly the same form of (4.31) is obtained by noting that $\mu \approx \rho \bar{v} l \approx \rho_1 v_1 l_1$. The reason of this coincidence is understood in a way that the energy transfer between the kinetic energy of the gas flow and the heat inside the discontinuity is caused by the viscous mechanism, and therefore Θ and μ has equivalent effect. It needs to be clarified that the only information from (4.31) is that **the shock thickness is on the order of a few mean free path**, which is about few hundreds of nm in the range of our interest. It cannot be interpreted as $\delta x \to 0$ when $M \to \infty$ because the derivation is based on the assumption of a weak perturbation. In addition, μ and Θ changes significantly inside a strong shock where the gradient of the temperature and the velocity is significant. The structure of a strong shock front must be treated with the kinetic theory of gases numerically [Holway, 1964; Yang and Huang, 1995; Holian et al., 1980; Alsmeyer, 1976; Schmidt, 1969].

4.3 The Formation of Clusters

In a gas of low temperature and high density, the van der Waals forces cause molecules to attract each other and form new particles composing of multiple atoms. Such process is called clustering. Since the cluster ion beams have broad applications from the surface treatment in modern industry to the nuclear fusion [Hagena, 1992; Ditmire et al., 1999], the generation process and the property of clusters has been studied extensively. Clusters are particles of sizes between atoms to macromolecules with geometries from icosahedral to face-centered cubic [Lee and Stein, 1987]. A single cluster contains from 2 up to 10^5 atoms [Smith et al., 1998]. The typical atomic sources of clusters are sub-sonic or supersonic jets, where the clustering occurs after the condensation around the throat of the jet. This condensation is modelled by the adiabatic cooling which shows the mean size of cluster remains almost constant if the increase of the backing pressure p_0 is compensated by the simultaneous increasing of the temperature T_0 in the gas reservoir according to the isentropic condition $p_0 {T_0}^{\frac{\kappa}{1-\kappa}} = const$ [Hagena and Obert, 1972]. The same model also predicts the condition to generate the same average size of clusters from the different geometry of jets where smaller throat diameters d_0 are compensated by larger p_0 such that $p_0 {d_0}^{\chi} = const$ where χ is a positive constant which depends on the type of gas and need to be determined experimentally [Hagena,

Table 4.1: Hagena parameters of selected gases.

Ar	He	Ne	Xe	H_2	N_2	D_2	CO_2
1650	3.85	185	5500	184	528	181	3660

1974]. For example, in the case of using argon as plenum gas, the measurement showed $\chi = 0.6$. Another model based on the kinetic models considers the onset of clustering by the generation of dimers from a three-body collision which happens at a sudden-freeze surface locating between a thermodynamic equilibrium source and a relaxation zone [Milne, 1967; Knuth, 1977]. This model was verified by measuring the third-order growth rate of argon clusters [Milne et al., 1970]. In this section, we are interested in the estimation of a potential influence of large size clusters in the gas on the enhancement of Rayleigh scattering signals which is used to determine the transition length of the shock front. The conditions of the condensation process from a sonic or supersonic jet is catalogued by an empirical scaling parameter Γ^* which is defined by

$$\Gamma^* = k^* \frac{\left(d_0 / \tan \frac{\vartheta}{2}\right)^{0.85}}{T_0^{2.29}} p_0 \tag{4.32}$$

where d_0 (μm) is the throat diameter, ϑ is the opening angle of the exit of the jet, p_0 and T_0 are in the reservoir in the unit of mbar and K respectively, and k^* is a gas-dependent parameter which is also called *Hagena parameter*. The values of k^* of selected gases are shown in Tab. 4.1 [Wörmer et al., 1989]. By comparing to various measurements, three classes of the clustering are clarified according to the values of Γ^* [Becker et al., 1956; Takagi et al., 1975; Yang and Lu, 1985; Hagena, 1987]:

- $\Gamma^* < 200$ No evidence of any observable clustering
- $200 < \Gamma^* < 1000$ Transition from no clusters to the onset of condensation
- $1000 < \Gamma^*$ Massive clustering with the expected mean size of clusters in excess of 100 atoms/cluster

The values of Γ^* as functions of the backing pressure under typical experimental conditions of a supersonic nozzle with an exit diameter of 300 μm are plotted in Fig. 4.4. It is noticed that **no clustering is expected when helium was used as the plenum gas during our experiments**. On the contrary, **a significant amounts of clusters are produced in the case of using argon as a medium during the measurements of the gas density calibration**. Both of these situations have been confirmed by our Rayleigh scattering measurements. Another

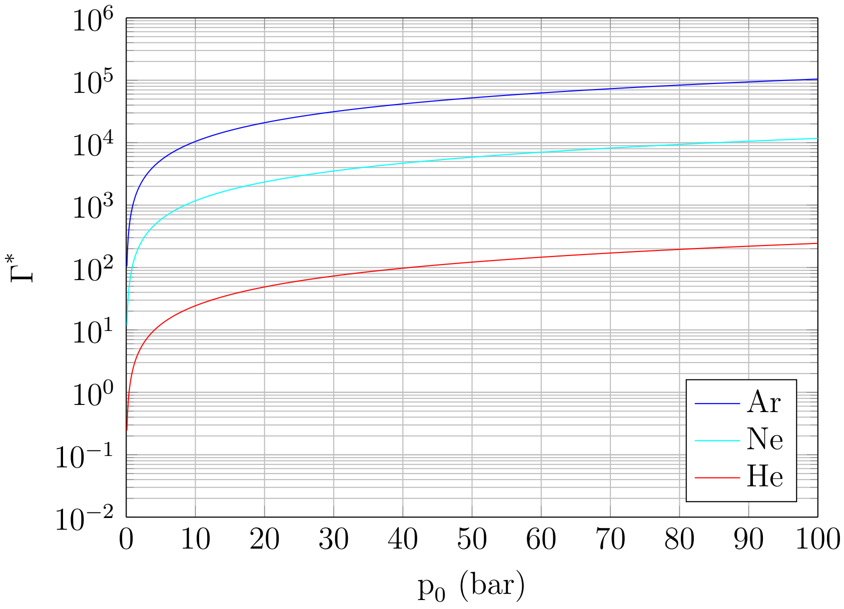

Figure 4.4: Scaling factor Γ^* of argon, neon and helium as functions of the backing pressure. The initial parameters are $d_0 = 100$ μm, $d_{exit} = 300$ μm, $T_0 = 298$ K and $\tan\frac{\vartheta}{2} = 1/8$.

important parameter of clustering is the mean size of cluster $\bar{n}$ which is estimated by

$$\bar{n} = \alpha^* \left(\frac{\Gamma^*}{1000}\right)^{\beta^*} \tag{4.33}$$

where α^* and β^* are two empirical parameters which depend on Γ^*. In the case of argon, from the measurements of the mass spectrometry and using the diffractive helium atoms scattering method showed that $(\alpha^*, \beta^*) = (38.4, 1.64)$ when $\Gamma^* < 1800$, and $(\alpha^*, \beta^*) = (33, 2.35)$ for $1800 < \Gamma^*$ [Hagena, 1974; Buck et al., 1985; Hagena, 1992; Buck and Krohne, 1996; Bush et al., 1998; Bell et al., 1993], and other measurements based on the comparison between Rayleigh scattering and interferometry gave $\alpha^* = 100$ and $\beta^* = 1.8$ [Dorchies et al., 2003]. These slightly different results are explained by the fact that the shock wave generated from the throat of a low quality jet strongly affects the clustering process, hence the different geometry and surface quality of the jets leads to the discrepancies between different measurements. Nevertheless, from the estimation based on these values, **the 300 μm jet gives $\bar{n}$ on the order of 10^4 atoms/cluster at 20 bar of the backing pressure of argon**. Since the cross section of the Rayleigh scattering is proportional to the square of the particle size, the consequence of this large size of cluster is that **the signal of Rayleigh scattering** which is observed during the density profile measurement **is dominated by the scattering from cluster instead of the large amounts of single atoms**.

4.4 Shock Front Generation

As mentioned in section 4.2, an obstacle in a supersonic flow generates a shock wave which has a thin transition boundary of a thickness on the order of the mean free path. This property was utilized to make the shock-front injection (see section 1.2.2). The experimental setup is shown in Fig. 4.5(a), where the sharp edge of a razor blade was used to trigger a shock wave on the top of the supersonic jet. The consequence of this shock wave is a sharp density jump between the subsonic and the supersonic zone on the axis of the laser propagation as shown in Fig. 4.5(b). Alternatively, a properly cut silicon wafer with 50-200 nm edge radius is also an ideal candidate to trigger shock waves [Yan et al., 2009]. The sharp edges in both cases are crucial to prevent the creation of multiple shock waves which disturb the gas profile and introduce the shot-to-shot instability. The sharpness of the razor blade degrades after shooting and needs to be exchanged from time to time, typically every month in our case. The blade was mounted on a piezo-drive linear stage (PI Line M-663) which offered 18 mm travel with 0.6 μm resolution. The movement of the blade was used to control the acceleration length of LWFA, and the blade is possible to be removed completely. The blade and injection position, which moved at different amount, were monitored by a high resolution CCD camera (Point Grey GRAS-50S5M-C) together with a long working distance microscopic objective which looked at the shadowgraph of the laser-generated plasma channel. The setup was very stable and reliable.

4.5 Absolute Density Calibration by Interferometry

As emphasized before the absolute electron density is critical for an LWFA experiment. Due to defects during manufacturing, all jets perform differently even if having the same geometry, and therefore it requires the calibration of the absolute density individually before experiments. The method which we used was based on the interferometry.

In a bulk material, the macroscopic electric susceptibility depends on the total molecular polarizability which is caused by the response of all molecular dipoles to the external electric field. Therefore, the particle density is retrieved by measuring its refractive index. The connection between gas density and refractive index is

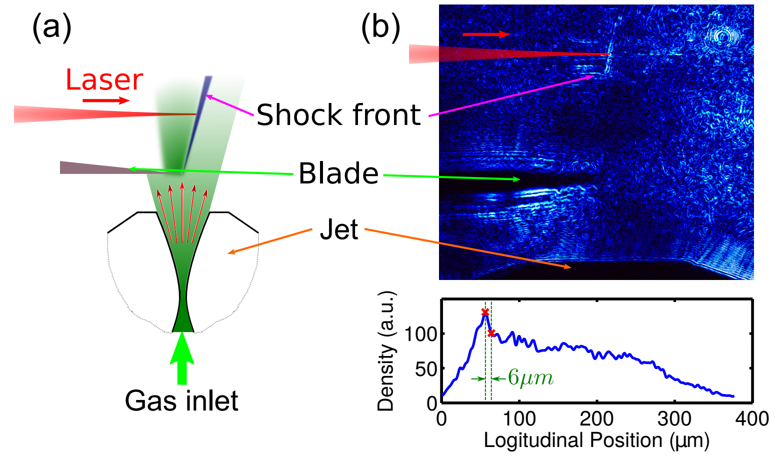

Figure 4.5: Experimental setup of the shock-front injection: (a) the illustration of the configuration of the setup; (b) the upper image shows the side view of the shock front during shooting, and the lower plot shows the result from the offline Rayleigh scattering measurement of the density profile of the shock front. The typical transition length is around 5 μm.

described by the Clausius-Mosotti equation [Jackson, 1999]:

$$\gamma_{mol} = \frac{3}{N}\left(\frac{n^2-1}{n^2+2}\right) \tag{4.34}$$

where n is the refractive index, N is the particle density and γ_{mol} is the molecular polarizability. The exact value of γ_{mol} is known from experiment. The refractive index is determined by the change of phase of light due to additional material in the beam path. The gas targets were supersonic de Laval nozzles which were developed by K. Schmid [Schmid, 2009]. All these jets had a ratio of 3 between the exit and the throat diameter and a full opening angle of the expansion at 14°. This all together provided a Mach number of 4.5 at the exit of jet which was obtained from simulations. Previous results showed that the density profile at the top of a jet at a distance approximately equal to the size of the exit diameter was trapezoidal-like and gradually became Gaussian-like when the distance was further away. We used the Mach-Zehnder interferometer to measure the phase shift between a reference beam and the beam which went through a gas jet, as shown in Fig. 4.6. To prevent the flow to be disturbed by the ambient gas, the gas jet was located in a vacuum chamber of a pressure below 10^{-2} mbar. The jet was mounted on a solenoid valve (Parker Hannifin, 9S1-A1-P4-9B04 valve) and driven in pulse mode to minimize the amount of the gas which needed to be pumped out from the chamber. Since the gas velocity of helium was on the order of 1 km/s, a pulse laser of 20 ps pulse duration (High-Q Laser, IC-3000PS) was used to prevent the washing out of the signal [6]. The rising time of the valve was about 0.5 ms, so the opening time needed to be set longer than 1 ms before the arrival of the laser pulse. Both argon and helium were used as gas medium during the measurement. The phase shift was easier to be observed with argon because of a much higher refractive index comparing to helium, as shown in Tab. 4.2 [A. Bideau-Mehu, Y. Guern, R. Abjean, 1981; Mansfield and Peck, 1969]. The results with argon, however, might be different from the results by using helium [Hofmann, 2015]. However, since the measured 3D phase map is projected into a 2D plane from one direction (as shown in Fig. 4.7), a complete 3D distribution of the gas density would require a complete 2π scan in fine steps, which is time-consuming and needs a complicated post hoc analysis [Landgraf et al., 2011]. The phase retrieval is greatly simplified by assuming that the density profile of the jet was axially symmetric, which was true in the case of perfect cylindrical jets, and then

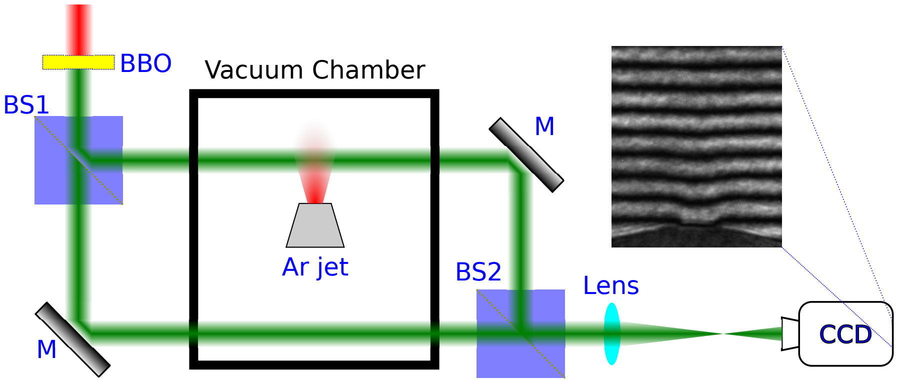

Figure 4.6: Experimental setup of the Mach-Zehnder interferometer for the gas density measurement. The 2 kHz laser pulses from a Nd:YLF amplifier (1064 nm, 20 ps and 0.6 mJ) were first frequency doubled by a BBO crystal to 532 nm (64 μJ) to enhance the phase shift (see Table 4.2). They were split into two by a 50/50 beamsplitter (BS1) and sent into vacuum chamber with only one arm penetrating through the gas target. Finally, both arms were recombined by the second beamsplitter (BS2) and imaged with an achromatic lens to a CCD camera (Point Grey, GRAS-14S3M-C, 1382×1032 pixels). The inset shows a typical interference pattern from a single-shot measurement, where the dark shadow shown in the bottom is the very top of the jet. A fast photodiode (not shown here) behind the mirror in the left corner was used to synchronize the opening time of the valve and the arrival time of the pulse.

---

[6] It was noticed later that since the gas flow was highly stable, a green diode laser together with a few ms shutter time of the camera was sufficient to measure the density of a continuous flow.

Table 4.2: Refractive index of argon and helium at 1.013 bar.

Wavelength (nm)	He $(n-1)$	Ar $(n-1)$
1064	3.47×10^{-5}	2.79×10^{-4}
532	3.50×10^{-5}	2.83×10^{-4}

the accumulated phase shifts are calculated by:

$$\Delta\Phi\left(y\right) = \frac{4\pi}{\lambda}\int_{y}^{\infty}\frac{n\left(r\right)-1}{\sqrt{r^{2}-y^{2}}}rdr \tag{4.35}$$

where the definitions of r and y are shown in 4.7. In a practical way, the interval of the integral only needs to be large compared to the extent of the space where the phase shift of the gas is small enough. The refractive index was calculated from the phase shift by the Abel transform [Tomassini and Giulietti, 2001]:

$$\frac{2\pi}{\lambda}\left(n\left(r\right)-1\right) = -\frac{1}{\lambda}\int_{r}^{\infty}\frac{d\left(\Delta\Phi\left(y\right)\right)}{dy}\frac{dy}{\sqrt{y^{2}-r^{2}}}, \tag{4.36}$$

and then the corresponding gas density N was calculated by (4.34). In the measurement, a distortion of interference pattern was visible when the gas valve was triggered, which is shown in the inset of Fig. 4.6. Figure 4.8(a) shows one example of an unwrapped phase map of a jet with 300 μm exit diameter and 62 bar backing pressure. To retrieve the density map, the direct Abel inversion is done by using an open source software IDEA (Technische Universität Graz). The calculation was, however, computational resource consuming and sensitive to the noise of the original data because of the derivative dependence in (4.36). Another algorithm which was used to extract the density profile more efficiently was inspired from the results of the Abel transformation that the lineouts of the density profile had

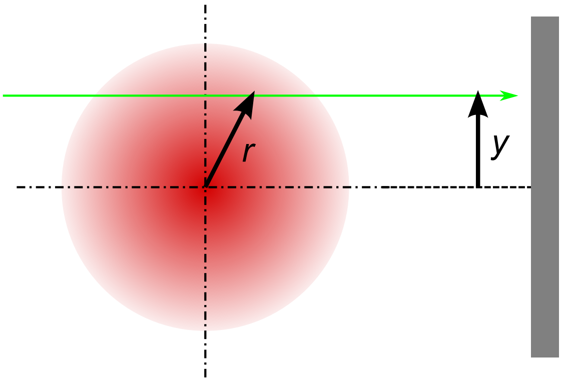

Figure 4.7: Phase projection of an axially symmetric object. The laser pulse (the green arrow) goes through the phase object (the gradient pattern) and accumulates the phase shift along its path and finally projects onto a phase detector (the grey block on the right hand side).

a trapezoidal shape up to a height approximately equals to the diameter of the jet exit, and which gradually evolved to a Gaussian-like profile with increasing height from the top of the jet. Therefore, the density is easily estimated by fitting the lineouts of the retrieved phase map directly by the Abel transform of the trapezoidal or the Gaussian function [Buck, 2011]. Figure 4.8(b) shows one example of a calculated density map by assuming flap top and Gaussian density profile. The results from this fast estimation are approximately the same as the results from a complete Abel transformation. The measurements indicates that the supersonic jet is highly stable as what is visible from Fig. 4.9(a). The shot-to-shot fluctuation of the absolute density was below 0.8%. The dependence of densities on the applied backing pressures is shown in Fig. 4.9(b), from which we conclude that the density is linearly proportional to the backing pressure.

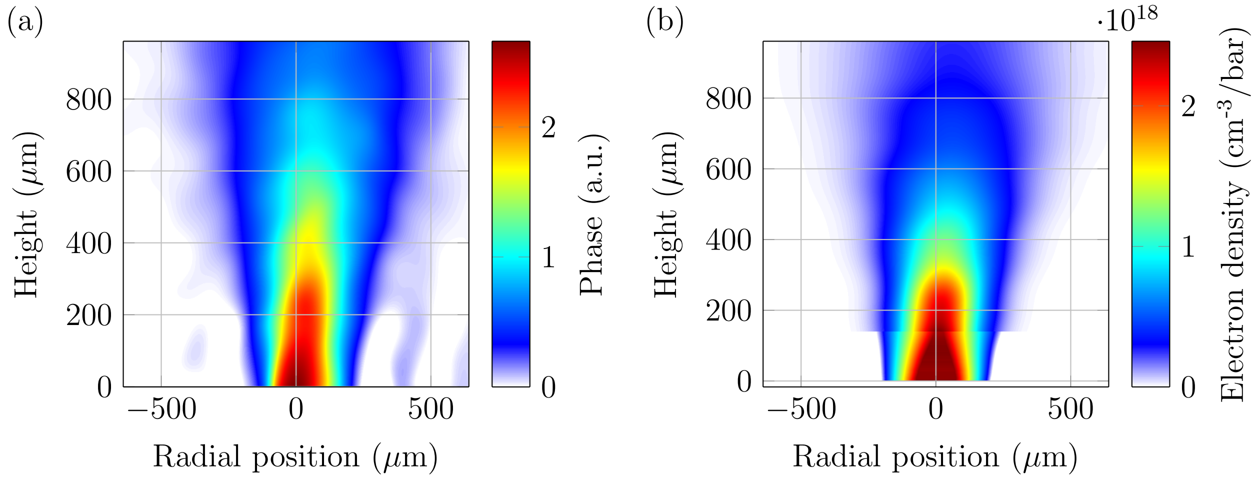

Figure 4.8: Example of the measurement result by interferometry. The nozzle of 300 μm used argon at 62 bar backing pressure. The density map was divided to the backing pressure for fully ionized helium. (a) Unwrapped phase map. (b) Retrieved density map. The jump at height around 180 μm was due to the transition of from trapezoidal to Gaussian profile.

4.6 Shock-front Profile Measurement by Rayleigh Scattering

Since the thickness of the shock front is critical for the electron injection in the LWFA, we used the 90° Rayleigh scattering to measure the longitudinal density profile of shock waves directly. The signal of the Rayleigh scattering from a non-clustering monoatomic gas is proportional to the local density of the gas times

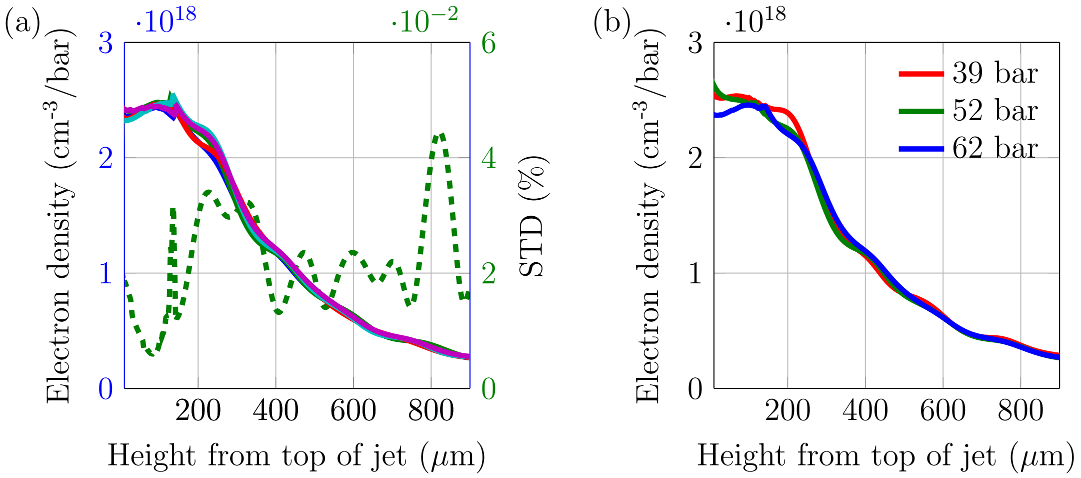

Figure 4.9: Height-dependent gas density along the symmetry axis of the jet. (a) Single-shot measurements at 62 bar backing pressure. The dashed line shows the standard deviation (STD) of the measured density normalized to the mean density. (b) Dependence of measured electron densities on backing pressures.

the scattering cross section of the atom. From section 4.2.3, we have learned that the thickness of the shock front is on the order of the mean free path. In reality, several measurements have shown that the thickness only agree with theory for weak shocks and begins to diverge from $M \geq 1.5$ and becomes significantly different from the theory as $M \geq 2$ [Cowan and Hornig, 1950; Greene et al., 1951; Alsmeyer, 1976; Hansen and Hornig, 1960]. A possible explanation, beside the assumption of a weak shock, as described in section 4.2.3, is that a regular hydrodynamic approach ignores the multiple collisions when a molecular gas passed through a shock front [Thomas, 1944]. Moreover, conventional computational fluid dynamics packages like ANSYS Fluent® or OpenFOAM® based on the Navier-Stokes equations cannot calculate the structure of a shock front correctly due to the instability of the solutions, and additional models must be applied [Holway, 1964; Holian et al., 1980; Yang and Huang, 1995; Uribe, 2011].

4.6.1 Experimental Setup

The experimental setup is shown in Fig. 4.10. The setup was located in a vacuum chamber which was pumped down to 10^{-2} mbar. The 5 ns laser pulses of 532 nm, ≈70 mJ, and 10 Hz (Litron Nanos SG150-10) were focused by a biconvex lens with an effective focal length of 100 mm to the gas targets (two argon jets, the second jet was used in the collective deceleration experiment which is discussed in chapter 5). The measured confocal length on the target was ≈3 cm which was long enough to cover the two gas jets. The scattered photons were collected by a long working distance objective (Mitutoyo Plan Apo NIR infinity corrected objective, 10×) and imaged to a CCD camera (same as what was used in Fig. 4.6). The optical resolution was 1.6 μm which was measured by using 1951 USAF resolution target. In addition, the imagining system had a depth of focus below 10 μm, which defined transverse resolution. The laser pulse after interaction was collimated by a silver coated 90°off-axis parabolic mirror to prevent reflection which disturbed measuement and finally sent to a beam dump outside of the chamber. The setup of the shock-front target was the same as what was described in section 4.4. The distance between razor blade and the top of nozzle was 270.6 μm, and the *Height* in all figures are measured from the tip of the razor blade if not mentioned separately.

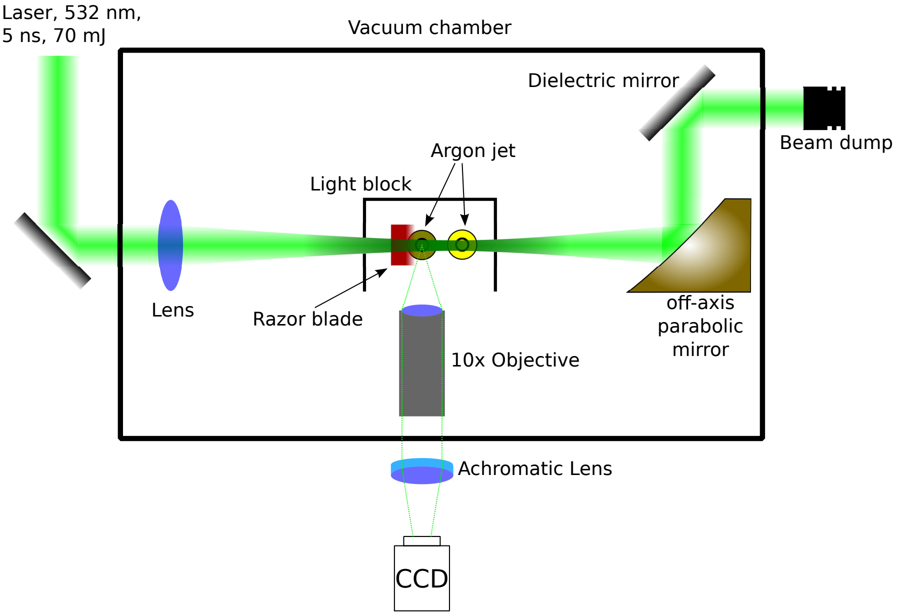

Figure 4.10: Experimental setup of Rayleigh scattering.

4.6.2 Results

The drawback of the high resolution Rayleigh scattering setup was that it collected only very little signals from the target. In order to prevent the requirement of using a high sensitivity camera, we exploited the enhanced scattering signal from clusters by simply using argon as the backing gas during the measurement, as discussed in section 4.3. For spherical clusters, the cross section of the Rayleigh scattering from a single cluster is proportional to $\bar{n}^2$. From the continuity condition, the total number of the clusters n_{TC} from the exit of the jet has a relation to backing pressure as $n_{TC} \propto \frac{\rho_0}{\bar{n}} \propto \frac{p_0}{\bar{n}}$ where ρ_0 is the particle density in the gas reservoir. Therefore, total signal from the Rayleigh scattering S_{RS} is $\propto n_{TC}\bar{n}^2 \propto p_0\bar{n} \propto \rho_0\bar{n}$. The last condition is valid not just in reservoir but also for general local density. By using (4.32) and (4.33) to substitute $\bar{n}$, one obtains relation between scattering signal and the states variable of reservoir

$$S_{RS} \propto {p_0}^{2.6-3.4} \propto {\rho_0}^{2.6-3.4} \tag{4.37}$$

[Murakami et al., 2010; Smith et al., 1998].

Both cases of the scattering from single atoms and clusters were observed. The linear dependence of S_{RS} was measured by filling the chamber with a constant pressure of argon while the jets were off, as shown in Fig. 4.11(a). After pumping down the chamber and turning the gas jet on, an obvious increase of the scattering signal was observed due to the formation of clusters by switching the backing gas from helium to argon. Another cross proof of the clustering was seen from the signals as a function of the backing pressure as shown in Fig. 4.11(b), and the coefficient of the power fit (${p_0}^{3.32}$) was similar to preceding results described by equation (4.37). The scattering signals from the shock front generated from different blade positions are shown in Fig. 4.12. The density profiles along the laser propagation axis correspond to lineouts of images, which are plotted in Fig. 4.13.

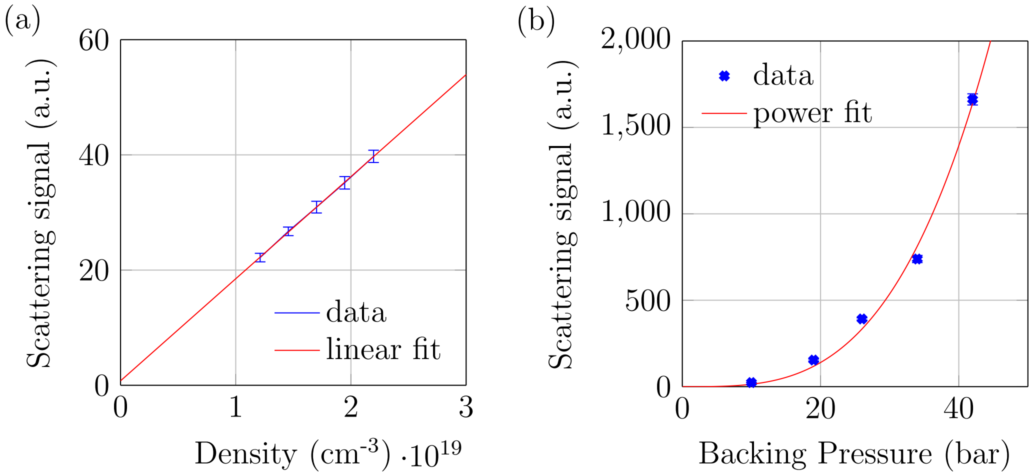

Figure 4.11: Calibration of scattered photon counts to densities. (a) Linear calibration of constant backing pressures in the gas-filled vacuum chamber. (b) Nonlinear dependence of signal counts from the jet of different backing pressures. The power fit gives the scattering signal $\propto {p_0}^{3.32}$. The two measurements used different filter and only relative value was compared.

The change in shock was more than the shift in blade position. The density profiles from different blade positions showed an identical pattern behind the shock fronts, which was also an indication that the gas flows were supersonic.

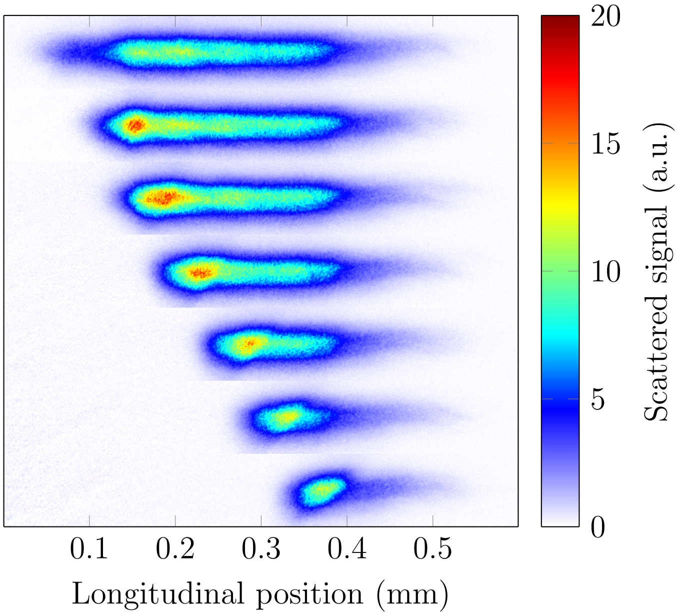

Figure 4.12: Images of Rayleigh scattering of different blade positions. All shots were taken at the same height. The staked images from top to bottom show shock positions at various blade positions.

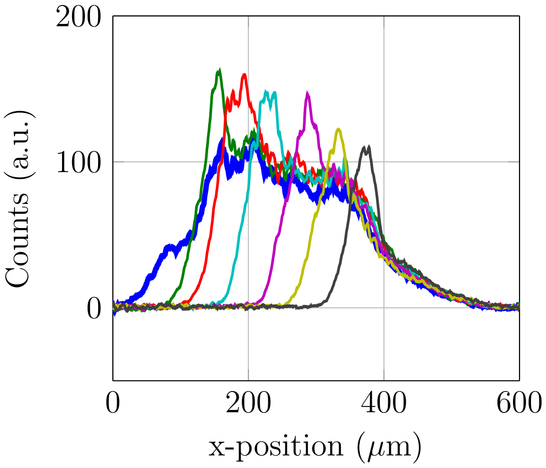

Figure 4.13: Lineouts along the laser propagation axis from the blade position scan (Fig. 4.12).

4.6.3 Data Analysis Procedure

The analysis of getting the shock width from the lineouts of the scattering signal was by imposing certain assumptions that a shock front must satisfy, such as

1. The starting point of the shock front was around the location of the peak density.
2. The shock existed in the section where the density dropped the fastest and the longest continuously.
3. The ending point was where the density stopped changing, i.e. a pedestal, or when the gradient turned positive.
4. The distance between the starting and the ending points was defined as the shock width.

A carefully chosen two dimensional Fast Fourier Transform (FFT) filter was applied to the noisy raw data before the analysis. Figure 4.14 depicts examples of the determined shock widths from different degrees of the filtering. It is clear that the retrieved width could be apparently smaller than in reality when the FFT window was too large because of the high noise background. By contrast, the feature of a sharp jump of the density profile was washed out when the FFT window was too narrow. However, the dependence of the width on the size of FFT windows was not monotonic. Figure 4.15 shows the calculated width as a function of the window size. The plot shows several 'stable' regions where the shock widths were minimized and insensitive to the variation of the window size. The optimized region was defined by the largest stable window and the minimized shock width. From our observations, this optimized region stayed almost the same in all measurements and depended only on the magnification and the resolution of the imagining system. Since the shock width was close to the limit of the optical resolution (1.6 μm), the evaluation had to be done by analyzing single shot measurements instead of average images to prevent any subtle shot-to-shot fluctuation of the gas flow which smeared out the sharpness of the shock front. A typical scenario was that the multiple peaks nearby the shock front made the determination of the exact position of shock front ambiguous. Examples of 'good' and 'bad' density profiles were demonstrated in Fig. 4.16(a) and Fig. 4.16(b) respectively. To solve this issue, we assumed: firstly, the positions of both starting points and ending points were linear functions of the height from the razor blade; secondly, the measured values had a symmetric probability distribution around the mean value that corresponds to the exact position. By doing linear regressions to the starting points and ending points separately, the shock width is calculated as a function of the height by subtracting the two lines as shown in Fig. 4.17,

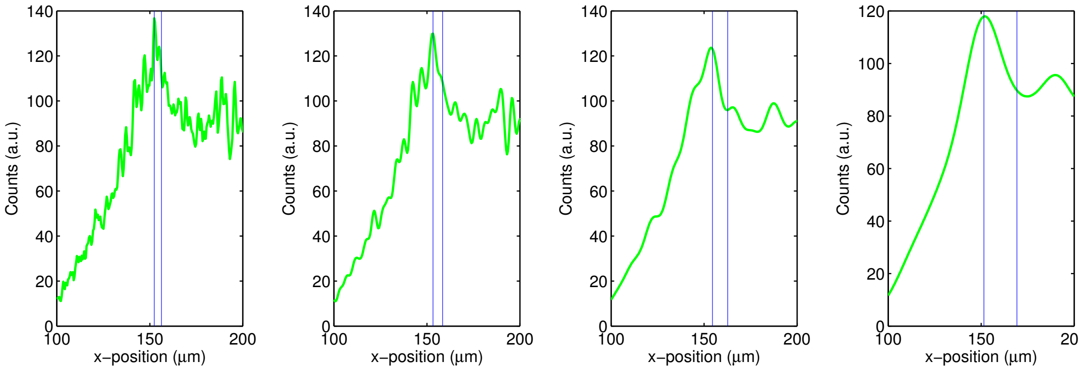

Figure 4.14: Influence of the size of the FFT windows on the retrieved shock width. The vertical blue lines in each plot indicate the determined starting and ending points according to the criteria specified in page 80. The sizes of sampling window are (from left to right): 1.67 μm^{-1}, 0.53 μm^{-1}, 0.20 μm^{-1}, and 0.10 μm^{-1}. The retrieved lengths of shock width are (from left to right): 4.33 μm, 5.2 μm, 8.66 μm and 17.75 μm.

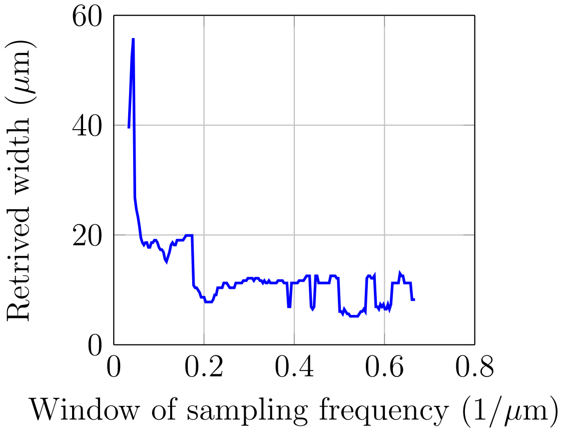

Figure 4.15: Influence of the chosen FFT windows on the retrieved shock widths. The plot shows the shock widths have stable minima around 0.2, 0.55 and 0.6 μm^{-1}. The optimized window of the filtering was chosen to be 0.53 μm^{-1}.

and the shock positions correspond to the mean of the lines. Interestingly, we observed that in the most of the situation the width increased with height which is contradictory to what is predicted by the theory and simulations. Both theory and simulations show that the Mach number M grows with the distance from the exit of the gas jet, which are supposed to decrease the thickness of the shock front as described by (4.31).

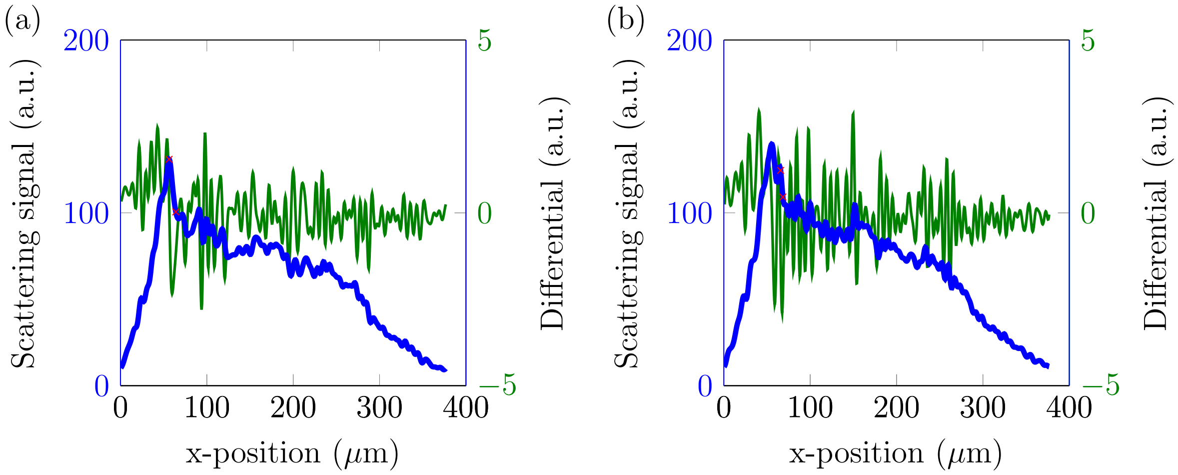

Figure 4.16: Examples of the ambiguity of the determination of the shock width. The blue lines are lineouts of the scattering signal which corresponds to the local density, and the green lines are the differentiates of the blue lines. The red crosses mark the evaluated starting and ending position of the shock fronts. (a) Good lineout for the determination of the density jump. (b) Lineout with an ambiguous shock position.

4.6.4 Discussion

In the following, we inspect the properties of the shock front qualitatively and quantitatively under certain LWFA experimental conditions. We first looks at the dependence of the thickness of shock front on the distance from the blade, which is shown in Fig. 4.18(a). The angle α between the shock and gas flow were increased when the blade was moved from left to right, and the thickness grew faster at larger α. Although we could not measure the width very close to the blade due to the bright scattered light from the blade, the shock width is expected to be much smaller than 3 μm when the height is below 300 μm. Similarly, the density jump between peak and foot density of shock front is shown in Fig. 4.18(b). The ratio of the jump is not always monotonically increasing with height, and the ratio for the height closer to the blade is around 1.3-1.6. A closer inspection of the influence of

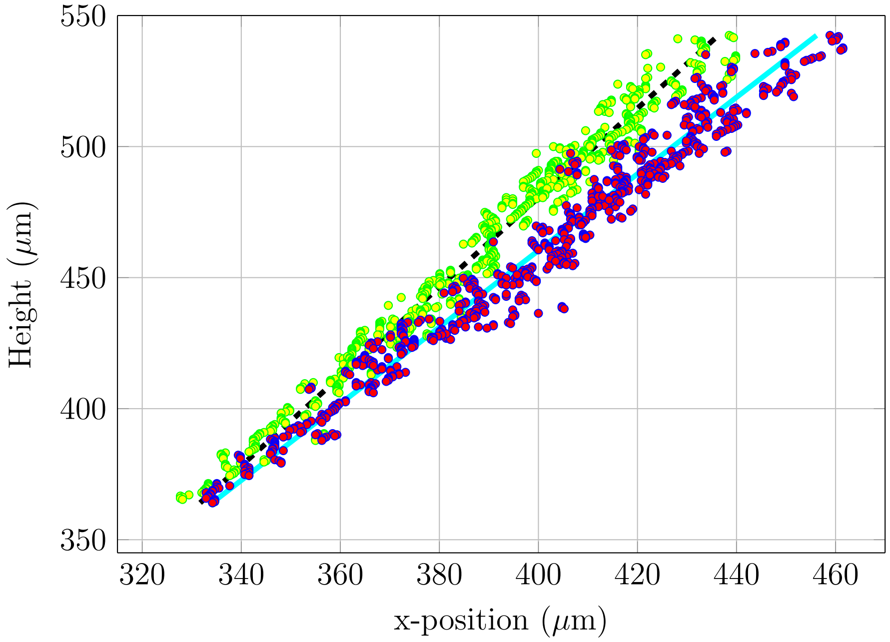

Figure 4.17: Linear regressions of the retrieved positions of shock fronts. The x-position is the longitudinal position, and the height was measured from the razor blade. The starting points are denoted by blue circles while the ending points are by green circles. The two lines are the linear fitting of all the starting and ending positions respectively.

the longitudinal positions of the blade on the thickness is shown in Fig. 4.19. The width stayed almost constant and then quickly increased after the blade blocked more than half of the gas flow. The last parameter is the backing pressure of the jet which is tuned frequently during LWFA experiments. The results are shown in Fig. 4.20. Unsurprisingly, the pressure did not play a major role on the properties

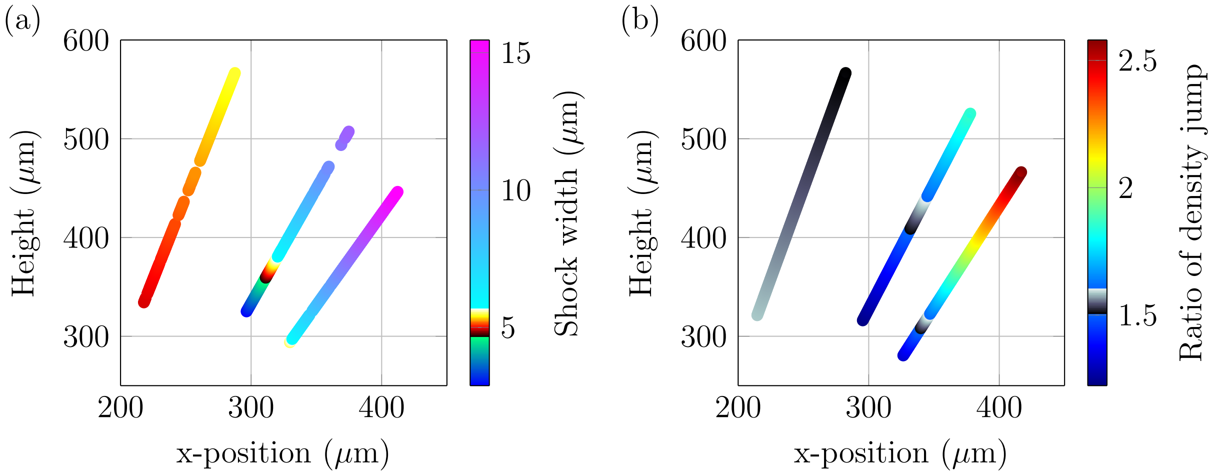

Figure 4.18: Dependence of thickness and ratio of density jump of the shock front on the position on the height from three different positions of the blade. The center of the jet was at 300 μm. (a) Thickness of shock fronts. The scattered circles are the fitting position of the shock front and are color-coded according to the thickness of the shock width. (b) Ratio of density jump between peak and foot density of shock front.

Figure 4.19: Dependence of the thickness of the shock front on the different blade positions. The data was taken at 400 μm above the razor blade. The definition of the coordinate of the unperturbed scattering signal is shown in the topmost image of Fig. 4.12, and its lineout is shown as the blue line in Fig. 4.13.

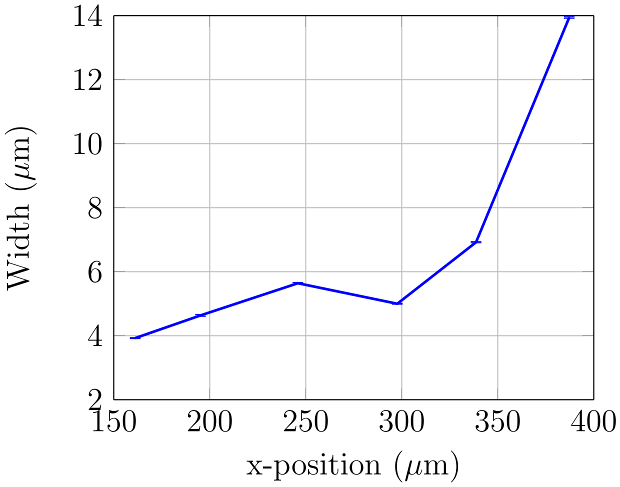

of the gas flow, and the positions and the thickness of the shock front remained the same. This is expected from two aspects of the first principles of the supersonic flow

1. The velocity of a gas flow from an ideal gas jet only depends on the variation of the cross section, as what is described in equation (4.13).
2. The properties of the state variables across the boundary of a shock layer as well as the thickness are functions of the ratios of any state variable instead of the absolute values, which are seen in equations (4.18)-(4.21) and (4.31).

The only influence of the different backing pressure was the blade being pushed by the gas flow mechanically, which caused the blade bending in a slightly different way and was indicated by a small shift of the shock position between the low pressure and the high pressure as shown in Fig. 4.20(a). This issue is critical when the exit of the nozzle has several mm diameter. The linear stage and the blade mount have to be fixed carefully, and other more stiff material like silicon wafer instead of steel razor blade should be considered as an alternative.

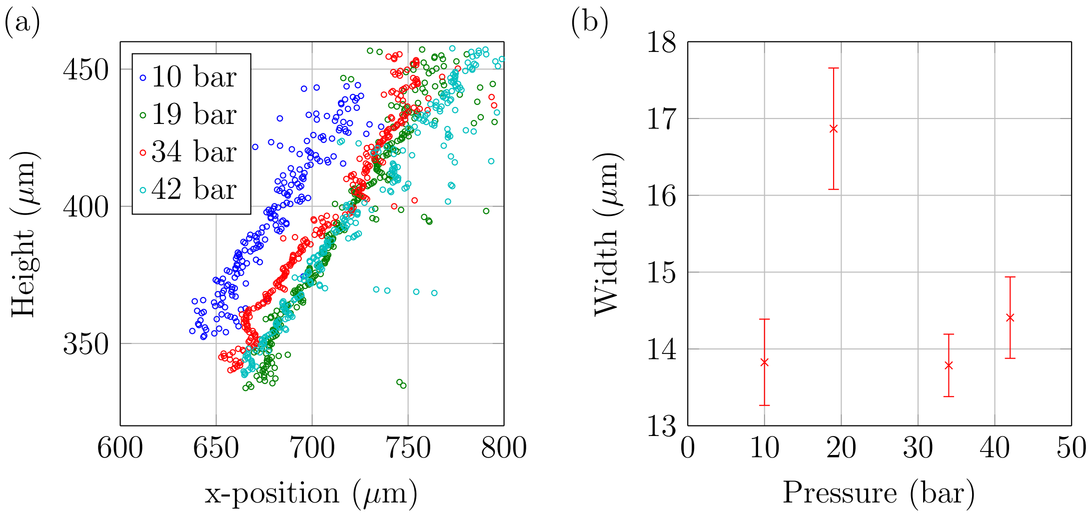

Figure 4.20: Influence of the backing pressure on the properties of the shock front. (a) Positions of the shock front at different backing pressures. (b) Thickness of the shock front at different backing pressures. The data was taken at 400 μm above the razor blade.

4.6.5 Summary

The thickness of shock front mainly depends on the distance from the blade and the position of the blade relative to the flow. The width is thinner than 3 μm when it is very close to the blade. The properties of shock front are independent of backing pressure. Therefore, in the high density LWFA experiment, the laser must be as close to the blade as possible to realize the shock-front injection, but not too close to burn the blade. In the low density experiments, where the larger jets are usually required, the position of the blade should be monitored to prevent the mechanical movement caused by the gas flow.

Chapter 5

LWFA Driven by ATLAS System and Observation of Collective Deceleration

In this chapter, we study properties of electron bunches generated from LWFA driven by ATLAS laser system. We first give a short review of the results from the gas cell experiment which was also used for measuring beam emittance. The major part of this chapter focuses on the study of collective deceleration of the ultra-short electron bunches in plasmas. This is also a proof-of-principle experiment to prove the idea purposed by Wu et al. [Wu et al., 2010] to apply the plasma as an efficient and economic beam dump.

5.1 LWFA Experiment in Gas Cell

In this section, we used a length tunable, hydrogen-filled gas cell to study the properties of electrons from different densities and lengths of the plasma. The details of the gas cell are discussed in section 4.1. The experiment was conducted in Max-Plank-Institut für Quantenoptik (MPQ) in Munich. Laser pulses of 1.5 J and 28 fs FWHM duration from the ATLAS laser system were focused by a $f/22$ parabola to a spot size of 22 μm in FWHM diameter. The LWFA was operated in self-injection regime. The raw images of the electron spectrometer from the acceleration length scan are shown in Fig. 5.1. The typical spectrum was quasi-monoenergetic which included an energetic peak and a long tail of low energy component. In this scan, the peak energy gradually increased from ≈210 MeV to ≈350 MeV by increasing the length of the gas cell from 2 to 5 mm with a electron density of 6.5×10^{18} cm^{-3}. As the length of the cell increased further, the peak energy dropped, also the peak spectral intensity faded out. The spectra from the lengths longer than 7 mm also showed higher shot-to-shot energy fluctuations. These results suggested that the highest electron energy was dephasing-limited, and the electron started to be decelerated again after 5 mm. However, the peak energy was not reduced significantly even for the longest length, which is inferred that the deceleration was limited by the laser energy depletion after dephasing. A more dedicated analysis based on the parabolic fitting of the relation between the peak energy and the length of the gas cell showed that the dephasing length was 4.93 mm, and the maximum of the acceleration gradient was 162 GV/m [Popp, 2011]. The calculation from the linear theory gives a dephasing length of 3.5 mm, depletion length of 9.5 mm and E_0 =245 GV/m [Shadwick et al., 2009].

The electron spectra at three different plasma densities are shown in Fig. 5.2. The peak energies rise up when the densities are increased from 2×10^{18} to 4×10^{18} cm^{-3} cm^{-3} and dropped again with higher density. The systematic discussion of various parameters scan is found from the PhD thesis written by A. Popp [Popp, 2011].

Additionally, the emittance of the LWFA electron beam was measured by using a pair of magnetic quadrupole lenses to image the electron beam from the exit of gas cell to the cerium-doped YAG crystal behind the electron spectrometer. The longitudinal position of the first lens was fixed behind the cell while the position of the second lens was scanned to find the minimum electron beam size of different energies. The magnification of the system was around 25 to 30 depending on the electron energies. The scintillation signal from the crystal was observed by an aspherically achromatic imaging system with 3.5 μm resolution. The transverse size of the beam envelope on the crystal showed quadratic dependence on the distance between two lenses, and the source size and the initial divergence was calculated from the fitting coefficient. The measurement showed an ultralow emittance of 0.66 mm mrad at 245 MeV. More details of this experiment is found in [Weingartner et al., 2011, 2012].

5.2 Study of Collective Deceleration

Beside the discussion of the generation process of electron beams, as discussed in section 1.1.1 and chapter 2, the ultra-short and dense electron bunches from LWFA are expected to drive a strong wakefield in a plasma. In this section, we use double gas jets and double gas cells to study the LWFA-electron-driven wakefield. The electrons were accelerated in the first jet (cell) and interacted with the underdense plasma in the second jet (cell). The experimental results clearly indicate the collective effect by observing an ultra-high gradient deceleration. This collective deceleration have been demonstrated previously by using much higher charge but longer electron bunches from conventional linear accelerators [Hogan

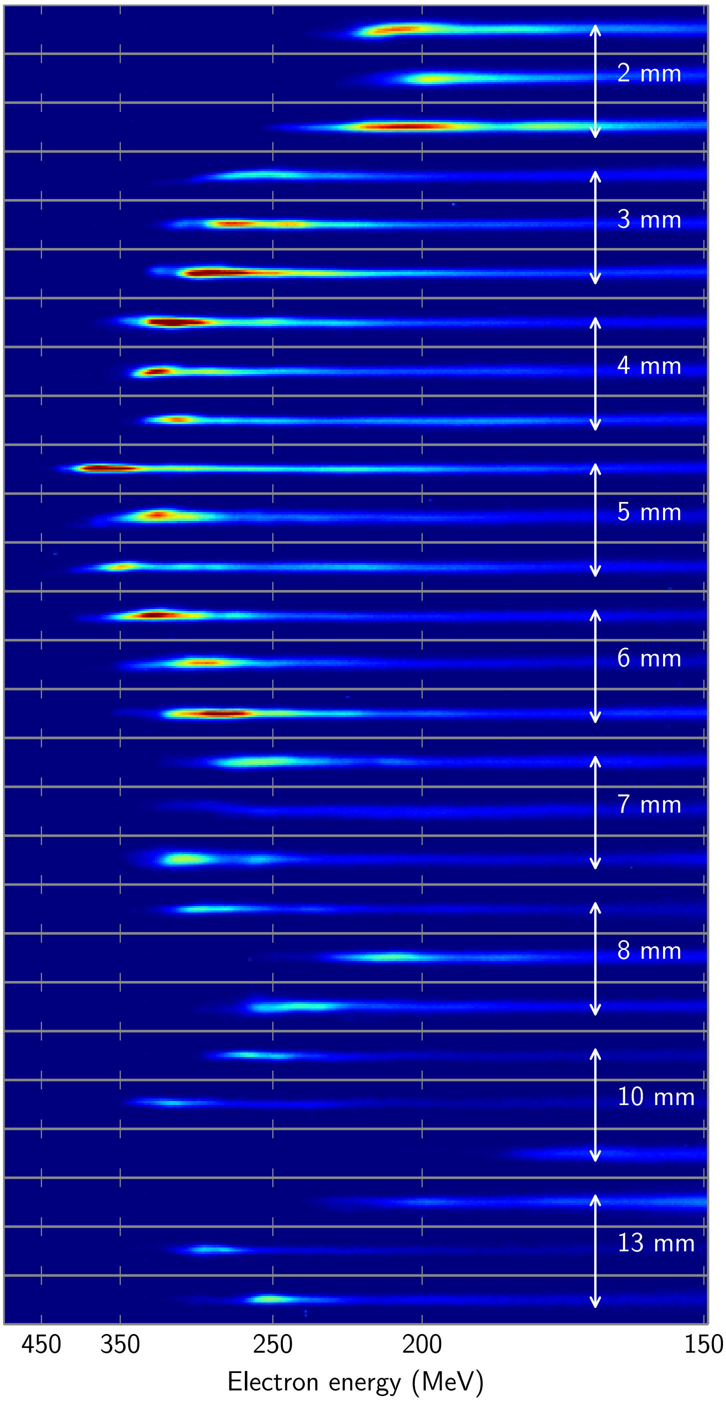

Figure 5.1: Electron spectra from the gas cell length scan. Typical shots with various lengths of the gas cell at the electron density of 6.5×10^{18} cm^{-3}. Data shown here as well as Fig. 5.2 is by courtesy of R. Weingartner.

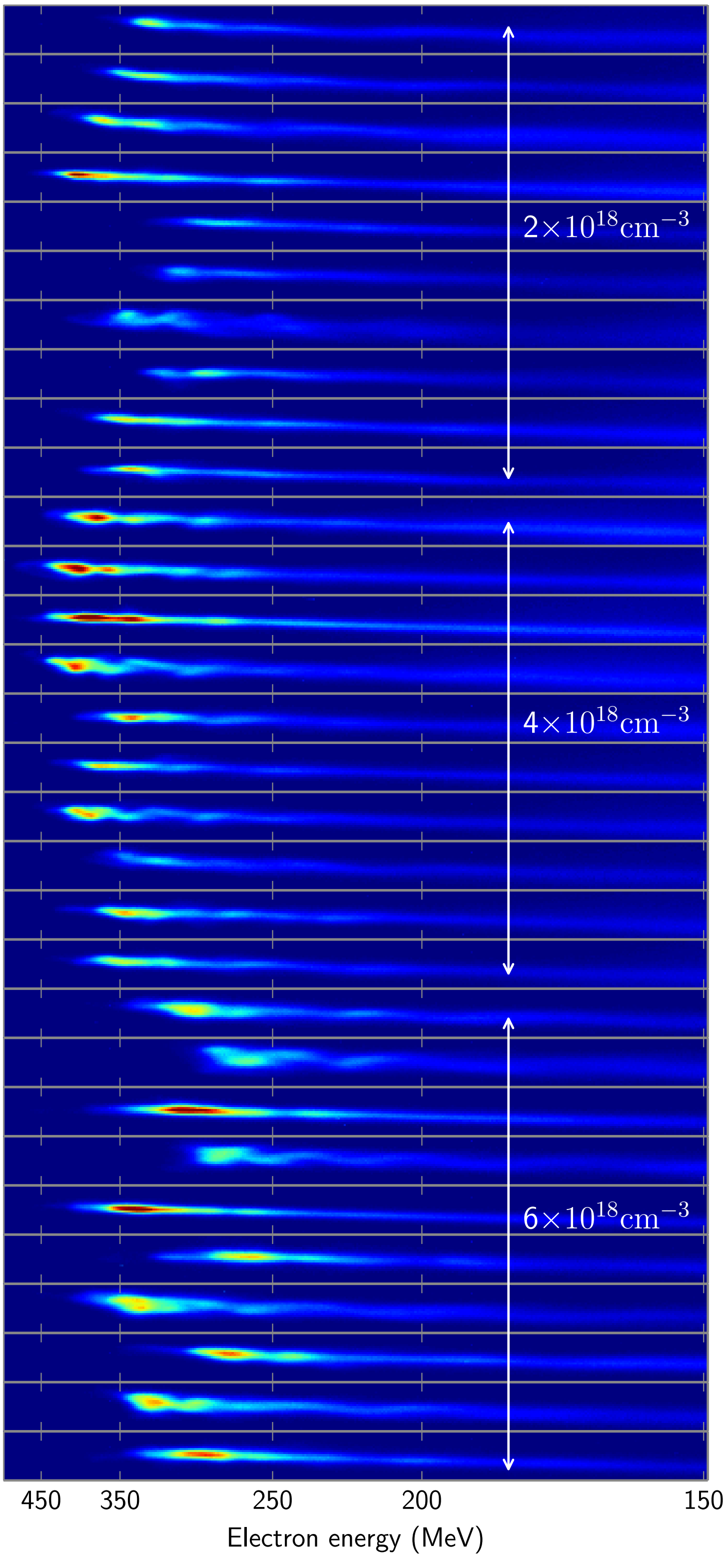

Figure 5.2: Electron spectra of plasma density scan. The length of the gas cell was 6 mm. The color scale shown here is the same as Fig. 5.1.

et al., 2005; Barov et al., 2000, 2001; Kallos et al., 2008; Blumenfeld et al., 2007; Litos et al., 2014]. To date, however, experimental study of this phenomenon from the ultra-short LWFA bunches has not been reported.

5.2.1 Experimental Setup

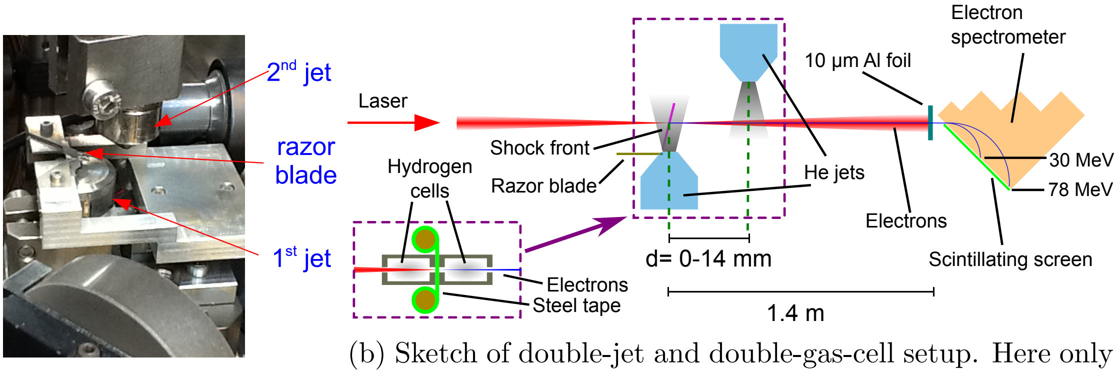

(a) Photograph of the double-jet and shock-front injection setup.

(b) Sketch of double-jet and double-gas-cell setup. Here only the spectrometer used in the double-jet experiment is shown. The spectrometer of the double-gas-cell experiment is described in [Popp, 2011].

Figure 5.3: Experimental setup of collective deceleration.

The overview of experimental setup including both of the double-jet and double-gas-cell experiment is shown in Fig. 5.3. The setup as well as the electron spectrometer was inside a vacuum chamber which was located in a radiation shielded bunker on the ground floor. During experiments, all devices were automatized and controlled remotely from a control room outside of the bunker. The chamber was connected through a 12 m long vacuum beamline to the ATLAS laser system on the first floor. In order to maximize the transmission, all mirrors inside beamline had high damage threshold dielectric coating. The ideal energy transmission through the beamline is $> 80\%$. However, during the double-jet experiment, the beamline had a much lower transmission than the designed value.

Double gas jets

In the double-jet experiment, the laser with 28 fs FWHM pulse duration was focused onto the target by an off-axis parabolic mirror with f/13 optical geometry to a 15.9 μm FWHM spot. Due to energy loss and wave-front distortion inside the beamline, we only reached 550 mJ within the first Airy ring of the focus from 870 mJ. The RMS energy fluctuation was $\leq 5\%$ and pointing instability <20 μrad.

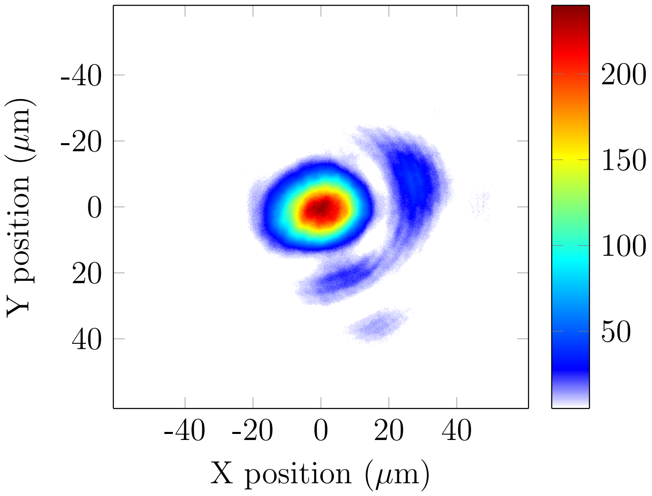

Figure 5.4: On-target focus of ATLAS during double-gas-jet experiment. The colorbar shows the relative intensity. The energy inside FWHM of the focus contained 32.2% of the total energy.

A typical focus is shown in Fig. 5.4. Beside the main beam to drive wakefield, a small part of the laser was used as a probe beam. It was coupled out by a wedge and sent perpendicularly with respect to the main beam and spatially and temporally overlapped on the target to look at the shadowgraph of the plasma channel. The probe beam path was equipped with a delay stage to adjust the delay between main and probe beams with sub-fs resolution.

The target was composed of two helium supersonic jets and well characterized by interferometry [Schmid, 2009] and Rayleigh scattering [Dorchies et al., 2003] (more details are described in chapter 4).

The distance between laser and jets was measured by shadowgraphy using the probe beam with an uncertainty below 10 μm. This information was used to determine density from interferometry result. The backing pressures of the jets were adjusted separately by two closed-loop electropneumatic pressure controllers (TESCOM ER3000), and the pressures were measured by thin film strain pressure transducers which offered an accuracy of 0.125%. A careful choice of PID parameters [Bennett, 1993] was critical to achieve fast and accurate adjustment of backing pressure during experiment. In practice, these parameters depended on the pressure, shooting frequency and pumping speed. An improper setting causes large oscillation in pressure and increase shot-to-shot uncertainty of density. The resulted error bar of the determined electron density was better than 10% in this measurement.

In order to prevent ambiguous results caused by unstable electron sources based on self-injection, we used the shock-front injection scheme. The electron bunches were injected from a shock front generated by the edge of a razor blade inside the supersonic flow in the first jet (see section 4.4),which had a 300 μm exit aperture and 1002 μm FWHM Gaussian-like density profile along the laser axis.

The electron bunch propagated into a second jet with 1500 μm exit aperture and 1503 μm flap-top profile. The distances between the laser and the first and the second jet were 1.6 mm and 0.88 mm respectively. The electron density of the first jet was fixed at 1.7×10^{18} cm^{-3} while the density in the second jet was varied between $1.2 - 4.8 \times 10^{18}$ cm^{-3}. The two jets were oriented on the top of each other in order to overcome the geometrical limit of jets to reach closer separation. Both jets were mounted on motorized 3-axis translation stages which offered 1 μm resolutions and were controlled remotely from control room. The separation d of two jets were defined as the distance between shock front and the middle position of second jet, which was tunable between d=0 and 14 mm. The electrons were detected by a spatially resolved electron energy spectrometer, as described in section 3.2, and the accompanied direct laser light was blocked by a 10 μm aluminum foil at the spectrometer entrance. The calculated collisional and radiative energy loss from the foil was less than 15 keV and the increase of divergence was negligible. The electrons were generated at 1 Hz repetition rate. The only limitation factor of repetition rate was the pumping speed of the vacuum system.

Double gas cells

Although, as it will be shown in the next section, the double-jet experiment gave a clear indication of the electron-driven wakefield, the laser was not blocked between two jets which might change the electron energies in the second jet. In order to completely exclude the influence of the laser, an additional experiment was conducted. In this experiment, two hydrogen-filled gas cells were put adjacent to each other with holes in the middle of the gas cell surfaces to let laser pass through it. Similarly, the gas densities in each cell were controlled separately by two closed-loop electropneumatic pressure controllers. The stability of the pressure was better than 1%. The two cells were separated by a 10 μm stainless steel tape which blocked the laser completely before being destroyed and was shifted/refreshed after every shot.

This automatic renewal of tape was also important for the density distribution because the holes on the gas cell were gradually damaged by the laser and got enlarged from 300 μm up to 2 mm which changed the density distribution between the cells. The length of plume at the exit of the first cell would also change significantly, as noticed in fluid simulation. The laser pulse of 1.7 J and 26 fs was focused by f/19 parabolic mirror to a 22 μm spot on the target.

The geometry of each cell is the same as what was used in section 5.1. The 1st gas cell was operated in the self-injection regime. Due to small divergence ($\sim$ 1.7 mrad) and $<$ 1 μm source size [Weingartner et al., 2012] of the electron bunches, the hydrogen gas in the second cell was field-ionized [Martinez de la

Ossa et al., 2013] by electron bunches in our configuration. The experiment was operated at one shot every 2 minutes because of the large volume of the gas cells.

5.2.2 Results

Double gas jets

The electron spectrum was retrieved from the image of scintillating screen in the back side of spectrometer by integration along the axis perpendicular to the dispersion axis, i.e. along the gap of the magnet. The integration of the whole spectrum gave the total charge of each shot. The energy dependent divergence was calculated from the line out of the image along of gap divided by the length of the path of a specified energy.

The shock-front injection gave tunable and stable electron spectra in a wide range of energy up to 200 MeV (injection probability >95%, peak energy fluctuation (RMS) <3 MeV, standard error of total charge fluctuation <2%) as what has also been observed in [Buck et al., 2013]. In this experiment, we fixed two configurations of shock front by moving the razor blade and shifting focus position which gave peak energy at 22 MeV and 36 MeV respectively. The spectra of consecutive shots from the shock-front injection are shown in Fig. 5.5. It needs to be emphasized that the spectra without second jet were monoenergetic and had non-detectable thermal-like background, which was an important property to clearly distinguish the effect of the second jet from the shot-to-shot fluctuation of the original bunches.

After inserting the second jet, a consistent deceleration of the majority of electrons was observed in a wide range of densities in the second jet as well as separations. One example of the spectra as a function of the separation are shown in Fig. 5.6, where the electron density of the second jet was fixed at 3.6×10^{18} cm^{-3}. The spectra became broader and extended towards the low energy as the separation became shorter. In the closest case, a secondary peak around 15 MeV appeared. The results from other backing pressures gave similar results. The modulation of the spectra was dominated by the distance between two jets. Beside the energy loss, reduction of divergence and charge loss was also observed. Although the total charge was reduced, an energy front corresponding to the original energy peak was preserved in most of the spectra.

To compare the results from different data sets, we use average REF and RCF (same as the definition in section 2.2) over all shots to represent the global behavior. The REF and RCF as a function of separation are shown in Fig. 5.7, indicating that the values of both parameters decreased monotonically with the distance between the two jets. The highest energy loss of over 94% was observed at d=3.5 mm. At this distance, the estimated average stopping power from the first momentum

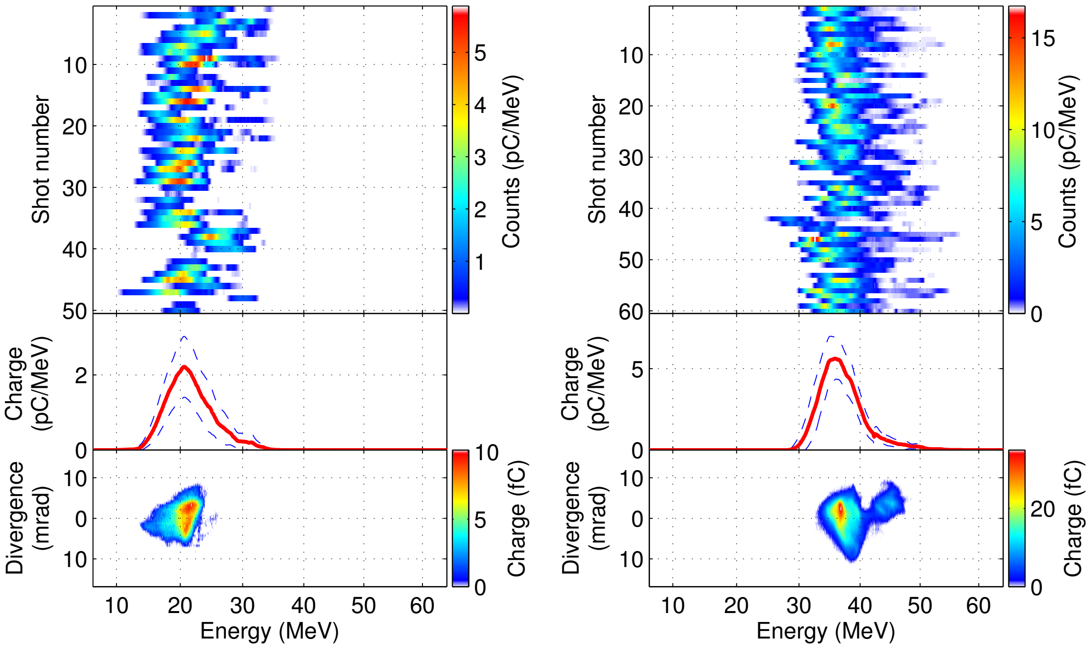

Figure 5.5: The original electron spectra without second jet. The top figure shows the angle-integrated spectra of consecutive shots. The average spectrum (solid line) and root-mean-square (dashed line) is shown in the middle plot, and a typical angularly-resolved single-shot spectrum is displayed in the bottom figure. *Left*: 21.8 ± 0.46 MeV, 17.5 ± 1.30 pC with average divergence 8.83 ± 0.32 mrad. *Right*: 35.8 ± 0.28 MeV, 44.3 ± 1.52 pC and 7.74 ± 0.17 mrad.

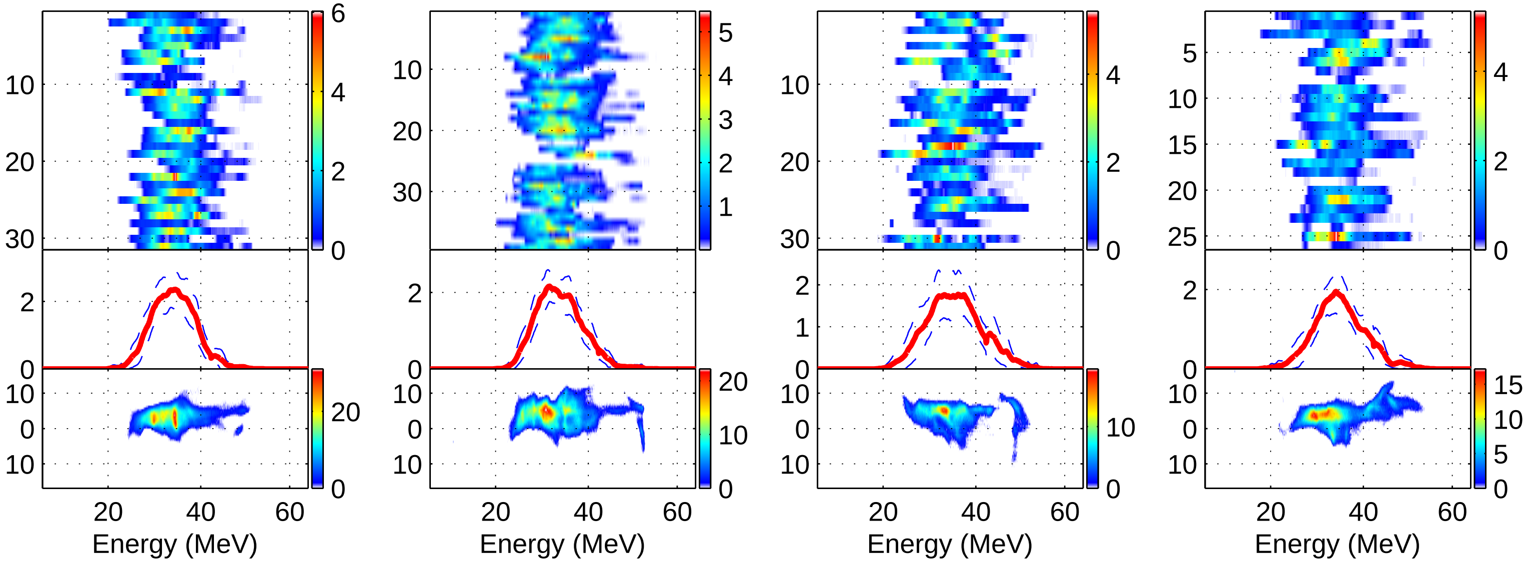

(a) d=10.4 mm (b) d=9.5 mm (c) d=8.5 mm (d) d=7.5 mm

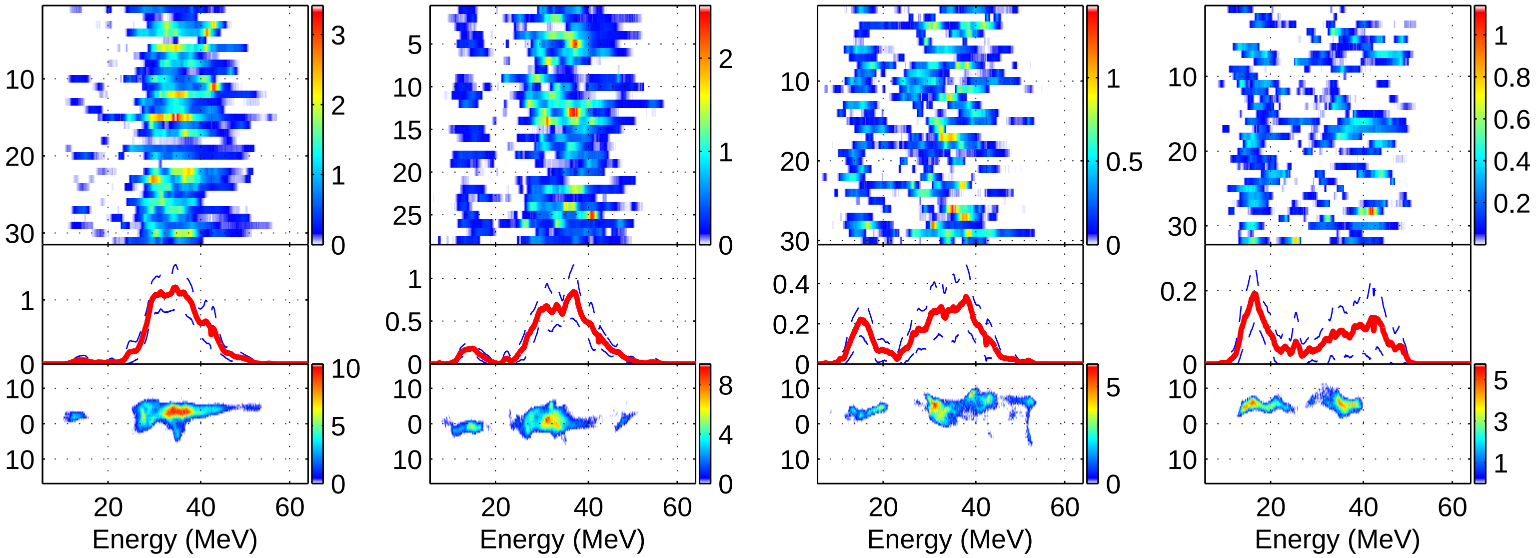

(e) d=6.5 mm (f) d=5.5 mm (g) d=4.5 mm (h) d=3.5 mm

Figure 5.6: Measured spectra as a function of distances between two jets. The definition and the units of the axes and color bars are same as in Fig. 5.5. The electron density of the second jet was 3.6×10^{18} cm^{-3}.

of the spectrum and a deceleration length of ≈1.5 mm corresponds to 5.1 GV/m deceleration gradient, and the peak-to-peak stopping power is estimated by the secondary peak around 15 MeV, which shows a gradient >14 GV/m. The RCF gives similar dependence on distance as REF, which is due to the correlation between deceleration and scattering as discussed in chapter 2.

Similarly, the divergences were compared by the average of the first moment of the energy dependent divergence of each experimental run (Fig. 5.8). The minimum divergence was reduced by more than a factor of 2 compared to the original divergence. The reason of this reduction might be caused by plasma lensing [Thaury et al., 2015] and will need a further study in the future.

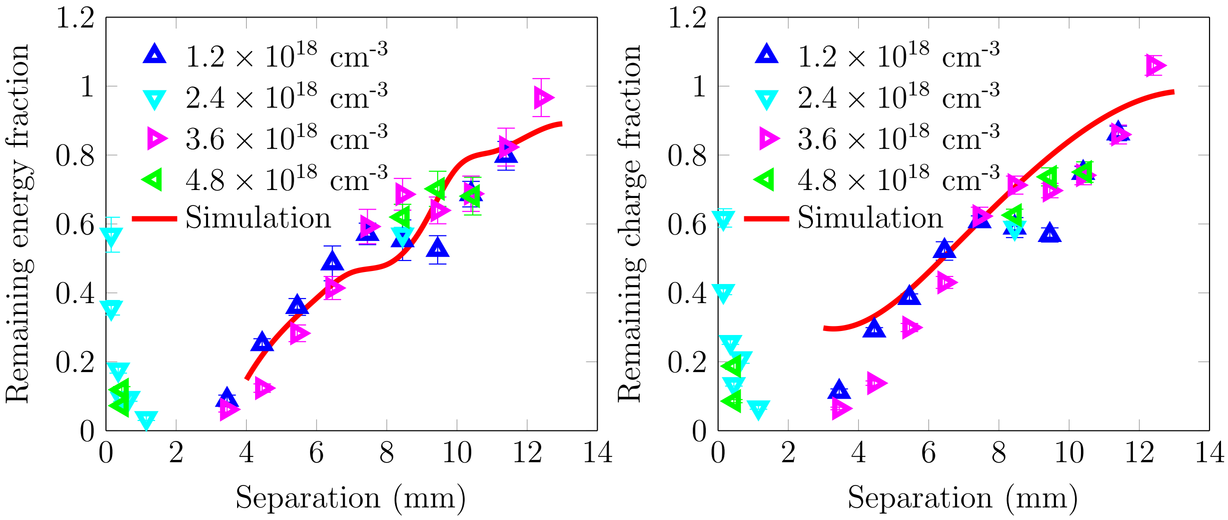

Figure 5.7: Remaining energy fraction and remaining charge fraction as a function of distance between two jets. The number in the legend shows the electron density of the second jet. The solid line is the result from PIC simulation which will be discussed in the next section.

Double gas cells

In this experiment, the laser focus position was optimized for self-injection [Lu et al., 2007] in the first cell, and therefore there was no any injection from the second cell observed when the first cell was in vacuum. The electron spectra with and without the gas in the second cell are shown in Fig. 5.9. When the second cell was off, the spectra showed a typical quasi-monoenergetic peak around 350 MeV and a plateau below from self-injection. The average of total charge inside spectrometer was ≈ 38 pC. Since only the electrons above 200 MeV were

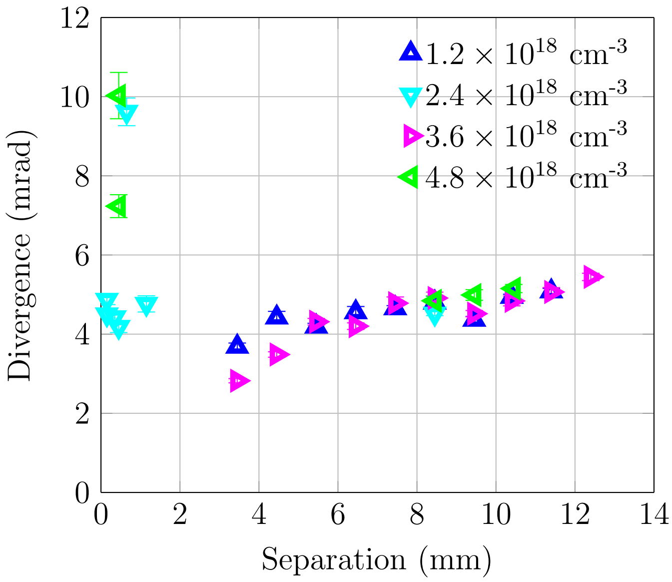

Figure 5.8: Divergence (FWHM) as a function of distance between two jets.

captured by the scintillating screen of spectrometer due to geometric limitation, the total injected charge was expected to be around 100 pC.

After filling gas into the second cell, despite the high instability and large energy spread from the first cell, electron spectra lost the quasi-monoenergetic peak, and showed clear energy and charge loss.

Since the laser was blocked, and only the electron bunches played a role, the only possible explanation of these spectral modifications was electron driven wakefield which decelerated the front part of the bunch and accelerated the rear part. The low probability of the influence could stem from the requirement of field ionization by the bunch, and such process was sensitive to any small fluctuations of driver bunch by its nature [Deng et al., 2006]. Nevertheless, the experiment gave a strong support to show the collective effect introduced by the electron driven wakefield.

5.2.3 Discussion

We have observed high-gradient energy loss of LWFA electron bunches in plasma in the experiment. Our results strongly suggest that the energy loss process is due to electron-driven wakefield. In this section, we focus on the discussion of the results from the double-jet experiment, and other factors which might contribute to the deceleration are ruled out.

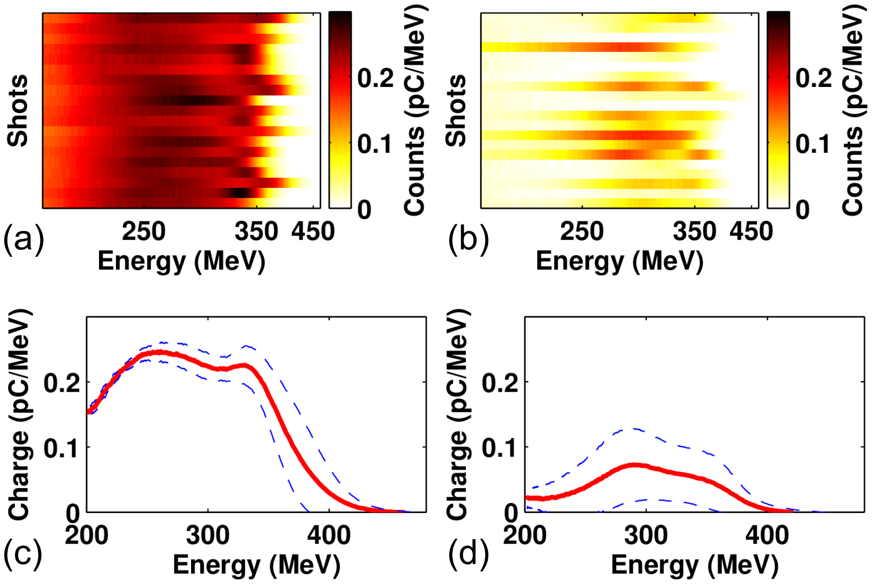

Figure 5.9: Electron spectra from double-cell experiment. Both gas cells had a length of 5 mm with density $6.8\times10^{18}\text{cm}^{-3}$ (a) Only the first gas cell was filled with hydrogen, and tape was inserted. The average total charge is 37.80±0.89 pC. (b) The spectra with both gas cells were filled with hydrogen and separated with tape. The average charge is 8.42±1.50 pC. (c) and (d) are the average spectrum of (a) and (b) respectively. The average observed REF=0.23±0.041 and RCF=0.22±0.040.

Energy loss (MeV/m)	Helium (at STP)	Graphite	Aluminum	Lead
Collisional	0.0466	434.8	498.7	1613.7
Radiative	0.0165	456.2	1002.8	1628.4

Table 5.1: Collisional and radiative energy loss of electrons at 100 MeV in different materials. The collisional stopping power of electrons with energies between 1 and 10 GeV is similar while the radiative stopping power is strongly increasing. STP: standard temperature (273.15 K) and pressure (1 bar).

Possible energy loss mechanism: Classical energy loss

The classical energy loss mechanism of charged particles is explained by particle-particle interaction such as collisional ionization and radiation, which is also the principle behind all conventional beam dumps in modern particle accelerators.

In the case of the collisional ionization, the bound electrons are excited or ionized on impact of the electron beam. The obtained kinetic energy is released through photon emission or thermal de-excitation. The stopping power due to collisional loss is quantified by Bethe-Bloch formula [Fermi, 1924; Barnett et al., 1996]. The other important energy loss of relativistic electrons in material is due to the bremsstahlung process [Seltzer and Berger, 1985], which happens when an electron is deflected by the Coulomb interaction with an atomic nucleus and converts its kinetic energy into radiation. It is possible to calculate the radiative stopping power analytically [Seltzer and Berger, 1985; Bloch, 1933]. The typical stopping powers from different materials are shown in Tab. 5.1. It needs to be noticed that, for relativistic electrons, the collisional energy loss is not strongly dependent on the electron energy while the radiative energy loss is roughly proportional to γ.

Apparently, the stopping powers from the classical theory are far too low to explain our results[1]. Our observation is clearly not caused by such particle-particle interaction.

Possible energy loss mechanism: Energy loss due to betatron radiation

Another possibility is radiation loss due to betatron movement [Phuoc et al., 2005]. As relativistic electron bunches propagate in a pre-formed ion channel, the restoring force of the channel causes the electron bunches to wiggle around the axis of propagation. This phenomenon is called betatron oscillation, and correspondingly a collimated synchrotron radiation is emitted, which is called *betatron radiation.*

---

[1] In addition to collisional energy loss, the direct elastic scattering of electrons from helium has very small cross section [McAllister and Hofstadter, 1956; Collard et al., 1965], which is even more unlikely to explain the results.

The energy loss of an electron due to the emission of betatron radiation is calculated by [Esarey et al., 2002]:

$$-\left(\frac{dE}{dx}\right)_{Betatron} \cong r_e mc^2 \cdot \frac{(\gamma_0 k_\beta a_\beta)^2}{3}$$

where γ_0 is the initial energy of electron, r_e and k_β are defined in (2.2), $a_\beta = \gamma_0 k_\beta r_\beta$, and r_β is the amplitude of the betatron orbit. The details of all parameters are not provided experimentally; nevertheless, an upper limit is estimated by assuming all electrons were monoegergetic and wiggling with maximum displacement and following single electron radiation energy loss rate. The maximum displacement is expected to be λ_p which is usually 10s of μm. The resulted radiation loss is less than 0.01% of our observed value, and therefore its contribution to the observed energy loss is also excluded.

Gas flow interference between jets

Beside the possible physical processes, mechanical problems such as gas density disturbance between two jets should also be taken into account. From former experience, the crucial element that determines the properties of electrons is the density profile around the shock front and the acceleration pedestal after it. We used an offline Rayleigh scattering measurement to clarify the influence of the second jet on the injection stage. The details of the setup is described in section 4.6. In this measurement, the configuration of the two jets was similar as in the deceleration experiment, and the shock front was positioned at the end of the gas distribution. The density profile in the middle of the first jet is shown in Fig. 5.10, where images are averaged over 5 shots to eliminate shot-to-shot fluctuation due to formation of clusters, and consequently the transition width of shock front is not as sharp as in reality. The measurements show that the gas flow from the second jet increases the density after the shock front when the two jets are too close (< 850 μm), and there is no detectable influence from the second jet when $d \geq 1150$ μm. Although the exact position of shock front was shifted in a range of 1 mm, the Rayleigh scattering measurement suggests that the possible disturbance between two jets is safely discarded for $d \geq 2.5$ mm.

Contribution of laser wakefield

After excluding most of the known process which might account for the energy loss, the only possible explanation for the observed strong energy loss is the interaction between electron and wakefield. In the double-jet experiment, the laser was not blocked between the two jets because of the sensitivity of the supersonic flow and the limited space. Therefore, it is necessary to ensure that the laser cannot drive

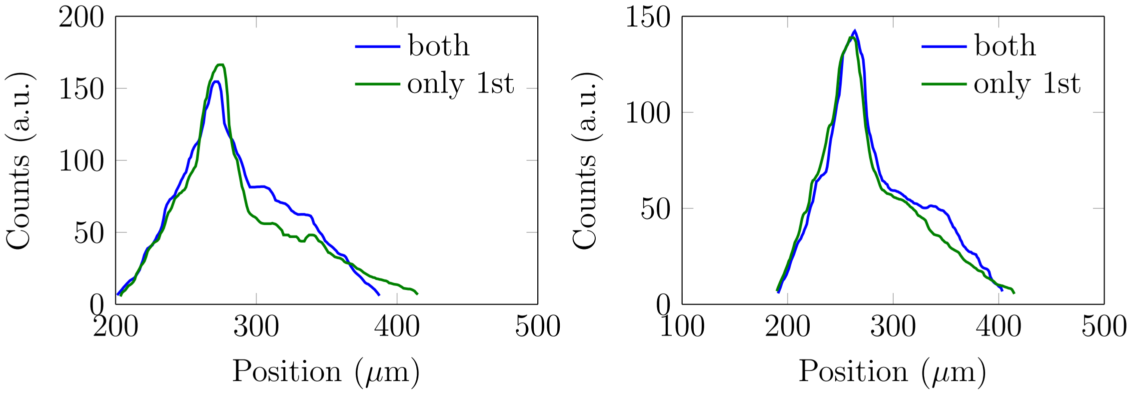

(a) $d = 400$ μm

(b) $d = 700$ μm

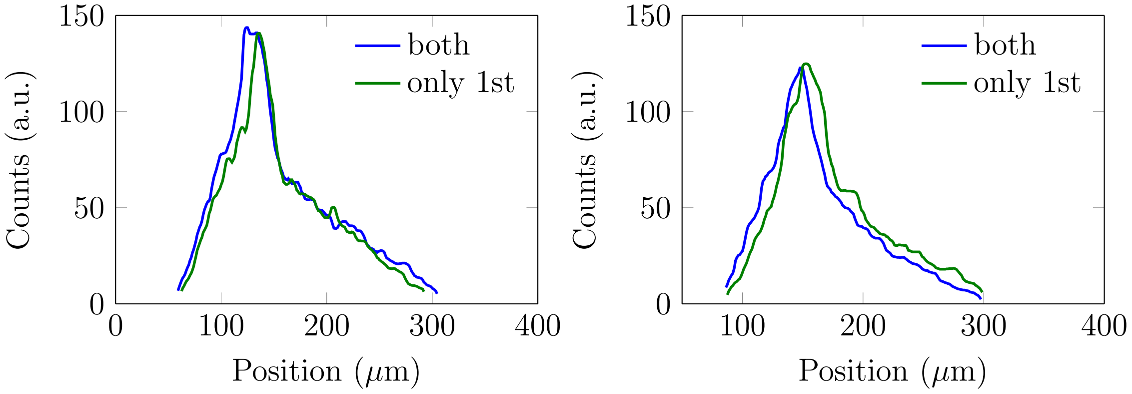

(c) $d = 850$ μm

(d) $d = 1150$ μm

Figure 5.10: Measurement of the density profile of double jets as a function of separation by Rayleigh scattering. Only the profile of the first jet including shock front is shown here, where the green lines show the profile without second jet, and the blue lines stand for the presence of both jets.

a strong wakefield in the second jet that causes a significant deceleration of the electrons. In order to draw more conclusions from our observations, we used 3D Particle-in-Cell simulations with the code OSIRIS [Fonseca et al., 2002] to model the wakefield that results from either the response of the plasma to the laser field or to the electron bunch.

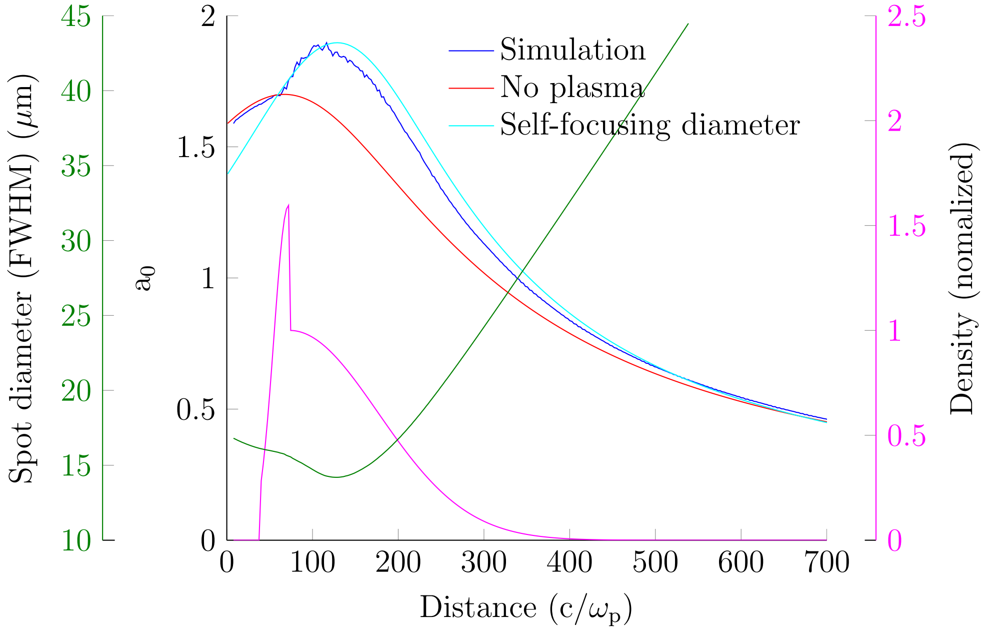

Figure 5.11: Laser self-focusing inside the jets. The laser was modeled with initial vacuum waist position at the shock front. The electron density is normalized to 1.7×10^{18} cm^{-3}. The blue line shows the a_0 from the 3D simulation, and red and cyan lines show the a_0 of Gaussian beams propagate with original vacuum beam waist and self-focusing spot size respectively.

The strength of any laser-driven wakefield in the second jet mainly depends on the laser pulse evolution in the first jet which sets the condition for self-focusing in the 2nd jet. The laser was modeled with initial conditions a_0=1.7, 28 fs (FWHM), and 15.9 μm (FWHM) spot diameter with its vacuum waist position at the shock front. An approximation of the Rayleigh scattering result of density profile was used in simulation. The computational window was 61.6 × 123 × 123 μm^3 corresponding to 1210 × 300 × 300 grid points. The results are shown in Fig. 5.11. The simulation results indicated that the laser was self-focused to 13.8 μm and a_0=1.9 in the first jet which agreed well with the theoretical prediction of 13.7 μm [Lu et al., 2006c], where the peak a_0 was calculated from the transverse electric field. After the laser diffracted through the vacuum gap and propagated through the second jet, it was only slightly self-focused. However, this led to less than 4%

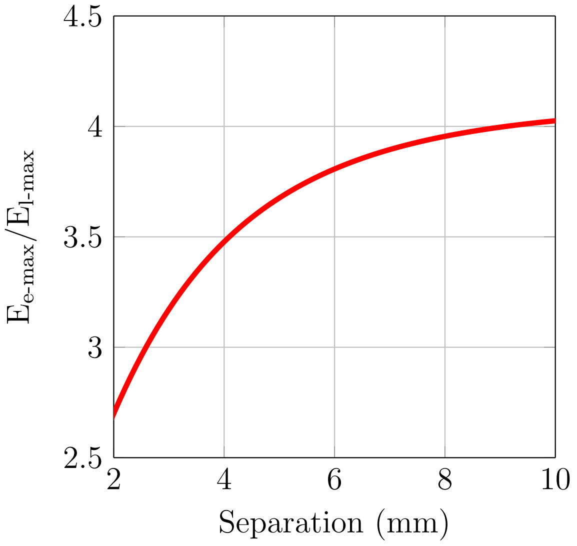

Figure 5.12: Ratio between electron-driven and laser-driven wakefield. The plasma density was 1.7×10^{18} cm^{-3}.

intensity enhancement (a_0=0.3 at d=4 mm) compared to Gaussian beam propagation in vacuum after the first jet (red line in Fig. 5.11). The enhancement by self-focusing dropped further with lower density and larger separation. The simulation provided the evidence that the evolution of a_0 is fairly approximated by a Gaussian-like propagation with initial conditions of self-focusing intensity and beam waist from analytical formula, and the contribution of the self-focusing in the first jet is neglected when the separation is large.

It should be emphasized that although the laser intensity was not enough to drive a strong wakefield in the second jet, it was sufficient to fully ionize gas to produce plasma[2].

In the next step, we compare the wakefield generated by the laser and electrons analytically. By assuming a bi-Gaussian electron bunch $n_b \cdot e^{-\frac{\xi^2}{2\sigma_z^2}} \cdot e^{-\frac{r^2}{2\sigma_r^2}}$, where n_b is the peak density, σ_r is the transverse RMS radius and σ_z is the RMS bunch length,

---

[2] The ionization process is dominated by tunneling ionization, where the required intensity of electric field to fully ionize helium is estimated by ADK model [Keldysh, 1965; Littman et al., 1978; Krainov and Ristic, 1992]:

$$I_{ion} \simeq 4 \times 10^{19} \frac{(E_{ion}(\text{eV}))^4}{Z^2} \frac{\text{W}}{\text{cm}^2},$$

where E_{ion} is the ionization potential, and Z is the charge number of the ion. The ionization potential for He$^+$ is 54.4 eV which requires $I_{ion} = 8.75 \times 10^{15}\ \frac{\text{W}}{\text{cm}^2}$ or equivalently $a_0 = 0.059$.

the initial electron-driven wakefield is calculated by equation (1.19)[3], where the electron bunch diameter was estimated by the measured divergence and separation of jets.

In comparison, the laser wakefield was estimated by assuming the wakefield is linear because of $a_0^2 \ll 1$. Since the laser propagation after the first jet is approximated by Gaussian-like propagation with initial conditions of self-focusing intensity and beam waist, the maximum magnitude of laser wakefield is calculated analytically by the formula (1.22). The calculation shows that the initial electron-driven wakefield is 3-5 times stronger than laser wakefield depending on the different plasma density and separation (Fig. 5.12), and the electron driven wakefield further increases due to electron self-focusing as discussed in chapter 2.

The estimation needs to be confirmed by simulations. However, since to simulate laser together with electrons needs a big volume and computational resource consuming; only the shortest jet separation (d=3 mm) is simulated within a reasonable CPU hour. In this example, at d=3: $\frac{E_{e-max}}{E_0}$=0.31 and $\frac{E_{l-max}}{E_0}$ =0.1 from analytical estimations, which agrees well with PIC results which give $\frac{E_{e-max}}{E_0}$=0.27 and $\frac{E_{l-max}}{E_0}$ =0.06. After propagating in plasma, the plasma wakefield increased significantly due to a strong self-focusing of the electron bunch but the laser wakefield does not, and the value of E_{e-max}/E_{l-max} increases further up to 30. Therefore, we conclude that simulations with only predefined electron drivers are sufficient for describing the reaction of the plasma in the second jet.

5.2.4 Comparison of Simulation and Experimental Results

The conclusion of the last section rules out all other mechanisms which might lead to deceleration of the electrons and indicates that our observation is caused by the electron bunch losing energy in the self-driven wakefield. In this section, consequently, the results of the double jets are compared to the simulations which use bi-Gaussian electron bunches as the sole wakefield drivers inside a pre-ionized plasma. The propagation of the bunches is excessively controlled by nonlinear processes such as self-focusing, collective deceleration and electron trapping as discussed in chapter 2.

The simulations use co-moving window and perfect-matched-layer (PML) absorbing boundary condition [Berenger, 1994]. The grid resolution is fixed at $1/220 \times 1/20 \times 1/20\ k_p^{-3}$. The initial conditions of the electron bunch are defined as: peak energy of 35 MeV, total charge of 40 pC and 4.5 fs FWHM bunch du-

---

[3] Although this formula does not include the evolution of the electron bunches, which, as what shown later, will experience strong self-focusing, the formula agrees well with 3D simulations for early time steps and is included here for the sake of estimating the minimum peak wakefield strength.

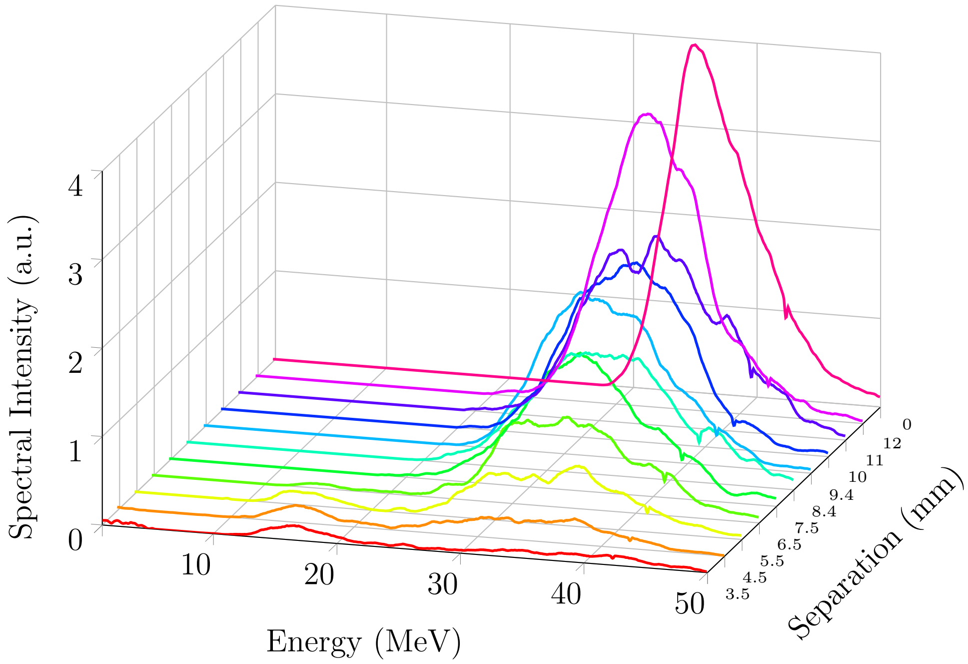

(a) Measured spectra as a function of separation.

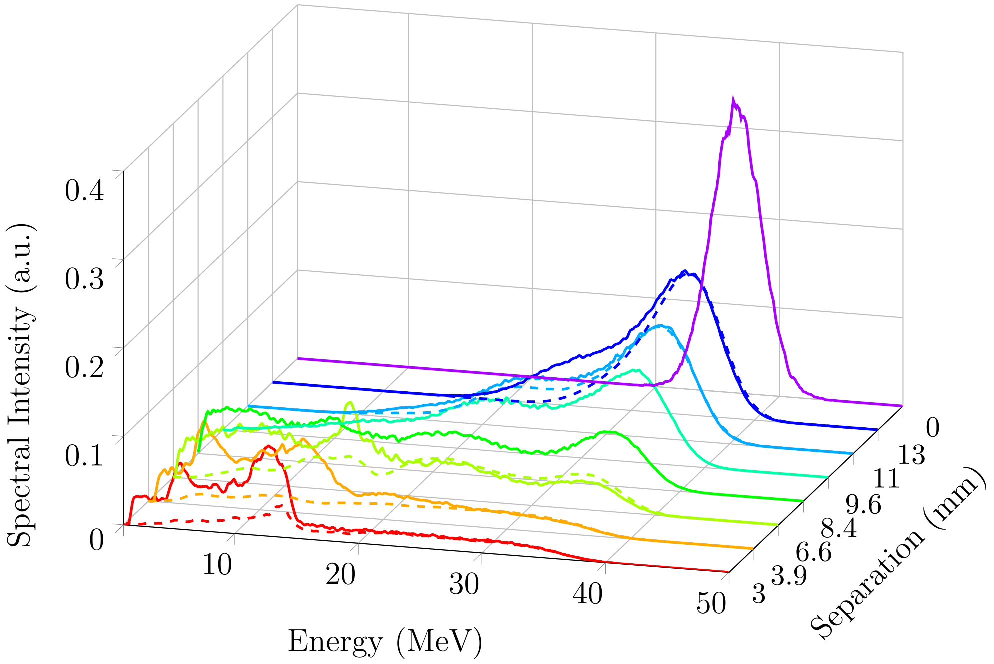

(b) Spectra from simulations. The dashed lines show the spectra of the particles with divergence below 30 mrad and solid lines of all particles.

Figure 5.13: Comparison of the measured spectra and the simulation results in the double-jet experiment.

ration. Since the plasma density and density ramp is not critical in our case as explained in chapter 2, the plasma is set to have a 2 mm long rectangular density profile with $n_0 = 3.6 \times 10^{18}$ cm^{-3}. In order to compare the experiment with simulation, we perform a series of simulations with different beam diameters including the measured divergence and fitted the experimental REF results to retrieve the bunch size that is linearly increasing with separation.

The simulation shows that the best fit requires the divergence of the electron bunch to be twice smaller than the measured divergence. By using the optimal fitted beam diameter and divergence, the REF and RCF between experiment and simulation are compared, as shown in Fig. 5.7, and the corresponding spectra are shown in Fig. 5.13. Note that since we only observed electrons within the spectrometer's acceptance angle (≈30 mrad) during experiment, an accompany charge loss is expectable.

After all, the results of the double-jet experiment is interpreted as following: more electrons loose more energy as the jet separation gets shorter, because the wakefields increase by stronger self-focusing of smaller bunches. These electrons are scattered out at low energy, and this causes RCF decrease. However, the decrease of REF is mainly caused by energy decrease since high energy electrons are not scattered out. In the case of very small separation, some of the decelerated electrons get considerably re-accelerated and generate secondary peaks around 15 MeV in spectra, which are visible in both experiment (Fig. 5.13a) and simulation (Fig. 5.13b).

5.3 Conclusion

We have observed a strong energy loss of LWFA electrons and attribute this deceleration to a self-driven collective force. A strong and density-insensitive deceleration of the electron bunches has been observed in 2 mm of underdense plasma with average 5.1 GV/m gradient (14 GV/m peak gradient). By comparing to the discussion in section 2.2, the charge loss was caused by the scattering of decelerated low energy electrons, and the overall stopping power is determined by local bunch size and local divergence. The results are stable in a wide range of parameters and consistent with simulations described in chapter 2. The collective deceleration paves the way towards building a compact and economical beam dump for upcoming high energy and ultra-short pulse LWFA beams. On the other hand, the observation also implies that the physics of plasma wakefield acceleration (PWFA) which typically requires large facility could be studied by table-top LWFA-driven electron sources.

Chapter 6

Sub-2-Cycle Laser-Driven Wakefield Electron Acceleration

As discussed in chapter 1, the minimum and maximum energy of the electron bunches from LWFA is determined by the phase velocity of the wakefield. For example, in the case of a wakefield driven by a laser pulse with a central wavelength at 800 nm in a plasma of a density 10^{18} cm^{-3}, only plasma electrons with energies above 20.8 MeV are trapped, and the highest energy after acceleration depends on the evolution of the laser pulse and wakefield. However, in some applications, for example, electron diffraction [Hastings et al., 2006; Li et al., 2009; Tokita et al., 2010], electrons with energies below 10 MeV are preferable, and it requires plasma density above 10^{19} cm^{-3} that trapping exists. Moreover, in order to resonantly drive wakefields, the length of laser pulses needs to be around half of the plasma wavelength. For example, if a minimum energy of 3 MeV is an aim, one will require to use laser pulses with temporal durations shorter than 6 fs to drive wakefield in a plasma with a density 7×10^{19} cm^{-3} from the trapping condition. In this chapter, we demonstrate the generation of sub-10 MeV electron bunches by using the sub-2-cycle (<5 fs) pulses of LWS-20 in both case of self-injection as well as shock-front injection.

6.1 Experimental Setup

The layout of the experimental setup is shown in Fig. 6.1. The laser pulses from the LWS-20 propagated through a vacuum beamline and were focused by an F/3.3 off-axis parabolic mirror (28.1°, 165 mm effective focal length and enhanced silver coated) to a supersonic gas jet to generate electrons in the target chamber. The beamline was highly stable, and root-mean-square (RMS) pointing fluctuation was better than 9 μrad. All optics in the beamline was enhanced silver coated, and

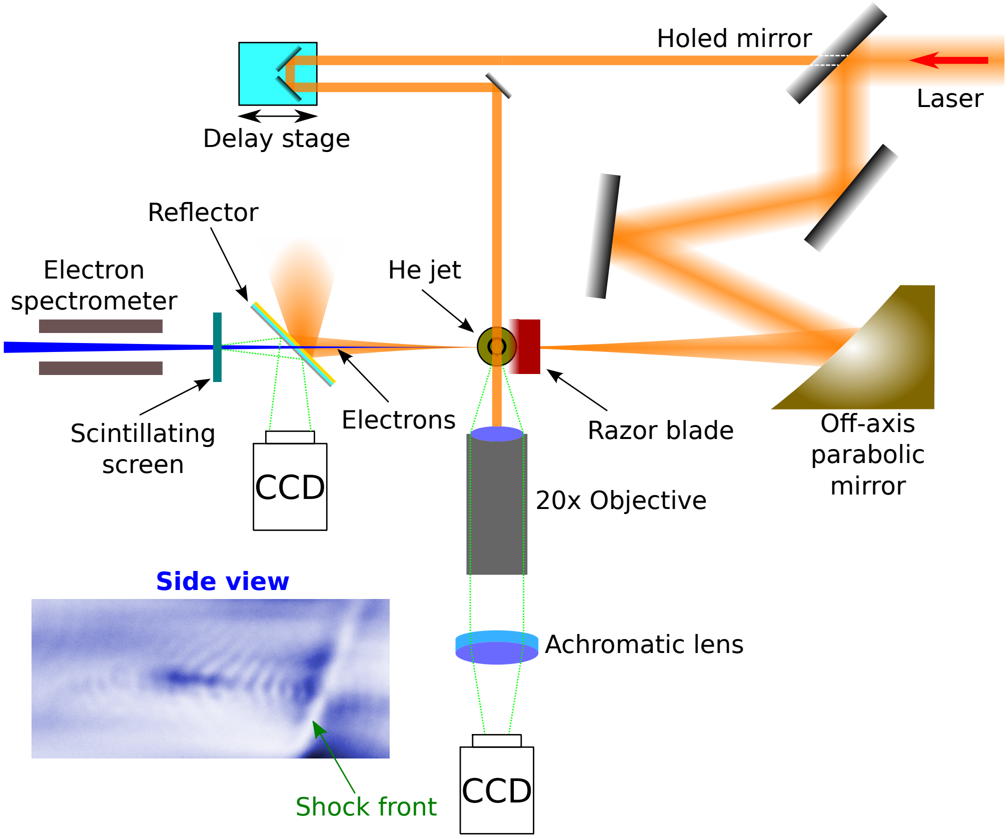

Figure 6.1: Setup of the LWS-20 driven LWFA experiment. The inset in the bottom left shows a typical shadowgraph measured by the side view CCD, where the shock front as well as plasma wave is clearly visible.

transmission from the last OPCPA stage to the focus position was 60%. The total energy on the target was ≈ 42 mJ during the experiment. The focal spot had a FWHM diameter of 5.8 μm, and the stability analysis showed 2% of the relative spot size fluctuation, 29% of the total energy within FWHM of the focus, ≈2% of the total energy fluctuation (RMS), and 6.1% of the peak intensity fluctuation (RMS). The spot size together with the 4.5 fs FWHM pulse duration gave peak $a_0 = 2.2$ in the focus. The gas target of LWFA was a supersonic helium nozzle with 300 μm exit diameter together with the setup of the shock-front injection. The details of the target are discussed in chapter 4. The residue of the laser pulse after the laser-plasma interaction was reflected and separated from the co-propagating electron beams by a reflector, which was a pellicle of 2″ diameter with a thickness of 2 μm, which was coated with 200 nm silver. However, a strong green light generated during the laser-plasma interaction penetrated the silver coating, and therefore an extra 3 μm thick gold foil was attached to the side of the pellicle facing to the target to block this direct light. The collisional and radiative energy loss of the electrons due to the reflector was estimated to be less than 50 keV. The reflector was also used to reflect the signal from the scintillating screen. The electrons passed through a reflector and were detected by either a scintillating screen to measure the beam profile or an electron spectrometer to measure energy spectrum. Due to the electron scattering from the scintillating screen, the beam profile and the electron spectrum were not measured simultaneously. The details of both setups are discussed in section 3.2. Additionally, one part of the beam was picked up as a probe by a holed mirror which had a hole of 5 mm diameter drilled in 45°with respect to the surface. The beam was used to probe the laser-plasma interaction by shadowgraphy. The temporal overlap between the main beam and the probe beam was fine adjusted by a delay stage which offered a precision up to 3 fs. The shadowgraphy was imaged by a 20× long working distance microscope objective (Mitutoyo M Plan Apo) together with an achromatic lens of 250 mm focal length onto a high resolution CCD camera (2448×2048 pixels, Point Grey, GRAS-50S5M). The optical resolution of the imaging system was 1.3 μm which was mainly limited by the objective. This side view was also used to determine the exact distance between the laser beam and the nozzle for the density calibration.

6.2 LWFA in Self-injection Regime

In the LWFA experiment, when the intensity of laser is fixed, the self-injection regime is achieved by increasing the plasma density. This is usually done by either increasing the backing pressure of the nozzle or reducing the height of laser beam with respect to the gas nozzle while the backing pressure is fixed. Since the total length of the plasma is determined by the longitudinal density profile of the gas jet which decreases with height, decrease of the height shortens the plasma length. Although increase of the plasma density usually enhances the injection, the dephasing length as well as the pump depletion length is reduced. To optimize the quality of the LWFA electron beam, a proper combination of plasma density and plasma length is critical. In the discussion of this section, the propagation axis of the laser beam was chosen to be 508 μm above the nozzle, and the backing pressure was fixed at 50 bar. The interferometry measurement showed that the peak electron density was 7×10^{19} cm^{-3}, and the density profile was Gaussian-like with a width of 347 μm in FWHM at this specific height. The injection probability was almost 100%. Typical beam profiles are shown in Fig. 6.2. The measured profiles showed three typical patterns, and each of them had approximately the same probability to be observed. The first type of profiles showed a single, well-collimated beam with FWHM divergence about 20 mrad and significantly higher charges than other cases and is the most favorable profile for the future application. The second type of pattern showed several bins within one beam, and each of the bins had comparable divergence and peak density. The last type was a highly diffused beam with a divergence larger than the screen. A possible explanation of these patterns was correlated to the injection position. The optimized pattern was expected to occur when the electrons were injected around an optimized position such that the interaction length led to a maximum effective acceleration. This statement will be supported later in the shock-front injection case. The optimized acceleration length corresponded to the dephasing length which was ≈ 100 μm at this density based on the experimental measurement [Daniel E. Cardenas, 2014]. The electron energy was the highest in this case among all others, and therefore the divergence was the smallest one. If the injection happened slightly earlier than the optimized position, the beam instability would cause a current filamentation and break the beam into separate bins [Huntington et al., 2011]. The pattern of highly divergent beams was created when the electrons are injected far too early or too late, and the divergences were large because of low energy electrons. If the electrons were injected too early, they would be decelerated and scattered. In the case that the electrons were injected too late, the acceleration length would be simply too short to achieve higher energy. The beam pointing of all shots is shown in Fig. 6.3, where the blue circles mark the position of the peak charge density. The measured electron spectra are shown in Fig. 6.4. The individual spectra were monoenergetic, but the peak energies were not shot-to-shot reproducible. The average peak energy was 4.99±0.31 MeV with energy spread 2.72±0.18 MeV and total charge 0.36±0.043 pC. In the optimum case, the peak energy was 6.26±0.37 MeV with energy spread 3.44±0.37 MeV, total charge 0.79±0.11 pC and with FWHM divergence of 34.8±1.81 mrad.

6.3 LWFA with Shock-front Injection

As it is observed in the last section, both beam pointing and electron spectra are highly fluctuated in the self-injection regime. This kind of electron beams is not suitable for applications. In order to improve the beam quality, the shock-front injection was implemented. The principle of the shock-front injection is described in section 1.2.2. To do a controlled injection experiment, the plasma density must be low enough to prevent self-injection caused by wave breaking. In the discussion of this section, we chose the laser axis to be 336 μm from the top of nozzle, and the backing pressure was 13 bar. The interferometry showed that the density profile was trapezoidal-like at this height with peak density of 4.2×10^{19} cm^{-3} and with a width of 271 μm in FWHM [1]. The acceleration length was controlled by moving

---

[1] The 300 μm nozzle used in this section was different from the one used in the last section, and the width of this jet was smaller.

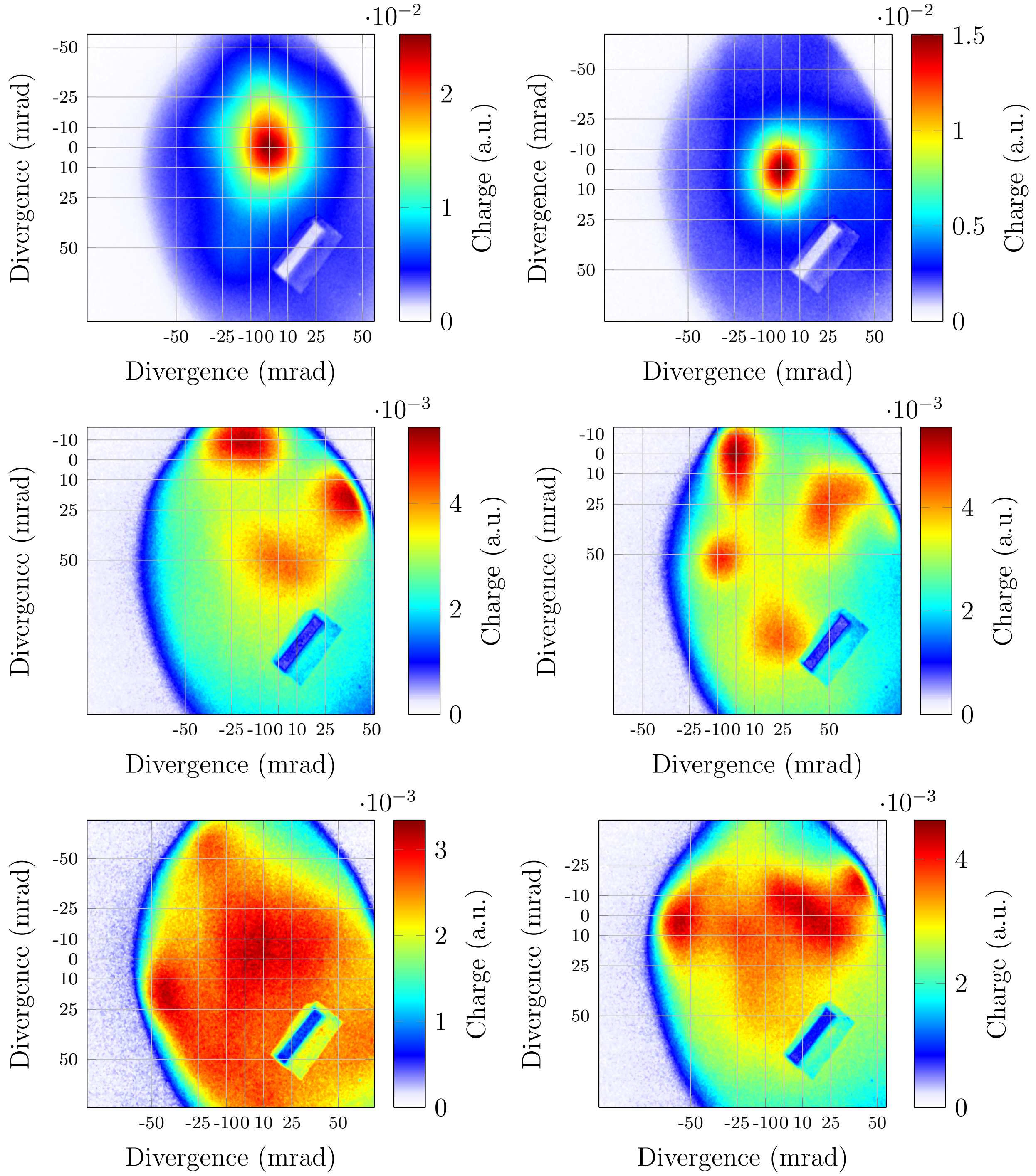

Figure 6.2: Examples of transverse beam profile of the self-injected electrons from the LWS-20 experiment. The rectangle shaped object located in the bottom right corner is the GTLS for the charge calibration. The profiles are sorted to show three typical types of beams: *top*: well-collimated electron beam; *middle*: multiple bins; *bottom*: highly divergent beam.

Figure 6.3: Pointing stability of the LWS-20 driven LWFA in the self-injection regime. The RMS pointing fluctuation was 39.4 mrad.

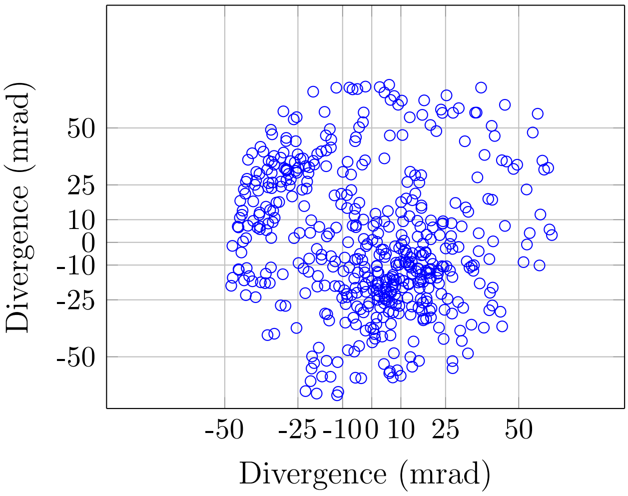

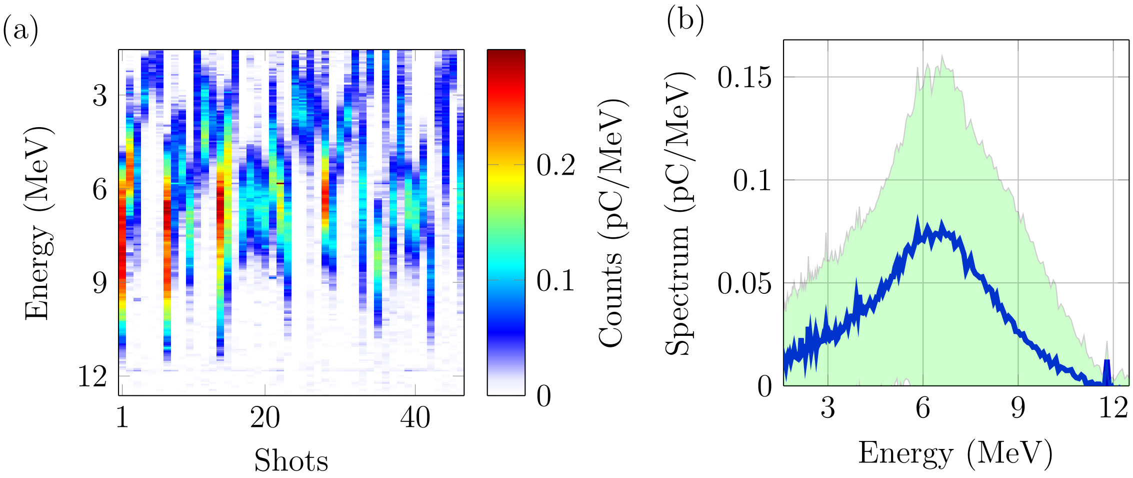

Figure 6.4: Electron spectra of the self-injected electrons from the LWS-20 experiment. (a) Spectra of consecutive shots. (b) The blue line shows the average spectrum, and the shaded area shows its standard deviation.

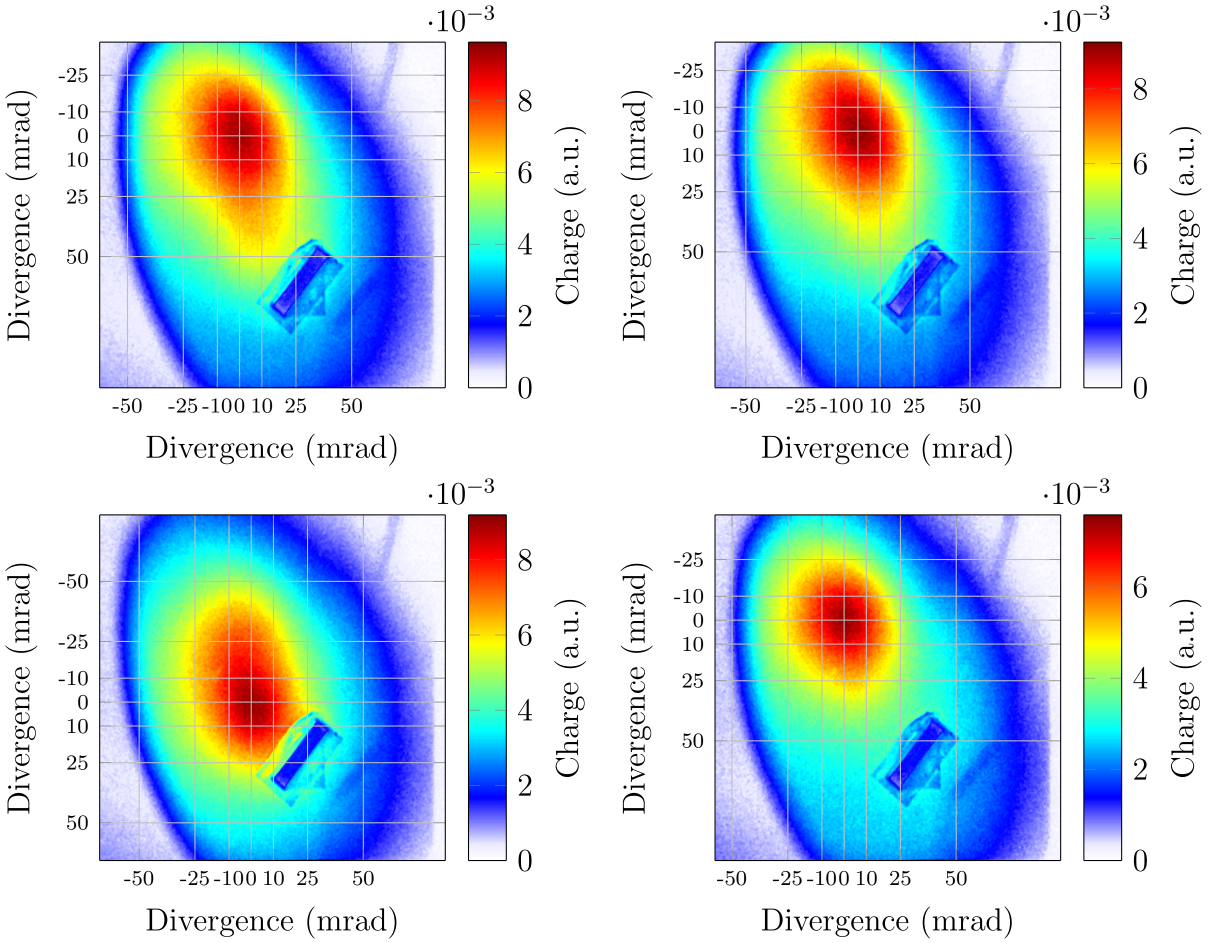

Figure 6.5: Examples of transverse beam profile of the shock-front-injected electrons from the LWS-20 experiment. These profiles are randomly chosen from the whole data set of a specific blade position. The average beam divergence in this case was 72.7±0.82 mrad.

the shock front in the pedestal part of the jet. The beam profile and pointing was much more stable in the shock-front injection regime compared to the self-injection. The injection probability was >99%. One example of typical profiles and beam pointing corresponding to a specific shock front position are shown in Fig. 6.5 and Fig. 6.6 respectively. The pointing stability was more than two times better than using self-injection (17.1 mrad versus 39.4 mrad).

Figure 6.6: Pointing stability of the LWS-20 driven LWFA in the shock-front injection regime. The RMS pointing fluctuation was 17.1 mrad.

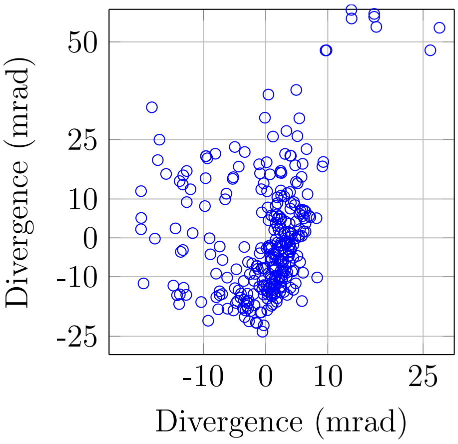

Figure 6.7: Electron spectra of consecutive shots from the shock-front injection electrons. The position of the shock front was the same as in Fig. 6.6. The peak energy was 5.13±0.026 MeV with energy spread 3.68±0.046 MeV and total charge 1.74±0.040 pC. The average spectrum is shown in Fig. 6.8(b).

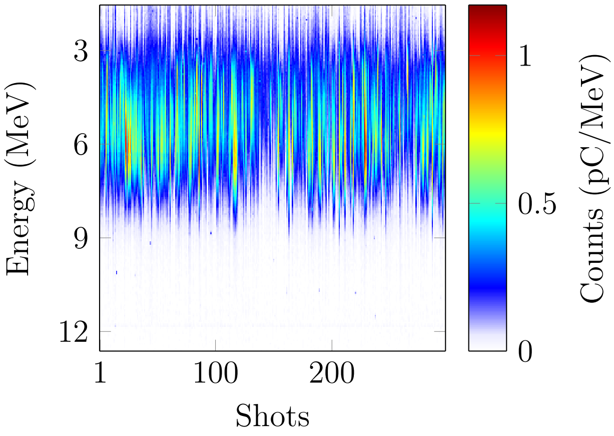

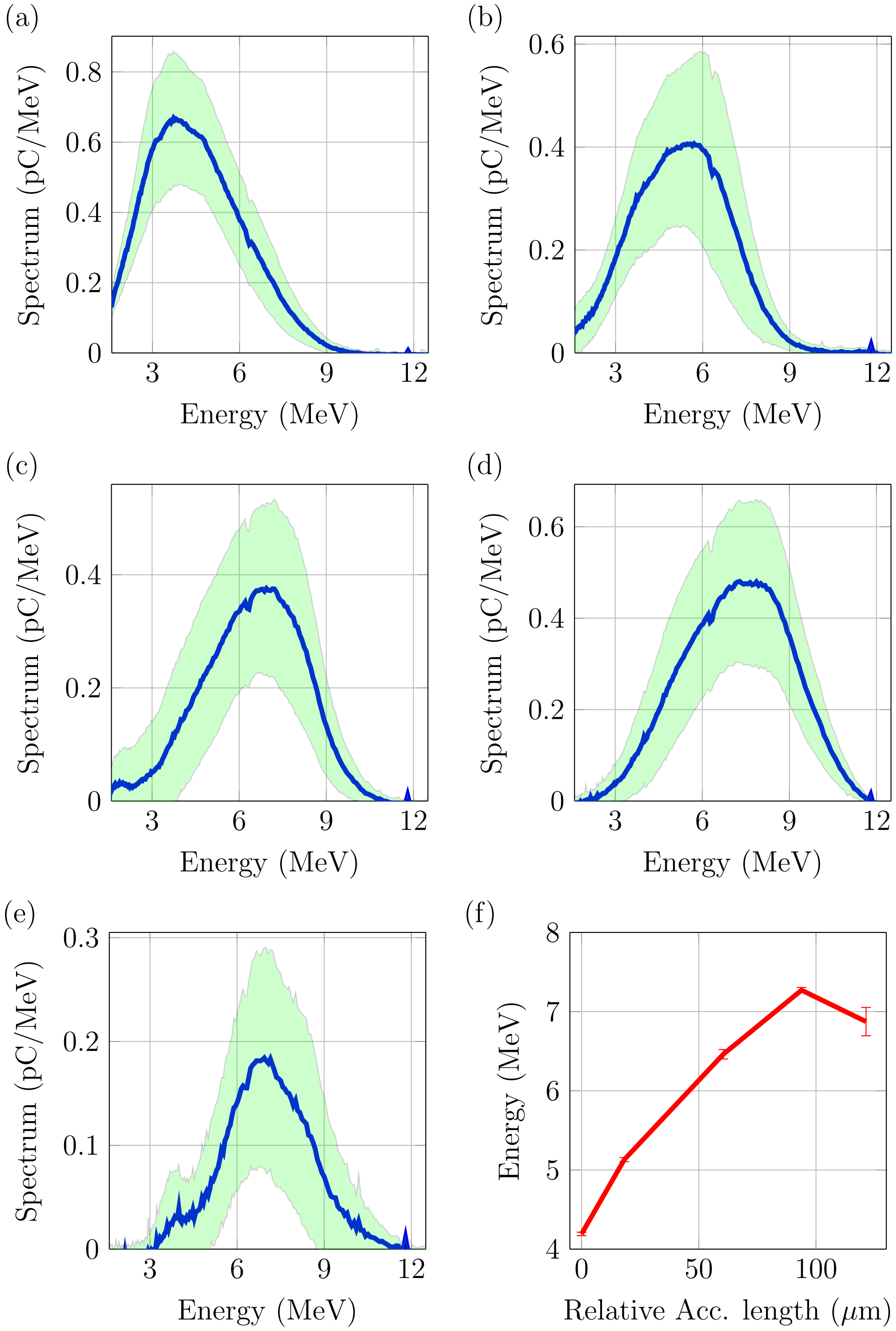

Figure 6.8: Average spectra from the shock-front injection with different acceleration length in the LWS-20 experiment. The blue lines show the average spectrum, and the shaded areas show their standard deviation. The acceleration lengths were gradually increased from (a) to (e), and (b) is the average spectra of Fig. 6.7. The peak energy and total charge ([E_{peak} (MeV), q_{tol} (pC)]) of each case is: (a) [4.19±0.022, 2.73±0.038], (b) [5.13±0.026, 1.74±0.04], (c) [6.46±0.06, 1.62±0.048], (d) [7.27±0.034, 2.33±0.057], and (e) [6.87±0.18, 0.63±0.072]. (f) Summary of peak energies versus the acceleration lengths, where the "0" length corresponds to the shortest acceleration lenth in the case of (a).

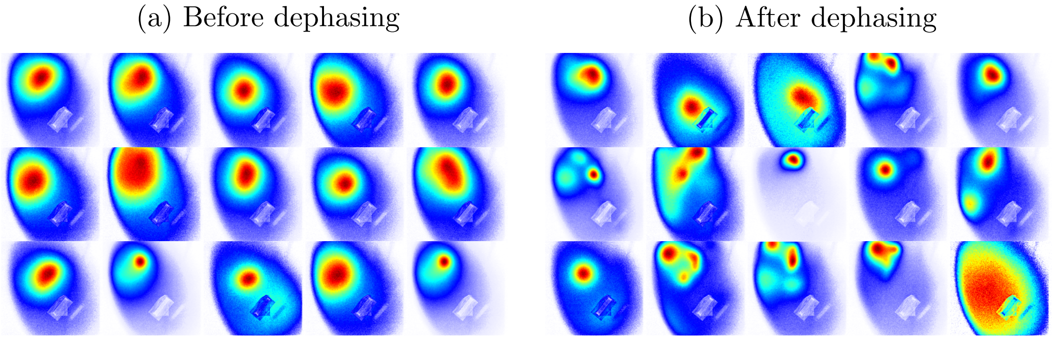

Figure 6.9: Comparison of electron beam profiles before and after dephasing. The profiles are randomly chosen from each data set. (a) Beam profiles right before dephasing, same configuration as in Fig. 6.8(d). (b) Beam profiles after dephasing, same configuration as in Fig. 6.8(e).

The electron spectra from the same shock front position as in Fig. 6.6 are shown in Fig. 6.7, which are highly reproducible and monoenergetic compared to Fig. 6.4. The peak energy was adjustable by changing the blade position. Since injection was highly localized at the shock-front position, acceleration length was increased by moving the blade toward the parabolic mirror, and vice versa. The peak energy was between 4-7 MeV in the discussion of this section, and it was possible to extend this range to 3-11 MeV by using different plasma density. The average spectra from different blade positions are shown in Fig. 6.8. The spectra remained monoenergetic in all blade positions with FWHM energy width ≈3.4 MeV, and the peak energies were higher for longer acceleration length from Fig. 6.8(a)-(d). In the case of Fig. 6.8(e), which had 26 μm longer acceleration length than Fig. 6.8(d), the peak energies started decreasing because electrons reached the dephasing regime and got decelerated (see section 1.4.3). These results were summarized in Fig. 6.8(f). The measurements also showed that the beam was more probable to experience instability after dephasing. The electron beam profiles of Fig. 6.8(d) and Fig. 6.8(e) are shown in Fig. 6.9. In the case of the acceleration length close to but less than the dephasing length, the profiles were generally well-collimated and reproducible as shown in Fig. 6.9a. In the contrary, as seen in Fig. 6.9b, the beams were often split into multiple bins when electrons reached dephasing.

Since the shock-front injection gave a clear correlation between acceleration length and electron energy (see Fig. 6.8(f)), this feature was used to measure the dephasing length. The results from a more systematic measurement by using different plasma densities are summarized in Fig. 6.10. The details of data analysis are described in Mr. Cardenas' master work [Daniel E. Cardenas, 2014]. The measurement shows a good agreement between the measured dephasing length

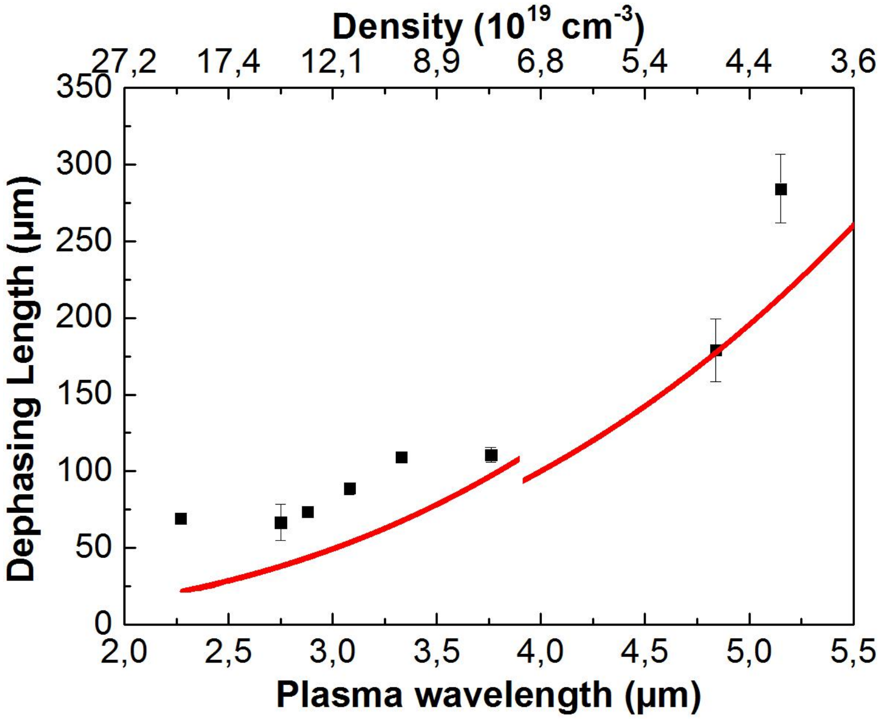

Figure 6.10: Results of the measurement of the dephasing length. (By courtesy of Daniel Cardenas.)

and the one predicted by theory [Gorbunov and Kirsanov, 1987; Esarey et al., 2009]. However, the measured acceleration gradient was around 100-200 GV/m, which is lower than the theoretical value; for example, when $n_p = 10^{19}$ cm^{-3}, linear theory gives a gradient of 303 GV/m which is even higher from the nonlinear theory [Esarey et al., 2009]. One possible explanation is that the plasma electrons were not fully evacuated from the plasma bubble due to the slightly relativistic laser intensities, and therefore the acceleration field was weaker.

6.4 Conclusion

We studied the LWFA driven by sub-2-cycle laser pulses from the LWS-20 laser system. The LWFA was operated in both the self-injection and controlled injection regime by changing gas density and using a shock front. The shock-front injection gave stable and monoenergetic electrons with tunable peak energies between 3 to 11 MeV, and the pointing fluctuation was half of self-injection case. The setup was used to measure the dephasing length which gave a good agreement between the experiment and theory. It has also been shown that electron beams were more susceptible to the beam profile instability after going into the dephasing regime.

Chapter 7

Summary and Outlook

In this work, electron acceleration/deceleration via laser- and electron-driven plasma waves, i.e., laser wakefield acceleration (LWFA) and plasma wakefield acceleration (PWFA) are covered. We study electron acceleration by LWFA using ATLAS and LWS-20 laser systems and investigate the first time PWFA driven by electron bunches from LWFA leading to strong collective deceleration.

The interaction between matter and electron bunches from the conventional rf linear accelerators has been intensively studied in the last decades. However, laser-driven electron sources have significantly different properties such as their ultrashort pulse duration ($\leq$5 fs) [Lundh et al., 2011; Buck et al., 2011], μm scale source size and ultralow emittance [Weingartner et al., 2012]. As these sources have been developed in recent years, the interactions have not been studied comprehensively. In chapter 2, PIC simulations was used to study the interaction of laser-driven electron bunches and plasmas. The results showed that, unlike conventional long electron bunches, the propagation of the ultrashort electron bunches was highly nonlinear and influenced by a strong self-driven wakefield. In the initial state of the propagation, self-modulation and self-focusing dominated and led to strong deceleration. The evolution continues until the structure of the original bunch collapsed since most of the electrons in the bunch were decelerated and scattered away at a significantly reduced energy. This phenomenon has been proposed as a compact beam dump [Wu et al., 2010]. Comparison of these results to experiments is discussed in chapter 5.

One of the major challenges in the field of LWFA is to produce electron bunches with stable properties. We successfully generated reproducible high quality electrons with tunable energies by using the shock-front injection scheme. In this scheme, electrons are injected in a shock front which is generated by inserting a knife edge into a supersonic jet from a supersonic de Laval nozzle. The density of the supersonic jet must be stable, and the transition width of the shock front needs to be smaller than the plasma wavelength which is typically ≈ 20 μm and

$\approx 5\ \mu$m in the case of LWFA driven by 26 fs pulses from the ATLAS system and 4.7 fs pulses from the LWS-20 system respectively under matching condition (see section 1.4.3). In chapter 4, the detailed characterization of the supersonic jets and the transition width of shock fronts is discussed. The absolute density was measured by interferometry. The measurements showed that the shot-to-shot fluctuation of the absolute density was below 0.8%, and the density was linearly proportional to the backing pressure. The structure of the shock front was characterized by Rayleigh scattering. The measurement showed that the transition width of the shock front at a specific height increased with its distance from the blade. The width was thinner than 3 μm in the closest case of the measurable range from the blade. The position as well as the width of the shock front was not influenced by the gas density which was controlled by changing the backing pressure of the nozzle. These results indicate that, in a LWFA experiment with high density, the distance between laser and the blade must be short enough to ensure a small transition width to realize the shock-front injection.

In the discussion of chapter 5, the electron bunches from LWFA driven by ATLAS laser system were used to demonstrate collective deceleration of the electron bunches in plasmas. Two separate experiments were conducted: the double-cell experiment based on self-injection and the double-jet experiment based on the shock-front injection. In both experiments, the electron spectra showed strong modulation and energy loss after the electron bunches propagated in plasmas created by either the external laser field or electric field of the electron bunches. In the double-jet experiment, a strong energy loss of the electron bunches with a peak deceleration gradient over 14 GV/m (5.1 GV/m in average) was observed after a 2 mm long plasma. The experiment also showed that the modulation depended only on the initial size of the electron bunches at the second jet but not the plasma densities. This high deceleration gradient was far above the energy loss rate of collisional ionization and any known radiative processes, and it was only possible to be explained by a collective deceleration in the self-driven wakefield. A series of PIC simulations were conducted to verify our results. Both spectral structure and energy loss as well as charge loss showed a good agreement between experimental results and simulations.

In the end of this work, the sub-2 cycle pulses from the LWS-20 light source were used to drive LWFA in both the self-injection and the shock-front injection regime. The electron spectra from the self-injection showed high shot-to-shot fluctuations. The beam profiles were also highly unstable, and three types of profiles appeared with approximately the same probability: a well-collimated beam, multiple bins, and a highly divergent beam. In contrary, the shock-front injection gave stable and monoenergetic electrons, also the pointing fluctuation was half of the self-injection case. The electron energies were tunable by changing the blade position to vary the acceleration length which gave peak energies between 3 and 11 MeV and total charge of 1-3 pC. We also observed that electron beams were more susceptible to the beam profile instability after entering the dephasing regime and showed profiles with multiple bins which were similar to what was observed in the case of self-injection. This stable and tunable electron source was used to measure the dephasing length which was 50-100 μm and agreed with theory.

These results pave several possible directions for future research:

LWFA electrons driving PWFA

First of all, our observation of a strong deceleration not only proves the feasibility of plasma as a compact beam dump for the upcoming several GeV scale LWFA electron sources but also indicates an effective wakefield driven by the ultrashort electron bunch. One of the main challenges in the research of PWFA is the generation of a meter-scaled preformed plasma channel [Green et al., 2014], which is necessary for a long driver and correspondingly low plasma density ($\approx 10^{16}$ cm^{-3}). The synchronization between the plasma channel and input electron beam becomes very important. The other factor which influences the performance of PWFA is the hosing instability. Several methods including using shaped or pre-modulated beams have been proposed to suppress this instability [Vieira, 2014; Vieira et al., 2014]. It is possible to overcome these issues by using ultrashort bunches from LWFA as a driver for PWFA. Due to the matching condition ($k_p\sigma_x$=1, see section 1.1.1), ultrashort bunches excite large amplitude wakefields in much higher density plasmas ($> 10^{19}$ cm^{-3} for σ_x $\leq$4.5 fs) corresponding to much higher electro-static fields, and this accordingly shortens the length scale of PWFA. It is also possible to utilize this property as a table-top test bench for studying the physics of PWFA driven by the large scale linear accelerator. On the other hand, simulations show that the hosing instability is significantly reduced by using unmatched ultra-short electron drivers, i.e. $k_p\sigma_x < 1$, when the ion channel is created non-adiabatically [Huang et al., 2007]. This implies that the PWFA experiment benefits from using the naturally ultrashort electron bunch from the LWFA as driver. Moreover, the residual energy of laser after driving LWFA is sufficient to create an intrinsically synchronized cm-scale plasma channel. Due to limitations of currently achievable charge and energy of the LWFA electron bunches, it is unlikely to reach 100 GeV gain using these drivers in a meter long plasma channel. However, it is possible to use PWFA as an “afterburner” after the depletion of the laser pulse in LWFA. The transition from LWFA to PWFA has been observed to post accelerate electrons from 400 MeV to 1 GeV in the cut-off energy [Masson-Laborde et al., 2014]. To improve the electron quality, a monoenergetic energy doubling is proposed by using two LWFA electron bunches separated by λ_p, similar to the large experiment in SLAC [Litos et al., 2014], where the first bunch with higher charge drives a wakefield to accelerate a low charge witness bunch behind it [Hidding et al., 2010].

Ultrafast electron diffraction

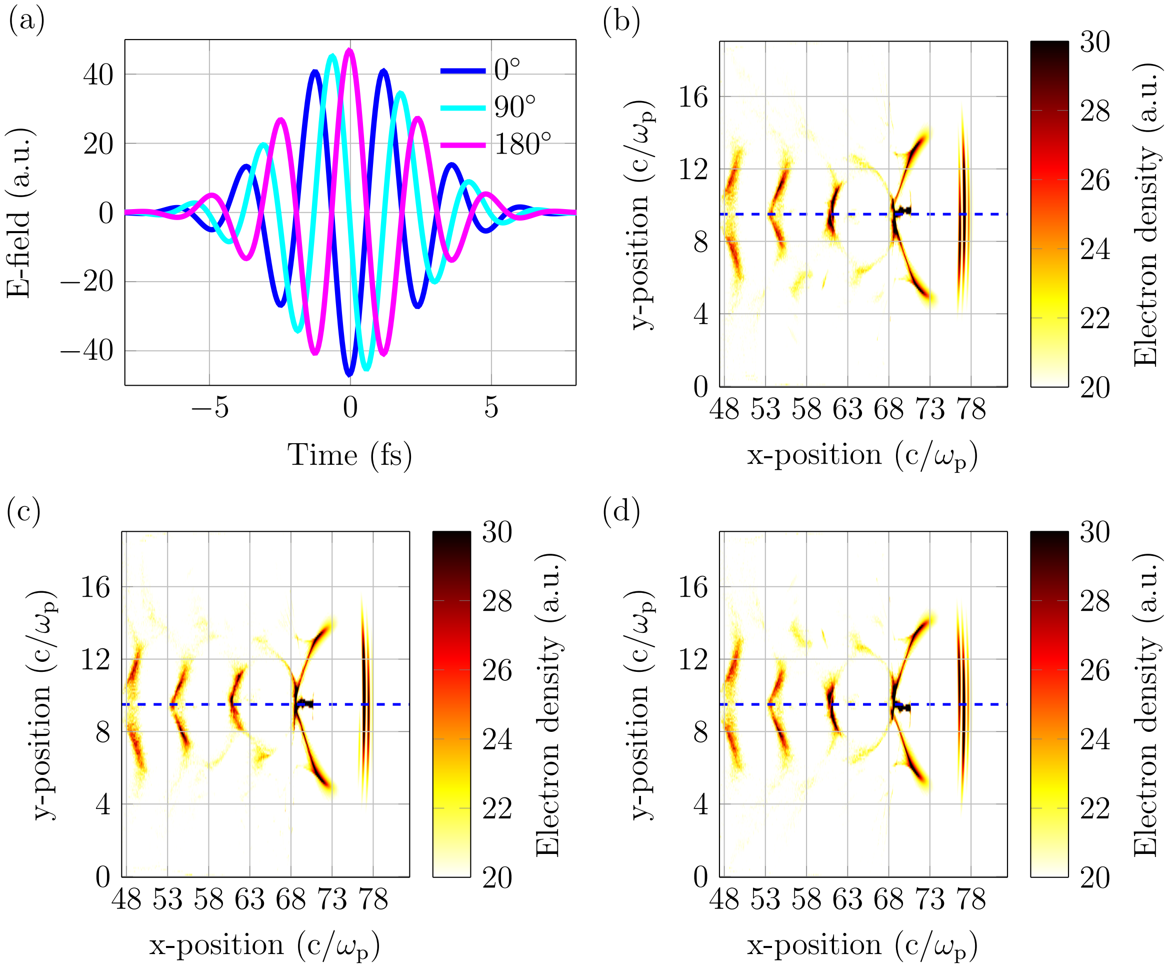

Figure 7.1: CEP-dependent wakefield driven by few-cycle pulse with three different initial CEP. (a) shows the transverse fields of laser pulses with three different CEP before interacting with plasma. (b)-(d) show the electron density of the wakefield after 35 μm propagation of the pulses in plasma. The initial CEP of the driver is (a) 0°, (b) 90°and (c) 180°. The color bar is set to be saturated in order to make the wakefield more visible. The blue dashed line marks the propagation axis of laser pulse. The laser pulses locate at x≈77, and the end of the first plasma period is at x≈68 where the electrons sit around the propagation axis and between x=69 and 70 are the self-injected electrons.

Dynamics of atomic motion defines characteristics of chemical reactions as well as phase transition. In condensed matter, the characteristic timescale of the lattice vibration and structure rearrangement is on the order of 10s to 100s fs [Srinivasan, 2005; Baum et al., 2007; Sciaini and Miller, 2011]. As a consequence, light pulses or particle bunches with sub-10 fs time duration are required for investigating the ultrafast dynamics through time-resolved structural analysis. Ultrafast electron diffraction (UED) is one of the most important tools for studies of molecular and phase transition. In conventional pump-probe UED experiments, electron bunches of 30 or 100 keV with 10s fs temporal duration are used as probes, and subjects are pumped by external laser pulses [Gliserin et al., 2015]. Due to space-charge interactions between electrons and energy dispersion, only very few down to single electrons are contained within each bunch to prevent temporal broadening, and millions of shots are required to collect enough signals for each pump-probe image. Alternatively, MeV electron bunches from a linear accelerator are proposed for UED experiments [Hastings et al., 2006; Li et al., 2009]. Since the electron-electron space charge interaction is much weaker for relativistic electron probe beams, MeV electron bunches are able to carry charges of several pC, which is sufficient for single-shot measurement. However, linear accelerators use photocathode rf guns to inject electrons which give a pulse length of 100s fs or longer and correspondingly limit time resolution. On the contrary, the sub-10 MeV electron bunches from LWFA driven by sub-2 cycle laser pulses have an ultra-short pulse length ($\leq$5 fs) and several pC in total charge, which are ideal for single-shot UED. Moreover, since the electron bunches are naturally synchronized to the laser pulses driving LWFA, the same laser pulses can be used directly as the pump pulse for the pump-probe experiment without any temporal jitter between electrons and laser.

CEP-dependent physics in LWFA

Beside the applications of LWFA electrons, the phased-tagged, sub-2 cycle laser pulses from LWS-20 offer an opportunity to study plasma phenomena correlated to the carrier-envelope phase of the driving pulses. Such effects have never been demonstrated experimentally so far. The classical model of the laser and plasma channel hosing instability in LWFA is based on the ponderomotive approximation which considers only average driving force from the laser field. This approximation breaks down in the case of LWFA driven by few-cycle laser pulses, where the plasma electrons are kicked asymmetrically in the polarization plane and the asymmetry depends on CEP. Since the CEP of the driving pulse varies continuously due to the plasma dispersion and nonlinear effects, the wakefield oscillates even when the laser hosing is absent [Nerush and Kostyukov, 2009].

One example of such oscillation is demonstrated by our 3D simulations as shown in Fig. 7.1, where pulses with three different initial CEP are assumed. The initial parameters of the pulses are: 4.7 fs pulse length at FWHM, $a_0 = 6.7$ in focus, FWHM focus size 2 μm and with total energy 25 mJ, which corresponds to tightly focused pulses from the LWS-20 system. The plasma density is 4×10^{19} cm^{-3} which gives $\lambda_p = 5.3$ μm. It is observed that the transverse positions of the injected electrons clearly depend on the initial CEP, and the shapes of the first and the second period of the 3D plasma wave also show visible difference between different CEP. This phenomenon is expected to be measurable by imaging the shadowgraph of the plasma channel with high resolution optics.

Publications by the author

- R.Weingartner, M. Fuchs, A. Popp, S. Raith, S. Becker, ***S. Chou***, M. Heigoldt, K. Khrennikov, J. Wenz, T. Seggebrock, B. Zeitler, Zs. Major, J. Osterhoff, F. Krausz, S. Karsch, and F. Grüner. **Imaging laser-wakefield-accelerated electrons using miniature magnetic quadrupole lenses** *Phys. Rev. ST Accel. Beams*, 14 (2011), 052801.
  - In this work, I designed the gas cell target, gas supply system, and optimization of the alignment procedure of quadrupole lenses.
- R. Weingartner, S. Raith, A. Popp, ***S. Chou***, J. Wenz, K. Khrennikov, M. Heigoldt, A. R. Maier, N. Kajumba, M. Fuchs, B. Zeitler, F. Krausz, S. Karsch, and F. Grüner. **Ultralow emittance electron beams from a laser-wakefield accelerator** *Phys. Rev. ST Accel. Beams*, 15 (2012), 111302.
  - In this work, I designed the gas target, and optimized the optical system of the imaging of scintillating crystal.
- M. Heigoldt, S. I. Bajlekov, A. Popp, K. Khrennikov, J. Wenz, ***S. Chou***, B. Schmidt, S. M. Hooker and S. Karsch. **Temporal evolution of longitudinal bunch profile in a laser wakefield accelerator** *accepted by Phy. Rev. ST Accel. Beams*
  - I took part in the experimental campaign and participated the calibration and the alignment of the THz detectors.
- ***S. Chou***, J. Xu, K. Khrennikov, D. Cardenas, J. Wenz, M. Heigoldt, L. Veisz, and S. Karsch. **Collective deceleration of laser-driven electron bunches** *submitted to Phy. Rev. Lett.*
  - I conducted the major part of the experiment together with other authors, did all the data analysis and simulations, and prepared the manuscript.

- D.E. Cardenas, ***S. Chou***, J. Xu, L. Hofmann, A. Buck, K. Schmid, C.M.S. Sears, D.E. Rivas, B. Shen, and L. Veisz. **Energy limitation of laser-plasma electron accelerators** *submitted to Phy. Rev. Lett.*
    - I built the major part of the experimental setup with the support of other authors, participated in the experimental campaign, and assisted the preparation of the manuscript.
- E. Guillaume, A. Döpp, C. Thaury, K. Ta Phuoc, A. Lifschitz, G. Grittani, J-P. Goddet, A. Tafzi, ***S.W. Chou***, L. Veisz, and V. Malka. **Electron rephasing in Laser-Wakefield Accelerators** *Phy. Rev. Lett.*, 115 (2015), 155002.
    - In this work, I characterized the properties of the gas target, and offered the experience of the operation of the shock-front injection.

Data Archiving

Chapter 1

The files are under folder */ch_introduction*.

Figure 1.1

►**figure file** */non_linear_1D_LWFA-crop*

Figure 1.2

►**figure file** */bubble*

Figure 1.3

►**figure file** */separatrix*

Figure 1.4

►**figure file** */shock_front_injection*

Figure 1.5

►**figure file** */pic_simulation*

Chapter 2

The files are under folder */ch_phy_dec*.

Figure 2.1

►**figure file** */beam_propa*

Figure 2.2

►**figure file** */emittance*

Figure 2.3

►**figure file** */matching_divergence*

Figure 2.4

►**figure file** */beam_evolve*

Figure 2.5

►**figure file**

(a) */spec_000200*
(b) */spec_001100*
(c) */spec_002200*
(d) */spec_003340*
(e) */spec_004420*
(f) */spec_005560*

Figure 2.6

►**figure file** */run118_15mrad_compare*

Figure 2.7

►**figure file** */density_field_overlap*

Figure 2.8

►**figure file** */par_trac_overview*

Figure 2.9

►**figure file** */par_mid_v1*

Figure 2.10

►**figure file** */field_mid*

Figure 2.11

►**figure file** */par_acc_max*

Figure 2.12

►**figure file**

(a) */v_p_denote*
(b) */v_p_eve*

Figure 2.13

►**figure file** */e1_evolve*

Figure 2.14

►**figure file** */energy_time_run218*

Chapter 3

The files are under folder */ch_experiment_facility*.

Figure 3.1

►**figure file** */CPA*

Figure 3.2

►**figure file** */atlas_v2*

Figure 3.3

►**figure file** */lws20*

Figure 3.4

►**figure file** */lws20_spectrum*

Figure 3.5

►**figure file** */lws20_ac*

Figure 3.6

►**figure file** */pointing_lanex_v2*

Figure 3.7

►**figure file** */spectrometer*

Figure 3.8

►**figure file** */test_dispersion*

Figure 3.9

►**figure file** */small_spectrometer*

Figure 3.10

►**figure file** */small_magnet*

Chapter 4

The files are under folder */ch_rayleigh*.

Figure 4.1

►**figure file** */modified_gascell*

Figure 4.2

►**figure file**

(a) */gas_cell_density*
(b) */gas_cell_velocity_stream*

Figure 4.3

►**figure file** */nozzle*

Figure 4.4

►**figure file** */hagena*

Figure 4.5

►**figure file** */nozzle_v3*

Figure 4.6

►**figure file** */interferometry_setup*

Figure 4.7

►**figure file** */abel*

Figure 4.8

►**figure file**

- (a) */interfero_phase*
- (b) */interfero_density*

Figure 4.9

►**figure file**

- (a) */density_comparison_std*
- (b) */density_comparison_pressure*

Figure 4.10

►**figure file** */rayleigh_setup*

Figure 4.11

►**figure file**

- (a) */thesis_counts_calibration*
- (b) */modi_thesis_peak_counts*

Figure 4.12

►**figure file** */all_single_shots*

Figure 4.13

►**figure file** */blade_scan_lineout*

Figure 4.14

►**figure file**

- (a) */fft_example_win_1_6691j_2_line_167*
- (b) */fft_example_win_0_5341j_2_line_167*
- (c) */fft_example_win_0_20029j_2_line_167*
- (d) */fft_example_win_0_10014j_2_line_167*

Figure 4.15

►**figure file** */fft_criteria*

Figure 4.16

►**figure file**

- (a) */blade_j_2_line_165*
- (b) */blade_j_2_line_155*

Figure 4.17

►**figure file** */flip_start_and_end*

Figure 4.18

►**figure file**

- (a) */ray_height_scan_width*
- (b) */ray_height_scan_jump*

Figure 4.19

►**figure file** */ray_blade_scan_width*

Figure 4.20

►**figure file**

- (a) */ray_pre_scan_pos*
- (b) */ray_pre_scan_width*

Chapter 5

The files are under folder */ch_deceleration*.

Figure 5.1

►**figure file** */analyse_spectra-length-scan*

Figure 5.2

►**figure file** */analyse_spectra-p-scan*

Figure 5.3

►**figure file**

(a) */dual_nozzle_pic_v2*
(b) */setup_v4*

Figure 5.4

►**figure file** */focus_test*

Figure 5.5

►**figure file**

(a) */spectrum/run1026_shot445*
(b) */spectrum/run1027_shot30*

Figure 5.6

►**figure file**

(a) */spectrum/run1031_shot296*
(b) */spectrum/run1031_shot246*
(c) */spectrum/run1031_shot202*
(d) */spectrum/run1031_shot171*
(e) */spectrum/run1031_shot137*
(f) */spectrum/run1031_shot101*
(g) */spectrum/run1031_shot69*
(h) */spectrum/run1031_shot34*

Figure 5.7

►**figure file**

(a) */ref_v1*
(b) */rcf_v1*

Figure 5.8

►**figure file** */div_v1*

Figure 5.9

►**figure file** */double_gas_cell_v3*

Figure 5.10

►**figure file**

(a) */rayleigh/ray_posi1*
(b) */rayleigh/ray_posi2*
(c) */rayleigh/ray_posi3*
(d) */rayleigh/ray_posi4*

Figure 5.11

►**figure file** */self_focusing_3*

Figure 5.12

►**figure file** */wake_ratio*

Figure 5.13

►**figure file**

(a) */exp_spec*
(b) */simu_spec_div*

Chapter 6

The files are under folder */ch_lws20_electron.*

Figure 6.1

►**figure file** */lws20_setup_v3*

Figure 6.2

►**figure file**

(a) */run2045_shot_17*
(b) */run2045_shot_108*
(c) */run2045_shot_10*
(d) */run2045_shot_342*
(e) */run2045_shot_135*
(f) */run2045_shot_121*

Figure 6.3

►**figure file** */run2045_pointing*

Figure 6.4

►**figure file**

(a) */run2066_spec_all_shot*
(b) */run2066_spec_avg*

Figure 6.5

►**figure file**

(a) */run2236_shot_22*
(b) */run2236_shot_27*
(c) */run2236_shot_251*
(d) */run2236_shot_258*

Figure 6.6

►**figure file** */run2236_pointing*

Figure 6.7

►**figure file** */run2234_spec_all_shot*

Figure 6.8

►**figure file**

(a) */run2237_spec_avg*
(b) */run2234_spec_avg*
(c) */run2240_spec_avg*
(d) */run2251_spec_avg*
(e) */run2258_spec_avg*
(f) */acc_ene*

Figure 6.9

►**figure file**

(a) */run2252*
(b) */run2262*

Figure 6.10

►**figure file** */dephasing/deph_length*

Chapter 7

The files are under folder */ch_outlook.*

Figure 7.1

►**figure file**

(a) */x2_t10*
(b) */x2x1_4001*
(c) */x2x1_4002*
(d) */x2x1_4003*

Bibliography

A. Bideau-Mehu, Y. Guern, R. Abjean, A. J.-G. (1981). Measurement of refractive indices of neon, argon, krypton and xenon in the 253.7140.4 nm wavelength range. Dispersion relations and estimated oscillator strengths. *J. Quant. Spectrosc. Radiat. Transf.*, 25(5):395–402.

Adli, E., Corde, S., England, R., and Frederico, J. (2012). FIRST RESULTS FROM THE ELECTRON HOSE INSTABILITY STUDIES IN FACET. *SLAC-PUB-15802*.

Alexander Wu Chao and Tigner, M. (2013). *Handbook of accelerator physics and engineering*. World Scientific Publishing Co. Pte. Ltd, Singapore, second edition.

Alsmeyer, H. (1976). Density profiles in argon and nitrogen shock waves measured by the absorption of an electron beam. *J. Fluid Mech.*, 74(03):497.

Amaldi, U. and Kraft, G. (2005). Radiotherapy with beams of carbon ions. *Reports Prog. Phys.*, 68(8):1861–1882.

Amiranoff, F., Baton, S., Bernard, D., Cros, B., Descamps, D., Dorchies, F., Jacquet, F., Malka, V., Marquès, J., Matthieussent, G., Miné, P., Modena, a., Mora, P., Morillo, J., and Najmudin, Z. (1998). Observation of Laser Wakefield Acceleration of Electrons. *Phys. Rev. Lett.*, 81(5):995–998.

Apolonski, A., Poppe, A., Tempea, G., Spielmann, C., Udem, T., Holzwarth, R., Hänsch, T. W., and Krausz, F. (2000). Controlling the phase evolution of few-cycle light pulses. *Phys. Rev. Lett.*, 85(4):740–743.

Asaki, M. T., Huang, C. P., Garvey, D., Zhou, J., Kapteyn, H. C., and Murnane, M. M. (1993). Generation of 11-fs pulses from a self-mode-locked Ti:sapphire laser. *Opt. Lett.*, 18(12):977–979.

Azechi, H. and Project, F. (2008). The FIREX program on the way to inertial fusion energy. *J. Phys. Conf. Ser.*, 112(1):012002.

Bajlekov, S. I., Heigoldt, M., Popp, A., Wenz, J., Khrennikov, K., Karsch, S., and Hooker, S. M. (2013). Longitudinal electron bunch profile reconstruction by performing phase retrieval on coherent transition radiation spectra. *Phys. Rev. Spec. Top. - Accel. Beams*, 16(4):040701.

Barnett, R. M., Carone, C. D., Groom, D. E., Trippe, T. G., Wohl, C. G., Armstrong, B., Gee, P. S., Wagman, G. S., James, F., Mangano, M., Mönig, K., Montanet, L., Feng, J. L., Murayama, H., Hernández, J. J., Manohar, A., Aguilar-Benitez, M., Caso, C., Crawford, R. L., Roos, M., Törnqvist, N. A., Hayes, K. G., Hagiwara, K., Nakamura, K., Tanabashi, M., Olive, K., Honscheid, K., Burchat, P. R., Shrock, R. E., Eidelman, S., Schindler, R. H., Gurtu, A., Hikasa, K., Conforto, G., Workman, R. L., Grab, C., and Amsler, C. (1996). Review of Particle Physics. *Phys. Rev. D*, 54(1):1–708.

Barov, N., Bishofberger, K., Rosenzweig, J. B., Angeles, L., Carneiro, J. P., Colestock, P., Edwards, H., Fitch, M. J., Hartung, W., and Santucci, J. (2001). Ultra high-gradient energy loss by a pulsed electron beam in a plasma. *Proc. 2001 Part. Accel. Conf.*, 90095(1):126–128.

Barov, N. and Rosenzweig, J. (1994). Propagation of short electron pulses in underdense plasmas. *Phys. Rev. E*, 49(5).

Barov, N., Rosenzweig, J., Conde, M., Gai, W., and Power, J. (2000). Observation of plasma wakefield acceleration in the underdense regime. *Phys. Rev. Spec. Top. - Accel. Beams*, 3(1):011301.

Batchelor, G. K. (2000). *An introduction to fluid dynamics.* Cambridge university press.

Baum, P., Yang, D.-S., and Zewail, A. H. (2007). 4D Visualization of Transitional Structures in Phase Transformations by Electron Diffraction. *Science (80-.).*, 318(5851):788–792.

Beaurepaire, B., Lifschitz, A., and Faure, J. (2014). Electron acceleration in sub-relativistic wakefields driven by few-cycle laser pulses. *New J. Phys.*, 023023(2):023023.

Becker, E. W., Bier, K., and Henkes, W. (1956). Strahlen aus kondensierten Atomen und Molekeln im Hochvakuum. *Zeitschrift für Phys.*, 146(3):333–338.

Becker, R. (1922). Stoßwelle und Detonation. *Zeitschrift für Phys.*, 8(1):321–362.

Bell, a. J., Mestdagh, J. M., Berlande, J., Biquard, X., Cuvellier, J., Lallement, A., Meynadier, P., Sublemontier, O., and Visticot, J. P. (1993). Mean cluster size by Rayleigh scattering. *J. Phys. D. Appl. Phys.*, 26(6):994–996.

Bennett, S. (1993). Development of the PID controller. *Control Syst. IEEE*, 13(6):58–62.

Bennett, W. H. (1934). Magnetically self-focussing streams. *Phys. Rev.*, 45(12):890–897.

Berenger, J.-P. (1994). A perfectly matched layer for the absorption of electromagnetic waves. *J. Comput. Phys.*, 114(2):185–200.

Berezhiani, V. and Murusidze, I. G. (1990). Relativistic wake-field generation by an intense laser pulse in a plasma. *Phys. Lett. A*, 148(6):338–340.

Bharadwaj, V. K., Bane, K., Clendenin, J., Emma, P., Sheppard, J. C., Woodley, M. D., Bharadwaj, V. K., Bane, K., Clendenin, J., Emma, P., Sheppard, J. C., Woodley, M. D., and Linear, S. (1997). Linac Design for the LCLS Project at SLAC. *SLACPUB7555*, (May).

Biberman, L. M., Mnatsakanyan, A. K., and Yakubov, I. T. (1971). IONIZATION RELAXATION BEHIND STRONG SHOCK WAVES IN GASES. *Sov. Phys. Uspekhi*, 13(6):728–744.

Bloch, F. (1933). Zur bremsung rasch bewegter teilchen beim durchgang durch materie. *Ann. Phys.*, 408(3):285–320.

Blumenfeld, I., Clayton, C. E., Decker, F.-J., Hogan, M. J., Huang, C., Ischebeck, R., Iverson, R., Joshi, C., Katsouleas, T., Kirby, N., Lu, W., Marsh, K. a., Mori, W. B., Muggli, P., Oz, E., Siemann, R. H., Walz, D., and Zhou, M. (2007). Energy doubling of 42 GeV electrons in a metre-scale plasma wakefield accelerator. *Nature*, 445(7129):741–4.

Blumenfeld, I., Clayton, C. E., Decker, F. J., Hogan, M. J., Huang, C., Ischebeck, R., Iverson, R. H., Joshi, C., Katsouleas, T., Kirby, N., Lu, W., Marsh, K. a., Mori, W. B., Muggli, P., Oz, E., Siemann, R. H., Walz, D. R., and Zhou, M. (2010). Scaling of the longitudinal electric field and transformer ratio in a nonlinear plasma wakefield accelerator. *Phys. Rev. Spec. Top. - Accel. Beams*, 13(11):111301.

Boyd, T. J. M. and Sanderson, J. J. (2003). *The Physics of Plasmas*. Cambridge University Press, Cambridge.

Brabec, T., Spielmann, C., Curley, P. F., and Krausz, F. (1992). Kerr lens mode locking. *Opt. Lett.*, 17(18):1292–1294.

Brantov, A. V., Esirkepov, T. Z., Kando, M., Kotaki, H., Bychenkov, V. Y., and Bulanov, S. V. (2008). Controlled electron injection into the wake wave using plasma density inhomogeneity. *Phys. Plasmas*, 15(7):073111.

Bromage, J., Millecchia, M., Bunkenburg, J., Jungquist, R. K., Dorrer, C., and Zuegel, J. D. (2012). A cylindrical Öffner stretcher for reduced chromatic aberrations and improved temporal contrast. In *Lasers Electro-Optics (CLEO), 2012 Conf.*, pages 1–2.

Brunetti, E., Shanks, R. P., Manahan, G. G., Islam, M. R., Ersfeld, B., Anania, M. P., Cipiccia, S., Issac, R. C., Raj, G., Vieux, G., Welsh, G. H., Wiggins, S. M., and Jaroszynski, D. a. (2010). Low Emittance, High Brilliance Relativistic Electron Beams from a Laser-Plasma Accelerator. *Phys. Rev. Lett.*, 105(21):215007.

Buchanan, H. L. (1987). Electron beam propagation in the ion-focused regime. *Phys. Fluids*, 30(1):221.

Büchner, J., Dum, C., and Scholer, M. (2003). *Space plasma simulation*, volume 615. Springer Science & Business Media.

Buck, A. (2011). *Advanced characterization and control of laser wakefield acceleration.* PhD thesis, Ludwig-Maximilians-Universität in München.

Buck, A., Nicolai, M., Schmid, K., Sears, C. M. S., Sävert, A., Mikhailova, J. M., Krausz, F., Kaluza, M. C., and Veisz, L. (2011). Real-time observation of laser-driven electron acceleration. *Nat. Phys.*, 7(7):543–548.

Buck, A., Wenz, J., Xu, J., Khrennikov, K., Schmid, K., Heigoldt, M., Mikhailova, J. M., Geissler, M., Shen, B., Krausz, F., Karsch, S., and Veisz, L. (2013). Shock-Front Injector for High-Quality Laser-Plasma Acceleration. *Phys. Rev. Lett.*, 110(18):185006.

Buck, A., Zeil, K., Popp, A., Schmid, K., Jochmann, A., Kraft, S. D., Hidding, B., Kudyakov, T., Sears, C. M. S., Veisz, L., Karsch, S., Pawelke, J., Sauerbrey, R., Cowan, T., Krausz, F., and Schramm, U. (2010). Absolute charge calibration of scintillating screens for relativistic electron detection. *Rev. Sci. Instrum.*, 81(3):033301.

Buck, U. and Krohne, R. (1996). Cluster size determination from diffractive He atom scattering. *J. Chem. Phys.*, 105(13):5408.

Buck, U., Meyer, H., and Pauly, H. (1985). Clusterformation in supersonic nozzle beams. *Flow Real Fluids.*

Bulanov, S., Naumova, N., Pegoraro, F., and Sakai, J. (1998). Particle injection into the wave acceleration phase due to nonlinear wake wave breaking. *Phys. Rev. E*, 58(5):R5257–R5260.

Bulanov, S. V., Pegoraro, F., Pukhov, A. M., and Sakharov, A. S. (1997). Transverse-Wake Wave Breaking. *Phys. Rev. Lett.*, 78(22):4205–4208.

Burtsev, V. A. and Kalinin, N. V. (2007). Recombination-nonequilibrium plasma in low-inductance discharge. *Tech. Phys. Lett.*, 33(2):139–142.

Bush, A. M., Bell, A. J., and Frey, J. G. (1998). Rayleigh Scattering of Laser and Synchrotron Radiation from Pulsed Free Jets of Ar. *J. Phys. Chem. A*, 102(3):6457–6463.

Caldwell, A., Lotov, K., Pukhov, A., and Simon, F. (2009). Proton-driven plasma-wakefield acceleration. *Nat. Phys.*, 5(5):363–367.

Chen, L. M., Kotaki, H., Nakajima, K., Koga, J., Bulanov, S. V., Tajima, T., Gu, Y. Q., Peng, H. S., Wang, X. X., Wen, T. S., Liu, H. J., Jiao, C. Y., Zhang, C. G., Huang, X. J., Guo, Y., Zhou, K. N., Hua, J. F., An, W. M., Tang, C. X., and Lin, Y. Z. (2007). Self-guiding of 100TW femtosecond laser pulses in centimeter-scale underdense plasma. *Phys. Plasmas*, 14(4):040703.

Chen, M., Cormier-Michel, E., Geddes, C., Bruhwiler, D., Yu, L., Esarey, E., Schroeder, C., and Leemans, W. (2013). Numerical modeling of laser tunneling ionization in explicit particle-in-cell codes. *J. Comput. Phys.*, 236:220–228.

Chen, P. (1987). A possible final focusing mechanism for linear colliders. *Part. Accel.*, 20:171.

Chen, P., Dawson, J., Huff, R., and Katsouleas, T. (1985). Acceleration of electrons by the interaction of a bunched electron beam with a plasma. *Phys. Rev. Lett.*, 54(7):693–696.

Clayton, C., Ralph, J., Albert, F., Fonseca, R., Glenzer, S., Joshi, C., Lu, W., Marsh, K., Martins, S., Mori, W., Pak, a., Tsung, F., Pollock, B., Ross, J., Silva, L., and Froula, D. (2010). Self-Guided Laser Wakefield Acceleration beyond 1GeV Using Ionization-Induced Injection. *Phys. Rev. Lett.*, 105(10):3–6.

Clayton, C. E., Marsh, K. A., Dyson, A., Everett, M., Lal, A., Leemans, W. P., Williams, R., and Joshi, C. (1993). Ultrahigh-Gradient Acceleration of Injected Electrons By Laser-Excited Relativistic Electron-Plasma Waves. *Phys. Rev. Lett.*, 70(1):37–40.

CMS Collaboration (2012). Observation of a new boson at a mass of 125 GeV with the CMS experiment at the LHC. *Phys. Lett. Sect. B Nucl. Elem. Part. High-Energy Phys.*, 716(1):30–61.

CMS Collaboration (2014). Evidence for the direct decay of the 125 GeV Higgs boson to fermions. *Nat. Phys.*, 10(8):557–560.

Collard, H., Hofstadter, R., Hughes, E. B., Johansson, A., Yearian, M. R., Day, R. B., and Wagner, R. T. (1965). Elastic Electron Scattering from Tritium and Helium-3. *Phys. Rev.*, 138(1B):B57—-B65.

Combs, S. E., Jäkel, O., Haberer, T., and Debus, J. (2010). Particle therapy at the Heidelberg Ion Therapy Center (HIT) Integrated research-driven university-hospital-based radiation oncology service in Heidelberg, Germany. *Radiother. Oncol.*, 95(1):41–44.

Corde, S., Thaury, C., Lifschitz, A., Lambert, G., Ta Phuoc, K., Davoine, X., Lehe, R., Douillet, D., Rousse, A., and Malka, V. (2013). Observation of longitudinal and transverse self-injections in laser-plasma accelerators. *Nat. Commun.*, 4:1501.

Couairon, A. and Mysyrowicz, A. (2007). Femtosecond filamentation in transparent media. *Phys. Rep.*, 441(2-4):47–189.

Courant, R., Friedrichs, K., and Lewy, H. (1928). *Über die partiellen Differenzengleichungen der mathematischen Physik*, volume 100. Springer-Verlag.

Cowan, G. R. and Hornig, D. F. (1950). The Experimental Determination of the Thickness of a Shock Front in a Gas. *J. Chem. Phys.*, 18(8):1008.

Cuevas, S. B. (2007). Spectrometer Development for Laser- Driven Electron Acceleration. Master's thesis, Ludwig-Maximilians-Universität in München.

Daniel E. Cardenas (2014). Sub-5-fs laser wakefield acceleration of electrons. Master thesis, Technische Universität München.

Dawson, J. (1959). Nonlinear electron oscillations in a cold plasma. *Phys. Rev.*, 113(2):383.

Dawson, J. and Oberman, C. (1962). HighFrequency Conductivity and the Emission and Absorption Coefficients of a Fully Ionized Plasma. *Phys. Fluids*, 5(5):517.

Deacon, D. A. G., Elias, L. R., Madey, J. M. J., Ramian, G. J., Schwettman, H. A., and Smith, T. I. (1977). First Operation of a Free-Electron Laser. *Phys. Rev. Lett.*, 38(16):892–894.

Debus, A. D., Bussmann, M., Schramm, U., Sauerbrey, R., Murphy, C. D., Major, Z., Hörlein, R., Veisz, L., Schmid, K., Schreiber, J., Witte, K., Jamison, S. P., Gallacher, J. G., Jaroszynski, D. A., Kaluza, M. C., Hidding, B., Kiselev, S., Heathcote, R., Foster, P. S., Neely, D., Divall, E. J., Hooker, C. J., Smith, J. M., Ertel, K., Langley, A. J., Norreys, P., Collier, J. L., and Karsch, S. (2010). Electron bunch length measurements from laser-accelerated electrons using single-shot thz time-domain interferometry. *Phys. Rev. Lett.*, 104(February):1–4.

Decker, C. D. and Mori, W. B. (1994). Group velocity of large amplitude electromagnetic waves in a plasma. *Phys. Rev. Lett.*, 72(4):490–493.

Deng, S., Barnes, C. D., Clayton, C. E., O'Connell, C., Decker, F. J., Fonseca, R. a., Huang, C., Hogan, M. J., Iverson, R., Johnson, D. K., Joshi, C., Katsouleas, T., Krejcik, P., Lu, W., Mori, W. B., Muggli, P., Oz, E., Tsung, F., Walz, D., Zhou, M., and OConnell, C. (2006). Hose Instability and Wake Generation by an Intense Electron Beam in a Self-Ionized Gas. *Phys. Rev. Lett.*, 96(4):045001.

der Linde, D. V., Engers, T., and Jenke, G. (1995). Generation of high-order harmonics from solid surfaces by intense femtosecond laser pulses. *Phys. Rev. A*, 52(1):25–27.

Ditmire, T., Zweiback, J., Yanovsky, V. P., Cowan, T. E., and Hays, G. (1999). Nuclear fusion from explosions of femtosecond laser-heated deuterium clusters. *Nature*, 398:489–492.

Dorchies, F., Blasco, F., Caillaud, T., Stevefelt, J., Stenz, C., Boldarev, A., and Gasilov, V. (2003). Spatial distribution of cluster size and density in supersonic jets as targets for intense laser pulses. *Phys. Rev. A*, 68(2):1–8.

Dou, T. H., Tautz, R., Gu, X., Marcus, G., Feurer, T., Krausz, F., and Veisz, L. (2010). Dispersion control with reflection grisms of an ultra-broadband spectrum approaching a full octave. *Opt. Express*, 18(26):27900–27909.

Duda, B., Hemker, R., Tzeng, K., and Mori, W. (1999). A Long-Wavelength Hosing Instability in Laser-Plasma Interactions. *Phys. Rev. Lett.*, 83(10):1978–1981.

Elder, F. R., Gurewitsch, a. M., Langmuir, R. V., and Pollock, H. C. (1947). Radiation from electrons in a synchrotron. *Phys. Rev.*, 71(11):829–830.

Ell, R., Morgner, U., Kärtner, F. X., Fujimoto, J. G., Ippen, E. P., Scheuer, V., Angelow, G., Tschudi, T., Lederer, M. J., Boiko, A., and Luther-Davies, B. (2001). Generation of 5-fs pulses and octave-spanning spectra directly from a Ti:sapphire laser. *Opt. Lett.*, 26(6):373–375.

Emma, P. and Iverson, R. (2001). Femtosecond electron bunch lengths in the SLAC FFTB beamline. *Proc. 2001 Part. Accel. Conf.*, pages 4038–4040.

England, R. and Ng, C.-K. (2012). High transformer ratio drive beams for wakefield accelerator studies. *AIP Conf. Proc.*, 553(1):553–558.

Esarey, E., Hubbard, R., Leemans, W., Ting, a., and Sprangle, P. (1997a). Electron Injection into Plasma Wakefields by Colliding Laser Pulses. *Phys. Rev. Lett.*, 22(14):2682–2685.

Esarey, E., Schroeder, C., and Leemans, W. (2009). Physics of laser-driven plasma-based electron accelerators. *Rev. Mod. Phys.*, 81(3):1229–1285.

Esarey, E. and Shadwick, B. (2004). Nonlinear pump depletion and electron dephasing in laser wakefield accelerators. *Adv. Accel. Concepts*, 737:578–584.

Esarey, E., Shadwick, B., Catravas, P., and Leemans, W. (2002). Synchrotron radiation from electron beams in plasma-focusing channels. *Phys. Rev. E*, 65(5):056505.

Esarey, E. and Sprangle, P. (1996). Overview of plasma-based accelerator concepts. *Plasma Sci. IEEE Trans.*, 24(2):252.

Esarey, E., Sprangle, P., Krall, J., and Ting, A. (1997b). Self-focusing and guiding of short laser pulses in ionizing gases and plasmas. *IEEE J. Quantum Electron.*, 33(11):1879–1914.

Esirkepov, T., Bulanov, S. V., Yamagiwa, M., and Tajima, T. (2006). Electron, positron, and photon wakefield acceleration: Trapping, wake overtaking, and ponderomotive acceleration. *Phys. Rev. Lett.*, 96(1):014803.

Evans, L. and Bryant, P. (2008). LHC Machine. *J. Instrum.*, 3(8):S08001.

Faure, J., Glinec, Y., Pukhov, A., and Kiselev, S. (2004). A laserplasma accelerator producing monoenergetic electron beams. *Nature*, 431(7008):541–544.

Faure, J., Glinec, Y., Santos, J., Ewald, F., Rousseau, J.-P., Kiselev, S., Pukhov, a., Hosokai, T., and Malka, V. (2005). Observation of Laser-Pulse Shortening in Nonlinear Plasma Waves. *Phys. Rev. Lett.*, 95(20):1–4.

Faure, J., Malka, V., Marques, J.-R., David, P.-G., Amiranoff, F., Ta Phuoc, K., and Rousse, a. (2002). Effects of pulse duration on self-focusing of ultra-short lasers in underdense plasmas. *Phys. Plasmas*, 9(3):756.

Faure, J., Rechatin, C., Lundh, O., Ammoura, L., and Malka, V. (2010). Injection and acceleration of quasimonoenergetic relativistic electron beams using density gradients at the edges of a plasma channel. *Phys. Plasmas*, 17(8):083107.

Faure, J., Rechatin, C., Norlin, A., Lifschitz, A., Glinec, Y., and Malka, V. (2006). Controlled injection and acceleration of electrons in plasma wakefields by colliding laser pulses. *Nature*, 444(7120):737–9.

Fermi, E. (1924). Über die Theorie des Stoßes zwischen Atomen und elektrisch geladenen Teilchen. *Zeitschrift für Phys.*, 29(1):315–327.

Fonseca, R. A., Silva, L. O., Tsung, F. S., Decyk, V. K., Lu, W., Ren, C., Mori, W. B., Deng, S., Lee, S., Katsouleas, T., and Adam, J. C. (2002). OSIRIS: A Three-Dimensional, Fully Relativistic Particle in Cell Code for Modeling Plasma Based Accelerators. In Sloot, P., Hoekstra, A., Tan, C., and Dongarra, J., editors, *Comput. Sci. ICCS 2002*, volume 2331 of *Lecture Notes in Computer Science*, pages 342–351. Springer Berlin Heidelberg.

Fubiani, G., Esarey, E., Schroeder, C. B., and Leemans, W. P. (2004). Beat wave injection of electrons into plasma waves using two interfering laser pulses. *Phys. Rev. E*, 70(1):016402.

Fuchs, M., Weingartner, R., Popp, A., Major, Z., Becker, S., Osterhoff, J., Cortrie, I., Zeitler, B., Hörlein, R., Tsakiris, G. D., Schramm, U., Rowlands-Rees, T. P., Hooker, S. M., Habs, D., Krausz, F., Karsch, S., and Grüner, F. (2009). Laser-driven soft-X-ray undulator source. *Nat. Phys.*, 5(11):826–829.

Gahn, C., Tsakiris, G., Pukhov, a., Meyer-ter Vehn, J., Pretzler, G., Thirolf, P., Habs, D., and Witte, K. (1999). Multi-MeV Electron Beam Generation by Direct Laser Acceleration in High-Density Plasma Channels. *Phys. Rev. Lett.*, 83(23):4772–4775.

Gahn, C., Tsakiris, G. D., Witte, K. J., Thirolf, P., and Habs, D. (2000). A novel 45-channel electron spectrometer for high intensity laser-plasma interaction studies. *Rev. Sci. Instrum.*, 71(4):1642.

Geddes, C., Nakamura, K., Plateau, G., Toth, C., Cormier-Michel, E., Esarey, E., Schroeder, C., Cary, J., and Leemans, W. (2008). Plasma-Density-Gradient Injection of Low Absolute-Momentum-Spread Electron Bunches. *Phys. Rev. Lett.*, 100(21):1–4.

Geddes, C., Toth, C., and Tilborg, J. V. (2004). High-quality electron beams from a laser wakefield accelerator using plasma-channel guiding. *Nature*, 431(7008):538–541.

Gibbon, P. (2005). *Short Pulse Laser Interactions with Matter: An Introduction.* Imperial College Press, London.

Giudice, G. F. (2012). Big Science and the Large Hadron Collider. *Phys. Perspect.*, 14(1):95–112.

Glinec, Y., Faure, J., Norlin, A., Pukhov, A., and Malka, V. (2007). Observation of Fine Structures in Laser-Driven Electron Beams Using Coherent Transition Radiation. *Phys. Rev. Lett.*, 98(19):194801.

Gliserin, A., Walbran, M., Krausz, F., and Baum, P. (2015). Sub-phonon-period compression of electron pulses for atomic diffraction. *Nat. Commun.*, 6(May):8723.

Goncharov, A. (2013). Invited review article: The electrostatic plasma lens. *Rev. Sci. Instrum.*, 84(2).

Goncharov, A., Dobrovolskiy, A., Litovko, I., Gushenets, V., and Oks, E. (2014). Focusing intense electron beams by positive space charge cloud plasma lens. *Phys. Scr.*, T161(014070).

Gorbunov, L. and Kirsanov, V. (1987). Excitation of plasma waves by an electromagnetic wave packet. *Sov. Phys. JETP*, 66(2):290–294.

Gorbunov, L. M., Kalmykov, S. Y., and Mora, P. (2005). Laser wakefield acceleration by petawatt ultrashort laser pulses. *Phys. Plasmas*, 12(3):033101.

Gordienko, S. and Pukhov, a. (2005). Scalings for ultrarelativistic laser plasmas and quasimonoenergetic electrons. *Phys. Plasmas*, 12(4):043109.

Gordon, D., Hafizi, B., Hubbard, R., Peñano, J., Sprangle, P., and Ting, A. (2003). Asymmetric Self-Phase Modulation and Compression of Short Laser Pulses in Plasma Channels. *Phys. Rev. Lett.*, 90(21):215001.

Grabenhofer, A., Palm, A., Barov, N., Eaton, D., and Shin, Y. (2014). Development of a ultra-short pulse electron beam source for advanced accelerator/radiation source research at Northern Illinois University. *Vac. Electron. Conf. IEEE Int.*, pages 533–534.

Green, S. Z., Adli, E., Clarke, C. I., Corde, S., Edstrom, S. A., Fisher, A. S., Frederico, J., Frisch, J. C., Gessner, S., Gilevich, S., Hering, P., Hogan, M. J., Jobe, R. K., Litos, M., May, J. E., Walz, D. R., Yakimenko, V., Clayton, C. E., Joshi, C., Marsh, K. a., Vafaei-Najafabadi, N., and Muggli, P. (2014). Laser ionized preformed plasma at FACET. *Plasma Phys. Control. Fusion*, 56(8):084011.

Greene, E. F., Cowan, G. R., and Hornig, D. F. (1951). The Thickness of Shock Fronts in Argon and Nitrogen and Rotational Heat Capacity Lags. *J. Chem. Phys.*, 19(4):427.

Hafz, N. a. M., Jeong, T. M., Choi, I. W., Lee, S. K., Pae, K. H., Kulagin, V. V., Sung, J. H., Yu, T. J., Hong, K.-H., Hosokai, T., Cary, J. R., Ko, D.-K., and Lee, J. (2008). Stable generation of GeV-class electron beams from self-guided laserplasma channels. *Nat. Photonics*, 2(9):571–577.

Hagena, O. F. (1974). Scaling laws for condensation in nozzle flows. *Phys. Fluids*, 17(5):894.

Hagena, O. F. (1987). Condensation in free jets: Comparison of rare gases and metals. *Zeitschrift für Phys. D Atoms, Mol. Clust.*, 4(3):291–299.

Hagena, O. F. (1992). Cluster ion sources (invited). *Rev. Sci. Instrum.*, 63(4):2374.

Hagena, O. F. and Obert, W. (1972). Cluster Formation in Expanding Supersonic Jets: Effect of Pressure, Temperature, Nozzle Size, and Test Gas. *J. Chem. Phys.*, 56(5):1793.

Hansen, K. and Hornig, D. F. (1960). Thickness of Shock Fronts in Argon. *J. Chem. Phys.*, 33(3):913.

Hansson, M., Aurand, B., Davoine, X., Ekerfelt, H., Svensson, K., Persson, a., Wahlström, C.-G., and Lundh, O. (2015). Down-ramp injection and independently controlled acceleration of electrons in a tailored laser wakefield accelerator. *Phys. Rev. Spec. Top. - Accel. Beams*, 18(7):071303.

Hastings, J. B., Rudakov, F. M., Dowell, D. H., Schmerge, J. F., Cardoza, J. D., Castro, J. M., Gierman, S. M., Loos, H., and Weber, P. M. (2006). Ultrafast time-resolved electron diffraction with megavolt electron beams. *Appl. Phys. Lett.*, 89(18):184109.

Hauff, T., Jenko, F., Shalchi, A., and Schlickeiser, R. (2010). Scaling Theory for Cross-Field Transport of Cosmic Rays in Turbulent Fields. *Astrophys. J.*, 711(2):997–1007.

He, Z.-H., Nees, J. a., Hou, B., Krushelnick, K., and Thomas, a. G. R. (2014). Enhancement of plasma wakefield generation and self-compression of femtosecond laser pulses by ionization gradients. *Plasma Phys. Control. Fusion*, 56(8):084010.

Helm, R., Lee, M., Morton, P., and Sands, M. (1973). Evaluation of synchrotron radiation integrals. *IEEE Trans. Nucl. Sci*, 1193.

Herrmann, D., Homann, C., Tautz, R., Scharrer, M., Russell, P. S. J., Krausz, F., Veisz, L., and Riedle, E. (2010). Approaching the full octave: noncollinear optical parametric chirped pulse amplification with two-color pumping. *Opt. Express*, 18(18):18752–18762.

Hidding, B., Königstein, T., Osterholz, J., Karsch, S., Willi, O., and Pretzler, G. (2010). Monoenergetic Energy Doubling in a Hybrid Laser-Plasma Wakefield Accelerator. *Phys. Rev. Lett.*, 104(19):1–4.

Hidding, B., Rosenzweig, J., and Xi, Y. (2012). Beyond injection: Trojan horse underdense photocathode plasma wakefield acceleration. *AIP Conf. Proc.*, 1507(2002):570–575.

Hofmann, L. (2015). *Density characterization of supersonic gas jets for laser wake eld acceleration*. PhD thesis, Ludwig-Maximilians-Universität in München.

Hogan, M., Barnes, C., Clayton, C., Decker, F., Deng, S., Emma, P., Huang, C., Iverson, R., Johnson, D., Joshi, C., Katsouleas, T., Krejcik, P., Lu, W., Marsh, K., Mori, W., Muggli, P., OConnell, C., Oz, E., Siemann, R., and Walz, D. (2005). Multi-GeV Energy Gain in a Plasma-Wakefield Accelerator. *Phys. Rev. Lett.*, 95(5):054802.

Hogan, M. J., Raubenheimer, T. O., Seryi, A., Muggli, P., Katsouleas, T., Huang, C., Lu, W., An, W., Marsh, K. A., Mori, W. B., Clayton, C. E., and Joshi, C. (2010). Plasma wakefield acceleration experiments at FACET. *New J. Phys.*, 12(5):055030.

Holian, B. L., Hoover, W. G., Moran, B., and Straub, G. K. (1980). Shock-wave structure via nonequilibrium molecular dynamics and Navier-Stokes continuum mechanics. *Phys. Rev. A*, 22(6):2798–2808.

Holway, L. H. (1964). Existence of Kinetic Theory Solutions to the Shock Structure Problem. *Phys. Fluids*, 7(6):911.

Honda, M., Meyer-Ter-Vehn, J., and Pukhov, A. (2000). Collective stopping and ion heating in relativistic-electron-beam transport for fast ignition. *Phys. Rev. Lett.*, 85(10):2128–31.

Honrubia, J. J. and Murakami, M. (2015). Ion beam requirements for fast ignition of inertial fusion targets. *Phys. Plasmas*, 22(1):012703.

Huang, C., Lu, W., Zhou, M., Clayton, C., Joshi, C., Mori, W., Muggli, P., Deng, S., Oz, E., Katsouleas, T., Hogan, M., Blumenfeld, I., Decker, F., Ischebeck, R., Iverson, R., Kirby, N., and Walz, D. (2007). Hosing Instability in the Blow-Out Regime for Plasma-Wakefield Acceleration. *Phys. Rev. Lett.*, 99(25):255001.

Huang, K. (1987). *Statistical mechanics.* John Wiley, New York, 2nd ed edition.

Huntington, C., Thomas, a., McGuffey, C., Matsuoka, T., Chvykov, V., Kalintchenko, G., Kneip, S., Najmudin, Z., Palmer, C., Yanovsky, V., Maksimchuk, a., Drake, R., Katsouleas, T., and Krushelnick, K. (2011). Current Filamentation Instability in Laser Wakefield Accelerators. *Phys. Rev. Lett.*, 106(10):1–4.

Hurricane, O. A., Callahan, D. A., Casey, D. T., Celliers, P. M., Cerjan, C., Dewald, E. L., Dittrich, T. R., Döppner, T., Hinkel, D. E., Berzak Hopkins, L. F., Kline, J. L., Le Pape, S., Ma, T., MacPhee, A. G., Milovich, J. L., Pak, A., Park, H.-S., Patel, P. K., Remington, B. A., Salmonson, J. D., Springer, P. T., and Tommasini, R. (2014). Fuel gain exceeding unity in an inertially confined fusion implosion. *Nature*, 506(7488):343–8.

Jackson, J. D. (1999). *Classical electrodynamics.* Wiley, New York, 3rd ed. edition.

Jansen, O., Tückmantel, T., and Pukhov, a. (2014). Scaling electron acceleration in the bubble regime for upcoming lasers. *Eur. Phys. J. Spec. Top.*, 223(6):1017–1030.

Jasak, H. (2009). OpenF FOAM : Open sourcce CFD in research and industry. *Int. J. Nav. Archit. Ocean Eng.*, 1(2):89–94.

Joshi, C., Blue, B., Clayton, C. E., Dodd, E., Huang, C., Marsh, K. a., Mori, W. B., Wang, S., Hogan, M. J., OConnell, C., Siemann, R., Watz, D., Muggli, P., Katsouleas, T., and Lee, S. (2002). High energy density plasma science with an ultrarelativistic electron beam. *Phys. Plasmas*, 9(5):1845.

Joshi, C. and Mori, W. B. (2006). The status and evolution of plasma Wakefield particle accelerators. *Philos. Trans. A. Math. Phys. Eng. Sci.*, 364(1840):577–84.

Kallos, E., Katsouleas, T., Kimura, W., Kusche, K., Muggli, P., Pavlishin, I., Pogorelsky, I., Stolyarov, D., and Yakimenko, V. (2008). High-Gradient Plasma-Wakefield Acceleration with Two Subpicosecond Electron Bunches. *Phys. Rev. Lett.*, 100(7):3–6.

Kaluza, M., Mangles, S., Thomas, A., Najmudin, Z., Dangor, A., Murphy, C., Collier, J., Divall, E., Foster, P., Hooker, C., Langley, A., Smith, J., and Krushelnick, K. (2010). Observation of a Long-Wavelength Hosing Modulation of a High-Intensity Laser Pulse in Underdense Plasma. *Phys. Rev. Lett.*, 105(9):095003.

Karsch, S., Osterhoff, J., Popp, A., Rowlands-Rees, T. P., Major, Z., Fuchs, M., Marx, B., Hörlein, R., Schmid, K., Veisz, L., Becker, S., Schramm, U., Hidding, B., Pretzler, G., Habs, D., Grüner, F., Krausz, F., and Hooker, S. M. (2007). GeV-scale electron acceleration in a gas-filled capillary discharge waveguide. *New J. Phys.*, 9(11):415–415.

Katsouleas, T. (1986). Physical mechanisms in the plasma wake-field accelerator. *Phys. Rev. A*, 33(3).

Keinigs, R. and Jones, M. E. (1987). Two-dimensional dynamics of the plasma wakefield accelerator. *Phys. Fluids*, 30(1):252.

Keldysh, L. (1965). Ionization in the field of a strong electromagnetic wave. *Sov. Phys. JETP*, 20(5):1307–1314.

Kelley, P. (1965). Self-focusing of optical beams. *Phys. Rev. Lett.*, 15(26):1005–1008.

Key, M. H. (2007). Status of and prospects for the fast ignition inertial fusion concept. *Phys. Plasmas*, 14(5):055502.

Khrennikov, K., Wenz, J., Buck, a., Xu, J., Heigoldt, M., Veisz, L., and Karsch, S. (2015). Tunable All-Optical Quasimonochromatic Thomson X-Ray Source in the Nonlinear Regime. *Phys. Rev. Lett.*, 114(19):1–5.

Kim, H. T., Pae, K. H., Cha, H. J., Kim, I. J., Yu, T. J., Sung, J. H., Lee, S. K., Jeong, T. M., and Lee, J. (2013). Enhancement of Electron Energy to the Multi-GeV Regime by a Dual-Stage Laser-Wakefield Accelerator Pumped by Petawatt Laser Pulses. *Phys. Rev. Lett.*, 111(16):165002.

Kneip, S., McGuffey, C., Martins, J. L., Bloom, M. S., Chvykov, V., Dollar, F., Fonseca, R., Jolly, S., Kalintchenko, G., Krushelnick, K., Maksimchuk, a., Mangles, S. P. D., Najmudin, Z., Palmer, C. a. J., Phuoc, K. T., Schumaker, W., Silva, L. O., Vieira, J., Yanovsky, V., and Thomas, a. G. R. (2012). Characterization of transverse beam emittance of electrons from a laser-plasma wakefield accelerator in the bubble regime using betatron x-ray radiation. *Phys. Rev. Spec. Top. - Accel. Beams*, 15(2):021302.

Knuth, E. (1977). Dimerformation rate coefficients from measurements of terminal dimer concentrations in freejet expansions. *J. Chem. Phys.*, 66(8):3515–3525.

Kodama, R. (2002). Fast heating scalable to laser fusion ignition. *Nature*, 418(August):933–934.

Kodama, R., Norreys, P., Mima, K., and Dangor, A. (2001). Fast heating of ultrahigh-density plasma as a step towards laser fusion ignition. *Nature*, 412(August).

Kostyukov, I., Pukhov, a., and Kiselev, S. (2004). Phenomenological theory of laser-plasma interaction in "bubble" regime. *Phys. Plasmas*, 11(11):5256–5264.

Kotaki, H., Kawase, K., Hayashi, Y., and Mori, M. (2015). Direct Observation of the Pulse Width of an Ultrashort Electron Beam. *J. Phys. Soc. Japan*, 84(7):074501.

Krainov, V. and Ristic, V. (1992). Electron energy spectra in tunneling ionization of atoms and ions by a strong low-frequency electromagnetic field. *Sov. physics, JETP*, 74(4):789–792.

Krall, J. and Joyce, G. (1995). Transverse stability of the primary beam in the plasma wake-field accelerator. *Phys. Plasmas*, 2(4):1326.

Krall, J., Nguyen, K., and Joyce, G. (1989). Numerical simulations of axisymmetric erosion processes in ion-focused regime-transported beams. *Phys. Fluids B Plasma Phys.*, 1(10):2099.

Krejcik, P., Decker, E.-j., Emma, P., Hacker, K., Hendrickson, L., Connell, C. L. O., Schlarb, H., Smith, H., Stanek, M., Decker, F., and O'Connell, C. (2003). Commissioning of the SPPS linac bunch compressor. *Proc. 2003 Part. Accel. Conf.*, pages 423–425.

Kung, P., Lihn, H. C., Wiedemann, H., and Bocek, D. (1994). Generation and measurement of 50-fs (rms) electron pulses. *Phys. Rev. Lett.*, 73(7):967–970.

Lampe, M., Joyce, G., Slinker, S. P., and Whittum, D. H. (1993). Electron-hose instability of a relativistic electron beam in an ion-focusing channel. *Phys. Fluids B Plasma Phys.*, 5(6):1888.

Landau, L. D. and Lifshits, E. M. (1959). *Fluid Mechanics: Transl. from the Russian by JB Sykes and WH Reid.* Addison-Wesley.

Landgraf, B., Schnell, M., Sävert, A., Kaluza, M. C., and Spielmann, C. (2011). High resolution 3D gas-jet characterization. *Rev. Sci. Instrum.*, 82(8):083106.

Lawson, J. D. (1958). Perveance and the Bennett Pinch Relation in Partially-Neutralized Electron Beams. *J. Electron. Control*, 5(2):146–151.

Lee, J. W. and Stein, G. D. (1987). Structure change with size of argon clusters formed in laval nozzle beams. *J. Phys. Chem.*, 91(10):2450–2457.

Leemans, W. P., Geddes, C. G. R., Faure, J., Tóth, C., van Tilborg, J., Schroeder, C. B., Esarey, E., Fubiani, G., Auerbach, D., Marcelis, B., Carnahan, M. a., Kaindl, R. a., Byrd, J., and Martin, M. C. (2003). Observation of terahertz emission from a laser-plasma accelerated electron bunch crossing a plasma-vacuum boundary. *Phys. Rev. Lett.*, 91(August):074802.

Leemans, W. P., Gonsalves, a. J., Mao, H.-S., Nakamura, K., Benedetti, C., Schroeder, C. B., Tth, C., Daniels, J., Mittelberger, D. E., Bulanov, S. S., and Et Al. (2014). Multi-GeV Electron Beams from Capillary-Discharge-Guided Subpetawatt Laser Pulses in the Self-Trapping Regime. *Phys. Rev. Lett.*, 113(24):245002.

Leemans, W. P., Nagler, B., Gonsalves, A. J., Tóth, C., Nakamura, K., Geddes, C. G. R., Esarey, E., Schroeder, C. B., and Hooker, S. M. (2006). GeV electron beams from a centimetre-scale accelerator. *Nat. Phys.*, 2(10):696–699.

Li, R., Tang, C., Du, Y., Huang, W., Du, Q., Shi, J., Yan, L., and Wang, X. (2009). Experimental demonstration of high quality MeV ultrafast electron diffraction. *Rev. Sci. Instrum.*, 80(8):083303.

Liepmann, H. W. (1957). *Elements of gasdynamics.* John Wiley, New York.

Litos, M., Adli, E., An, W., Clarke, C. I., Clayton, C. E., Corde, S., Delahaye, J. P., England, R. J., Fisher, A. S., Frederico, J., Gessner, S., Green, S. Z., Hogan, M. J., Joshi, C., Lu, W., Marsh, K. a., Mori, W. B., Muggli, P., Vafaei-Najafabadi, N., Walz, D., White, G., Wu, Z., Yakimenko, V., and Yocky, G. (2014). High-efficiency acceleration of an electron beam in a plasma wakefield accelerator. *Nature*, 515(7525):92–95.

Littman, M., Kash, M., and Kleppner, D. (1978). Field-ionization processes in excited atoms. *Phys. Rev. Lett.*, 4(2):103–107.

Liu, J., Xia, C., Wang, W., Lu, H., Wang, C., Deng, a., Li, W., Zhang, H., Liang, X., Leng, Y., Lu, X., Wang, C., Wang, J., Nakajima, K., Li, R., and Xu, Z. (2011). All-Optical Cascaded Laser Wakefield Accelerator Using Ionization-Induced Injection. *Phys. Rev. Lett.*, 107(3):2–5.

Lu, W., Huang, C., Zhou, M., Mori, W. B., and Katsouleas, T. (2006a). Nonlinear Theory for Relativistic Plasma Wakefields in the Blowout Regime. *Phys. Rev. Lett.*, 96(16):165002.

Lu, W., Huang, C., Zhou, M., and Tzoufras, M. (2006b). A nonlinear theory for multidimensional relativistic plasma wave wakefields. *Phys. Plasmas*, 056709(2006).

Lu, W., Huang, C., Zhou, M., Tzoufras, M., Tsung, F. S., Mori, W. B., and Katsouleas, T. (2006c). A nonlinear theory for multidimensional relativistic plasma wave wakefields. *Phys. Plasmas*, 13(5):056709.

Lu, W., Huang, C., Zhou, M. M., Mori, W. B., and Katsouleas, T. (2005). Limits of linear plasma wakefield theory for electron or positron beams. *Phys. Plasmas*, 12(6):063101.

Lu, W., Tzoufras, M., Joshi, C., Tsung, F., Mori, W., Vieira, J., Fonseca, R., and Silva, L. (2007). Generating multi-GeV electron bunches using single stage laser wakefield acceleration in a 3D nonlinear regime. *Phys. Rev. Spec. Top. - Accel. Beams*, 10(6):1–12.

Lundh, O., Lim, J., Rechatin, C., Ammoura, L., Ben-Ismaïl, A., Davoine, X., Gallot, G., Goddet, J.-P., Lefebvre, E., Malka, V., and Faure, J. (2011). Few femtosecond, few kiloampere electron bunch produced by a laserplasma accelerator. *Nat. Phys.*, 7(3):219–222.

Lundh, O., Rechatin, C., Lim, J., Malka, V., and Faure, J. (2013). Experimental Measurements of Electron-Bunch Trains in a Laser-Plasma Accelerator. *Phys. Rev. Lett.*, 110(6):065005.

Malka, V. (2002). Electron Acceleration by a Wake Field Forced by an Intense Ultrashort Laser Pulse. *Science (80-.).*, 298(5598):1596–1600.

Malka, V., Faure, J., Gauduel, Y., and Lefebvre, E. (2008). Principles and applications of compact laserplasma accelerators. *Nat. Phys.*, 4(June).

Malka, V., Fritzler, S., Lefebvre, E., Aleonard, M.-M., Burgy, F., Chambaret, J.-P., Chemin, J.-F., Krushelnick, K., Malka, G., Mangles, S. P. D., Najmudin, Z., Pittman, M., Rousseau, J.-P., Scheurer, J.-N., Walton, B., and Dangor, A. E. (2002). Electron acceleration by a wake field forced by an intense ultrashort laser pulse. *Science*, 298(5598):1596–600.

Manahan, G. G., Brunetti, E., Aniculaesei, C., Anania, M. P., Cipiccia, S., Islam, M. R., Grant, D. W., Subiel, a., Shanks, R. P., Issac, R. C., Welsh, G. H., Wiggins, S. M., and Jaroszynski, D. a. (2014). Characterization of laser-driven single and double electron bunches with a permanent magnet quadrupole triplet and pepper-pot mask. *New J. Phys.*, 16(10):103006.

Mangles, S., Kaluza, M., and Thomas, A. (2005). Electron beam pointing instability in a self-injected laser wakefield accelerator. *Cent. Laser Facil. Annu. Rep. 2004/2005*, 4(2):11–13.

Mangles, S. P. D., Murphy, C. D., Najmudin, Z., Thomas, a. G. R., Collier, J. L., Dangor, a. E., Divall, E. J., Foster, P. S., Gallacher, J. G., Hooker, C. J., Jaroszynski, D. a., Langley, a. J., Mori, W. B., Norreys, P. a., Tsung, F. S., Viskup, R., Walton, B. R., and Krushelnick, K. (2004). Monoenergetic beams of relativistic electrons from intense laser-plasma interactions. *Nature*, 431(7008):535–538.

Mansfield, C. and Peck, E. (1969). Dispersion of helium. *J. Opt. Soc. Am.*, 59(2):199–204.

Martin, W., Caporaso, G., and Fawley, W. (1985). Electron-beam guiding and phase-mix damping by a laser-ionized channel. *Phys. Rev. Lett.*, 54(7):685–689.

Martinez, O. (1987). Design of high-power ultrashort pulse amplifiers by expansion and recompression. *IEEE J. Quantum Electron.*, 23(8):1385–1387.

Martinez de la Ossa, A., Grebenyuk, J., Mehrling, T., Schaper, L., and Osterhoff, J. (2013). High-Quality Electron Beams from Beam-Driven Plasma Accelerators by Wakefield-Induced Ionization Injection. *Phys. Rev. Lett.*, 111(24):245003.

Martins, S. F., Fonseca, R. A., Silva, L. O., Deng, S., Katsouleas, T., Tsung, F., Mori, W. B., and Angeles, L. (2004). Tunneling ionization in OSIRIS. In *EPS Conf. Plasma Phys.*, volume 28, page 33.

Massimo, F., Marocchino, a., Chiadroni, E., Ferrario, M., Mostacci, a., Musumeci, P., and Palumbo, L. (2014). Transformer ratio studies for single bunch plasma wakefield acceleration. *Nucl. Instruments Methods Phys. Res. Sect. A Accel. Spectrometers, Detect. Assoc. Equip.*, 740:242–245.

Masson-Laborde, P. E., Mo, M. Z., Ali, A., Fourmaux, S., Lassonde, P., Kieffer, J. C., Rozmus, W., Teychenne, D., and Fedosejevs, R. (2014). GeV electrons due to a transition from laser wakefield acceleration to plasma wakefield acceleration. *Phys. Plasmas*, 21(123113):1–12.

McAllister, R. W. and Hofstadter, R. (1956). Elastic Scattering of 188-Mev Electrons from the Proton and the Alpha Particle. *Phys. Rev.*, 102(3):851–856.

McGuffey, C., Thomas, A. G. R., Schumaker, W., Matsuoka, T., Chvykov, V., Dollar, F. J., Kalintchenko, G., Yanovsky, V., Maksimchuk, A., Krushelnick, K., Bychenkov, V. Y., Glazyrin, I. V., and Karpeev, A. V. (2010). Ionization Induced Trapping in a Laser Wakefield Accelerator. *Phys. Rev. Lett.*, 104(2):025004.

Mehrling, T. J. (2011). *Studying laser wakefield acceleration of relativistic electron bunches in inhomogeneous plasma with PIC simulations.* PhD thesis, Technische Universität München.

Menter, F. R. (1993). Zonal two equation k-turbulence models for aerodynamic flows. In *AIAA*, page 2906.

Miller, J. D., Schneider, R. F., Weidman, D. J., and Nguyen, K. T. (1992). Plasma wake-field effects on high-current relativistic electron beam transport in the ion-focused regime. *Phys. Fluids B Plasma Phys.*, 4(12):4121.

Milne, T. A. (1967). Mass Spectrometric Observations of Argon Clusters in Nozzle Beams. I. General Behavior and Equilibrium Dimer Concentrations. *J. Chem. Phys.*, 47(10):4095.

Milne, T. A., Vandegrift, A. E., and Greene, F. T. (1970). Mass-Spectrometric Observations of Argon Clusters in Nozzle Beams II. The Kinetics of Dimer Growth. *J. Chem. Phys.*, 52(1970):1552–1560.

Mora, P. and Antonsen, T. M. (1997). Kinetic modeling of intense, short laser pulses propagating in tenuous plasmas. *Phys. Plasmas*, 4(1):217–229.

Mori, W. B. (1997). The physics of the nonlinear optics of plasmas at relativistic intensities for short-pulse lasers. *IEEE J. Quantum Electron.*, 33(11):1942–1953.

Mourou, G., Tajima, T., and Bulanov, S. (2006). Optics in the relativistic regime. *Rev. Mod. Phys.*, 78(2):309–371.

Muggli, P., Blue, B., Clayton, C., Deng, S., Decker, F.-J., Hogan, M., Huang, C., Iverson, R., Joshi, C., Katsouleas, T., Lee, S., Lu, W., Marsh, K., Mori, W., O'Connell, C., Raimondi, P., Siemann, R., and Walz, D. (2004). Meter-Scale Plasma-Wakefield Accelerator Driven by a Matched Electron Beam. *Phys. Rev. Lett.*, 93(1):014802.

Muggli, P. and Hogan, M. J. (2009). Review of high-energy plasma wakefield experiments. *Comptes Rendus Phys.*, 10(2-3):116–129.

Munawar, I. and Ul, I. G. (2013). Electron Beam Guns for High Energy Electron Accelerators: An Overview. *J. Mod. Pysics*, 2013(November):1536–1539.

Murakami, A., Miyazawa, J., Tsuchiya, H., Murase, T., Ashikawa, N., Morisaki, T., Sakamoto, R., and Yamada, H. (2010). Characteristics of hydrogen supersonic cluster beam generated by a Laval nozzle. *J. Plasma Fusion Res. Ser.*, 9:79–83.

Murphy, C. D., Trines, R., Vieira, J., Reitsma, a. J. W., Bingham, R., Collier, J. L., Divall, E. J., Foster, P. S., Hooker, C. J., Langley, a. J., Norreys, P. a., Fonseca, R. a., Fiuza, F., Silva, L. O., Mendonca, J. T., Mori, W. B., Gallacher, J. G., Viskup, R., Jaroszynski, D. a., Mangles, S. P. D., Thomas, a. G. R., Krushelnick, K., and Najmudin, Z. (2006). Evidence of photon acceleration by laser wake fields. *Phys. Plasmas*, 13(3):033108.

Nakajima, K., Fisher, D., Kawakubo, T., Nakanishi, H., Ogata, A., Kato, Y., Kitagawa, Y., Kodama, R., Mima, K., Shiraga, H., Suzuki, K., Yamakawa, K., Zhang, T., Sakawa, Y., Shoji, T., Nishida, Y., Yugami, N., Downer, M., and Tajima, T. (1995). Observation of Ultrahigh Gradient Electron Acceleration by a Self-Modulated Intense Short Laser Pulse. *Phys. Rev. Lett.*, 74(22):984–984.

Nakanii, N., Kondo, K., Suzuki, S., Kobayashi, T., Asaka, T., Yanagida, K., Tsuji, K., Makino, K., Yamane, T., Yabuuchi, T., Miyamoto, S., Horikawa, K., Aratani, T., Kashihara, M., Mori, Y., Hanaki, H., Kitagawa, Y., Mima, K., and Tanaka, K. a. (2008). Absolute calibration of imaging plate for electron spectrometer measuring GeV-class electrons. *J. Phys. Conf. Ser.*, 112(3):032073.

Nerush, E. and Kostyukov, I. (2009). Carrier-Envelope Phase Effects in Plasma-Based Electron Acceleration with Few-Cycle Laser Pulses. *Phys. Rev. Lett.*, 103(3):035001.

Ng, J. S., Chen, P., Baldis, H., Bolton, P., Cline, D., Craddock, W., Crawford, C., Decker, F. J., Field, C., Fukui, Y., Kumar, V., Iverson, R., King, F., Kirby, R. E., Nakajima, K., Noble, R., Ogata, A., Raimondi, P., Walz, D., and Weidemann, A. W. (2001). Observation of plasma focusing of a 28.5 GeV positron beam. *Phys. Rev. Lett.*, 87(24):244801.

Norris, T. B. (1992). Femtosecond pulse amplification at 250 kHz with a Ti:sapphire regenerative amplifier and application to continuum generation. *Opt. Lett.*, 17(14):1009–1011.

Nozawa, I., Kan, K., Yang, J., Ogata, A., Kondoh, T., Gohdo, M., Norizawa, K., Kobayashi, H., Shibata, H., Gonda, S., and Yoshida, Y. (2014). Measurement of 20 fs bunch length using coherent transition radiation. *Phys. Rev. Spec. Top. - Accel. Beams*, 17(7):072803.

Ohkubo, T., Maekawa, A., Tsujii, R., Hosokai, T., Kinoshita, K., Kobayashi, K., Uesaka, M., Zhidkov, A., Nemoto, K., Kondo, Y., and Shibata, Y. (2007). Temporal characteristics of monoenergetic electron beams generated by the laser wakefield acceleration. *Phys. Rev. Spec. Top. - Accel. Beams*, 10:1–6.

Ohmae, G., Yagi, T., Nanri, K., and Fujioka, T. (2000). Spatial spectrum chirp characteristic of a Martinez-type multipass pulse stretcher. *Japanese J. Appl. Physics, Part 1 Regul. Pap. Short Notes Rev. Pap.*, 39(10):5864–5869.

O'Neil, T. M. (1971). Nonlinear Interaction of a Small Cold Beam and a Plasma. *Phys. Fluids*, 14(6):1204.

Osterhoff, J. (2009). *Stable, ultra-relativistic electron beams by laser-wakefield acceleration.* PhD thesis, Ludwig-Maximilians-Universität in München.

Osterhoff, J., Popp, a., Major, Z., Marx, B., Rowlands-Rees, T., Fuchs, M., Geissler, M., Hörlein, R., Hidding, B., Becker, S., Peralta, E., Schramm, U., Grüner, F., Habs, D., Krausz, F., Hooker, S., and Karsch, S. (2008). Generation of Stable, Low-Divergence Electron Beams by Laser-Wakefield Acceleration in a Steady-State-Flow Gas Cell. *Phys. Rev. Lett.*, 101(8):1–4.

Pak, A., Marsh, K., Martins, S., Lu, W., Mori, W., and Joshi, C. (2010). Injection and Trapping of Tunnel-Ionized Electrons into Laser-Produced Wakes. *Phys. Rev. Lett.*, 104(2):025003.

Pathak, V. B., Vieira, J., Fonseca, R. A., and Silva, L. O. (2012). Effect of the frequency chirp on laser wakefield acceleration. *New J. Phys.*, 14.

Perry, M. D., Ditmire, T., and Stuart, B. C. (1994). Self-phase modulation in chirped-pulse amplification. *Opt. Lett.*, 19(24):2149–2151.

Phuoc, K., Corde, S., Shah, R., Albert, F., Fitour, R., Rousseau, J.-P., Burgy, F., Mercier, B., and Rousse, A. (2006). Imaging Electron Trajectories in a Laser-Wakefield Cavity Using Betatron X-Ray Radiation. *Phys. Rev. Lett.*, 97(22):225002.

Phuoc, K. T., Burgy, F., Rousseau, J.-P., Malka, V., Rousse, A., Shah, R., Umstadter, D., Pukhov, A., and Kiselev, S. (2005). Laser based synchrotron radiation. *Phys. Plasmas*, 12(2):023101.

Piot, P. (2004). State-of-the-Art Electron Bunch Compression. *Proc. LINAC 2004*, pages 528–532.

Pirumov, U. G. (1986). *Gas flow in nozzles.* Springer-Verlag, Berlin.

Plateau, G. R., Geddes, C. G. R., Thorn, D. B., Chen, M., Benedetti, C., Esarey, E., Gonsalves, a. J., Matlis, N. H., Nakamura, K., Schroeder, C. B., Shiraishi, S., Sokollik, T., Tilborg, J. V., Toth, C., van Tilborg, J., Trotsenko, S., Kim, T. S., Battaglia, M., Stöhlker, T., Leemans, W. P., Rykovanov, S., and Stohlker, T. (2013). Low-Emittance Electron Bunches from a Laser-Plasma Accelerator Measured using Single-Shot X-Ray Spectroscopy. *Phys. Rev. Lett.*, 278(6):278–283.

Pollock, B., Clayton, C., Ralph, J., Albert, F., Davidson, a., Divol, L., Filip, C., Glenzer, S., Herpoldt, K., Lu, W., Marsh, K., Meinecke, J., Mori, W., Pak, a., Rensink, T., Ross, J., Shaw, J., Tynan, G., Joshi, C., and Froula, D. (2011). Demonstration of a Narrow Energy Spread, 0.5GeV Electron Beam from a Two-Stage Laser Wakefield Accelerator. *Phys. Rev. Lett.*, 107(4):1–4.

Popp, A. (2011). *Dynamics of electron-acceleration in laser-driven wakefields: Acceleration limits and asymmetric plasma waves.* PhD thesis, Ludwig-Maximilians-Universität in München.

Powers, N. D., Ghebregziabher, I., Golovin, G., Liu, C., Chen, S., Banerjee, S., Zhang, J., and Umstadter, D. P. (2013). Quasi-monoenergetic and tunable X-rays from a laser-driven Compton light source. *Nat. Photonics*, 8(1):28–31.

Pretzler, G., Kasper, A., and Witte, K. (2000). Angular chirp and tilted light pulses in CPA lasers. *Appl. Phys. B Lasers Opt.*, 70(1):1–9.

Pukhov, A. (2003). Strong field interaction of laser radiation. *Reports Prog. Phys.*, 65:R1–R55.

Pukhov, A. and Meyer-ter Vehn, J. (1997). Laser Hole Boring into Overdense Plasma and Relativistic Electron Currents for Fast Ignition of ICF Targets. *Phys. Rev. Lett.*, 79(14):2686–2689.

Pukhov, a. and Meyer-ter Vehn, J. (2002). Laser wake field acceleration: the highly non-linear broken-wave regime. *Appl. Phys. B Lasers Opt.*, 74(4-5):355–361.

Ralph, J. E., Marsh, K. a., Pak, a. E., Lu, W., Clayton, C. E., Fang, F., Mori, W. B., and Joshi, C. (2009). Self-Guiding of Ultrashort, Relativistically Intense Laser Pulses through Underdense Plasmas in the Blowout Regime. *Phys. Rev. Lett.*, 102(17):1–4.

Reiser, M. (1994). *Theory and design of charged particle beams.* John Wiley & Sons.

Ren, C., Duda, B. J., Hemker, R. G., Mori, W. B., Katsouleas, T., Antonsen, T. M., and Mora, P. (2001). Compressing and focusing a short laser pulse by a thin plasma lens. *Phys. Rev. E - Stat. Nonlinear, Soft Matter Phys.*, 63(2):026411.

Ren, C. and Mori, W. B. (2001). Physical picture for the laser hosing instability in a plasma. *Phys. Plasmas*, 8(6):3118–3119.

Roberts, T. and Bennett, W. (1968). The pinch effect in pulsed streams at relativistic energies. *Plasma Phys.*, 10:381–389.

Rosenzweig, J. (1987). Nonlinear Plasma Dynamics in the Plasma Wakefield Accelerator. *IEEE Trans. Plasma Sci.*, 15(2):186–191.

Rosenzweig, J., Barov, N., Thompson, M., and Yoder, R. (2004). Energy loss of a high-charge bunched electron beam in plasma: Analysis. *Phys. Rev. Spec. Top. - Accel. Beams*, 7(6):061301.

Rosenzweig, J., Breizman, B., Katsouleas, T., and Su, J. (1991). Acceleration and focusing of electrons in two-dimensional nonlinear plasma wake fields. *Phys. Rev. A*, 44(10).

Roth, M., Cowan, T., Key, M., Hatchett, S., Brown, C., Fountain, W., Johnson, J., Pennington, D., Snavely, R., Wilks, S., Yasuike, K., Ruhl, H., Pegoraro, F., Bulanov, S., Campbell, E., Perry, M., and Powell, H. (2001). Fast Ignition by Intense Laser-Accelerated Proton Beams. *Phys. Rev. Lett.*, 86(3):436–439.

Rousse, A., Ta Phuoc, K., Shah, R., Pukhov, A., Lefebvre, E., Malka, V., Kiselev, S., Burgy, F., Rousseau, J. P., Umstadter, D., and Hulin, D. (2004). Production of a keV X-ray beam from synchrotron radiation in relativistic laser-plasma interaction. *Phys. Rev. Lett.*, 93(September):1–4.

Ruth, R., Chao, A., Morton, P., and Wilson, P. (1985). A plasma wake field accelerator. *Part. Accel.*, 17:171–189.

Schlenvoigt, H.-P., Haupt, K., Debus, A., Budde, F., Jäckel, O., Pfotenhauer, S., Schwoerer, H., Rohwer, E., Gallacher, J. G., Brunetti, E., Shanks, R. P., Wiggins, S. M., and Jaroszynski, D. a. (2007). A compact synchrotron radiation source driven by a laser-plasma wakefield accelerator. *Nat. Phys.*, 4(2):130–133.

Schmid, K. (2009). *Supersonic Micro-Jets And Their Application to Few-Cycle Laser-Driven Electron Acceleration.* PhD thesis, Ludwig-Maximilians-Universität in München.

Schmidt, B. (1969). Electron beam density measurements in shock waves in argon. *J. Fluid Mech.*, 39(02):361.

Schoenlein, R. W., Leemans, W. P., Chin, A. H., Volfbeyn, P., Glover, T. E., Balling, P., Zolotorev, M., Kim, K., Chattopadhyay, S., and Shank, C. V. (1996). Femtosecond X-ray Pulses at 0.4Å Generated by 90° Thomson Scattering : A Tool for Probing the Structural Dynamics of Materials. *Science (80-.).*, 274(5285):236–238.

Schreiber, J., Bellei, C., Mangles, S. P. D., Kamperidis, C., Kneip, S., Nagel, S. R., Palmer, C. a. J., Rajeev, P. P., Streeter, M. J. V., and Najmudin, Z. (2010). Complete temporal characterization of asymmetric pulse compression in a laser wakefield. *Phys. Rev. Lett.*, 105(23):235003.

Schroeder, C. B., Lee, P. B., Wurtele, J. S., Esarey, E., and Leemans, W. P. (1999). Generation of ultrashort electron bunches by colliding laser pulses. *Phys. Rev. E. Stat. Phys. Plasmas. Fluids. Relat. Interdiscip. Topics*, 59(5 Pt B):6037–47.

Sciaini, G. and Miller, R. J. D. (2011). Femtosecond electron diffraction: heralding the era of atomically resolved dynamics. *Reports Prog. Phys.*, 74(9):096101.

Sears, C. M. S., Buck, A., Schmid, K., Mikhailova, J., Krausz, F., and Veisz, L. (2010a). Emittance and divergence of laser wakefield accelerated electrons. *Phys. Rev. Spec. Top. - Accel. Beams*, 13(9):092803.

Sears, C. M. S., Cuevas, S. B., Schramm, U., Schmid, K., Buck, A., Habs, D., Krausz, F., and Veisz, L. (2010b). A high resolution, broad energy acceptance spectrometer for laser wakefield acceleration experiments. *Rev. Sci. Instrum.*, 81(7):073304.

Seltzer, S. M. and Berger, M. J. (1985). Bremsstrahlung spectra from electron interactions with screened atomic nuclei and orbital electrons. *Nucl. Instruments Methods Phys. Res. Sect. B Beam Interact. with Mater. Atoms*, 12(1):95–134.

Sennyu, K., Inoue, F., Hara, H., Kanaoka, K., and Okihira, K. (2013). Industrialization of ILC From a View Point of Industry. In *IPAC2013*, pages 2110–2114.

Shadwick, B. a., Schroeder, C. B., and Esarey, E. (2009). Nonlinear laser energy depletion in laser-plasma accelerators. *Phys. Plasmas*, 16(5):056704.

Shalchi, A. (2011). Charged-particle transport in space plasmas: an improved theory for cross-field scattering. *Plasma Phys. Control. Fusion*, 53:074010.

Smith, R. A., Ditmire, T., and Tisch, J. W. G. (1998). Characterization of a cryogenically cooled high-pressure gas jet for laser/cluster interaction experiments. *Rev. Sci. Instrum.*, 69(11):3798.

Sprangle, P., Esarey, E., and Ting, A. (1990). Nonlinear theory of intense laser-plasma interactions. *Phys. Rev. Lett.*, 64(17):2011–2014.

Sprangle, P., Krall, J., and Esarey, E. (1994). Hose-modulation instability of laser pulses in plasmas. *Phys. Rev. Lett.*, 73(26):3544–3547.

Srinivasan, R. (2005). Dark Structures in Molecular Radiationless Transitions Determined by Ultrafast Diffraction. *Science (80-.).*, 307(5709):558–563.

Strickland, D. and Mourou, G. (1985). Compression of amplified chirped optical pulses. *Opt. Commun.*, 55(6):447–449.

Su, J., Dawson, J., Katsouleas, T., Wilks, S., Chen, P., Jones, M., and Keinigs, R. (1987). Stability of the driving bunch in the plasma wakefield accelerator. *IEEE Trans. Plasma Sci.*, 15(2):192–198.

Su, J., Katsouleas, T., Dawson, J., and Fedele, R. (1990). Plasma lenses for focusing particle beams. *Phys. Rev. A*, 41(6):3321–3331.

Swanekamp, S. B., Holloway, J. P., Kammash, T., and Gilgenbach, R. M. (1992). The theory and simulation of relativistic electron beam transport in the ion-focused regime. *Phys. Fluids B Plasma Phys.*, 4(5):1332–1348.

Ta Phuoc, K., Corde, S., Thaury, C., Malka, V., Tafzi, A., Goddet, J. P., Shah, R. C., Sebban, S., and Rousse, A. (2012). All-optical Compton gamma-ray source. *Nat. Photonics*, 6(5):308–311.

Tabak, M., Hammer, J., Glinsky, M. E., Kruer, W. L., Wilks, S. C., Woodworth, J., Campbell, E. M., Perry, M. D., and Mason, R. J. (1994). Ignition and high gain with ultrapowerful lasers. *Phys. Plasmas*, 1(5):1626.

Tajima, T. and Dawson, J. (1979). Laser electron accelerator. *Phys. Rev. Lett.*, 43(4):267–270.

Takagi, T., Yamada, I., and Sasaki, A. (1975). Ionized-cluster beam deposition. *J. Vac. Sci. Technol.*, 12(6):1128.

Takayama, K. and Hiramatsu, S. (1988). Ion-channel guiding in a steady-state free-electron laser. *Phys. Rev. A*, 37(1):173–177.

Thaury, C., Guillaume, E., Döpp, a., Lehe, R., Lifschitz, a., Ta Phuoc, K., Gautier, J., Goddet, J.-P., Tafzi, a., Flacco, a., Tissandier, F., Sebban, S., Rousse, a., and Malka, V. (2015). Demonstration of relativistic electron beam focusing by a laser-plasma lens. *Nat. Commun.*, 6:6860.

Thomas, L. H. (1944). Note on Becker's Theory of the Shock Front. *J. Chem. Phys.*, 12(11):449.

Ting, A., Esarey, E., and Sprangle, P. (1990). Nonlinear wake-field generation and relativistic focusing of intense laser pulses in plasmas. *Phys. Fluids B Plasma Phys.*, 2(6):1390.

Tokita, S., Hashida, M., Inoue, S., Nishoji, T., Otani, K., and Sakabe, S. (2010). Single-Shot Femtosecond Electron Diffraction with Laser-Accelerated Electrons: Experimental Demonstration of Electron Pulse Compression. *Phys. Rev. Lett.*, 105(21):215004.

Tomassini, P. and Giulietti, A. (2001). A generalization of Abel inversion to non-axisymmetric density distribution. *Opt. Commun.*, 199(November):143–148.

Treacy, E. (1969). Optical pulse compression with diffraction gratings. *IEEE J. Quantum Electron.*, 5(9):454–458.

Trisorio, A., Paul, P. M., Ple, F., Ruchert, C., Vicario, C., and Hauri, C. P. (2011). Ultrabroadband TW-class Ti:sapphire laser system with adjustable central wavelength, bandwidth and multi-color operation. *Opt. Express*, 19(21):20128.

Tsung, F. S., Ren, C., Silva, L. O., Mori, W. B., and Katsouleas, T. (2002). Generation of ultra-intense single-cycle laser pulses by using photon deceleration. *Proc. Natl. Acad. Sci. U. S. A.*, 99(1):29–32.

Uhm, H. S. and Joyce, G. (1991). Theory of wake-field effects of a relativistic electron beam propagating in a plasma. *Phys. Fluids B Plasma Phys.*, 3(7):1587.

Umstadter, D., Chen, S.-Y., Maksimchuk, A., Mourou, G., and Wagner, R. (1996). Nonlinear Optics in Relativistic Plasmas and Laser Wake Field Acceleration of Electrons. *Science (80-.).*, 273(5274):472–475.

Uribe, F. (2011). The Shock Wave Problem Revisited: The NavierStokes Equations and Brenners Two Velocity Hydrodynamics. In Gorban, A. N. and Roose, D., editors, *Coping with Complex. Model Reduct. Data Anal.*, volume 75 of *Lecture Notes in Computational Science and Engineering*, pages 207–229. Springer Berlin Heidelberg.

Vafaei-Najafabadi, N., Marsh, K. a., Clayton, C. E., An, W., Mori, W. B., Joshi, C., Lu, W., Adli, E., Corde, S., Litos, M., Li, S., Gessner, S., Frederico, J., Fisher, A. S., Wu, Z., Walz, D., England, R. J., Delahaye, J. P., Clarke, C. I., Hogan, M. J., and Muggli, P. (2014). Beam Loading by Distributed Injection of Electrons in a Plasma Wakefield Accelerator. *Phys. Rev. Lett.*, 112(2):025001.

van Tilborg, J., Schroeder, C., Filip, C., Tóth, C., Geddes, C., Fubiani, G., Huber, R., Kaindl, R., Esarey, E., Leemans, W., and vanTilborg, J. (2006). Temporal Characterization of Femtosecond Laser-Plasma-Accelerated Electron Bunches Using Terahertz Radiation. *Phys. Rev. Lett.*, 96(1):014801.

Vieira, J. (2014). Hosing Instability Suppression in Self-Modulated Wakes Driven by Non-Uniform Density Profile Particle Bunches. In *IPAC2014*, page 1473.

Vieira, J., Fiúza, F., Silva, L. O., Tzoufras, M., and Mori, W. B. (2010). Onset of self-steepening of intense laser pulses in plasmas. *New J. Phys.*, 12(4):045025.

Vieira, J., Mori, W. B., and Muggli, P. (2014). Hosing instability suppression in self-modulated plasma wakefields. *Phys. Rev. Lett.*, 112(20):205001.

Walker, P. A., Bourgeois, N., Rittershofer, W., Cowley, J., Kajumba, N., Maier, A. R., Wenz, J., Werle, C. M., Symes, D. R., Rajeev, P. P., and Others (2012). Electron acceleration driven in plasma channels at the Astra-Gemini laser facility. In *AIP Conf. Proc.*, volume 1507, pages 193–198. AIP Publishing.

Wang, H. Y., Lin, C., Sheng, Z. M., Liu, B., Zhao, S., Guo, Z. Y., Lu, Y. R., He, X. T., Chen, J. E., and Yan, X. Q. (2011). Laser Shaping of a Relativistic Intense, Short Gaussian Pulse by a Plasma Lens. *Phys. Rev. Lett.*, 107(26):265002.

Wang, X., Zgadzaj, R., Fazel, N., Li, Z., Yi, S. a., Zhang, X., Henderson, W., Chang, Y.-Y., Korzekwa, R., Tsai, H.-E., Pai, C.-H., Quevedo, H., Dyer, G., Gaul, E., Martinez, M., Bernstein, a. C., Borger, T., Spinks, M., Donovan, M., Khudik, V., Shvets, G., Ditmire, T., and Downer, M. C. (2013). Quasi-monoenergetic laser-plasma acceleration of electrons to 2GeV. *Nat. Commun.*, 4(May):1988.

Weingartner, R., Fuchs, M., Popp, a., Raith, S., Becker, S., Chou, S., Heigoldt, M., Khrennikov, K., Wenz, J., Seggebrock, T., Zeitler, B., Major, Z., Osterhoff, J., Krausz, F., Karsch, S., and Grüner, F. (2011). Imaging laser-wakefield-accelerated electrons using miniature magnetic quadrupole lenses. *Phys. Rev. Spec. Top. - Accel. Beams*, 14(5):1–7.

Weingartner, R., Raith, S., Popp, A., Chou, S., Wenz, J., Khrennikov, K., Heigoldt, M., Maier, A. R., Kajumba, N., Fuchs, M., Zeitler, B., Krausz, F., Karsch, S., and Grüner, F. (2012). Ultralow emittance electron beams from a laser-wakefield accelerator. *Phys. Rev. Spec. Top. - Accel. Beams*, 15(11):111302.

Whitham, G. B. (1958). On the propagation of shock waves through regions of non-uniform area or flow. *J. Fluid Mech.*, 4(04):337–360.

Whittum, D. (1997). Electron-hose instability in an annular plasma sheath. *J. Phys. D. Appl. Phys.*, 30(21):2958.

Whittum, D., Sharp, W., Simon, S., Lampe, M., and Joyce, G. (1991). Electron-hose instability in the ion-focused regime. *Phys. Rev. Lett.*, 67(8):991–994.

Wittmann, T., Horvath, B., Helml, W., Schätzel, M. G., Gu, X., Cavalieri, A. L., Paulus, G. G., and Kienberger, R. (2009). Single-shot carrier-envelope phase measurement of few-cycle laser pulses. *Nat. Phys.*, 5(5):357–362.

Wörmer, J., Guzielski, V., Stapelfeldt, J., and Möller, T. (1989). Fluorescence excitation spectroscopy of xenon clusters in the VUV. *Chem. Phys. Lett.*, 159(4):321–326.

Wu, H.-C., Tajima, T., Habs, D., Chao, A., and Meyer-ter Vehn, J. (2010). Collective deceleration: Toward a compact beam dump. *Phys. Rev. Spec. Top. - Accel. Beams*, 13(10):1–8.

Yan, J., Zhao, H., and Kuriyagawa, T. (2009). Effects of tool edge radius on ductile machining of silicon: an investigation by FEM. *Semicond. Sci. Technol.*, 24(7):075018.

Yang, J. and Huang, J. (1995). Rarefied Flow Computations Using Nonlinear Model Boltzmann Equations.

Yang, J., Kondoh, T., Kan, K., Kozawa, T., Yoshida, Y., and Tagawa, S. (2006). Femtosecond single electron bunch generation by rotating longitudinal bunch phase space in magnetic field. *Nucl. Instruments Methods Phys. Res. Sect. A Accel. Spectrometers, Detect. Assoc. Equip.*, 556(1):52–56.

Yang, J., Sakai, F., Yanagida, T., Yorozu, M., Okada, Y., Takasago, K., Endo, A., Yada, A., and Washio, M. (2002). Low-emittance electron-beam generation with laser pulse shaping in photocathode radio-frequency gun. *J. Appl. Phys.*, 92(3):1608.

Yang, S.-N. and Lu, T.-M. (1985). Condensation of metal and semiconductor vapors during nozzle expansion. *J. Appl. Phys.*, 58(1):541.

Yeremian, A. D., Adolphsen, C., Chan, J., Decontreras, G., Fant, K., Nantista, C., National, S., and Park, M. (2015). LCLS-II HIGH POWER RF SYSTEM OVERVIEW AND PROGRESS. *SLAC-PUB-16408*, pages 2–5.

Yin, L., Albright, B. J., Hegelich, B. M., Bowers, K. J., Flippo, K. a., Kwan, T. J. T., and Fernandez, J. C. (2007). Monoenergetic and GeV ion acceleration from the laser breakout afterburner using ultrathin targets. *Phys. Plasmas*, 14(5):056706.

Zeldovich, Y. B. Y. B. (2002). *Physics of shock waves and high-temperature hydrodynamic phenomena*. Dover Publications, Mineola, N.Y.

Zhidkov, a., Koga, J., Kinoshita, K., and Uesaka, M. (2004). Effect of self-injection on ultraintense laser wake-field acceleration. *Phys. Rev. E*, 69(3):035401.

Acknowledgment

First of all, I want to thank Prof. Dr. László Veisz for his great support during my PhD as well as a good friend. He is the one who teaches me most of knowledge. I would also like to thank Prof. Dr. Stefan Karsch who accepted my application and offered me the opportunity to start my career in his group. The most important person is Prof. Ferenc Krausz who funds the high-field and attosecond physics group. With his enthusiasm, there is little to be worried about the funding of research. I would like to thank Prof. Dr. Malte Kaluza to be the reviewer of my thesis. Many thanks go to the ATLAS, PFS and FEL teams: Johannes Wenz, Matthias Heigoldt, Konstantin Khrennikov, Antonia Schmalz, Sandro Klingebiel, Christoph Wandt, Christoph Skrobol, Alexander Kessel, Mathias Krüger, Andreas Münzer, Olga Lysov, Zsuzsanna Major and Rapheal Weingartner. They are not only good colleagues and friends but also gave me a memorable time during my study. Especially Johannes Wenz, with whom I learned most of my knowledge regarding German culture, and he is always a faithful and helpful friend. I would like to thank members of LWS-20 team: Daniel Cardenas, Luisa Hofmann, who spent most of time with me in the lab; Matthew Weidman who correct my poor English and share his life experience; Daniel Rivas, Boris Bergues, Antonin Borot, Dmitri Kormin, Alexander Muschet, Jeryl Tan and Pascal Weinert, who build up a friendly environment and offer me a lot of help. I would like to thank our former members: Jiancai Xu and Guangjin Ma, with whom I shared a pleasant period in the lab and office. Other many external members such as Jianhui Bin, Wenjun Ma and Casey Chew offer me a lot of support. My PhD would be much more difficult and tougher without their care and valuable opinions. In the end, I want to thank all of people who accompany me through this long journey.